MICHIGAN STATE UNIVERSITY LIBRARIES
3 1293 00629 4999
L24980675
L
LIBRARY
Michigan State
University

This is to certify that the

dissertation entitled

CONTROL OF SINGLE-LINK FLEXIBLE MANIPULATORS FABRICATED FROM ADVANCED COMPOSITE LAMINATES AND SMART MATERIALS INCORPORATING ELECTRO-RHEOLOGICAL FLUIDS

presented by

SEUNG-BOK CHOI

has been accepted towards fulfillment
of the requirements for

Ph.D. degree in M.E.

M.V. Gandhi
Major professor

Date 1 May 1990

MSU is an Affirmative Action/Equal Opportunity Institution

O-12771

PLACE IN RETURN BOX to remove this checkout from your record.
TO AVOID FINES return on or before date due.

DATE DUE	DATE DUE	DATE DUE
158		
OCT 29		

MSU Is An Affirmative Action/Equal Opportunity Institution

CONTROL OF SINGLE-LINK FLEXIBLE MANIPULATORS FABRICATED FROM ADVANCED COMPOSITE LAMINATES AND SMART MATERIALS INCORPORATING ELECTRO-RHEOLOGICAL FLUIDS

by

Seung-Bok Choi

A DISSERTATION

Submitted to
Michigan State University
in partial fulfillment of the requirements
for the degree of

DOCTOR OF PHILOSOPHY

Department of Mechanical Engineering

1990

605966

ABSTRACT

CONTROL OF SINGLE-LINK FLEXIBLE MANIPULATORS FABRICATED FROM ADVANCED COMPOSITE LAMINATES AND SMART MATERIALS INCORPORATING ELECTRO-RHEOLOGICAL FLUIDS

By

Seung-Bok Choi

Three different control schemes for a single-link flexible manipulator fabricated from composite laminates or smart materials incorporating electro-rheological fluids are developed in this study ; an output feedback controller, a hybrid controller, and a nonlinear state feedback controller.

The output feedback controller featuring two colocated sensors is designed by utilizing the root-locus technique and the Lyapunov method after a description of the dynamic modeling of the flexible manipulator. It is shown in the analytical and experimental investigation that the arm fabricated from composite laminates has superior system performances such as faster settling-time, smaller input torque, smaller overshoot, and superior stability characteristics relative to the arm fabricated from aluminum.

The hybrid controller which consists of an output feedback controller and a pseudo-state feedback controller is proposed for the flexible manipulator fabricated from smart materials incorporating

electro-rheological fluids. A phenomenological equation of motion is developed from experimental observations of the modal characteristics. And an empirical model of a distributed electro-rheological fluid actuator which characterizes the pseudo-state feedback controller is obtained as an explicit function of the electrical intensities. It is shown in the experimental implementation that the robustness of the output feedback controller subjected to a disturbance which has a forcing frequency close to the clamped-mode natural frequency of the arm is impressively enhanced by employing the proposed pseudo-state feedback controller.

The nonlinear state feedback controller, which is robust to system parameter variations caused by uncertain parameters such as varying payload and mismatched lamina angle, is developed for the flexible manipulator fabricated from composite laminates. The effects of each uncertain parameter as well as the interaction of all parameters are considered without assuming matching conditions. The properties of the uniform and uniform ultimate boundedness of the solution of system state equations are employed to formulate the controller. It is demonstrated through the simulation that the proposed nonlinear feedback controller has much better capability of arresting the unwanted vibration than the linear controller in the presence of the uncertain parameters.

This thesis is dedicated to the memory of my father, Kyung-Hyun Choi (1909-1988) and father-in-law, Hong-Nam Kim (1931-1989), who passed away during the course of this research program. Their immense love and sacrifices remain forever.

ACKNOWLEDGMENTS

I would like to express my deepest gratitude and appreciation to my co-advisors, Dr. Brian S. Thompson and Dr. Mukesh V. Gandhi, for their expert guidance, friendship and continuous encouragement throughout the course of this research program, and for providing the unique research environment. Sincere appreciation is extended to the other guidance committee, Dr. Steven W. Shaw and Dr. David H.Y. Yen, for their valuable comments and suggestions. I also thank Dr. Clark Radcliffe for his constructive comments on this research.

Particular gratitude goes to my lovely wife Yeon-Ook, my smart son Min-Kyu and my pretty daughter Eun-Young for being a wonderful family with patience and understanding.

I, of course, wish to express sincere gratitude to my mother, Bo-Bae Cho, mother-in-law, Soon-Sun Jang, eldest brother, Seung-Bae and his wife Soon-Lim Lee, elder brother, Seung-Keun and his wife Keun-Soon Kim, younger sister, Seung-Yi and her husband Young-Hyun Kim, brother-in-law, Ha Kim and his wife Soon-Lim Bae, and sister-in-law, Hyo-Sook Kim, for their providing moral support and encouragement.

Special thanks go to my friends at Michigan State University for making my graduate career a successful experience. Also, I would like to thank all the students in Machinery Elastodynamics Laboratory and Intelligent Materials and Structures Laboratory for their technical assistance.

Finally, I wish to gratefully acknowledge the financial support of this research program by the Defence Advanced Research Projects Agency, under contract DAAL03-87-K-0018, the U.S. Army Research Office, under contract DAAL03-K-0022, and also the State of Michigan, Department of Commerce, Research Excellence and Economic Development Fund.

TABLE OF CONTENTS

	Page
LIST OF TABLES	x
LIST OF FIGURES	xi
CHAPTER I. INTRODUCTION	1
1.1 Motivation	1
1.2 Literature Review	4
1.2.1 Dynamic Modeling	5
1.2.2 Controller Design	11
1.2.3 Related Works on Modeling and Active Control of Large Flexible Structures	19
1.2.4 Related Works on Smart Materials and Structures	26
1.3 Thesis Organization	36
1.4 Principal Contributions	38
CHAPTER II. MODELING OF A SINGLE-LINK FLEXIBLE MANIPULATOR FABRICATED FROM ADVANCED COMPOSITE LAMINATES	41
2.1 Introduction	41
2.2 Derivation of Equations of Motion	42
2.3 Finite Element Formulation	50
2.4 State Space Representation of the Model	53
2.5 Summary of the Chapter	56
CHAPTER III. EXPERIMENTAL APPARATUS AND IDENTIFICATION OF SYSTEM MODEL PARAMETERS	57
3.1 Introduction	57
3.2 Experimental Apparatus	57
3.2.1 Flexible Arm	59
3.2.1.1 Aluminum Arm	59
3.2.1.2 Composite Arm	61
3.2.2 DC Motor and Servo-Drive	66

3.2.3 Servo-Positioning Assembly 67
3.2.4 Sensors 68
3.2.4.1 Angular Position Sensor 68
3.2.4.2 Angular Velocity Sensor 68
3.2.4.3 Tip Deflection Sensor 69
3.2.5 Microprocessor 70
3.3 Identification of System Model Parameters 71
3.3.1 Predicted 72
3.3.2 Measured 81
3.4 Summary of the Chapter 87

CHAPTER IV. OUTPUT FEEDBACK CONTROL ASSOCIATED WITH TWO COLOCATED OUTPUT SENSORS 88
4.1 Introduction 88
4.2 Controller Design 89
4.3 Implementation Results and Discussions 99
4.3.1 Step Responses without Disturbances 101
4.3.2 Step Responses with Disturbances 117
4.3.3 Instability of the System 128
4.4 Summary of the Chapter 136

CHAPTER V. HYBRID CONTROL FEATURING A DISTRIBUTED ELECTRO-RHEOLOGICAL FLUID ACTUATOR 138
5.1 Introduction 138
5.2 Background on Electro-Rheological Fluids 139
5.3 Phenomenological Equation of Motion 144
5.4 Controller Formulation 151
5.5 Experimental Implementation 162
5.5.1 Apparatus and Instrumentation 162
5.5.2 Results and Discussions 170
5.6 Summary of the Chapter 181

CHAPTER VI. NONLINEAR STATE FEEDBACK CONTROL ROBUST TO SYSTEM PARAMETER VARIATIONS 183
6.1 Introduction 183
6.2 Problem Formulation 185

6.3 Controller Design 190
6.4 Illustrative Example 209
6.5 Summary of the Chapter 222

CHAPTER VII. CONCLUSIONS AND RECOMMENDATIONS 224
7.1 Conclusions of the Thesis 224
7.2 Recommendations for Future Work 227

APPENDIX 231
List of Publications 231
BIBLIOGRAPHY 236

LIST OF TABLES

		Page
Table 3.1	Material and Geometrical Properties of the Aluminum Arm	60
Table 3.2	Material and Geometrical Properties of the Composite Arm	64
Table 3.3	Comparison of the System Model Parameters of the Aluminum and Composite Arm without Payload	73
Table 3.4	Comparison of the System Model Parameters of the Aluminum and Composite Arm with Payload of 0.061 kg	73
Table 3.5	Comparison of the Calculated and Measured Natural Frequency without Payload	85
Table 3.6	Comparison of the Calculated and Measured Natural Frequency with Payload of 0.061 kg	85
Table 4.1	Closed-Loop Poles with the Compensator Zero Z_{co} = -2	102
Table 4.2	Closed-Loop Poles with the Compensator Zero Z_{co} = -5	107
Table 4.3	Closed-Loop Poles with the Compensator Zero Z_{co} = -1	111
Table 4.4	Closed-Loop Poles with K_p=0.406, K_v=0.254 for the Aluminum Arm, and K_p= 0.403, K_v= 0.252 for the Composite Arm	114
Table 5.1	Coherence Factor of the First and Second Mode at Different Voltage	149
Table 5.2	Measured System Model Parameters of the Smart ER Arm in the Absence of the Electric Field	169
Table 6.1	Geometrical and Material Properties of the Nominal Composite Arm	210
Table 6.2	System Model Parameters of the Nominal System	212
Table 6.3	Comparison of the Tip Displacement Response (Settling Time and Maximum Overshoot)	220

LIST OF FIGURES

		Page
Figure 2.1	Schematic Diagram of a Single-Link Flexible Manipulator	43
Figure 2.2	Composite Laminate Configuration	44
Figure 2.3	Two-Node Beam Element	51
Figure 3.1	Photograph of Overall Robotic System	58
Figure 3.2	Schematic Diagram of Overall Robotic System	58
Figure 3.3	Photograph of the Experimental Aluminum Arm	59
Figure 3.4	Design Methodology of the Composite Arm	62
Figure 3.5	Curing Cycle for AS4/3501 Graphite-Epoxy	63
Figure 3.6	Photograph of the Experimental Composite Arm	65
Figure 3.7	Load-Deflection Curve for the Aluminum and Composite Arm	66
Figure 3.8	Relationship between the Velocity and the Measured Voltage of the Tachometer	69
Figure 3.9	Relationship between the Amplified Voltage and the Tip (End-Point) Deflection	70
Figure 3.10	Frequency Variation with respect to the Ratio of the Hub Moment of Inertia to the Beam Moment of Inertia	76
Figure 3.11	Frequency Variation with respect to the Ratio of the Payload to the Beam Mass	77
Figure 3.12	First Three Pinned-Mode Shape for the Aluminum and Composite Arm	78
Figure 3.13	Calculated Open-Loop Transfer Function for the Angular Velocity without Payload	79
Figure 3.14	Calculated Open-Loop Transfer Function for the Angular Velocity with Payload of 0.061 kg	80
Figure 3.15	Calculated and Measured Frequency Response of the Aluminum Arm without Payload	83

Figure 3.16 Calculated and Measured Frequency Response of the Composite Arm without Payload 84

Figure 3.17 Calculated Open-Loop Transfer Function for the Angular Velocity with $\dot{\theta}(s)=(s/(s/a+1))\theta(s)$ 86

Figure 4.1 Block-Diagram of the Output Feedback Control System 89

Figure 4.2 Open-Loop Pole-Zero Location with the Compensator Zero Z_{co}= -1 91

Figure 4.3 Root-Locus with the Compensator Zero Z_{co}= -1 92

Figure 4.4 Open-Loop Pole Zero Location with the Compensator Zero Z_{co}= -15 94

Figure 4.5 Root-Locus with the Compensator Zero Z_{co}= -15 95

Figure 4.6 Experimental Set-Up for Output Measurements 99

Figure 4.7 Circuit Diagram of Two Channel Operational Amplifier 100

Figure 4.8 Measured Step Responses without Payload. K_p=0.534, K_v=0.267 for the Aluminum Arm, and K_p=0.292, K_v=0.146 for the Composite Arm 103

Figure 4.9 Simulated Step Responses without Payload. K_p=0.534, K_v=0.267 for the Aluminum Arm, and K_p=0.292, K_v=0.146 for the Composite Arm 104

Figure 4.10 Simulated Open-Loop Step Responses of the Aluminum Arm without Payload 105

Figure 4.11 Measured Step Responses without Payload. K_p=1.0 and K_v=0.2 for both Aluminum and Composite Arms 108

Figure 4.12 Simulated Step Responses without Payload. K_p=1.0 and K_v=0.2 for both Aluminum and Composite Arms 109

Figure 4.13 Measured Step Responses with Payload of 0.061 kg. K_p=K_v=0.48 for the Aluminum Arm, and K_p=K_v=0.24 for the Composite Arm 112

Figure 4.14 Simulated Step Responses with Payload of 0.061 kg. K_p=K_v=0.48 for the Aluminum Arm, and K_p=K_v=0.24 for the Composite Arm 113

Figure 4.15 Measured Step Responses without Payload. K_p=0.406, K_v=0.254 for the Aluminum Arm, and K_p=0.403, K_v=0.252 for the Composite Arm 115

Figure 4.16 Simulated Step Responses without Payload. K_p=0.406, K_v=0.254 for the Aluminum Arm, and K_p=0.403, K_v=0.252 for the Composite Arm 116

Figure 4.17 Block-Diagram of the PD Output Feedback Control System with the Disturbance of $\tilde{d}(t)$ 118

Figure 4.18 Measured Step Responses of the Aluminum Arm without Payload. K_p= 0.534, K_v= 0.267, and $\tilde{d}(t)$=0.08 sin(3.25 Hz)t 120

Figure 4.19 Comparison of the Measured Step Responses of the Aluminum Arm with and without the Disturbance. K_p=0.534, K_v=0.267 and $\tilde{d}(t)$=0.08 sin(3.25 Hz)t 121

Figure 4.20 Comparison of the Simulated and Measured Step Responses of the Aluminum Arm with the Disturbance. K_p=0.534, K_v=0.267 and $\tilde{d}(t)$=0.08 sin(3.25 Hz)t 122

Figure 4.21 Measured Step Responses of the Composite Arm without Payload. K_p=0.292, K_v=0.146 and $\tilde{d}(t)$=0.08 sin(4.75 Hz)t 124

Figure 4.22 Comparison of the Measured Step Responses of the Composite Arm with and without the Disturbance. K_p=0.292, K_v=0.146, and $\tilde{d}(t)$=0.08 sin(4.75 Hz)t 125

Figure 4.23 Comparison of the Simulated and Measured Step Responses of the Composite Arm with the Disturbance. K_p=0.292, K_v=0.146 and $\tilde{d}(t)$=0.08 sin(4.75 Hz)t 126

Figure 4.24 Measured Step Responses of the Composite Arm without Payload. K_p= 0.292, K_v= 0.146, and $\tilde{d}(t)$=0.4 sin(34.5 Hz)t 127

Figure 4.25 In-Position Band of the Servo-Drive System 129

Figure 4.26 Measured Step Responses of the Aluminum Arm without Payload. K_p=6.2 and K_v=0.4 131

Figure 4.27 Simulated Step Responses of the Aluminum Arm without Payload. K_p=6.2 and K_v=0.4 132

Figure 4.28 Measured Step Responses with Feedback Gains of K_p=6.2 and K_v=0.4 for both Aluminum and Composite Arms 133

Figure 4.29 Measured Step Responses of the Composite Arm without Payload. K_p= 11.8 and K_v= 0.4 134

Figure 4.30 Simulated Step Responses of the Composite Arm without Payload. K_p= 11.8 and K_v= 0.4 135

Figure 5.1 Electro-Rheological Fluid in Liquid and Solid State 140

Figure 5.2 Interaction between Charges on Electrodes and Those in Electro-Rheological Fluid 141

Figure 5.3 Photomicrograph of Electro-Rheological Fluid 142

Figure 5.4 Smart Cantilevered Beam Structure 146

Figure 5.5 Mode Shapes of the Smart Cantilevered Beam 147

Figure 5.6 Measured Frequency Response of the Smart ER Arm without Payload 155

Figure 5.7 Governing Characteristics of the Employed Electro-Rheological Fluid Actuator 157

Figure 5.8 Block-Diagram of the Hybrid Control System 159

Figure 5.9 Bang-off-Bang Type Input Voltage 161

Figure 5.10 Experimental Set-Up for the Frequency Response Measurement of the Smart Cantilevered Beam 163

Figure 5.11 Frequency Response of the Smart Cantilevered Beam 165

Figure 5.12 Schematic Diagram of the Smart ER Arm 166

Figure 5.13 Flow Diagram for Fabrication Procedures of the Smart ER Arm 167

Figure 5.14 Photograph of the Smart ER Arm 168

Figure 5.15 Measured Step Responses with Feedback Gains of K_p= 0.5 and K_v= 0.25 172

Figure 5.16 Simulated Step Responses with Feedback Gains of K_p= 0.5 and K_v= 0.25 173

Figure 5.17 Measured Step Responses with Feedback Gains of K_p= 1.4 and K_v= 0.25 174

Figure 5.18 Simulated Step Responses with Feedback Gains of K_p= 1.4 and K_v= 0.25 175

Figure 5.19 Measured Step Responses with Bang-off-Bang Type Input Voltage. K_p=1.4 and K_v=0.25 176

Figure 5.20 Measured Step Responses with the Disturbance. K_p= 0.5, K_v= 0.25 and $\tilde{d}(t)$=0.08 sin(4.1 Hz)t 178

Figure 5.21 Simulated Step Responses with the Disturbance. K_p= 0.5, K_v= 0.25 and $\tilde{d}(t)$=0.08 sin(4.1 Hz)t 179

Figure 5.22 Measured Step Response with the Disturbance. K_p= 0.5, K_v= 0.25 and $\tilde{d}(t)$=0.4 sin(16.8 Hz)t 180

Figure 6.1 Parameter Variation of the Composite Arm with respect to the Payload 211

Figure 6.2 Parameter Variation of the Composite Arm with respect to the Lamina Angle 211

Figure 6.3 Open-Loop Tip Displacement of the Nominal System 216

Figure 6.4 Comparison of Step Responses with the Linear and the Nonlinear Controller 218

Figure 6.5 Comparison of Step Responses with ϵ=0.1 and ϵ=0.003 ... 221

CHAPTER I

INTRODUCTION

1.1 Motivation

Most of current day industrial robots depend on bulky design and can handle objects no heavier than five percent of their own weight. The bulkiness is mainly due to an inherent design requirement to minimize structural vibration by increasing the mechanical stiffness of each component. This massive structural design makes the robot slow and heavy; hence, requires large actuators and high mounting strength and rigidity, which consequently leads to high energy consumption and high overall operating cost [26].

The insatiable demand in the international marketplace for high performance articulating robotic systems has triggered a vigorous research thrust in various multi-disciplinary areas such as design and control. The high performance of robots may be quantified by high-speed of operation, high end-point positional accuracy, lower or elimination of friction and backlash incorporating indirect drive mechanism, and lower overall cost. In order to achieve these high performances, light-weight, flexible robotic arms have been proposed and developed.

One can simply reduce the weight of the links of the robot in order to achieve these goals. However, it is not possible to move lightweight arms quickly without the onset of structural vibration which is a manifestation of inadequate structural damping as well as lower

structural strength and stiffness. Attempts have been and are being made to overcome these deficiencies through optimization of the stiffness-to-weight ratio by varying the length and cross section of each metallic link [67]. A more innovative approach employs advanced composite materials in the construction of high-speed manipulators to achieve larger structural damping and higher stiffness-to-weight ratio [38, 118, 145, 146, 147]. Recent studies [38, 146] have demonstrated both analytically and experimentally that transverse deflection can be reduced substantially when links are made of advanced composite materials. Moreover, to increase structural damping, optimization approaches have been developed [82]. This is usually called a passive damping method or passive control. However, present studies indicate that the increased damping due to passive means is not sufficient by itself to eliminate structural deflection [24]. Therefore, active control method, i.e., the design of control algorithms that take into consideration of the flexible dynamics is needed.

A variety of dynamic modeling and control strategies for flexible robotic manipulators fabricated from conventional isotropic materials such as steel and aluminum have been developed, and a few of them have been experimentally implemented as described in the literature review. However, up to now, the research areas on dynamic modeling and control of flexible robotic manipulators fabricated from advanced composite materials are considerably rare.

This study addresses the dynamic modeling and feedback control of a single-link flexible manipulator fabricated from advanced composite materials by undertaking an analytical and experimental investigation. The advantages of employing composite materials relative to the

conventional isotropic materials can be divided into three categories; design, control, and economics and safety. The advantages of the design area are well presented in [145, 146]. The advantages of control area may be described as a larger bandwidth due to the high stiffness-to-weight ratio of the material, an increase of the stability margin due to larger structural damping, a decrease of the control spillover effects due to the inherent high natural frequency of the unmodelled dynamics. Furthermore, more appropriate sampling time associated with observed and controlled modes can be achieved by adjusting the high frequency and large damping properties during the implementation [24]. The advantages of the last category will include lower energy consumption, lower overall cost due to high productivity on rate, and safer operation due to reduced inertia forces. Some of these advantages relating control and economic area will be observed both analytically and experimentally in this study.

It is also addressed in this study that the closed-loop system with the conventional output feedback controller associated with two colocated output sensors is very sensitive to an external disturbance which has a forcing frequency close to the cantilevered-mode natural frequency of the flexible arm. This attempt is made here to introduce a single-link flexible manipulator fabricated from smart materials incorporating electro-rheological fluids. The robustness of the conventional output feedback controller to the disturbance is to be expected by employing the distributed parameter actuator which is characterized by embedded electro-rheological fluids in the structure. It has been verified [41,56] that the vibrational characteristics such as natural frequencies and damping capacities of the flexible structures incorporating electro-rheological fluids can be controlled in a very short time by imposing

electric potentials, hence providing the possibility of the elimination of resonance phenomenon of the structures or systems.

Another important issue to be considered for controlling of flexible robotic manipulators is system parameter variations such as natural frequencies which may always arise in practice due to a wide spectrum of various conditions associated with manufacturing of flexible arms, dynamic modeling, and operating environments. The parameter variations are more serious in the robotic systems featuring composite-based flexible arms than those in the robotic systems featuring metallic-based flexible arms. The reason is that the composite-based arms involve more design variables, more complicated manufacturing process, and also higher sensitivities to environmental conditions such as temperature and moisture. In order to respond this problem, a nonlinear state feedback controller robust to parameter variations caused by the varying payload which may be encountered in the operation, and the mismatched lamina angle which may be encountered in the manufacturing process, is developed in this study.

These proposed observations which may provide significant impact on the diverse marketplace such as automobile industry and aerospace industry, coupled with the dearth of relevant research areas on the control of flexible robotic manipulators fabricated from advanced composite materials and smart materials have motivated the comprehensive research program reported in this study.

1.2 Literature Review

Although this research program discusses on the dynamic modeling and control of a single-link flexible manipulator, some of the major

contributions on the dynamic modeling and control of multi-link flexible manipulators will be also reviewed here. Furthermore, some research works on the modeling and active vibration control of the large flexible structures will be reviewed in order to provide a flavor of applicability of the proposed research to the relevant structural systems. Finally, the literature on the smart materials and smart structures will be reviewed in order to introduce the proposed single-link flexible manipulator fabricated from smart materials incorporating electro-rheological fluids. It is noted that the materials employed for the fabrication of flexible arms in the following references are assumed to be conventional isotropic materials such as aluminum and steel unless specific statement is made.

1.2.1 Dynamic Modeling

Schmitz [127] derived governing equations of motion and associated boundary conditions for a single-link flexible manipulator by employing the Hamilton's principle. The flexible link assumed to be governed by Euler-Bernoulli beam theory. The characteristic equation for the determination of natural frequencies and the eigenfunction for the determination of mode shapes are obtained for both cantilevered-mode and pinned-mode. Two different reduced-order models; reduced-order model with system modes and cantilevered modes are derived from finite modal expansion. The system model parameters such as natural frequencies and modal slope coefficient are verified through experimental identification, and shows good agreement between two results. Low [88,89,90] applied the Hamilton's principle in order to derive the coupled, nonlinear integro-differential governing equations for a manipulator containing both rigid and flexible links. The method accounts for the distribution of the mass

and flexibility and its nonlinear dynamic effects. The formulation is based on expressing the kinetic and potential energies of the robotic system in terms of a set of independent generalized coordinates. A two-link manipulator with one rigid link and one flexible link [90], and a three-link flexible manipulator with three revolute joints [88] are adopted to illustrate the proposed methodology.

Book [26,27] employed the transfer matrix method [114] to describe the dynamic model in the frequency domain for a two-link planar elastic arm. The method requires linear assumptions including small motions about an equilibrium position with no Coriolis, centrifugal or gravity forces. The model also was developed in the time domain by employing Lagrange's equation, and showed good agreement to the results obtained from the frequency domain. Book [22,23] also used 4x4 coordinate transformation matrix [49] to derive the nonlinear dynamic equations of motion for flexible manipulator arms containing of rotary joint and pairs of flexible links. The computations resulting from the Lagrangian formulation of the dynamics are reduced to recursive form similar to that which has proved so efficient in the rigid-link case. The preliminary programs were written [23] to evaluate computational efficiency showing that the proposed method requires 2.7 times as many computations as the most efficient rigid formulation with the same number of degrees of freedom. Singh [134] used the 4x4 coordinate transformation matrix incorporating a Lagrange approach to formulate a dynamic model for PUMA type robot which has two rigid-links and one last flexible link.

The finite element method has been applied by many researchers [16,46, 105,135,142,153] to produce an accurate model of a flexible manipulator. The justification for employing this method is three folds.

First, the finite element method is well known by many investigators. Second, the method is generally versatile, hence the model can be easily adapted to include as many, or as few, degrees of freedom as desired, and also the structural damping can be accommodated more easily than some other approaches such as Hamilton's principle. Third, the method can be easily incorporated with different material properties, different boundary conditions and change in cross section in a simple and straightforward manner. Bayo [16] used a finite element method incorporating Euler-Bernoulli beam theory to derive the discretized equations of motion for a single-link flexible arm. The discretized equations of motion in the time domain were reformulated in the frequency domain to calculate the required input torque using Fast Fourier Transformation (FFT). Dado [46] utilized the finite element technique to derive a general dynamic equations for multi-link flexible manipulators. In the forward analysis, the inertial loads are determined using the known acceleration vector, while the acceleration of the driven coordinates are determined by solving the dynamic equilibrium equations of the system in the inverse analysis. Naganathan [105] obtained a finite-element-based nonlinear model of flexibility effects in manipulators. The governing equations of motion include rotary inertia, shear deformation and the effects of gross nonlinear motion of each of the links. The model was applied to the planar 2-R manipulator and demonstrated that the nonlinear interactions contribute significantly to the displacement errors, and hence they should not be ignored in the modeling process. Skaar [135] used a finite element discretization of distributed structures with fractional viscoelastic constitutive model for the purpose of approximating the governing equations of motion. The

distributed structures are characterized by rotating viscoelastic beam with rigid hub or rigid body with axial deflection of viscoelastic rod.

Usoro [153] developed a nonlinear dynamic model for a two-link flexible manipulator by utilizing the finite element method, Lagrangian method and the generalized inertia matrix. The modeling methodology involves lumping each link into a number of elements, determining the Lagrange functions for the overall system and invoking variational principles to derive the governing dynamic equations. The final model derived is extremely nonlinear and complex. It reflects the variation in the effective inertia of the system as the manipulator configuration changes as well as the interaction between the rigid-body dynamics and vibration modes of the link. The axial deformation, viscous damping at the joint and the flexibility of power train are ignored in the modeling process. Sunada [142,143] developed a dynamic model for industrial manipulators including the effects of distributed mass and flexibility, and their dynamic nature. The individual link dynamic models are obtained from standard finite-element formulation. Then these link models are combined with the descriptions of the manipulator joint, expressed by 4x4 coordinate transformation matrix, to obtain complete dynamic model of a flexible industrial manipulator system. Chang [33] used 4x4 coordinate transformation matrix to describe kinematics for the large deformation, and the finite element method to discretize the deformations.

Rakhsha [117] obtained a dynamic model for a single-link flexible robot arm with a rigid mass attached to the tip by employing a Newton-Euler method. The flexibility effects are modelled as an internal disturbance torque generated by lateral bending which affects the rigid-body motion. The method of constrained modes [148] is utilized to

determine the natural frequencies and mode shapes. Wang [155] developed a dynamic model for a flexible robot arm with moving slender prismatic beam by applying Newton's second law, and the model was approximated by Galerkin method [119]. It is found that the extending and contracting motions have destabilizing and stabilizing effects on the vibratory motions. Truckenbrodt [150] developed a dynamic model so-called hybrid multibody model for the manipulator with rigid and flexible elements. The model includes the effect of bending and torsion, and the Ritz-Kantorovitch series expansion of the distributed deformation coordinates was employed to derive the governing equations of motion which are nonlinear, ordinary differential equations. The experimental verification of the proposed dynamic model was undertaken by considering a single-link fabricated from aluminum. Good agreement between theory and experiment was shown by comparing the first four natural frequencies. Davis [47] developed a class of hybrid robot arm model to study tracking problem without the necessity for a priori approximation in the flexibility model for the link. The model includes a distributed model of the dynamics of the structural elements of a robot link, combined with a discrete model for the actuator and load dynamics.

Asada [5] derived the equations of motion for two-link flexible arms based on Lagrange method, then transformed to the virtual link coordinate systems which consider the virtual links that are rigid and connecting adjacent arm joints by straight line. Actuator torques required to track a given trajectory in the plane are computed by a simple and efficient method using virtual link coordinate system through inverse dynamics. It is shown that the virtual link coordinates are not only convenient for solving the inverse dynamics problem, but also advantages to reduce

computational complexity. Barraco [14] developed two methods for dynamic modeling of multi-link flexible manipulators based on the choice of reference configuration. In the first approach, part of unknown variables represent the finite rigid-body moment while the remaining part deals with the infinitely small deformation of members. In the second formulation, an incremental form of the virtual principle is derived by subtracting virtual work equations written at two successive time steps. Nicosia [110] used a generalized Lagrange approach to derive the equations of motion for single-link and double-link flexible manipulators, and Streit [141] applied Lagrange approach to obtain governing equations of motion containing parametric excitation terms for a two-link flexible manipulator which has one translational and one revolute joint. The dynamic model is converted to the first order form in order to facilitate the stability analysis by using Floquet theory. It is shown in the illustrative example that the stability diagrams are significantly influenced by change in joint stiffnesses and mean operating position.

Everett [51] utilized a variational principle to provide an integral formulation of the governing differential equations, which is easily discretized incorporating with the finite element method. A functional expression is obtained by introducing appropriate Lagrange multipliers and using vector techniques, and the variation of the functional was undertaken before the discretization. Thompson [146,147] developed a dynamic model for industrial robotic manipulator constructed from composite materials by utilizing a variational theorem and a finite element method. The variational theorem was formulated by considering employed composite materials as linear viscoelastic homogeneous

materials. In the finite element formulation, the deflections of the elastic members are assumed to be governed by the Euler-Bernoulli beam theory. The difference of variational formulation from the work done in [51] is that the vectors are transformed into a fixed reference coordinate before the variation is computed, while Everett [51] present a technique whereby this transformation need not be applied.

1.2.2 Controller Design

Cannon [31] designed a linear optimal state feedback control law associated with noncolocated tip position sensor and experimentally implemented the control law on a single-link flexible manipulator. The experimental arm made of aluminum has a length of 1.13 m, a width of 6.6 cm and a thickness of 1 mm. It is shown through experiments that the tip position feedback is much more sensitive to model errors than one that uses only joint-angle feedback. It is also shown that the closed-loop bandwidth achieved with tip position feedback is two times the first cantilevered-mode natural frequency, which corresponds to a factor of four improvement over typical bandwidth achieved with the joint-angle feedback. Finally it has been investigated that the position feedback yields substantially better disturbance rejection to end-point external forces than does joint-angle feedback. Chassiakos [34] formulated a Linear Quadratic Gaussian (LQG) controller with a torque actuator and optimally located force actuator. The optimal location for force actuator is chosen so as to minimize the bending during the arm motion. An illustrative numerical example is given to demonstrate the proposed methodology showing that the step response of the robot arm with the torque and force actuator exhibits superior performances over the robotic

arm with only the torque actuator, such as faster settling-time and increment of attenuation of flexible vibration mode. Hastings [64,65] designed linear optimal state feedback control laws with a prescribed degree of stability and experimentally implemented the control laws on a single-link flexible robot arm. The experimental arm made of aluminum has a length of 1.22 m, a width of 1.905 cm and a thickness of 4.76 mm. Angular position from the potentiometer, angular velocity from the tachometer and strain from the strain gages mounted on the root and midpoint of the link are used to estimate actual states through Luenberger reduced order observer. It is shown in the experimental investigation [65] that the controller cycle time affects significantly to the step response of a colocated controller associated with joint position and joint velocity, resulting the increment in the excitation of the third flexible mode with larger cycle time. It is also shown that the optimal modal controller with large prescribed degree of stability yields instabilities in the higher flexible modes.

Nelson [106] presented a method adjusting the control gain to maintain the desired arm response by using an on-line estimator which provides periodic updates of load mass estimates to a parametric optimal controller. It is shown through an illustrative example that the proposed method provides capability of achieving rapid, smooth and accurate motion of flexible robotic arm under varying load conditions. Matsuno [91] and Sakawa [123] designed linear optimal state feedback control laws with prescribed degree of stability. 1.05 m long, 1.5 mm thickness of stainless steel experimental arm [123] is used to investigate system performances. The output sensors associated with optical encoder for angular position, tachometer for angular velocity and strain gage mounted

on the root of the link for strain are employed to provide information for estimating the actual states. The first two dominant modes are controlled, and third mode was estimated in order to estimate the first two modes to be controlled. It has been demonstrated that the experimental implementation of the proposed control schemes performed well. Book [27] and Neto [108] proposed three different linear state feedback control schemes : joint angle and velocity feedback with (GRC) and without (IJC) cross joint feedback, and feedback of flexible state variables (FFC). It is shown through simulation for a two-link flexible arm that the bandwidth of GRC and IJC is limited to the fundamental natural frequency by inadequate damping, and the FFC is very sensitive to parameter perturbations and somewhat higher torque requirement. Fukuda [53] considered a flexible robot arm with two degrees of freedom such as a SCARA type of robotic arm for precise position control. The state feedback control laws are designed and experimentally implemented. The feedback gains could be adjusted adaptively in order to improve transient performance due to nonlinearities and varying unknown payloads. Collision and Contouring control using flexibility of the arm was formulated and implemented successfully. And also a reliable control structure was implemented on the basis of the fault-tolerant configuration, employing dual-processor control systems. Chalhoub [32] designed the integral plus state feedback controller based on the linearized equations of motion. It is shown in experimental investigation that the proposed feedback controller by considering rigid-body and first flexible mode exhibits superior responses to that designed by considering only rigid-body.

Wang [157] proposed an output feedback controller for a single-link flexible manipulator. The two colocated output sensor associated with

angular position and angular velocity are used as feedback sensors. Feedback gains guaranteeing the stability of the closed-loop system are obtained by the least square method and the minimum norm pseudo-inverse method [28]. It is shown in the simulation work that the proposed output feedback controller performs well and robust to parameter variations such as change of natural frequencies. Wang [158] also conducted an experimental investigation of the position control capability of a single-link flexible robot arm by employing an output feedback controller. The employed output sensors include a shaft encoder for the measurement of hub angle, and a laser beam for the measurement of the deflection slope of the flexible link. It was shown that the performance of the overall closed-loop system was satisfactory and the controller was robust to parameter variations such as different payload. Siciliano [131] designed an output fast feedback controller which includes a fixed order dynamic compensator based on convergent numerical algorithm for calculating LQG optimal gains [102]. A composite control is adopted such that a slow mode control which is of the same order as that of a rigid arm, and a linear fast state control which models the deflections of the arm. The slow mode controller is first designed to track a desired joint trajectory, and fast state controller is subsequently designed to stabilize the deformations along the trajectory.

Meldrum [98] proposed a direct model following adaptive controller for a single-link flexible robot arm to control the torque at the pinned end of the arm so as to command the free end to track a prescribed sinusoidal motion. The control law was formulated by employing positive realness condition which is easily satisfied for colocation but not for noncolocation of the sensors and actuators. It is shown through

simulation work that the precise tracking of the reference model trajectory is achieved by colocating the actuator and sensor to satisfy the Command Generator Tracker [11] condition which assumes ideal intermediate system. Siciliano [132] and Yuan [162] developed a nonlinear robust adaptive control laws based on Lyapunov function for a single-link flexible arm. This is accomplished by separating the system dynamics into two parts ; linear and nonlinear (uncertainty in the linear model). Simulation work shows that the proposed adaptive control laws perform better than the typical linear optimal controller in spite of nonlinearities or uncertainties, as it contributes to obtain better tracking accuracy, smaller vibration amplitudes. Rovner [122] performed experiments for the system identification with the aim of implementing adaptive controller on a single-link flexible manipulator associated with tip position and angular velocity sensors. The adaptive controller maintains accurate position control of the manipulator while it picks and places varying loads. The identification algorithm employed is a filtered version of the recursive least squares algorithm.

Lee [78] proposed a nonlinear state feedback controller in order to control the tip position of a single-link flexible manipulator. The form of feedback is products of state variables to obtain a lightly damped system in the beginning of a step response and a more heavily damped system when it is close to the commanded position. It is shown from the illustrative example that the proposed controller provides reduced settling-time by 32 percent without increasing the percent overshoot, comparing to a linear optimal controller. Singh [134] derived a nonlinear feedback controller for the PUMA type of robot which has two rigid links and one last flexible link. The control law decouples the joint angle

motion from the flexible motion and asymptotically decomposes the elastic dynamics into two subsystems, representing the transverse vibrations of the elastic link in two orthogonal planes. In the simulation, the complete closed-loop system is shown to be globally asymptotically stable and robust to uncertainty in system parameters. Siciliano [129] introduced a singularly perturbed model in order to design a nonlinear composite controller which consists of a slow control and a fast control. A slow control is designed for the slow subsystem, which is shown to be the model of the equivalent rigid-link manipulator. Then a fast control is designed to stabilize the fast subsystem around the equilibrium trajectory set up by the slow subsystem under the effect of the slow control. A single-link flexible robot arm is chosen as a case study, and the comparison work with typical linear state feedback was undertaken showing satisfactory system performances.

Goldenberg [60] presented a computed torque technique to control the rotary joint of a single-link flexible robot arm. The nominal torque, required for a given desired trajectory, is calculated from the rigid-body model of the robot, and this provides a feedforward compensator. Proportional plus derivative (PD) feedback controller associated with two colocated angular position and velocity sensors as well as feedforward one provide almost pole-zero cancellation of the dominant closed-loop poles of the system, hence resulting in better transient response and smaller steady-state error comparing with only PD feedback controller. Schmitz [126] used a PD feedback controller associated with joint angle and joint rate sensors for controlling of two-link flexible manipulator. It is shown in the simulation work that with increasing shoulder position gain, two rigid-body poles travel towards a pair of zeros which are very

close to the first locked-joints (cantilevered-mode) vibration frequency which represents a limit on the maximum bandwidth attainable with colocated feedback controller. Skaar [135] used a classical root-locus technique to design a controller for viscoelastic systems. The controllers are formulated based on the fractional derivatives of the constitutive law of the material itself, which makes the proposed feedback control laws too difficult to be implemented physically. Also it is found that time-domain behavior of the stabilized closed-loop system is not self-evident.

Wang [156] proposed a method for synthesizing open-loop control inputs to move a flexible robot arm precisely along a given desired trajectory. Proportional-integral-derivative (PID) controller for three-axis Cartesian manipulator is formulated to minimize excessive residual vibrations at the end of a movement. The computed reference error adjustment technique was also introduced to obtain substantial reduction in output error. Meckl [93] designed a open-loop controller for a three-axis Cartesian manipulator using bang-bang control function. The function provides optimal-time response to eliminate residual vibration of a robot arm at the end of a movement. Book [25] developed a minimum time control of a two-link flexible arm with actuator constraints and without constraints on the flexible modes. The near minimum time trajectories for robotic manipulators moving along the pre-defined path are modified such that the flexible vibrations will be bounded. It is shown in simulation that flexible manipulators with same actuator capabilities are faster than rigid-body manipulators. Morimoto [103] used transfer function data of the input-output relation to predict vibratory motion of the end effector of the flexible manipulator which was commanded to move

according to a trapezoidal velocity pattern. The transfer function data were obtained through experimental modal analysis technologies. It is shown that the proposed method is very effective for suppression of the flexibility-induced vibration of the robot arm.

Korolov [73] developed a robust controller for a one-link flexible robot arm subjected to uncertainties. The control scheme was formulated by treating the natural frequency variation, which may be possibly occurred in practice, as bounded uncertainty. The proposed robust controller consists of a linear part which is optimal state feedback controller with a reduced order observer, and a nonlinear part which depends on the boundedness of the parameter variations. The reduced order observer for the state estimator was designed independent of the control input. Nemir [107] presented a self-tuning type algorithm for the control of a single rotating compliant link. The self-tuning control is devised by treating angular position obtained from first mode information of flexibility measured from strain gage and hub position measured from position encoder, as belonging to an equivalent rigid link. The angle of the hub to tip projection (the pseudo-link) is presented using an auto regressive exogeneous type time series model. The laboratory experimental investigation shows that the proposed control leads to an improved performances over a control which ignores compliance. Liegeois [83] introduced a calibration procedure based on a learning technique to identify the structural parameters of the system. The damping of oscillations induced by fast transient motions is carried out by means of the measurement of cable deformations and their derivatives using the strain gages.

Choi [37] proposed an integrated strategy for both the optimal structural and controller design of a single-link flexible manipulator fabricated from composite laminates. The formulation of the optimal structural design is accomplished by integrating composite laminate design variables such as stacking sequence, fiber volume fraction and lamina thickness which characterize the mass, stiffness and damping properties of the structure, and an objective function which characterizes the elastodynamic response of the closed-loop system. It is shown in an illustrative example that the optimally designed arm exhibits superior performance characteristics such as the smaller control spillover effects and faster rise-time without increasing the overshoot. Mesquita [99] considered structural optimization of the laminated composite materials to maximize the structural frequencies subjected to frequency separation constraints and an upper bound on weight. The control problem was solved by employing the independent modal space technique introduced in [96].

1.2.3 Related Works on Modeling and Active Control of Large Flexible Structures

Large flexible beam-like or truss-like structures are a characteristic feature of many spacecraft appendages, such as space station, for example. While these large structures are a prerequisite for attaining the goals and objectives of these pioneering space projects, the inherent low stiffness characteristics of these structures have triggered research efforts focused on the development of dynamic modeling and active vibration control strategies for these large flexible

structures which represent similar characteristics occurred in the case of flexible manipulators. Two most important quantities which characterize the vibrational behavior of flexible structures are the natural frequencies and inherent damping capacities of these systems. Since these continuum structures are characterized by an infinite number of vibrational modes, modal truncation must be employed in the modeling process. Hughes [66] discussed the existence and the selection of critical modes of the flexible structures or systems. He suggested that the appropriate number of modes should be selected based on the the order of natural frequency as well as dynamical grounds of the system such as boundary conditions. Balas [10] and Johnson [68] summarized on the dynamic modeling methodologies and active vibration strategies developed so far. Some of them will be reviewed in this section.

Most of purposes it is satisfactory to neglect shear deformation and rotary inertia of the beam-like structures in the modeling process as described by Archer [4]. While the Euler-Bernoulli beam theory leads to very accurate model for the lower modes of long and thin beam, significant error may be caused if no account is taken of shear deformation and rotary inertia for higher modes of any beam structures, or thick beam. Hence some references relating to Timoshenko beam theory are reviewed for appropriate dynamic modeling of large flexible structures. Davis [48] formulated a Timoshenko beam element which includes the effects of shear deformation and rotary inertia. The convergence tests are performed for a simply-supported beam and a cantilevered beam. It is shown that the element is converged to an exact solution of the elasticity equations for a simply-supported beam provided that the correct value of the shear coefficients is used. Gamache [54]

compared the Timoshenko and the Euler-bernoulli beam theories by modeling of planar linkage mechanism. The four-bar linkage with flexible coupler and rocker links is chosen for simulation work and it is shown that the percent error between two theories is function of the aspect ratio, i.e. the thickness to length ratio of the linkages. Kapur [71] formulated a beam element incorporating Timoshenko beam theory which is applicable to uniform and nonuniform beams with any boundary conditions. Thomas [144] developed Timoshenko beam element by considering three degrees of freedom at each of two nodes and applied to a cantilevered beam to calculate natural frequencies.

Bodden [21] proposed a minimum modification strategy for structure and control parameter optimization for the vibration arrests of flexible structures. Linear output feedback gains are determined using a novel optimization strategy, and it is shown that the sensor and actuator locations, and feedback gains can be modified to achieve satisfactory results. Hale [62] discussed an optimization problem for maneuvering flexible spacecraft in order to achieve both structural parameters and active control forces. A specific cost functional which consists of a set of structure parameters and control forces is chosen as an objective function which is supposed to be minimized. Khot [72] developed an integrating strategy for the structure and control design to reduce the structural response from a disturbance. The structural modification of some nominal finite element model, which is controlled in an optimal fashion by a linear regulator, was employed to increase the active modal damping factor. The objective function is the weight of the structure with a constraints on the damping parameters of the closed-loop system. Onoda [112] presented an approach to the simultaneous optimal design of

structure and control system for large flexible beam-like spacecrafts by choosing the total cost of structure and control system as an objective function with constraints represented by a given disturbance involving both rigid-body and elastic modes. Direct feedback and linear quadratic optimal control laws are used with both inertial and noninertial disturbing forces, and it is shown that the simultaneous optimization of the structure and control system is indeed useful.

Arbel [3] showed that when an output feedback gain matrix is chosen as symmetric negative-definite, a linear quadratic optimization problem can be stated and solved in closed-form via an inverse optimal control formulation. This, in turn, allows to be used the well-studied properties of the linear quadratic regulator for stability problem at hand. Balas [9] formulated a direct velocity output feedback control that may guarantee that all vibration modes remain stable when the active control is in operation. However, it is pointed out that the proposed feedback controller has some stringent restrictions, such as an equal number of colocated force actuators and velocity sensors, and a non-negative definiteness of the feedback gain matrix in order to achieve stabilization of all vibration modes. Elliott [50] proposed a robustness of the control system which arises from the fact that the stability of the system is dependent only on the controller and is not a function of the system model parameters. It is pointed out that even though sensors and actuators are colocated, it is not required that the signal from the sensors drive only the colocated actuator, and the sensor signal may drive all of the actuators. Lin [85] surveyed on the output feedback control method for possible application to vibration control of large flexible space structures ; output feedback control via modal decoupling,

output feedback control by pole assignment, optimal output feedback control and suboptimal output feedback control. The underlying theory, assumptions made, techniques used, computations required, and strength and weakness associated with above methods are investigated in details. Lin [86] derived an output feedback control associated with displacement and velocity sensors. However, the controller has restrictions such that the number of sensors and actuators should be same and the sensors should be located with force actuators.

Baruh [15] developed a natural control based on a set of admissible functions instead of the actual eigenfuctions in order to achieve the robustness of controller to both parameter uncertainties and discretization errors. It is shown that if natural control is considered in conjunction with modal filters and an adequate number of sensors, implementation of the control action by admissible function leads to a stable closed-loop system under uncertainties. Joshi [70] discussed the robustness properties of two types of control laws for large space flexible structures that use colocated sensors and actuators. The two types of controllers are attitude controller which uses negative-definite feedback of measured attitude and rate, and damping enhancement controller which uses only velocity feedback. McLaren [92] used a positive real approach for robust controller design which leads to guaranteed closed-loop system stability in the presence of erroneous modal information and unmodelled modes. It is shown that the closed-loop stability can be maintained in the event of sensor and/or actuator failure. Preumont [116] developed a robust nonlinear saturation controller based on the second method of Lyapunov to eliminate the spillover instability associated with the uncertainties such as neglected

dynamics in the modeling process. Simulation work shows that the instability is alleviated by a local modification of the control in the vicinity of the equilibrium, which reinstates the asymptotic stability properties of the open-loop system.

Bar-Kana [12] proposed a direct multivariable modal reference adaptive control scheme for large flexible structural systems such as beams, plates and frames. The adaptive control law is formulated based on the positivity condition which depends on the location of actuators and sensors, and inherent damping of the structure. It is shown that when colocated actuators and combined position and rate sensors are used, the error approaches to zero, provided the ratio of the position-to-rate output is limited by a function dependent on the damping ratio and the lowest structural frequency. Mufti [104] formulated a model reference adaptive technique for active control of large flexible structural systems based on the Command Generator Tracker (CGT) procedure and Lyapunov stability theory. It is improved from Bar-Kana [12] that the ratio of position-to-rate output is limited by twice the product of the damping ratio and the lowest natural frequency. The control law in the form of integral, proportional and relay adaptations along with the integral of the output error is also proposed. Balas [7,8] used a linear optimal state feedback controller with state estimator for a finite number of modes of the flexible system, and applied it to a simply-supported Euler-Bernoulli beam with a single actuator and sensor. It is shown that the control and observation spillover due to the residual modes causes the instability of the closed-loop system. Some remedies for spillover, including a straightforward phase-locked loop prefilter, are suggested to remove the instability mechanism. Meirovitch [96,97]

introduced an independent modal space control method, which features invariant natural coordinates in the presence of feedback control, to provide a unique and globally optimal closed-form solution to the linear optimal control problem for the distributed parameter system. The proposed distributed control can be approximated by finite-dimensional control through a process that does not require truncation of the plant.

Meirovitch [95] implemented experimentally the independent modal space controller developed in [96,97] in conjunction with a nonlinear, on-off controller for the modal forces on a free-free uniform aluminum beam which has a length of 3.657 m, a width of 15.24 cm and a thickness of 4.76 mm. Four electromagnetic force actuators and nine displacement sensors are employed. It has been demonstrated that the proposed independent controller are very effective in suppressing the motion of the beam, even though there is about a 50 percent difference between the actual and computational natural frequencies. Schaechter [124] tested experimentally the static shape control, active dynamic control, adaptive control and optimal control laws by implementing these control laws on a pinned-free stainless steel flexible beam which has a length of 3.8 m, a width of 15.24 cm and a thickness of 0.794 mm. Excellent control performances are obtained with these control laws through experimental investigation and it is pointed out that the unmodelled torsional modes, sensor and actuator nonlinearilities, computational delays are only a few of difficulties to be overcome in future research. Schafer [125] implemented experimentally a direct velocity feedback controller on a clamped-free flexible beam in order to study the active vibration control. Sensing is provided by a purely optimal displacement sensor, while an electrodynamic force system provides the actuating forces. The

experimental beam was made of nonmagnetic stainless steel with a length of 2.9 m, a width of 10 cm and a thickness of 1 mm. It is shown that the closed-loop performance is satisfactory for both the colocated and noncolocated actuator/sensor positions.

Lindberg [87] presented a new formulation of independent modal space control which can provide an analytical solution for the optimal control law for very high dimensional systems. An optimal actuator locations are developed using open-loop and closed-loop approach in order to minimize the actual control effort. Omatu [111] established a criterion for the optimal sensor location to minimize the trace of the optimal filtering error covariance function by employing the existence and uniqueness theorem concerning a solution of the optimal filtering error covariance function for the pointwise observation case. West-Vukovich [159] proposed a decentralized robust servomechanism problem with constant disturbance and set points for the large flexible space structures. Simulation work shows that the controller eliminates the spillover problem which cause instability of the closed-loop system.

1.2.4 Related Works on Smart Materials and Structures

Recently great attention has been focussed on the development of technologies associated with 'smart' or 'intelligent' materials and structures. This terminology has been used to describe or classify materials and structures which have their own sensing, actuating, tuning, controlling and computational capabilities. Typically, smart materials and structures are employed to control the static and elastodynamic responses of distributed parameter systems. This may be accomplished by

controlling the mass distribution, the stiffness and the energy dissipation characteristics of the structures. Recently significant progress has been made in the development smart materials and structures which feature piezoelectric materials, electro-rheological fluids, shape memory alloys and optical fibers. The piezoelectric materials are aptly named as smart due to the capabilities of actuating and sensing through the polarization a polymer. Electro-rheological (ER) fluids are adaptive in that definition since it can be either fluid or solid state, as need be for certain objectives. The shape memory alloys are also aptly named as smart for they remember own shape history and can recover the memorized shape with appropriate heat supply. The optical fibers have own merits for being named smart since they are one of the potential candidates of sensor technologies for applications in smart materials and structures. The distinct characteristics, possible applications and existing problems of these smart materials and structures are well summarized by Gandhi and Thompson [55].

Bailey [6], Burke [30], Miller [100] and Plump [115] used a distributed parameter actuator incorporating piezoelectric polymer for active vibration damper. The dynamics of the proposed actuator are derived for the simplest possible damper configuration which features a layer of piezoelectric polymer bonded to one side of the cantilevered beam. The nonlinear control law was formulated based on the Lyapunov second method. A Lyapunov functional of the system is the sum of the squares of the curvature and velocity. Hence, integrating of the functional along the length of the beam provides a measure of how far the beam is from its equilibrium position or a measure of the energy stored in the system. Minimizing the time derivative of this functional is then

equivalent to trying to bring the system to equilibrium as fast as possible. The controller was successfully implemented for a cantilevered beam [6,115] and a simply-supported beam [30] yielding increment of loss factor for small amplitude vibrations. Crawley [45] presented an analytical and experimental investigation of piezoelectric actuators as elements of smart structures. A static and dynamic models for segmented piezoelectric actuators, which are either bonded to an flexible structure or embedded in composite laminates, are derived based on the force equilibrium and the strain-displacement relationships. Some suggestions for the selection of actuator location and actuator material are presented. The actuators should be placed at the locations to excite the primary vibrational modes effectively. The actuator materials should be carefully chosen based on the property of piezoelectric-mechanical coupling effectiveness, mechanical properties of the original structures and the type of actuator, i.e., a surface-bonded actuator or an embedded actuator. Three experimental cantilevered beams : an aluminum beam with surface-bonded actuators, a glass-epoxy beam with embedded actuators and a graphite-epoxy beam with embedded actuators, are used to investigate the steady-state resonant vibration. It has been shown in the static test that the ultimate strength of the glass-epoxy beam was reduced by approximately 20 percent, although the modulus of the beam was not affected significantly. Hanagud [63] discussed the effects of the location or placement of the surface-bonded or embedded actuators and sensors incorporating piezoelectric materials. It is shown through simulation work that the actuator and sensor location is very important in controlling flexible structures resulting in that the centralized controls are effective on the basis of selective locations.

Baz [17] developed a dynamic model and control method for an composite beam which consists of a surface-bonded actuator, bonding layer and the original beam structure. The stiffness matrix is obtained by integrating the mechanical properties of the three sub-structures : piezoelectric actuator, bonding layer and original beam. The mass matrix are determined using the lumped mass method in which the mass and rotational inertia of each element is distributed among the nodes. A modified independent modal space control is presented to select the optimal locations of the piezoelectric actuators, control gains and input voltage to the actuators. This method accounts for the spillover from the controlled modes into the uncontrolled modes due to the use of fewer actuators than the modelled modes. The effectiveness of this proposed control method in conjunction with the effect of bonding layer material, actuator location and number of finite elements are investigated in details through simulation work. Lawson [77] investigated a frequency characteristics of infinite piezoelectric plates vibrating between two grounded infinite electrodes. It is shown that the frequencies depend on the piezoelectric constants as well as the elastic constants of the piezoelectric crystal. It is also found that the frequencies of free vibration depend on the gap of the electrodes, and this dependence is not linear. Mindlin [101] derived the approximate equations so as to accommodate the frequencies of the shear modes of thick rectangular plates incorporating piezoelectric crystal. The two-dimensional equations of coupled flexural and extensional motion of crystal plates are deduced from the three-dimensional equations of linear elasticity based on the series expansion method and variational method. The uniqueness of

solution and orthogonality condition are also discussed in the deriving process of the approximate equations.

Winslow [160] described for the first time some phenomena of the induced fibration of small particles in liquid suspension. Various properties of these fluids are discussed regarding to the micromechanism of the induced fibration and its application in slip clutch and hydraulic devices. It is mentioned that the observed values of induced shear resistance are very similar to those predictable from elastic and magnetic cases. Block [20] reviewed literatures on electro-rheological (ER) fluids by describing the nature of these fluids and the influence of important parameters such as shear rate, field intensity, stability of the fluids, temperature and fluid composition. This review also includes the dielectric characteristics of dispersions in flow, various modeling methodologies and practical applications that have currently and may have in the future. Stangroom [140] introduced some chemical and mechanical properties of ER fluids as well as their possible applications to the practical devices such as clutch and servo-valves. It is also mentioned about the minimum requirement for ER activity such that the base liquid must be hydrophobic and the solid must be hydrophilic and porous so that it can contain an appropriate amount of absorbed water which greatly influence the properties of the final ER fluids. It is suggested that insulating materials for use ER fluids require good surface and bulk dielectric strength and resistivity as well as chemical and mechanical stability. Adriani [2] developed a microscopic model for an ER fluid by considering a concentrated suspension of hard spheres with aligned field-induced electric dipole moments. The presence of dipole moments causes clustering of the particle into an anisotropic suspension characterized

by a particle probability distribution function. It is shown that dynamic viscosity is insensitive to dipole strength, while elastic shear modulus increases significantly with dipole strength indicating the relative importance of the particle distribution to elastic properties.

Bullough [29] proposed a vibration isolation system for the investigation of the usefulness and effectiveness of a controllable and nonlinear damper incorporating ER fluids. This is accomplished by considering the performance of a simple model suspension system which is an idealized form of a prototype damper controlled by imposing an electric field on the associated electroviscous valves. The proposed suspension model consists of two springs, one linear viscous damper and one nonlinear Coulomb damper. Simulation result shows that it is possible to control this idealized suspension system so as to achieve much improved performance characteristics. Stevens [137,138] performed experimental investigation of ER clutch to examine the utilization of ER fluids for torque transmission, and also to provide guidelines for the development of practical ER devices. The proposed ER clutch which involves a horizontal shaft with a totally enclosed reservoir for the ER fluids, and the adjustable space of the clutch plates was proposed, built and tested. Experimental results show that the amount of transmitted torque can be made a linear function of the available stressed area of the ER fluids and can be controlled by the electric field intensity. It has been also found that as the ER fluid temperature increases, the viscosity of the base fluid (thus the viscous shear force) decreases, leading to an overall decrease in transmitted torque. Stevens [139] also conducted experimental testing to obtain mechanical properties of ER fluids such as shear stresses. The influence of the critical dimensions

such as spacing, electrode area and the viscosity of the base fluid on the shear stress are investigated with respect to externally applied electric field. Stanway [136] proposed an approach for identifying the damping law of an ER fluid in vibration. The damping law is achieved by employing a nonlinear sequential filter to estimate the system parameters associated with an nth-power velocity model of the damping mechanism. It is shown in experimental study that the proposed method performed well at the lower electric field strength (less than 1 kV/mm) because the ER damping force did not depart significantly from a viscous characteristics, however, some trial and error was required to obtain an estimate of the actual state at 1 kV/mm and above.

Choi [39] described possible applications the ER fluids to the machine and robotic systems. A robot with structural member incorporating ER fluids, ER hydraulics and conceptual design of an ER-based hydraulic servomotor are discussed in terms of dynamic modeling. Gandhi [58] developed a phenomenological dynamic modeling for an ER-based articulating robotic manipulator. The dynamic modeling is accomplished based the variational theorem characterizing the linear viscoelastic homogeneous materials, and the finite element formulation. It is shown through simulation work that the smaller vibration amplitude, faster settling time is achieved by employing the robotic system featuring smart structures incorporating ER fluids. Choi [41] conducted experimental investigation of beam-like structures fabricated from ER fluid to examine the change of natural frequencies and damping properties of the structure with respect to electric potential. The experimental studies were undertaken under diverse conditions such as different ER fluids, different interface condition at the boundary between solid and fluid

domains, different ER volume fraction, different electrode area and different embedded ER locations. Gandhi [56] proposed a new generation of revolutionary, intelligent, ultra-advanced composite materials featuring ER fluids for active vibrational control of structures and mechanical systems. The graphite-epoxy composite beam filled with ER fluids are fabricated and tested in a variety of different operating condition in order to provide a basis for evaluating the controllability of these structures in real time. It is shown that the first mode natural frequency and damping ratio of the cantilevered beam was increased by 25 percent and 45 percent respectively with 2 kV/mm of electric field. Choi [40] proposed an active vibration tuning methodology for smart flexible structures incorporating ER fluids through proof-of-concept investigation. The tuning methodology was developed by employing a pseudo proportional-plus-derivative feedback control which was deduced from the phenomenological equations of motion incorporating modal analysis. A free vibration of cantilevered beam filled with ER fluids was tested and showed good correlation between the predicted and measured results. Gandhi [57] performed experimental test to investigate the forced vibrational response of slider-crank mechanism featuring a smart connecting-rod incorporating ER fluids. This is the first time to experimentally demonstrate the ability of smart materials to tailor their vibrational behavior by approximately selecting the voltage imposed on the embedded ER fluids in the member when it is subjected to forced excitations. It has been shown that the magnitude of the midspan deflection was reduced by 15-73 percent with 2 kV/mm of electric field, depending on the crank angle, at the mechanism operating speed of 95 rpm.

Rogers [120] proposed a shape memory alloy reinforced composite for active modal modification and active strain energy tuning. The active modal modification uses the shape memory alloy's capability of changing its stiffness properties during a temperature activated, reversible, phase transformation modifying the modal response of the composite structure. The active strain energy tuning concepts induces from the shape memory alloy's ability to impart large distributed loads through the material to alter the stored strain energy within the composite structure. This active strain energy tuning allows for greater authority and versatility of control to be exercised over active modal modification to vary the natural frequencies and to change the mode shapes of the structure. It is shown the experimental test that the natural frequency of the composite beam changes from 2.2 Hz without actuators to 3.8 Hz with six actuators featuring nitinol-based shape memory alloy. Yaeger [161] developed a one-point three-quarter-inch-stroke linear actuator using a spring type of nitinol-based shape memory wire. The design includes prevention from ancillary jams.

Claus [42] described potential applications of optical fiber sensors for measurement of phase,polarization, mode, strain, chemical concentration, resin cure, acoustic vibration, crack propagation and impact. The optical fiber sensors deserve their merits as a candidate of sensor technologies due to the small size, low weight, large bandwidth, lower power, multiple mutiplexing options and dielectric property. The fiber sensors are either bonded on the external surfaces of structures or embedded within materials. Rogowski [121] used a laser-radiated optical fiber to measure static and dynamic strain in composite materials. This was accomplished by integrating technologies of modal domain

interference, optical time domain reflectometry, an optical phased-locked loop and the laser radiation. Waite [154] used a polarization maintaining optical fiber embedded in a woven glass-epoxy composite three point bending specimen for the detection of damage and strain of the structure. The experimental optical system consists of a helium-neon laser which injected light into the optical fiber, two photodiode detectors for signal recording and a microcomputer controlled stepper motor. Various fiber surface treatments such as stripped and silane treated, stripped and release agent treated, and buffered are tested and compared.

The research fields on dynamic modeling and control of single-link or multi-link flexible manipulators, dynamic modeling and control of large flexible structures, and smart materials and structures have been reviewed. Numerous research studies have been done on the dynamic modeling and control of flexible manipulators fabricated from conventional isotropic materials such as aluminum and steel. However, none of the current literature did attempt to model and control of flexible manipulators fabricated from advanced composite materials or smart materials incorporating electro-rheological fluids. Moreover, it is clearly evident from this literature review that only a few of researchers conducted experimental implementation of control laws for controlling flexible manipulators. Therefore, this research program combining analytical, computational and experimental work will provide a complete quantitative and qualitative in a sense comparison of control performances of the flexible manipulators fabricated from aluminum, composite materials and smart materials. In addition, this study will furnish viable guidelines and directions for future work in this or relevant research fields.

1.3 Thesis Organization

In Chapter II, the fourth-order partial differential equation and associated boundary conditions for a single-link flexible manipulator fabricated from advanced composite laminates are derived. The governing equation of motion is developed by employing the Hamilton's principle. The equation is then discretized using a finite element method incorporating the Euler-Bernoulli beam theory. The inherent damping of the structure is modeled in the finite element formulation based on the hypothesis that the damping matrix is proportional to the stiffness matrix of the structure. The coupled discretized equation of motion is decoupled through modal analysis and expressed in the state space representation which is convenient form for controller design.

A detailed description of the experimental apparatus of the proposed robotic system featuring an output feedback controller associated with two colocated output sensors is presented in Chapter III. The apparatus is divided into five functional groups; flexible arms, a DC servo-motor, a servo-positioning assembly, sensors and a microprocessor. After a description of the apparatus, an experimental identification of the system model parameters such as natural frequencies is undertaken, and the measured parameters are compared with the predicted ones.

Chapter IV presents an output feedback control associated with two colocated output sensors. The proportional-plus-derivative feedback controller is designed using the root-locus technique and the Lyapunov method. The controller is then experimentally implemented by incorporating the apparatus described in Chapter III. Experimental results such as step responses to a commanded step angular position, and the characteristics of the system instability are presented and compared

between two robotic systems featuring the flexible arm fabricated from aluminum and composite laminates respectively. The corresponding simulated results are also presented.

In Chapter V, a hybrid controller which consists of the output feedback controller implemented in Chapter IV and a pseudo-state feedback controller featuring the distributed electro-rheological (ER) fluid actuator is presented. A brief background on the electro-rheological fluids is presented prior to developing a phenomenological equation of motion of the robotic system featuring a flexible arm fabricated from ER fluids. The phenomenological equation of motion is developed based on the experimental observation of the modal characteristics of the smart beam structure. Then, the hybrid controller is formulated by incorporating an empirical model of the distributed ER actuator. The experimental implementation of the proposed hybrid controller is undertaken, and the results are presented by considering step responses of the system subjected to no disturbances and disturbances.

Chapter VI presents a nonlinear robust state feedback controller for a flexible manipulator fabricated from composite laminates by introducing uncertain parameters which may cause system parameter variations such as natural frequencies. The varying payload encountered in the operation and the mismatched lamia angle encountered in the manufacturing process are considered as uncertain parameters. The controller design is accomplished by utilizing the properties of uniform and uniform ultimate boundedness of the solution. A so-called matching condition which says that the uncertain quantities can not enter arbitrary into the state equations is excluded in the process of controller design. An illustrative example is

taken and simulated to demonstrate the robustness of the proposed nonlinear controller in the presence of uncertain parameters.

Finally, conclusions of this research program and recommendations for future work are given in Chapter VII.

1.4 Principal Contributions

1. The output feedback controller featuring two colocated angular position and velocity sensors to one actuator was designed and experimentally implemented in order to investigate and compare the control performances of single-link flexible manipulators fabricated from aluminum (aluminum arm in short) and composite laminates (composite arm in short) respectively. So far the author is aware, this is the first experimental investigation on complete quantitative comparison of control performances between two flexible manipulators.

   It has been demonstrated through the analytical and experimental investigation that the composite arm had superior control performances such as faster settling-time, smaller input torque, smaller overshoot and a superior increment of stability relative to the aluminum arm. It was obtained from the measured step responses that with certain position and velocity feedback gains the delay time was 0.26 second for the aluminum arm, while that was 0.21 second for the composite arm, and the maximum overshoot was 1.02 degree for the aluminum arm, while that was 0.3 degree for the composite arm. It was also observed that the reduction of the energy consumption by 40-50 percent for the commanded motion, and the decrease of the tip deflection up to 50 percent were achieved by employing the composite arm.

2. It has been also shown that the implemented output feedback controller was very sensitive to the external input (considered as disturbance), which has a forcing frequency close to the cantilevered-mode natural frequency of the arm, regardless of the aluminum and composite arm. This attempt has been made here to introduce a single-link flexible manipulator fabricated from smart materials incorporating electro-rheological fluids (smart ER arm in short) for the purpose of obtaining the robustness of the output feedback controller to the imposed disturbance with the help of distributed parameter actuator, which is characterized by embedded electro-rheological fluids in the structure.

The phenomenological equation of motion of the robotic system featuring the smart ER arm has been developed based on experimental observations of the modal characteristics of the smart beam structure. The hybrid controller which consists of the output feedback controller and the pseudo-state feedback controller was formulated by employing the empirical dynamic model of the electro-rheological fluid actuator. It has been shown through the experimental implementation that the robustness of the employed conventional output feedback controller was significantly enhanced by employing the proposed pseudo-state feedback controller in the presence of the disturbance which has a forcing frequency close to the cantilevered-mode natural frequency of the robot arm. The author strongly believes that this work is unique and initial accomplishment.

3. The nonlinear robust state feedback controller for the composite arm was designed for the first time to overcome uncertain parameters associated with the varying payload encountered in the operation and the mismatched lamina angle encountered in the manufacturing process. The controller design was accomplished by utilizing the properties of uniform and uniform ultimate boundedness of the solution. A matching condition which says that the uncertain quantities can not enter arbitrary into the state equations was excluded in nature in the process of controller design from the point of dynamic characteristics of the proposed flexible manipulator. It was demonstrated through the simulation that the proposed nonlinear controller could tolerate larger system parameter variations than the conventional linear controller, showing much faster settling-time and smaller overshoot with the nonlinear controller.

CHAPTER II

MODELING OF A SINGLE-LINK FLEXIBLE MANIPULATOR FABRICATED FROM ADVANCED COMPOSITE LAMINATES

2.1 Introduction

Two most important quantities which characterize the control performance of flexible manipulators are the natural frequencies and the inherent damping capacities of these systems. Since these continuum structures are characterized by an infinite number of vibrational modes, in the modeling process it is essential to choose a suitable number of modes based on dynamic conditions encountered in practice and practical limitations other than the order of natural frequencies alone [66]. This modal truncation procedure invariably results in performance trade-offs such as control and observation spillover effects when designing a controller for distributed parameter systems [8]. However, in most cases this modal truncation is justified by the boundness of energy, and the fact that most of actuators and sensors cannot operate in the high frequency range [31,74]. Another issue which should be carefully considered in the modeling process of flexible robotic manipulators is the effects of rotary inertia and shear deformation on the vibrational behaviour of the systems. In other words, the problem follows that whether the system should be modeled based on Euler-Bernoulli or Timoshenko beam theory. Up to now, many of related works on the dynamic modeling of the single-link flexible manipulator have verified that the

model based on Euler-Bernoulli beam theory agreed well to experimental results [65,127].

In this chapter, the fourth-order partial differential equation and associated boundary conditions for a single-link flexible manipulator fabricated from composite laminates (composite arm in short) are derived. The governing equation of motion is developed by employing the Hamilton's principle. The equation is then discretized using a finite element method incorporating the Euler-Bernoulli beam theory. The inherent damping of the structure is modeled in the finite element formulation based on the hypothesis that the damping matrix is proportional to stiffness matrix of the structure. The coupled discretized equations of motion is decoupled through the modal analysis and expressed in the state space representation which is convenient form for controller design.

2.2 Derivation of Equations of Motion

Consider the horizontal motion of a single-link flexible manipulator as shown in Figure 2.1. The arm is modeled as a continuous and uniform beam of length L whose moment of inertia about the root is I_B, with an additional lumped inertia I_H at the actuator assembly (hub). The payload of m_t is attached to the other end of the arm. The ox' is the fixed reference line and ox is the tangential line to the beam's neutral axis at the hub. The total displacement of any point along the beam's neutral axis at a distance x from the root of the beam is the sum of the small elastic deflection $\tilde{w}(x,t)$ and hub angle $\theta(t)$ which can be arbitrary large. Before determining the kinetic and potential energy of the proposed system, following assumption is made.

Assumption 2.1 : (1) Elastic deflection is small. (2) Axial deflection is neglected. (3) Rotary inertia and shear deformation are ignored (Euler-Bernoulli beam model). (4) Internal damping forces are neglected (they will be included later on in the finite element formulation).

Under this assumption, if the total displacement w(x,t) (arc length measured from the fixed reference line ox') is defined as

$$w(x,t) = \tilde{w}(x,t) + (x+r)\theta(t) \tag{2.1}$$

then, the total kinetic energy of T can be given by

$$T = \frac{1}{2}\int_0^L \tilde{m}\left(\frac{\partial w(x,t)}{\partial t}\right)^2 dx + \frac{1}{2} I_H \dot{\theta}^2(t) + \frac{1}{2} m_t \left(\frac{\partial w(L,t)}{\partial t}\right)^2 \tag{2.2}$$

where $\tilde{m}$ is the mass per unit length of the beam and $(\dot{})$ denotes time derivative.

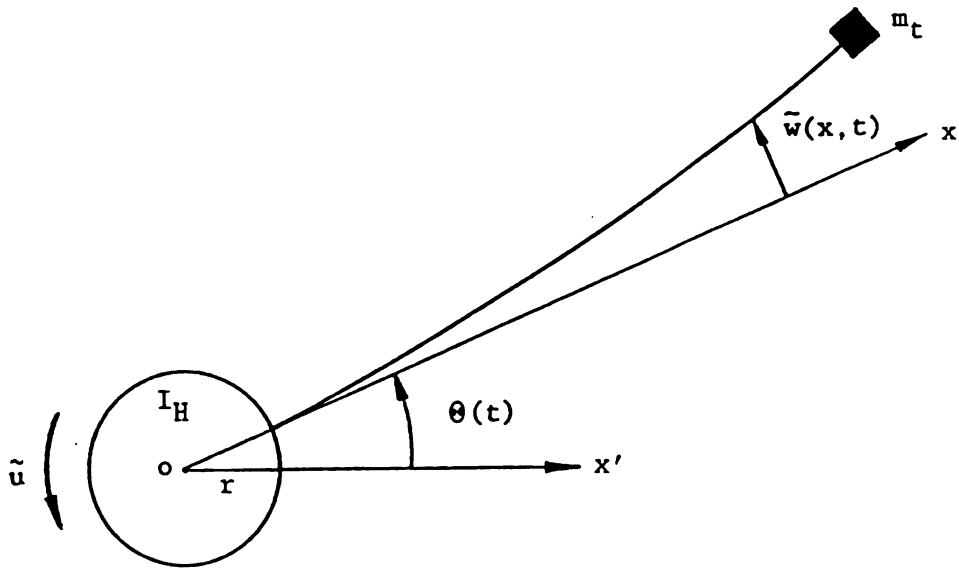


Figure 2.1 Schematic Diagram of a Single-Link Flexible Manipulator

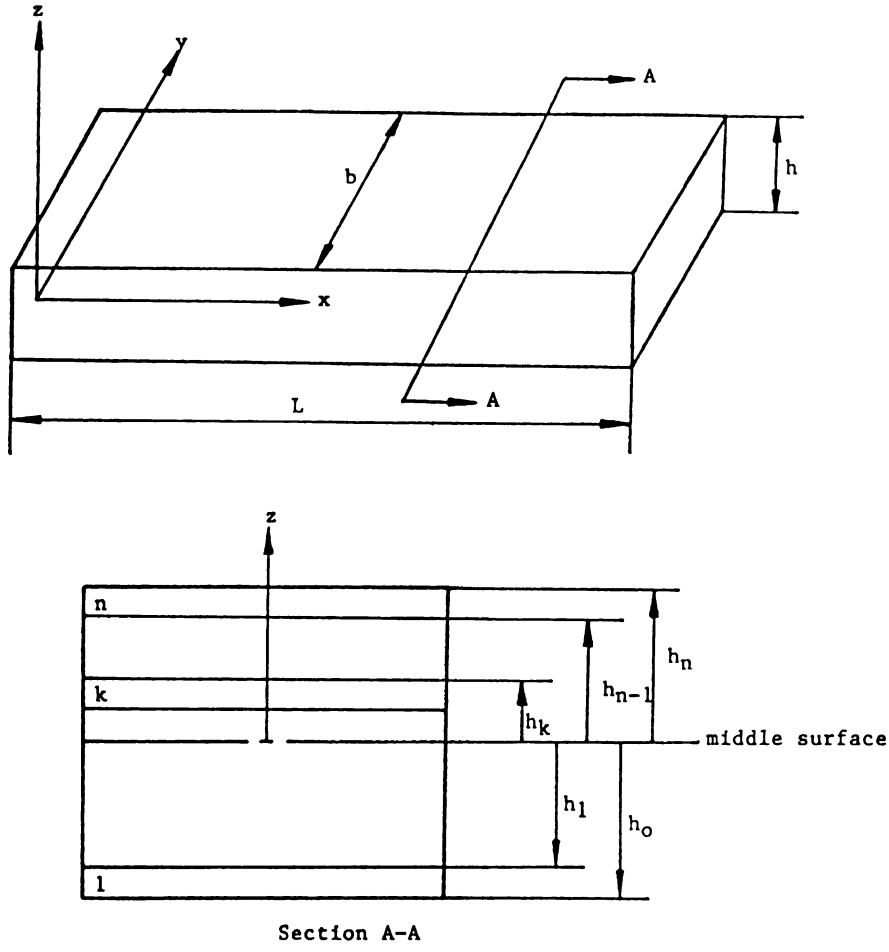


Figure 2.2 Composite Laminate Configuration

In order to determine the potential energy, consider the composite laminate as shown in Figure 2.2. It is seen from this figure that h_k is the vertical distance from the laminate middle surface (z=o) to the upper surface of the k^{th} lamina and h is the total thickness of the laminate. The strain-displacement equations of the laminate are given from the classical lamination theory [69], hence:

$$\epsilon_x = \epsilon_x^o + z\kappa_x$$

$$\epsilon_y = \epsilon_y^o + z\kappa_y \qquad (2.3)$$

$$\epsilon_{xy} = \epsilon_{xy}^o + z\kappa_{xy}$$

where ϵ_i, ϵ_i^o and κ_i are strains at arbitrary location (x,y,z), strains on the middle surface (x,y,o) and curvature changes, respectively.

The stress-strain relation of the k^{th} lamina is also given by

$$\begin{Bmatrix}\sigma_1\\ \sigma_2\\ \sigma_{12}\end{Bmatrix} = \begin{bmatrix}Q_{11} & Q_{12} & 0\\ Q_{12} & Q_{22} & 0\\ 0 & 0 & Q_{66}\end{bmatrix}^k \begin{Bmatrix}\epsilon_1\\ \epsilon_2\\ \epsilon_{12}\end{Bmatrix} \triangleq [Q]^k \{\epsilon\}_{1-2} \qquad (2.4)$$

where the Q_{ij}, so-called reduced stiffnesses, are

$$Q_{11} = \frac{E_1}{1-\nu_{12}\nu_{21}} \quad , \quad Q_{12} = \frac{\nu_{12}E_2}{1-\nu_{12}\nu_{21}}$$

$$Q_{22} = \frac{E_2}{1-\nu_{12}\nu_{21}} \quad , \quad Q_{66} = G_{12} \qquad (2.5)$$

In equation (2.4) and (2.5), σ_1 and σ_2 represent stress in principal material (fiber) and its perpendicular direction respectively, and σ_{12} denotes shear stress in the 1-2 plane. ϵ_1, ϵ_2 and ϵ_{12} define strain corresponding to σ_1, σ_2 and σ_{12} respectively. E_1 and E_2 denote Young's modulus in principal material and its perpendicular direction respectively, and G_{12} defines shear modulus in 1-2 plane. ν_{ij} represents Poisson's ratio and is defined by

$$\nu_{ij} = -\frac{\epsilon_j}{\epsilon_i} \tag{2.6}$$

And the Young's modulus E_1, E_2 and the shear modulus G_{12} are given by

$$\begin{aligned} E_1 &= E_f V_f + E_m V_m \\ E_2 &= E_f E_m/(E_f V_m + E_m V_f) \\ G_{12} &= G_f G_m/(G_f V_m + G_m V_f) \end{aligned} \tag{2.7}$$

where E_f and E_m are Young's modulus of the fiber and matrix, V_f and V_m are volume fraction of the fiber and matrix, and G_f and G_m are shear modulus of the fiber and matrix respectively.

The stress-strain relation for the k^{th} lamina of arbitrary orientation can be obtained by employing the transformation matrix relating 1-2 coordinate system and x-y coordinate system, which has the form

$$[T_1] = \begin{bmatrix} \cos^2\theta & \sin^2\theta & 2\sin\theta\cos\theta \\ \sin^2\theta & \cos^2\theta & -2\sin\theta\cos\theta \\ -\sin\theta\cos\theta & \sin\theta\cos\theta & \cos^2\theta - \sin^2\theta \end{bmatrix} \tag{2.8}$$

where θ represents fiber orientation (lamina angle), which is defined as positive in the counter-clockwise direction. This matrix provides the stress-strain relation in the x-y coordinate, that is

$$\begin{Bmatrix} \sigma_x \\ \sigma_y \\ \sigma_{xy} \end{Bmatrix} = [T_1]^{-1}[Q]^k [T_1]^{-T} \begin{Bmatrix} \epsilon_x \\ \epsilon_y \\ \epsilon_{xy} \end{Bmatrix} \triangleq [\bar{Q}]^k \{\epsilon\}_{x\text{-}y} \tag{2.9}$$

where $[\bar{Q}]^k$ represents the transformed reduced stiffness matrix of the k^{th} lamina. Then the constitutive equation of the laminate is given by

$$\begin{Bmatrix} F_x \\ F_y \\ F_{xy} \\ \cdots \\ M_x \\ M_y \\ M_{xy} \end{Bmatrix} = \left[\begin{array}{ccc} & \vdots & \\ \bar{A} & \vdots & \bar{B} \\ & \vdots & \\ \cdots & \cdots & \cdots \\ & \vdots & \\ \bar{B} & \vdots & \bar{D} \\ & \vdots & \end{array}\right] \begin{Bmatrix} \epsilon^o_x \\ \epsilon^o_y \\ \epsilon^o_{xy} \\ \cdots \\ \kappa_x \\ \kappa_y \\ \kappa_{xy} \end{Bmatrix} \tag{2.10}$$

where the matrices $\bar{A}$, $\bar{B}$ and $\bar{D}$ denote extensional, extensional-bending coupling and bending stiffnesses of the laminate, respectively, and their elements are defined by

$$(\bar{A}_{ij}, \bar{B}_{ij}, \bar{D}_{ij}) = \sum_{k=1}^{n} (\bar{Q}_{ij})^k (h_k - h_{k-1}, \tfrac{1}{2}(h_k^2 - h_{k-1}^2), \tfrac{1}{3}(h_k^3 - h_{k-1}^3)) \tag{2.11}$$

where n is the total number of lamina. And in equation (2.10), the F_i and M_i describe the resultant forces and moments respectively.

The potential energy for the laminate can be obtained from the strain energy and takes the form of

$$V = \frac{1}{2} \sum_{k=1}^{n} \iint_{A_1} \int_{h_{k-1}}^{h_k} \{\sigma_x \epsilon_x + \sigma_y \epsilon_y + \sigma_{xy} \epsilon_{xy}\} \, dz dA_1 \tag{2.12}$$

where A_1 refers to the area of the laminate. The substitution of the strain-displacement relationship (2.3), stress-strain relations (2.9), and constitutive equation (2.10) for the symmetric laminate with respect

to the middle surface ($\bar{B}_{ij}$=0 from the equation (2.11)) into the equation (2.12) yields the following potential energy.

$$V = \iint_{A_1} \left\{ \frac{\bar{A}_{11}}{2} \left(\frac{\partial \bar{u}}{\partial x} \right)^2 + \frac{\bar{D}_{11}}{2} \left(\frac{\partial \bar{\alpha}}{\partial x} \right)^2 + \bar{A}_{12} \left(\frac{\partial \bar{u}}{\partial x} \frac{\partial \bar{v}}{\partial y} \right) \right.$$

$$+ \bar{D}_{12} \left(\frac{\partial \bar{\alpha}}{\partial x} \frac{\partial \bar{\beta}}{\partial y} \right) + \bar{A}_{16} \left(\frac{\partial^2 \bar{u}}{\partial x \partial y} + \frac{\partial \bar{u}}{\partial x} \frac{\partial \bar{v}}{\partial x} \right)$$

$$+ \bar{D}_{16} \left(\frac{\partial^2 \bar{\alpha}}{\partial x \partial y} + \frac{\partial \bar{\alpha}}{\partial x} \frac{\partial \bar{\beta}}{\partial x} \right) + \frac{\bar{A}_{22}}{2} \left(\frac{\partial \bar{v}}{\partial y} \right)^2 + \frac{\bar{D}_{22}}{2} \left(\frac{\partial \bar{\beta}}{\partial y} \right)^2 \qquad (2.13)$$

$$+ \bar{A}_{26} \left(\frac{\partial \bar{v}}{\partial y} \frac{\partial \bar{u}}{\partial y} + \frac{\partial^2 \bar{v}}{\partial x \partial y} \right) + \bar{D}_{26} \left(\frac{\partial \bar{\alpha}}{\partial y} \frac{\partial \bar{\beta}}{\partial y} + \frac{\partial^2 \bar{\beta}}{\partial x \partial y} \right)$$

$$+ \bar{A}_{66} \left(\frac{1}{2} \left(\frac{\partial \bar{u}}{\partial y} \right)^2 + \frac{\partial \bar{u}}{\partial y} \frac{\partial \bar{v}}{\partial x} + \frac{1}{2} \left(\frac{\partial \bar{v}}{\partial x} \right)^2 \right)$$

$$\left. + \bar{D}_{66} \left(\frac{1}{2} \left(\frac{\partial \bar{\alpha}}{\partial y} \right)^2 + \frac{\partial \bar{\alpha}}{\partial y} \frac{\partial \bar{\beta}}{\partial x} + \frac{1}{2} \left(\frac{\partial \bar{\beta}}{\partial x} \right)^2 \right) \right\} dA_1$$

where $\bar{u}$ and $\bar{v}$ are the middle surface displacement with respect to x and y direction respectively, and $\bar{\alpha}$, $\bar{\beta}$ are defined by

$$\bar{\alpha} = - \frac{\partial \bar{w}}{\partial x} \quad , \quad \bar{\beta} = - \frac{\partial \bar{w}}{\partial y} \qquad (2.14)$$

where $\bar{w}$ is the displacement along the z direction.

Thus, by considering the proposed orthotropic composite laminate that has no twisting coupling effect, and one-dimensional beam model shown in Figure 2.1, the equation (2.13) simply reduces to

$$V = \frac{1}{2} \int_0^L b \, \bar{D}_{11} \left(\frac{\partial \bar{\alpha}}{\partial x} \right)^2 dx$$

$$- \frac{1}{2} \int_0^L b \, \bar{D}_{11} \left(\frac{\partial^2 \tilde{w}(x,t)}{\partial x^2} \right)^2 dx \tag{2.15}$$

It is noted that the displacement $\bar{w}$ in equation (2.14) is equivalent to the deflection denoted by $\tilde{w}(x,t)$ in Figure 2.1.

The work done by the nonconservative external torque $\tilde{u}$ is given by

$$W = \tilde{u}(t)\theta(t) \tag{2.16}$$

The dissipated energy due to the inherent damping property of the structure is not considered at this point, however the damping matrix which is proportional to the stiffness matrix will be augmented in the finite element formulation.

Now, the substitution of equations (2.2),(2.15) and (2.16) into the Hamilton's principle

$$\delta \int_{t_1}^{t_2} (T - V + W) \, dt = 0 \tag{2.17}$$

and integrating by parts yield following equations of motion and associated boundary conditions.

$$b\bar{D}_{11} \frac{\partial^4 w(x,t)}{\partial x^4} + \tilde{m} \frac{\partial^2 w(x,t)}{\partial t^2} = 0 \tag{2.18}$$

$$\int_0^L \tilde{m}(x + r) \frac{\partial^2 w(x,t)}{\partial t^2} \, dx + I_H \ddot{\theta}(t)$$

$$+ m_t(L + r) \frac{\partial^2 w(L,t)}{\partial t^2} = \tilde{u}(t)$$

$$\tilde{w}(0,t) = 0 \tag{2.19}$$

$$\frac{\partial \tilde{w}(0,t)}{\partial x} = 0$$

$$b\bar{D}_{11} \left. \frac{\partial^2 w(x,t)}{\partial x^2} \right|_{x=L} = 0$$

$$b\bar{D}_{11} \left. \frac{\partial^3 w(x,t)}{\partial x^3} \right|_{x=L} = m_t \left. \frac{\partial^2 w(x,t)}{\partial t^2} \right|_{x=L}$$

In equation (2.17), t_1 and t_2 are two arbitrary times ($t_2 > t_1$), and the virtual displacements $\delta\tilde{w}(x,t)$ and $\delta\Theta(t)$ are independent and taken equal to zero at x=0 and x=L.

2.3 Finite Element Formulation

There are several ways to solve the governing equation (2.18) in order to obtain system model parameters such as natural frequencies and mode shapes which will be used for designing of feedback controllers. Herein, a finite element formulation incorporating Euler-Bernoulli beam theory is developed to obtain system model parameters. The displacement of the governing partial differential equation (2.18) can be discretized as follows.

$$w(x,t) = [N] \{U\} \tag{2.20}$$

where [N] is the row vector containing shape function which is dependent upon the position only and {U} is the column vector containing the nodal variables U_1, U_2,U_3 and U_4 which is function of time only. In this study, two-node element was employed with two degrees of freedom at each node as shown in Figure 2.3. And a cubic polynomial is chosen to develop shape

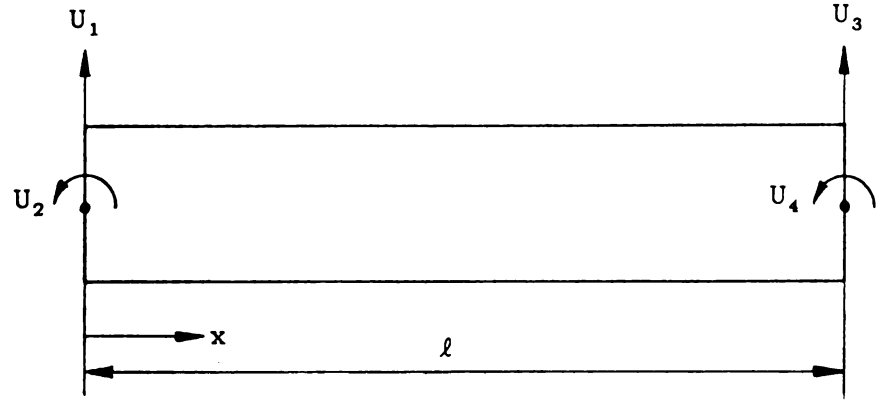


Figure 2.3 Two-Node Beam Element

function which satisfies the conditions for admissibility. The polynomial is given by

$$w(x,t) = a_0 + a_1 x + a_2 x^2 + a_3 x^3 \tag{2.21}$$

After some manipulations, following coefficients of the cubic polynomial are determined.

$$\begin{Bmatrix} a_0 \\ a_1 \\ a_2 \\ a_3 \end{Bmatrix} = \frac{1}{\ell^2} \begin{bmatrix} \ell^2 & 0 & 0 & 0 \\ 0 & \ell^2 & 0 & 0 \\ -3 & -2\ell & 3 & -\ell \\ \frac{2}{\ell} & 1 & \frac{-2}{\ell} & 1 \end{bmatrix} \begin{Bmatrix} U_1 \\ U_2 \\ U_3 \\ U_4 \end{Bmatrix} \tag{2.22}$$

$$\triangleq [A] \{U\}$$

where ℓ is the length of the element. Then the shape function [N] is given by

$$[N] = [\underline{x}] [A] = [N_1 \quad N_2 \quad N_3 \quad N_4] \tag{2.23}$$

where $[\underline{x}] = [\,1 \quad x \quad x^2 \quad x^3\,]$

$$N_1 = \frac{1}{\ell^2}\left[\ell^2 - 3x^2 + \frac{2}{\ell}x^3\right]$$

$$N_2 = \frac{1}{\ell^2}\left[\ell^2 x - 2\ell x^2 + x^3\right] \tag{2.24}$$

$$N_3 = \frac{1}{\ell^2}\left[3x^2 - \frac{2}{\ell}x^3\right]$$

$$N_4 = \frac{1}{\ell^2}\left[-\ell x^2 + x^3\right]$$

The effective mass density of the k^{th} lamina shown in Figure 2.2 is obtained by

$$\rho^k = \rho_m V_m + \rho_f V_f \tag{2.25}$$

where ρ_m is the density of matrix, ρ_f is the density of fiber. Then, the mass per unit length of the beam is expressed by

$$\tilde{m} = b \sum_{k=1}^{n} \rho^k (h_k - h_{k-1}) \tag{2.26}$$

Now, the local mass and stiffness matrix is given by

$$[\hat{M}] = \tilde{m} \int_0^L [N]^T [N]\, dx \tag{2.27}$$

$$[\hat{K}] = b \int_0^L [B]^T \tilde{D}_{11} [B]\, dx \tag{2.28}$$

where $[B]$ is the strain transformation matrix which is given by

$$[B] = \frac{2}{\ell^2}\left[-3 + \frac{6}{\ell}x \quad -2\ell + 3x \quad 3 - \frac{6}{\ell}x \quad -\ell + 3x\right] \tag{2.29}$$

It is generally known that an appropriate modeling of the damping matrix is the most difficult in the modeling process of the flexible structures. The model for the damping matrix, what is considered here, is based on the hypothesis that damping is proportional to the stiffness matrix, i.e.

$$[\hat{C}] = \beta\,[\hat{K}] \tag{2.30}$$

where β is constant damping coefficient and it is very similar to effective Rayleigh damping coefficient. It is noted that the hypothesis made here is only valid for small damping or the beam-like structures which possess well separated eigenvalues (natural frequencies) [94]. The proportionality of the damping matrix to the stiffness matrix allows the governing equations to be decoupled as shown in the next section.

Now by incorporating the boundary conditions described by equation (2.19) and using the transformation matrices relating the local and global reference frames yield the global finite element equation, governing the motion of the proposed robotic system, which has the form of

$$[M]\{\ddot{U}\} + [C]\{\dot{U}\} + [K]\{U\} = \{Q\} \tag{2.31}$$

where the global mass, damping and stiffness matrices are denoted by [M], [C] and [K], respectively, and {Q} represents the generalized forces.

2.4 State Space Representation of the Model

Since the governing equation of the motion described by equation (2.31) is coupled, it is convenient to decouple and represent in the

state space for controller design. By introducing modal coordinate $\{\eta\}$ and modal matrix $[\Phi]$, i.e.

$$\{U\} = [\Phi]\{\eta\} \tag{2.32}$$

the governing equation of motion can be transformed into a set of decoupled modal equations and then written in state space representation as follows.

$$\begin{aligned} \dot{\tilde{x}} &= \tilde{A}\tilde{x} + \tilde{B}\tilde{u} \\ \tilde{y} &= \tilde{C}\tilde{x} \end{aligned} \tag{2.33}$$

where

$$\tilde{x} = \begin{Bmatrix} \eta_0 \\ \dot{\eta}_0 \\ \eta_1 \\ \dot{\eta}_1 \\ \cdot \\ \cdot \\ \cdot \\ \eta_n \\ \dot{\eta}_n \end{Bmatrix}, \qquad \tilde{A} = \begin{bmatrix} 0 & 1 & 0 & 0 & \cdots & 0 & 0 \\ 0 & 0 & 0 & 0 & \cdots & 0 & 0 \\ 0 & 0 & 0 & 1 & \cdots & 0 & 0 \\ 0 & 0 & -\omega_1^2 & -2\zeta_1\omega_1 & \cdots & 0 & 0 \\ \cdot & \cdot & \cdot & \cdot & \cdots & \cdot & \cdot \\ \cdot & \cdot & \cdot & \cdot & \cdots & \cdot & \cdot \\ \cdot & \cdot & \cdot & \cdot & \cdots & \cdot & \cdot \\ 0 & 0 & 0 & 0 & \cdots & 0 & 1 \\ 0 & 0 & 0 & 0 & \cdots & -\omega_n^2 & -2\zeta_n\omega_n \end{bmatrix}$$

$$\tilde{B} = \frac{1}{I_T}\left[0 \quad 1 \quad 0 \quad \frac{d\phi_1(o)}{dx} \quad \cdots \quad 0 \quad \frac{d\phi_n(o)}{dx}\right]^T \tag{2.34}$$

$$\tilde{C} = \begin{bmatrix} 1 & 0 & \frac{d\phi_1(o)}{dx} & 0 & \cdots & \frac{d\phi_n(o)}{dx} & 0 \\ 0 & 1 & 0 & \frac{d\phi_1(o)}{dx} & \cdots & 0 & \frac{d\phi_n(o)}{dx} \\ L & 0 & \phi_1(L) & 0 & \cdots & \phi_n(L) & 0 \end{bmatrix}$$

In equation (2.34), ω_i and ζ_i are the natural frequency and damping ratio of the ith mode respectively, I_T is the total moment of inertia (hub, beam and payload), $d\phi_i(o)/dx$ is the modal slope coefficient and $\phi_i(L)$ is the tip sensor gain. It is noted that the output matrix $\tilde{C}$ includes the gains associated with two colocated sensors - hub angle (first row) and hub angular velocity (second row), and one noncolocated sensor - tip position (third row).

Since the dynamical model given by the equation (2.33) contains many modes in general, all of modes cannot be controlled in practice. Hence, the equation (2.33) should be decomposed into two subdynamic equations by considering the rigid-body mode and the first few critical flexible modes as primary modes, and the remaining modes as residual modes. Two subdynamic equations are

$$\begin{aligned} \dot{\tilde{x}}_p &= \tilde{A}_p \tilde{x}_p + \tilde{B}_p \tilde{u} \\ \tilde{y}_p &= \tilde{C}_p \tilde{x}_p \end{aligned} \tag{2.35}$$

and

$$\begin{aligned} \dot{\tilde{x}}_r &= \tilde{A}_r \tilde{x}_r + \tilde{B}_r \tilde{u} \\ \tilde{y}_r &= \tilde{C}_r \tilde{x}_r \end{aligned} \tag{2.36}$$

where subscript (p) denotes the primary modes and (r) represents the residual modes. In general, there is no certain rule differentiating the primary and residual modes. The differentiation heavily depends upon the geometrical and material properties of the flexible arm and the dynamic characteristics of the employed experimental apparatus such as actuators and sensors [74].

2.5 Summary of the Chapter

The governing partial differential equation and associated boundary conditions for the single-link flexible manipulator fabricated from composite laminates were derived from the Hamilton's principle, and the equation was discretized using the finite element method incorporating the Euler-Bernoulli beam theory. Then, the decoupled linear dynamic model was obtained through the modal analysis and presented in the state space representation, which is convenient form for controller design. It is noted that the relative simplicity of the dynamic model for the proposed composite arm disappears when considering multi-link flexible manipulators. However, the approach employed in this study could be extended to the case of multi-link flexible manipulators or other complicate flexible structures such as helicopter blades and appendages of the satellites fabricated from advanced composite materials.

CHAPTER III

EXPERIMENTAL APPARATUS AND IDENTIFICATION OF SYSTEM MODEL PARAMETERS

3.1 Introduction

A detailed description of the experimental hardware employed for the proposed single-link flexible robotic system featuring the aluminum or the composite arm will be presented in this chapter. Also, an experimental identification of the system model parameters such as natural frequencies and damping ratios will be undertaken. The measured parameters will be compared with the predicted ones. This chapter establishes a point of reference and sets a physical scale of the experiment for the subsequent chapter, which presents the design and implementation of the output feedback controller associated with two colocated sensors for the proposed robotic system.

3.2 Experimental Apparatus

The experimental hardware of the proposed single-link flexible robotic system can be separated into five functional groups; flexible arms (aluminum or composite arm), a DC motor and a servo-drive, a servo-positioning assembly, sensors, and a microprocessor for controller implementation. Figure 3.1 presents a photograph showing these functional groups, and Figure 3.2 shows a schematic diagram of overall robotic

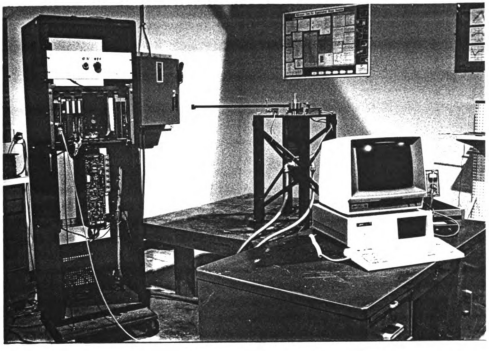


Figure 3.1 Photograph of Overall Robotic System

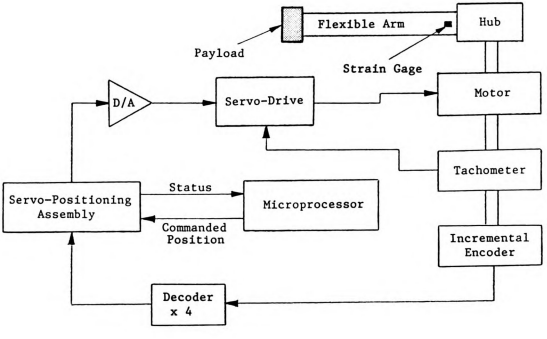


Figure 3.2 Schematic Diagram of Overall Robotic System

system consisting of these functional groups. In this section, The detailed description of each functional group will be presented.

3.2.1 Flexible Arm

3.2.1.1 Aluminum Arm

The aluminum arm is a 0.812 m long, flexible beam which can be easily bended in the horizontal plane, but it is designed to be hard to bend in the vertical and torsional direction to prevent or reduce the torsional effects which were neglected in the modeling process. The arm is clamped on a rigid-body hub which has a radius of 4.3 cm and a moment of inertia of 0.00496 $kg \cdot m^2$, and is mounted directly on the vertical

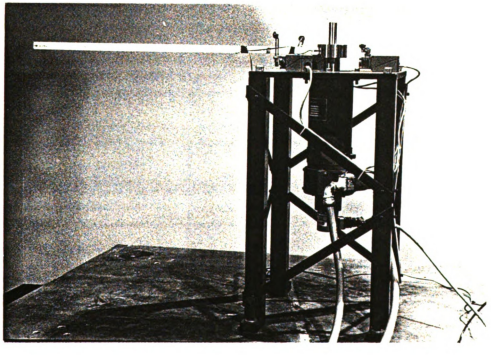


Figure 3.3 Photograph of the Experimental Aluminum Arm

shaft of the DC servo-motor as shown in Figure 3.3. Therefore the rotation of the arm in the horizontal plane is activated by the torque applied to the motor without speed reduction factor. It is seen from Figure 3.3 that the two extreme travel limit switches and one home position limit switch are mounted on the plate of the fixture supporting the motor. The purpose of the installation of the limit switches is prevent overtravel in the emergency case such as instability of the system. When the arm touches one of the limit switches, the main power for the whole system will be turned off automatically. The home position switch is installed in order to obtain high repeatability of the experimental results. With this home position detective switch the robot arm can always start to move from the same position like zero-position in typically industrial robotic manipulators. The payload made of aluminum is attached to the free end of the arm. The 30 mm (length) x 40 mm

Table 3.1 Material and Geometrical Properties of the Aluminum Arm

Properties	Specifications
Beam Material	Aℓ 606-T6511-QQA200/8
Young's Modulus	64.3 GPa
Beam Length	0.812 m
Beam Width	19.02 mm
Beam Thickness	3.14 mm
Beam Mass	0.132 kg

(width) x 8.56 mm (thickness) size of payload is used and its mass is 0.061 kg. Table 3.1 presents the material and geometrical properties of the experimental aluminum arm.

3.2.1.2 Composite Arm

The design and fabrication of the composite arm is not as simple as the case of the aluminum arm. Once the geometrical and material properties of the aluminum arm has been determined, the design of the composite arm can be started based on some design constraints and design criteria which depend upon the objective of experimental investigation and the adaptability of the experimental apparatus. Herein, since the objective of the experimental investigation is to compare quantitatively the control performances between the aluminum and composite arm, following design constraints and a criterion are imposed.

Design Constraints:

$$\text{beam length(L)};\ (L)_{al} = (L)_{com} \tag{3.1}$$

$$\text{beam width(b)};\ (b)_{al} = (b)_{com}$$

Design Criterion:

$$\text{flexural rigidity(FR)};\ (FR)_{al} = (FR)_{com} \tag{3.2}$$

where subscripts (al) denotes the aluminum arm and (com) represents the composite arm. The hub which was employed for the aluminum arm can be easily used for the composite arm with the constraint of same width. The selection of the design criterion, i.e., flexural rigidity (bending stiffness) is somewhat rational way rather than logical manner. Someone

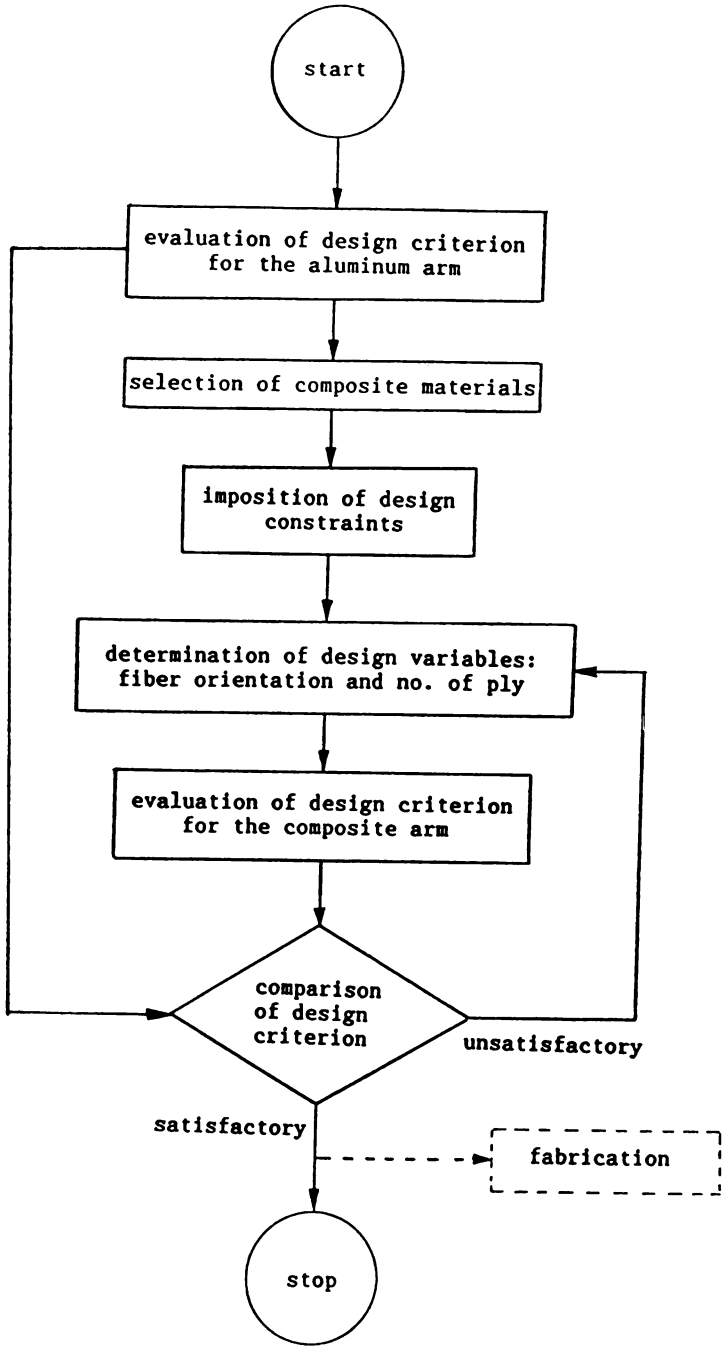


Figure 3.4 Design Methodology of the Composite Arm

can choose other design criteria such as beam geometry. However, it seems to be reasonable start to choose such design constraints and a criterion, since it is well-known that the composite materials has higher strength- and stiffness-weight ratio than that of the aluminum, hence resulting in significant reduced inertia forces in the dynamic motion of the system.

Once the design constraints and design criterion have been decided, the design procedure can be accomplished based on a design methodology presented in Figure 3.4. The design variables are restricted to the fiber orientation (lamina angle) and the number of the prepreg ply, since the manufacturing company generally provides the prepreg which has a certain fixed fiber volume fraction. The flexural rigidity of the composite arm

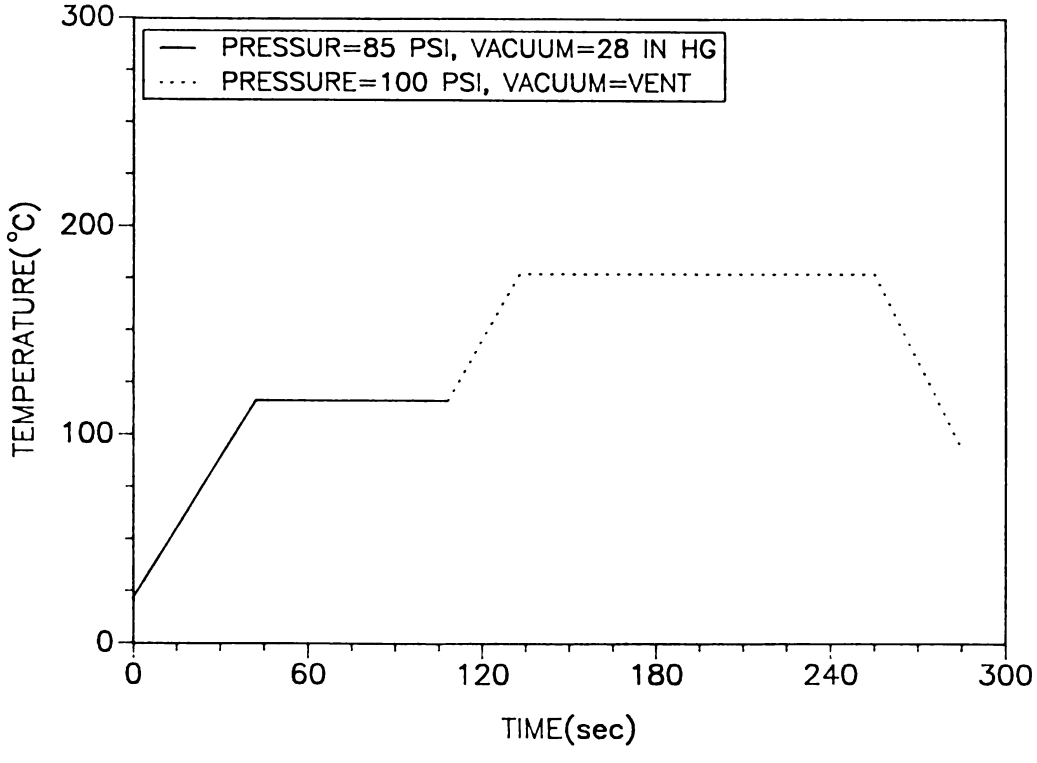


Figure 3.5 Curing Cycle for AS4/3501 Graphite-Epoxy

is calculated from the finite element analysis by changing the design variables to satisfy the imposed design criterion. Several combinations of the design variables were determined through simulation. However, in this study, the 0^{o} of lamina angle was chosen for simplicity of fabrication.

Magnamite graphite prepreg tape, type AS4/3501-5A, manufactured by Hercules Inc., was employed to fabricate the composite arm. The arm was fabricated and cured by Auto Air Corporation, Lansing, Michigan, using the hand lay-up technique, vacuuming and autoclaving based on the curing cycle provided from Hercules Inc. as shown in Figure 3.5. The cure cycle depends upon the resin used, and the material properties are dependent

Table 3.2 Material and Geometrical Properties of the Composite Arm

Properties	Specifications
Beam Material	AS4/3501 - 5A
Young's Modulus	115.0 GPa
Beam Length	0.812 m
Beam Width	19.02 mm
Beam Thickness	2.5 mm
Beam Mass	0.06 kg
Fiber Orientation	0^{o}
Ply Thickness	0.12 - 0.13 mm
Number of Ply	20

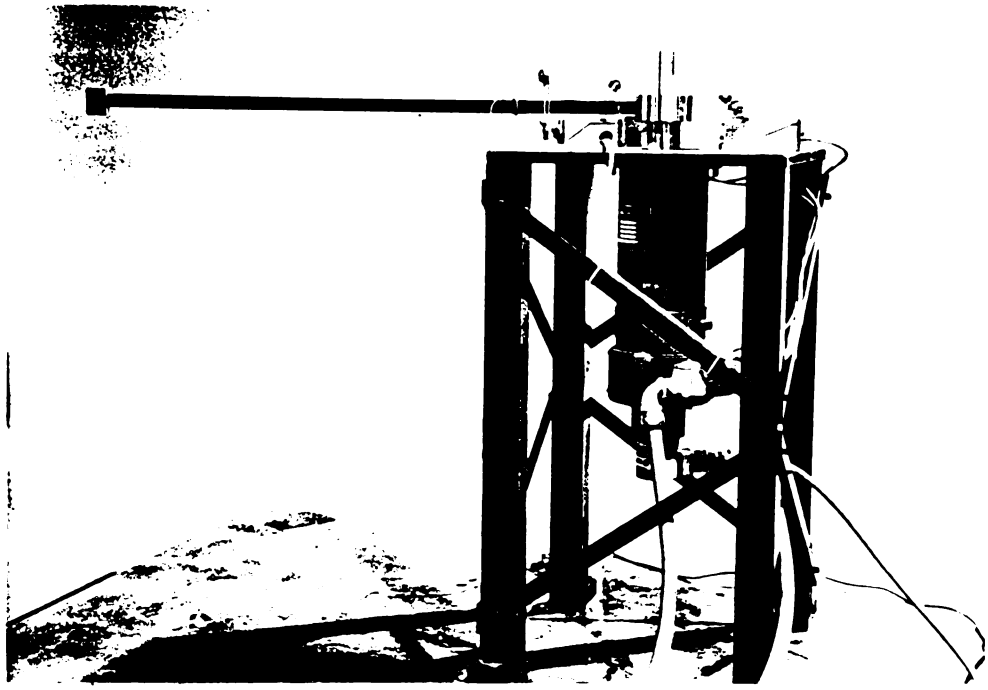


Figure 3.6 Photograph of the Experimental Composite Arm

upon the curing process provided from the manufacturer. The cure process also suggests a post-cure to allow for final cross linking of the polymer chains. The post-cure process has been done at 300^{o}F for three hours with ambient pressure and no vacuum before the cutting laminate with the constrained geometry. Table 3.2 presents the geometrical and material properties of the composite arm, and Figure 3.6 shows the photograph of the composite arm mounted on the rigid hub.

In order to experimentally evaluate the imposed design criterion, the load-deflection characteristics of the both aluminum and composite arms were obtained through the static testing. One end of the arm was clamped on the working table and monotonically increasing load was imposed on the other end of the arm, and the corresponding end-point (tip) deflection was measured subsequently.

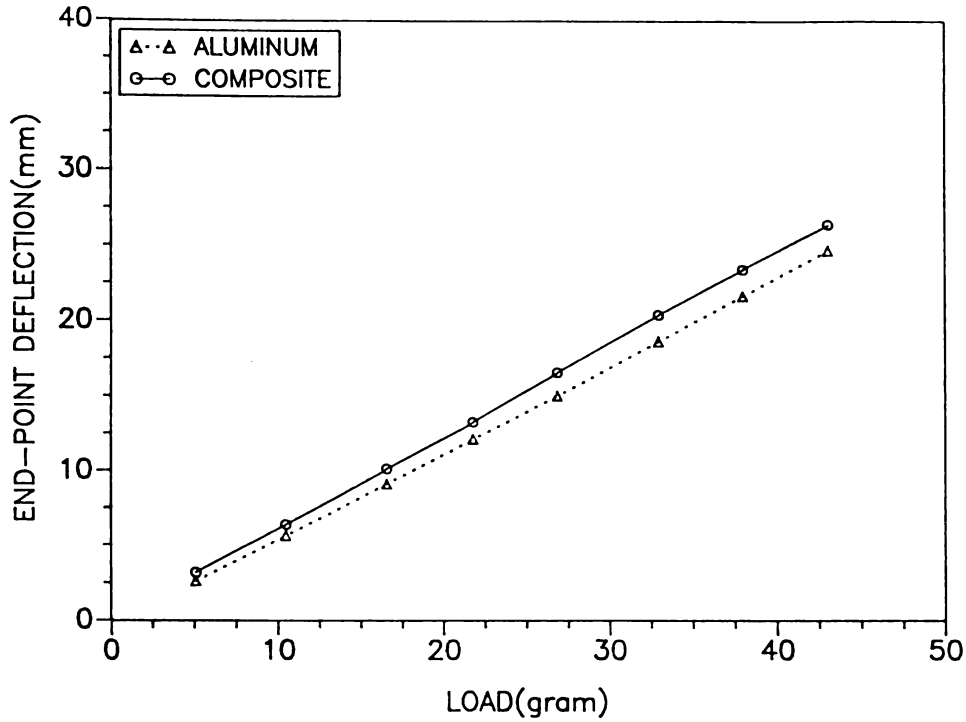


Figure 3.7 Load-Deflection Curve for the Aluminum and Composite Arm

Figure 3.7 presents the load-deflection curve of the both arms. It is seen from this figure that the flexural rigidity (bending stiffness) of the composite arm is little smaller than that of the aluminum arm. The flexural rigidity of the composite arm is approximately 92 percent of that of the aluminum arm. It is recognized that the error is attributed to the manufacturing process such as curing cycle. From this figure, the Young's modulus of the aluminum was distilled by 64.3 GPa, and the Young's modulus in the fiber direction of the composite material was distilled by 115.0 GPa.

3.2.2 DC Motor and Servo-Drive

The DC servo-motor shown in Figure 3.1 is a permanent magnet field, step-free torque motor, model 1338B-AV20, manufactured by Allen-Bradley.

The motor has some standard features such as the capability of 100 percent rated torque output at stall, the minimization of torque ripple and motor cogging by employing a skewed armature. The peak stall torque of this motor is 19.7 N•m and the peak stall current is 50 amperes at the temperature of 40^{o}C. It is noted that the fundamental flexural bending and torsional natural frequencies of the motor shaft are 4.9 kHz and 2.1 kHz respectively, which are of course far beyond the natural frequencies of the aluminum and composite arm. The servo-motor is driven by a servo-drive, model 1388-series B, manufactured by Allen-Bradley. This servo-drive is a pulse width modulated (PWM) driving system which consists of a 150V DC power supply, a transistorized power amplifier, and isolated current sensing and performance testing points such as current feedback signal, current error signal to the power amplifier, and tachometer signal.

3.2.3 Servo-Positioning Assembly

The servo-positioning assembly consists of a servo-controller module, model 1773-M3 and a servo-expander module, model 1771-ES, both manufactured by Allen-Bradley. The commanded position data from the microprocessor is sent to the servo-controller module, and the update status from the servo-expander is sent to the microprocessor. The servo-controller sends axis motion commands to the servo-expander which commands the axis motion by sending an analog signal to the servo-drive through D/A converter which has a 12 bits resolution. The servo sampling period is 2.4 milliseconds and the servo output voltage is ±10V DC maximum.

3.2.4 Sensors

3.2.4.1 Angular Position Sensor

An optical incremental encoder was mounted on the shaft of motor using a flexible encoder coupling adapter,model 1326DP-MOD-M1-C2, manufactured by Allen-Bradley, in order to measure hub angular position. The incremental digital encoder, model 845N-SJH-N4-CRY2, manufactured by Allen-Bradley, has 2500 lines and provides feedback signals that indicate the magnitude and direction of any change of axis position. Also the phase relationship of the encoder output signals allows the decoding circuit to count either 1,2 of 4 feedback pulses for each line of the encoder, hence increasing the resolution of the feedback signal.

3.2.4.2 Angular Velocity Sensor

The tachometer mounted on the shaft of the motor was used to measure hub angular velocity feedback signal. The tachometer has voltage gradient of 0.3 v•sec/rad and 2.0 percent of ripple. The tachometer has 20 turn potentiometer that scales the tachometer feedback signal, and the gain of potentiometer is adjustable through the pot which has ten graduated increments. In order to verify the voltage gradient provided from the manufacturer, the joint was rotated at constant velocity, and the output voltage of the tachometer was measured, then the corresponding velocity was computed. Figure 3.8 presents the relationship between the velocity and the measured output voltage. It is distilled from this figure that the voltage gradient is 0.298 v•sec/rad which is almost same as the value provided by the manufacturer.

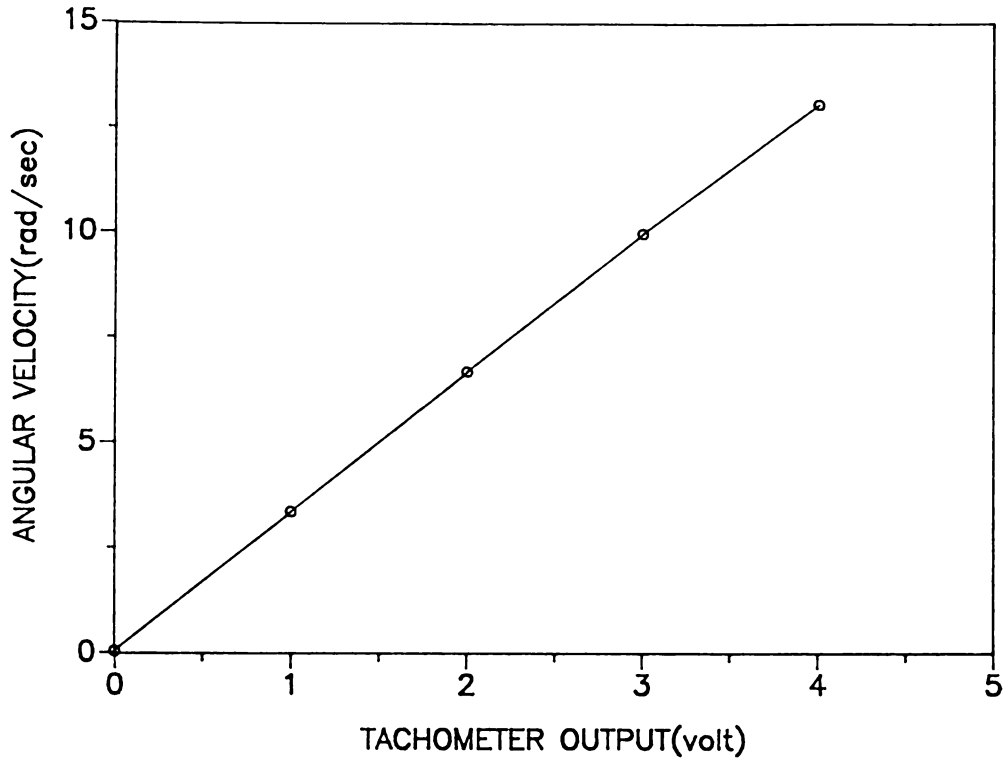


Figure 3.8 Relationship between the Velocity and the Measured Voltage of the Tachometer

3.2.4.3 Tip Deflection Sensor

The strain gages, type WD-DY-250BG-350, manufactured by Micromeasurement Group Inc., were mounted on the root of the arm in order to measure tip deflection, even though the signal was not used as a feedback signal in this study. The half-bridge circuit was arranged to measure the strain. The measured strain was conditioned and amplified through Wheatstone bridge conditioner/amplifier, model 2100, manufactured by Micromeasurement Group Inc. In order to obtain calibration factor between the amplified voltage (strain) and tip deflection, the series of load was imposed monotonically on the free end of arm and the corresponding deflection and amplified voltage were measured. Figure 3.9

shows the test results of this calibration for the both aluminum and composite arms.

3.2.5 Microprocessor

The microprocessor, model PLC-2/16, manufactured by Allen-Bradley was employed for the implementation of the output feedback controller associated with two colocated output sensors - angular position and velocity. The microprocessor has features such as 3K words of memory size, computation capability up to 12 digits and conversion binary to binary coded decimal (BCD) which is a numbering system used to express individual decimal digits (0-9) in four bit binary notation. The personal

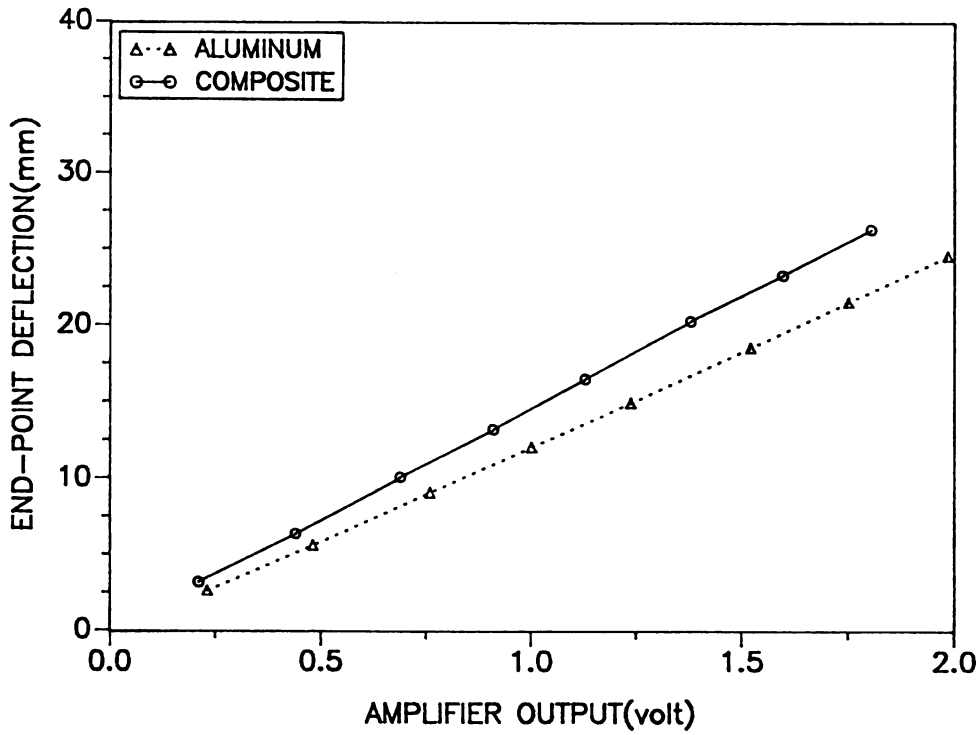


Figure 3.9 Relationship between the Amplified Voltage and the Tip (End-Point) Deflection

computer, model ZVC-159-2, manufactured by Zenith Data Systems, was used as a program operating system. The program was written as relay-like language developed by ICOM Inc. [152].

3.3 Identification of System Model Parameters

In this study, the rigid-body mode and the first two flexible modes are retained as the primary modes. Hence, the equation (2.35) becomes

$$\begin{aligned} \dot{\tilde{x}}_p &= \tilde{A}_p \tilde{x}_p + \tilde{B}_p \tilde{u} \\ \tilde{y}_p &= \tilde{C}_p \tilde{x}_p \end{aligned} \tag{3.3}$$

where

$$\tilde{A}_p = \begin{bmatrix} 0 & 1 & 0 & 0 & 0 & 0 \\ 0 & 0 & 0 & 0 & 0 & 0 \\ 0 & 0 & 0 & 1 & 0 & 0 \\ 0 & 0 & -\omega_1^2 & -2\zeta_1\omega_1 & 0 & 0 \\ 0 & 0 & 0 & 0 & 0 & 1 \\ 0 & 0 & 0 & 0 & -\omega_2^2 & -2\zeta_2\omega_2 \end{bmatrix}$$

$$\tilde{B}_p = \frac{1}{I_T} \begin{bmatrix} 0 & 1 & 0 & \frac{d\phi_1(o)}{dx} & 0 & \frac{d\phi_2(o)}{dx} \end{bmatrix}^T$$

$$\tilde{C}_p = \begin{bmatrix} 1 & 0 & \frac{d\phi_1(o)}{dx} & 0 & \frac{d\phi_2(o)}{dx} & 0 \\ 0 & 1 & 0 & \frac{d\phi_1(o)}{dx} & 0 & \frac{d\phi_2(o)}{dx} \end{bmatrix}$$

It is noted that the output matrix $\tilde{C}_p$ includes sensor gains associated with two colocated output sensors - angular position and velocity. In

this section, the system model parameters such as ω_i, ζ_i and $d\phi_i(o)/dx$ will be identified through the simulation and measurement.

3.3.1 Predicted

For the calculation of the system model parameters, the governing equation of motion given by the equation (2.31) was solved without considering the damping and generalized forcing terms,i.e.,

$$[M]\{\ddot{U}\} + [K]\{U\} = \{0\} \tag{3.4}$$

The two-node element with two degrees of freedom at each node as shown in Figure 2.3 was used and the number of element was ten. Table 3.3 presents the system model parameters obtained from the inhousing finite element program for the both aluminum and composite arms without payload. The geometrical and material properties given in Tables 3.1 and 3.2 were employed for the aluminum and composite arm respectively. The Ω_i in the Table 3.3 represents the natural frequency of the ith cantilevered-mode (clamped-mode). It is observed from Table 3.3 that the pinned-mode fundamental natural frequency (ω_1) of the composite arm is increased by 7.5 percent relative to that of the aluminum arm, while the clamped-mode fundamental natural frequency (Ω_1) of the composite arm is increased by 29.2 percent. This increment of the clamped-mode fundamental natural frequency can increase the equivalent rigid-body mode control bandwidth of the closed-loop system which is limited by Ω_1 with a certain compensator zero as will be observed in the subsequent chapter.

Table 3.4 presents the system model parameters for the aluminum and composite arm with payload of 0.061 kg. It is interesting to observe that

Table 3.3 Comparison of the System Model Parameters of the Aluminum and Composite Arm without Payload

Parameters	Aluminum Arm	Composite Arm
ω_1(Hz)	8.961	9.688
ω_2(Hz)	25.232	34.147
Ω_1(Hz)	3.738	5.269
Ω_2(Hz)	23.425	33.024
$\frac{d\phi_1(o)}{dx}$	2.1534	1.5385
$\frac{d\phi_2(o)}{dx}$	1.0135	0.4978

Table 3.4 Comparison of the System Model Parameters of the Aluminum and Composite Arm with Payload of 0.061 kg

Parameters	Aluminum Arm	Composite Arm
ω_1(Hz)	7.425	7.424
ω_2(Hz)	20.337	25.835
Ω_1(Hz)	2.201	2.318
Ω_2(Hz)	18.068	24.337
$\frac{d\phi_1(o)}{dx}$	3.1545	3.0273
$\frac{d\phi_2(o)}{dx}$	1.8573	1.1858

the pinned-mode fundamental natural frequency of the aluminum arm is almost same as that of the composite arm, even though the second mode frequency of the composite arm is larger than that of the aluminum arm. And also the clamped-mode fundamental natural frequency of the composite arm is larger than that of the aluminum arm by only 5 percent. The reason follows from the ratio of the payload to the beam mass. It is seen from Tables 3.1 and 3.2 that the ratio of payload to beam mass is 46.2 percent and 101.6 percent for the aluminum and composite arm respectively.

Figure 3.10 presents the first pinned-mode natural frequency (ω_1) variation (with respect to the first cantilevered-mode natural frequency (Ω_1) as a function of the the ratio of the hub moment of inertia (I_H) to the beam moment of inertia (I_B). It is noted that the I_B of the aluminum arm is 0.029 kg•m^2, while that of the composite arm is 0.0132 kg•m^2. It is apparent from this figure that even a small ratio of the hub moment of inertia to the beam moment of inertia has significant effect in decreasing the pinned-mode natural frequency. The pinned-mode natural frequency approaches to the cantilevered-mode natural frequency as the ratio increases as expected. Figure 3.11 shows the fundamental natural frequency variation with respect to the ratio of the payload (m_t) to the beam mass (m_b). It is noted that the mass of the aluminum arm is 0.132 kg, while that of the composite arm is 0.06 kg. The effect of the payload on the frequency variation is not as significant as the effect of the hub moment of inertia, even though the frequency noticeably decreases in the small ratio of the payload to the beam mass.

Figure 3.12 shows the first three pinned-mode shape for the aluminum and composite arm without payload. The slopes of the mode shapes at the hub (x=0) have been chosen positive by convention. It is observed that the slope at the hub decreases by increasing the mode due to the presence of lumped inertia of the hub. Thus, the pinned-mode natural frequency becomes closer to the clamped-mode natural frequency by increasing the mode. It is also interesting that the modal magnitude at the end of the arm (x/L) has alternating sign from one mode to next mode. This phenomenon is interpreted as nonminimum phase of the tip position which should be carefully considered in controller design associated with the tip position sensor.

Figure 3.13 presents the calculated Bode plot of open-loop transfer function for the angular velocity of the aluminum and composite arm without payload. The damping ratio of the aluminum arm was chosen by 0.005 for each flexible mode, while that of the composite arm was chosen by 0.007 for each flexible mode. The peaks correspond to the pinned-mode natural frequencies ω_i, and the valleys correspond to the clamped-mode natural frequencies Ω_i. At the pinned-mode, the output signal of angular velocity is maximum (equivalent to saying that the strain energy of the root of the beam is minimum), and at the clamped-mode, the angular velocity output signal is minimum (equivalent to saying that the strain energy of the root of the beam is maximum). It is seen from this figure that the output magnitude at the second mode natural frequency of the composite arm is less than that of the aluminum arm by 40 percent. This implies that the output signal effect induced from the second mode of the composite arm is not as significant as the case of the aluminum arm. Hence somehow the second mode can be neglected in the modeling process

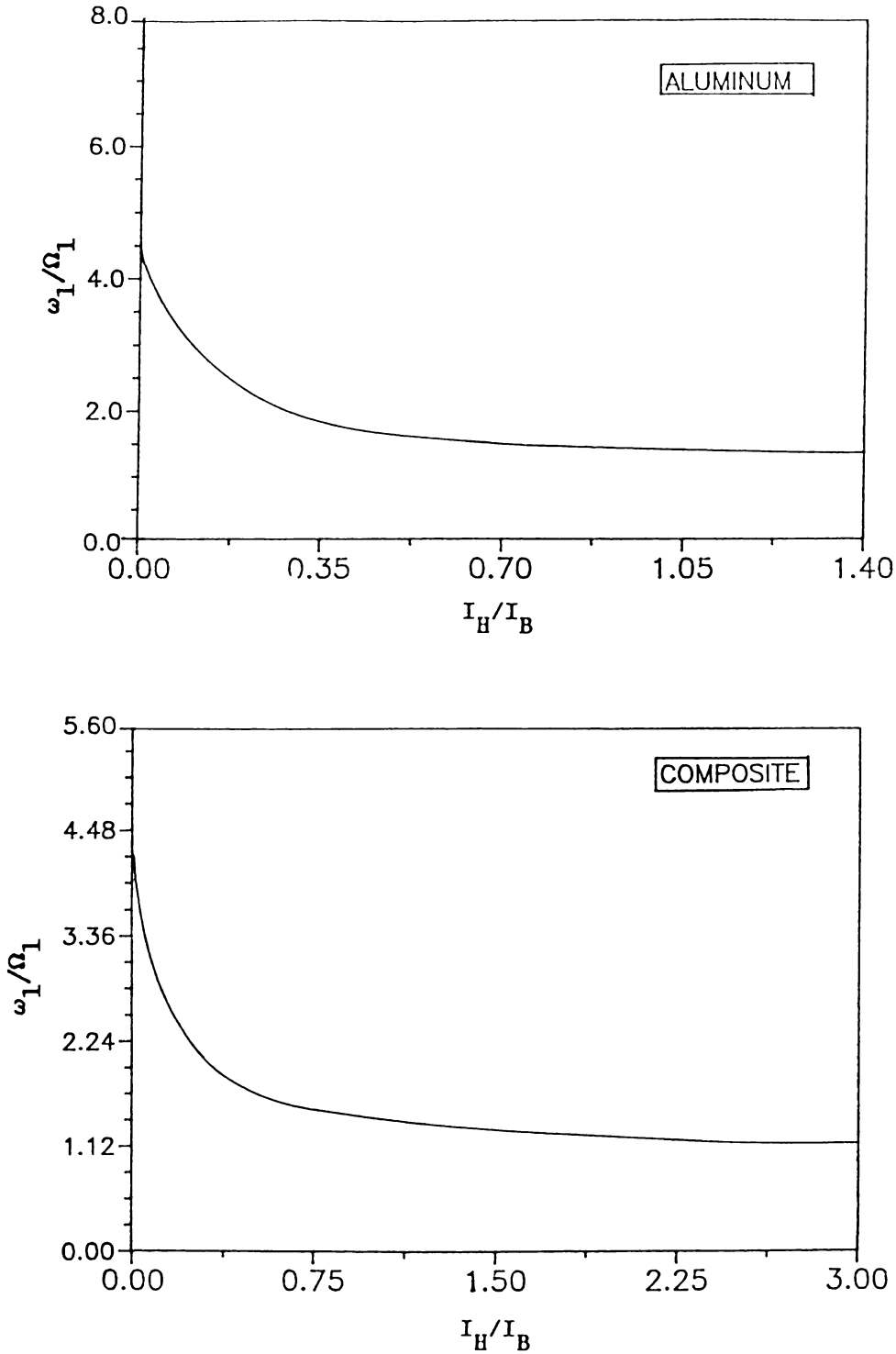


Figure 3.10 Frequency Variation with respect to the Ratio of the Hub Moment of Inertia to the Beam Moment of Inertia

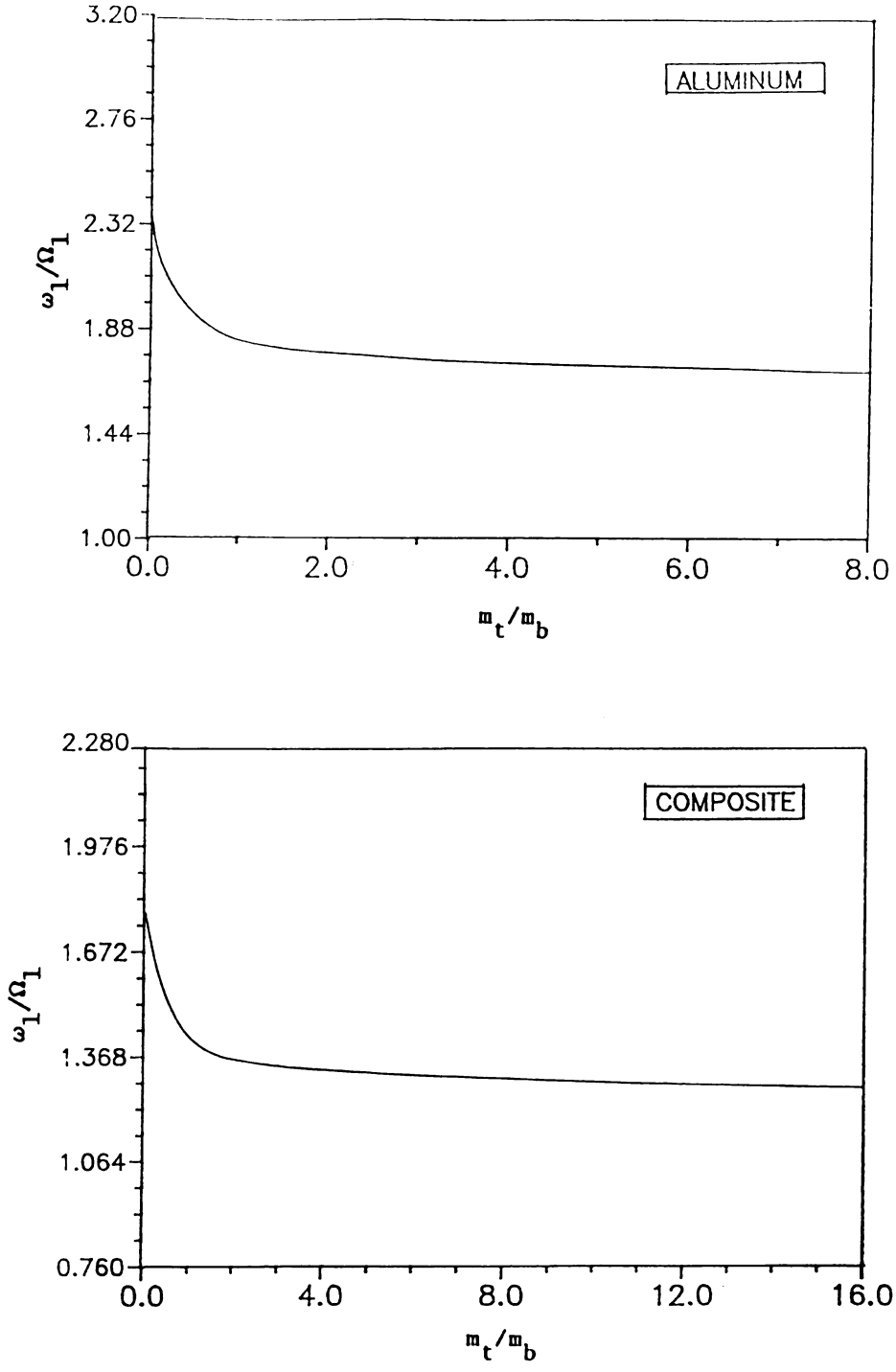


Figure 3.11 **Frequency Variation with respect to the Ratio of the Payload to the Beam Mass**

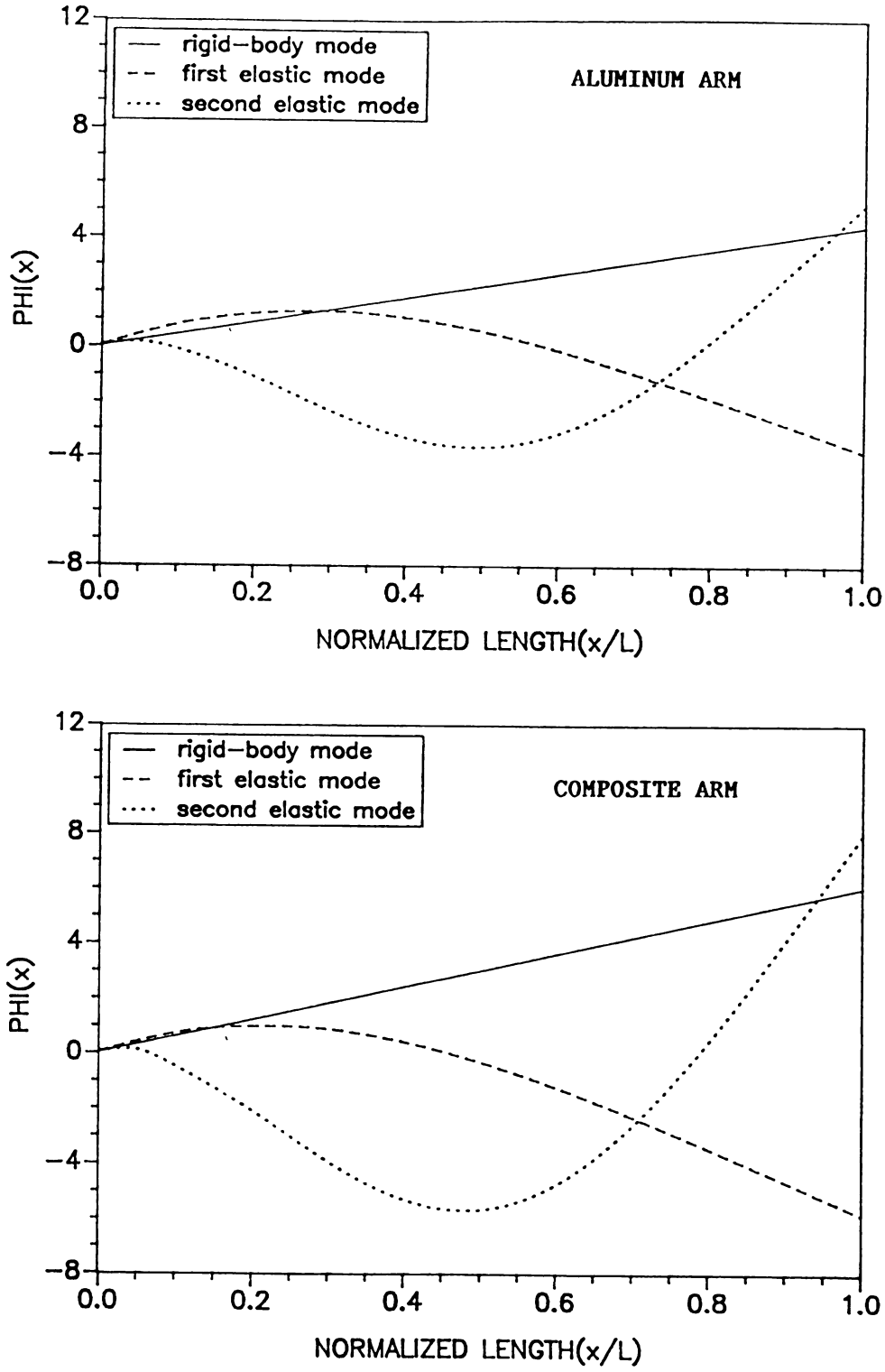


Figure 3.12 First Three Pinned-Mode Shape for the Aluminum and Composite Arm

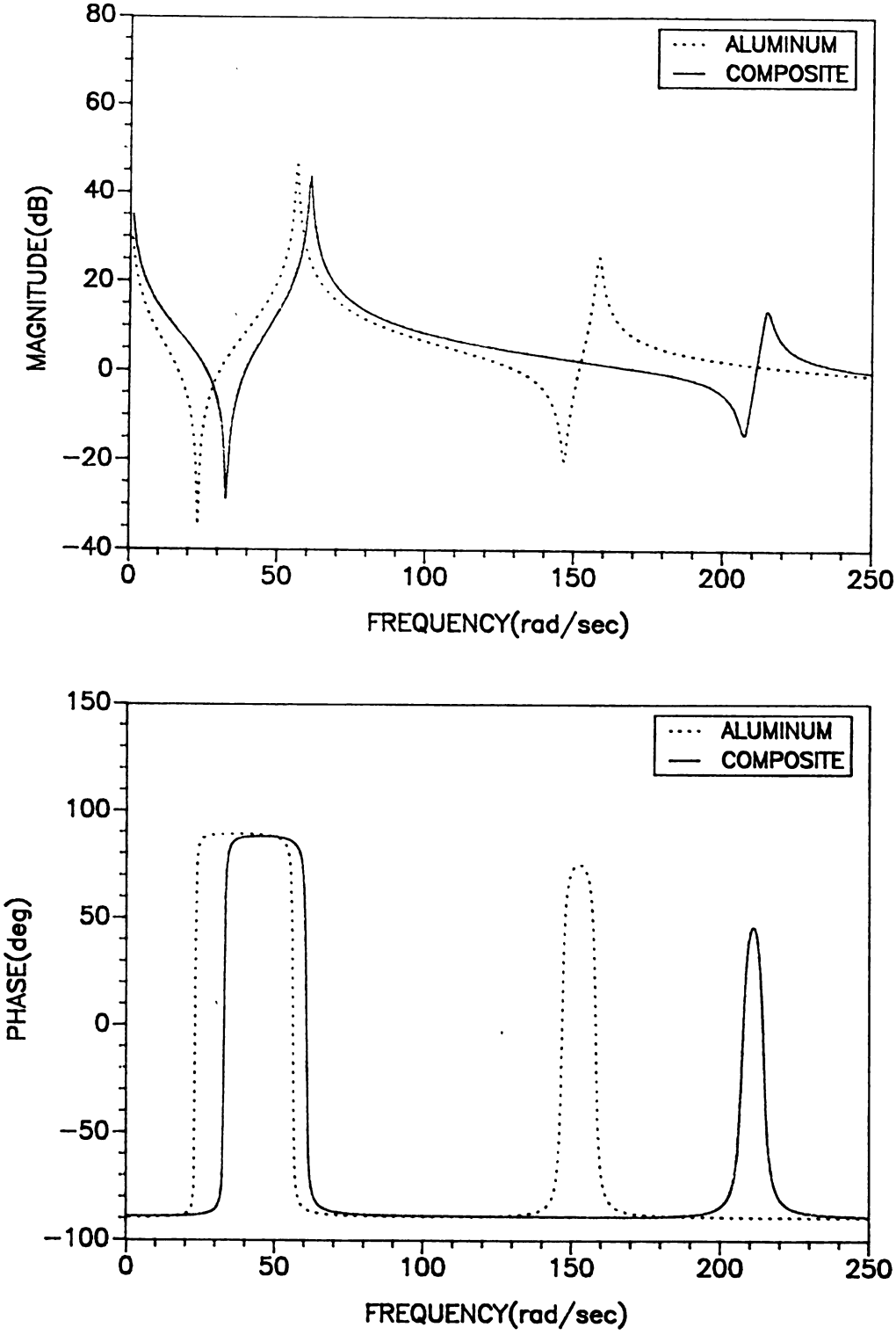


Figure 3.13 Calculated Open-Loop Transfer Function for Angular Velocity without Payload

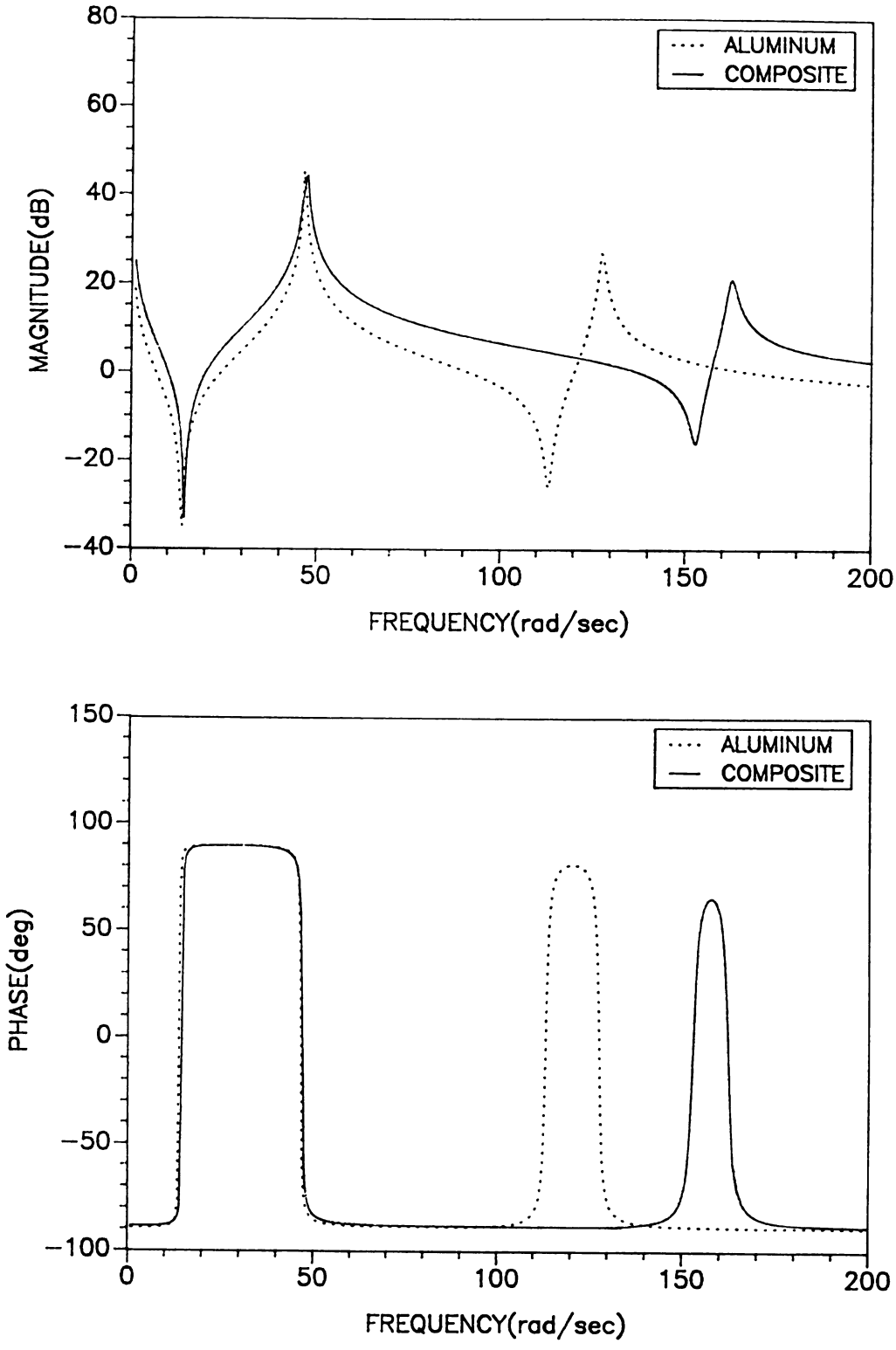


Figure 3.14 Calculated Open-Loop Transfer Function for Angular Velocity with Payload of 0.061 kg

without causing serious error. Herein, the second mode of the both aluminum and composite arms was maintained for reasonable quantitative comparison. It is also interesting to observe from Figure 3.13 that the phase margin corresponding to the first gain crossover at ω = 16.3 rad/sec for the aluminum arm and ω = 25.8 rad/sec for the composite arm is 90 degree. However, the phase margin will be lower for any practical system due to the unmodelled dynamics of the actuators and sensors as well as sampling delays of the output feedback signals. This phenomenon will be investigated in the next section. Figure 3.14 shows the calculated Bode plot of the open-loop transfer function for the angular velocity of the aluminum and composite arm with payload of 0.061 kg.

3.3.2 Measured

In order to measure the natural frequency and damping ratio of each mode for the aluminum and composite arm, a sinusoidal input voltage was applied to the servo-drive and its frequency response was swept in the range of interest (0.8 Hz-32 Hz for the aluminum arm and 0.8 Hz-40 Hz for the composite arm). The 12 MHz programmable function generator, model 275, manufactured by Wavetek, was employed to provide the sinusoidal input and the output signal (magnitude and phase) from the tachometer was measured using the oscilloscope, model T912, manufactured by Tektronix.

Figure 3.15 shows the calculated and measured frequency response of the aluminum arm without payload from the servo-drive input to the tachometer output. It is seen from this figure that the cantilevered-mode natural frequencies (valleys) match very well between the calculated and measured values, while the pinned-mode natural frequencies (peaks) do not match well. The poor agreement of the pinned-mode natural frequencies is

attributed to the motor joint friction which may produce significant effect to the pinned boundary conditions. This joint friction may exit as a Coulomb friction and is hard to model incorporating with the linear model employed in this study. It is also observed from the measured phase response that the phase margin corresponding to the first gain crossover at ω = 16.1 rad/sec is 63 degree which is much lower than the calculated value of 90 degree. This reduced phase margin limits the stability of the system in practice whose stability is guaranteed theoretically with the infinite gain margin and 90 degree of the phase margin. The damping ratio of the proposed structural system may be obtained from this frequency response. Herein, a half-power point method [148] was employed to determine the damping ratio of each mode. The damping ratio ζ_1= 0.0224 and ζ_2= 0.0143 were distilled from the Figure 3.15.

Figure 3.16 presents the calculated and measured frequency response of the composite arm without payload from the servo-drive input to the tachometer output. Same phenomena as those of the aluminum arm are observed from this figure. The phase margin corresponding to the first gain crossover at ω = 25.0 rad/sec is 81 degree which is larger than that of aluminum arm by 22.2 percent, hence implying the increment of the stability margin of the practical system featuring the composite arm. The damping ratio ζ_1=0.0237 and ζ_2= 0.0148 were distilled from this frequency response by using a half-point method. Tables 3.5 and 3.6 present a comparison of the calculated and measured natural frequencies of the aluminum and composite arm without and with payload.

The phase lag observed in the Figures 3.15 and 3.16 was arisen from the inherent dynamic characteristics of the employed velocity sensor -

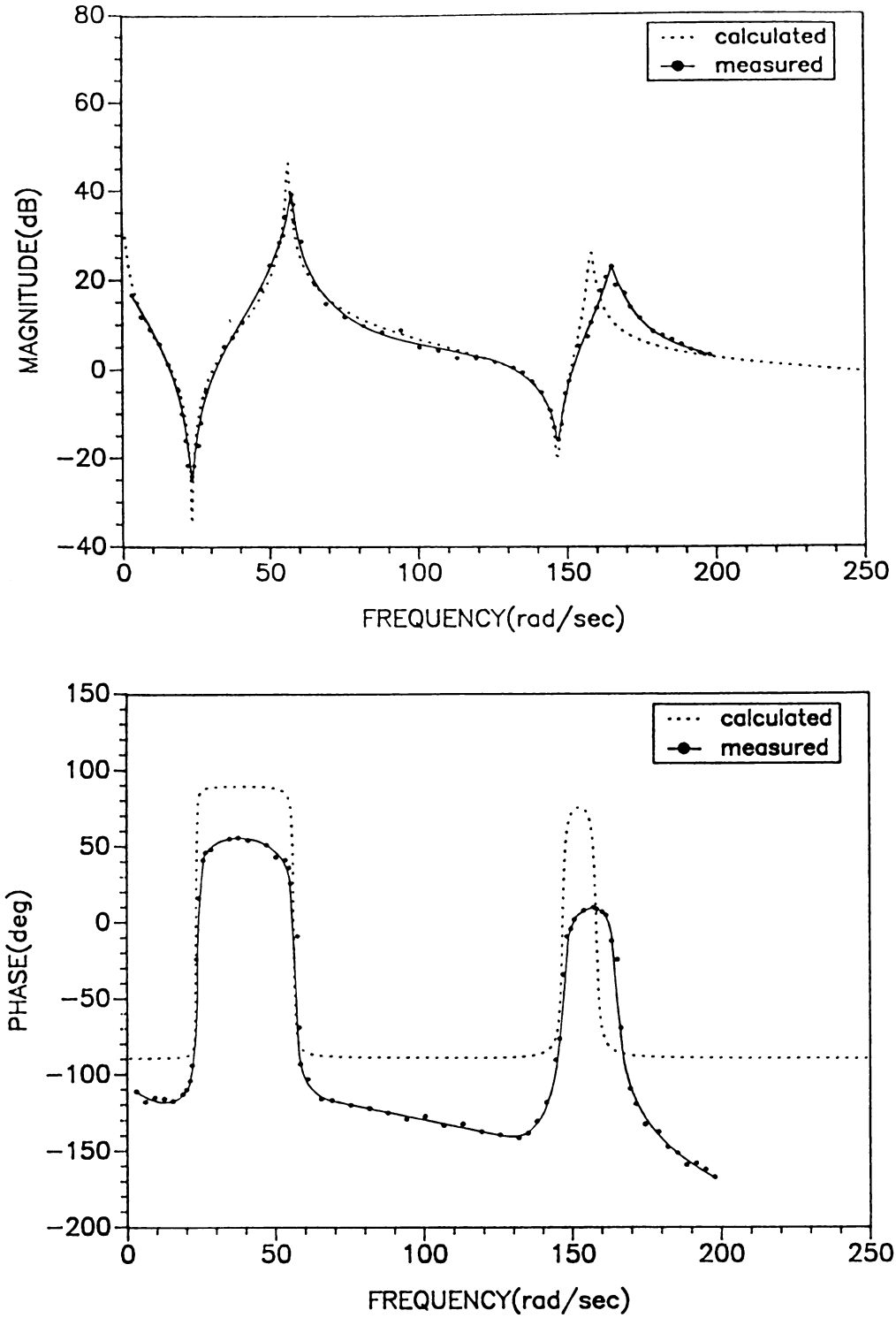


Figure 3.15 Calculated and Measured Frequency Response of the Aluminum Arm without Payload

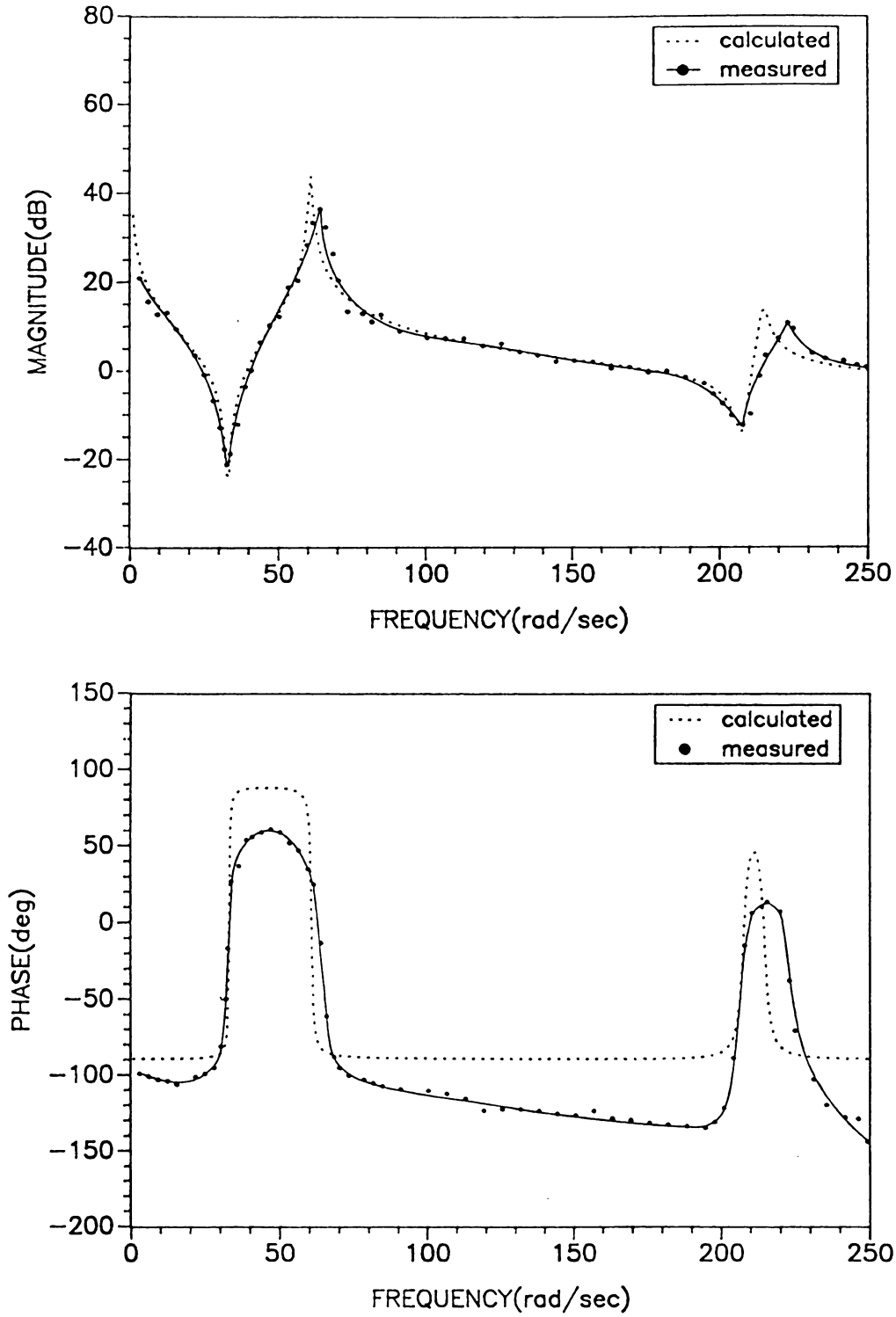


Figure 3.16 Calculated and Measured Frequency Response of the Composite Arm without Payload

Table 3.5 Comparison of the Calculated and Measured Natural Frequency without Payload

Frequency (Hz)	Aluminum Arm		Composite Arm	
	Calculated	Measured	Calculated	Measured
ω_1	8.961	9.15	9.688	10.20
ω_2	25.232	26.30	34.147	35.50
Ω_1	3.738	3.73	5.269	5.22
Ω_2	23.425	23.40	33.024	33.09

Table 3.6 Comparison of the Calculated and Measured Natural Frequency with Payload of 0.061 kg

Frequency (Hz)	Aluminum Arm		Composite Arm	
	Calculated	Measured	Calculated	Measured
ω_1	7.425	7.83	7.428	7.89
ω_2	20.337	21.10	25.835	26.70
Ω_1	2.201	2.12	2.318	2.29
Ω_2	18.068	18.10	24.337	25.5

tachometer. Ideally, the angular velocity is given by $\dot{\theta}(s) = s\theta(s)$ where s is Laplace variable. However, it is hard to say in practice that the actual hub rate is exact derivative of the hub angle. Hence, there exist always unmodelled sensor dynamics. For more clear observation, let the angular velocity have a relationship with the angular position by $\dot{\theta}(s) = (s/(s/a + 1))\,\theta(s)$ so that the phase lag of the response can be caused depending on the value of a. Figure 3.17 presents the simulated open-loop transfer function for the angular velocity with three different values of a. It is clearly observed from this figure that the phase lag increases as the value of a decreases, and furthermore, as the value of a

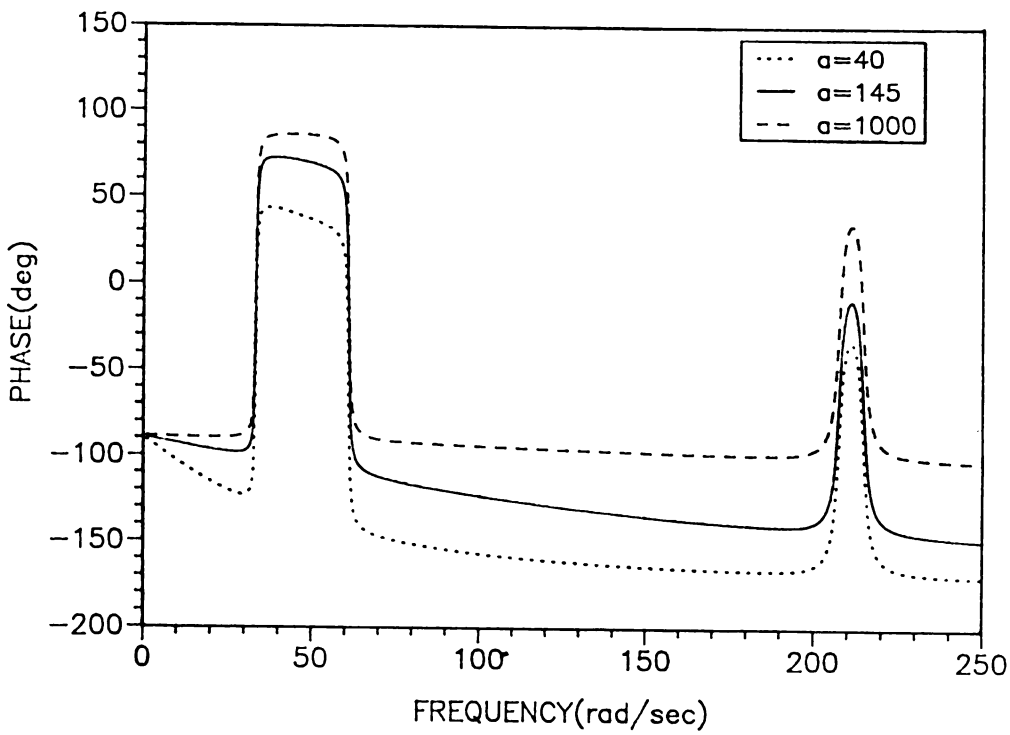


Figure 3.17 Calculated Open-Loop Transfer Function for the Angular Velocity with $\dot{\theta}(s)=(s/(s/a+1))\theta(s)$

goes to infinity,the response becomes to the ideal case, i.e., $\dot{\theta}(s) = s\theta(s)$. Hence, the larger value of a, the smaller phase lag. For the employed velocity sensor in this study, the corresponding value of a is approximately 145 which is equivalent to 6.89 milliseconds of time delay. Therefore, attention should be paid to the unmodelled dynamics of sensors or actuators in order to predict the stability of the practical system.

Now, the system parameters of the dynamic model given by the equation (3.3) were identified through the calculation and measurement. Since all parameters were not available from the experimental measurement, herein, the available data from the both calculation and measurement were adopted to provide the necessary numerical values in the model. The measured data about the natural frequencies and damping ratios and the calculated data about the modal slope coefficients at the hub ($d\phi_i(o)/dx$) were adopted.

3.4 Summary of the Chapter

The detailed description of the experimental apparatus of the proposed robotic system featuring the output feedback controller associated with two colocated output sensors has been presented. Each functional group of the overall robotic system was described in terms of the manufacturers and specifications as well as verification of the performance requirements. The system model parameters such as natural frequencies and damping ratios of the flexible modes have been identified through the calculation and measurement. Good agreement between two results was achieved.

CHAPTER IV

OUTPUT FEEDBACK CONTROL ASSOCIATED WITH TWO COLOCATED OUTPUT SENSORS

4.1 Introduction

A proportional-plus-derivative (PD) output feedback controller associated with two colocated output sensors for angular position and velocity is designed based on the reduced-order model containing the primary modes only. Then, the controller is experimentally implemented in order to investigate and compare the control performances of the flexible manipulators fabricated from aluminum (aluminum arm) and composite laminates (composite arm). The advantages of the implementation of such a simple feedback controller are that some guidelines for the comparison of control performances between the aluminum and the composite arm can be provided easily and the dynamic model parameters can be readily identified and compared between experimental and theoretical results.

In this chapter, the PD output feedback controller will be formulated using the root-locus technique and the Lyapunov method. Experimental results such as step responses to a commanded step angular position, step responses in the presence of the sinusoidal disturbances which have forcing frequencies close to the clamped-mode natural frequencies of the arms, and the instability of the employed system will be presented and compared between the aluminum and composite arm. The

simulated results corresponding to the measured results will be also presented.

4.2 Controller Design

The dynamic model given by the equation (3.3) is employed for the controller design. Consider the block-diagram of the closed-loop system as shown in Figure 4.1 which features a proportional-plus-derivative output feedback controller associated with two colocated sensors. The output equation in (3.3) can be rewritten as

$$\tilde{y}_p = \begin{bmatrix} \tilde{y}_1 \\ \tilde{y}_2 \end{bmatrix} = \begin{bmatrix} \tilde{C}_1 \\ \tilde{C}_2 \end{bmatrix} \tilde{x}_p \tag{4.1}$$

where the output $\tilde{y}_1$ represents angular position and $\tilde{y}_2$ denotes angular velocity. $\tilde{C}_1$ and $\tilde{C}_2$ represent the output matrix associated with $\tilde{y}_1$ and $\tilde{y}_2$ respectively. In Figure 4.1, $\tilde{r}$ represents the commanded angular position, K_p is the position feedback gain and K_v is the velocity feedback gain.

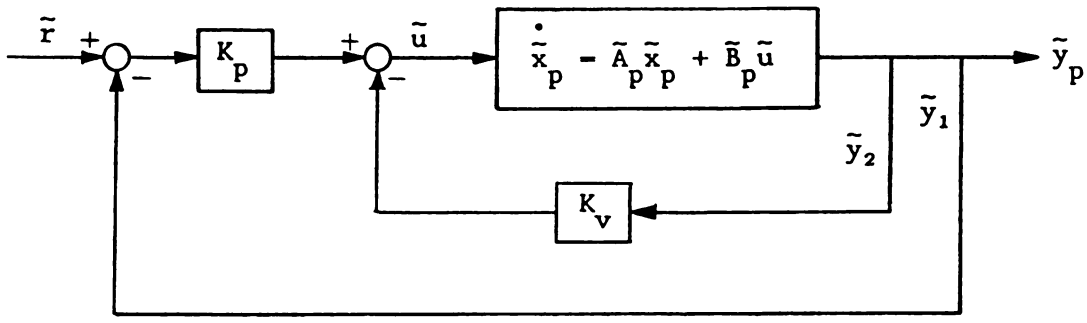


Figure 4.1 Block-Diagram of the Output Feedback Control System

The open-loop transfer function from the input torque to angular position is given by

$$\frac{\tilde{y}_1(s)}{\tilde{u}(s)} \triangleq G_o(s) = \tilde{C}_1 \, (sI - \tilde{A}_p \,)^{-1} \, \tilde{B}_p \tag{4.2}$$

where s is the Laplace variable. The control torque $\tilde{u}(s)$ is given by

$$\tilde{u}(s) = K_p(\, \tilde{r}(s) - y_1(s)) - K_v y_2(s) \tag{4.3}$$

Assuming the angular velocity sensor output is the exact derivative of the angular position sensor, the equation (4.3) becomes

$$\tilde{u}(s) = K_p \, (\, \tilde{r}(s) - \tilde{y}_1(s)) - sK_v \tilde{y}_1(s) \tag{4.4}$$

Now, the closed-loop transfer function of the system is obtained by

$$\frac{\tilde{y}_1(s)}{\tilde{r}(s)} \triangleq G_{c\ell}(s) = \frac{K_p \, G_o(s)}{1 + K_V(s + K_p/K_v) \, G_o(s)} \tag{4.5}$$

Therefore, the closed-loop poles of the system are roots of the following characteristic equation given by

$$1 + K_v \, (s + K_p \, / \, K_v) \, G_o(s) = 0 \tag{4.6}$$

The shape of the loot-locus of the closed-loop system, that is, the closed-loop system performance depends on the location of the compensator zero, defined by $Z_{co} \triangleq -K_p/K_v$. With the certain compensator zero, the rigid-body closed-loop poles may move from the origin of the s-plane (two open-loop poles are zeros) toward the open-loop zeros of the system which are characterized by cantilevered-modes, or toward the real axis of the s-plane resulting in sluggish motion.

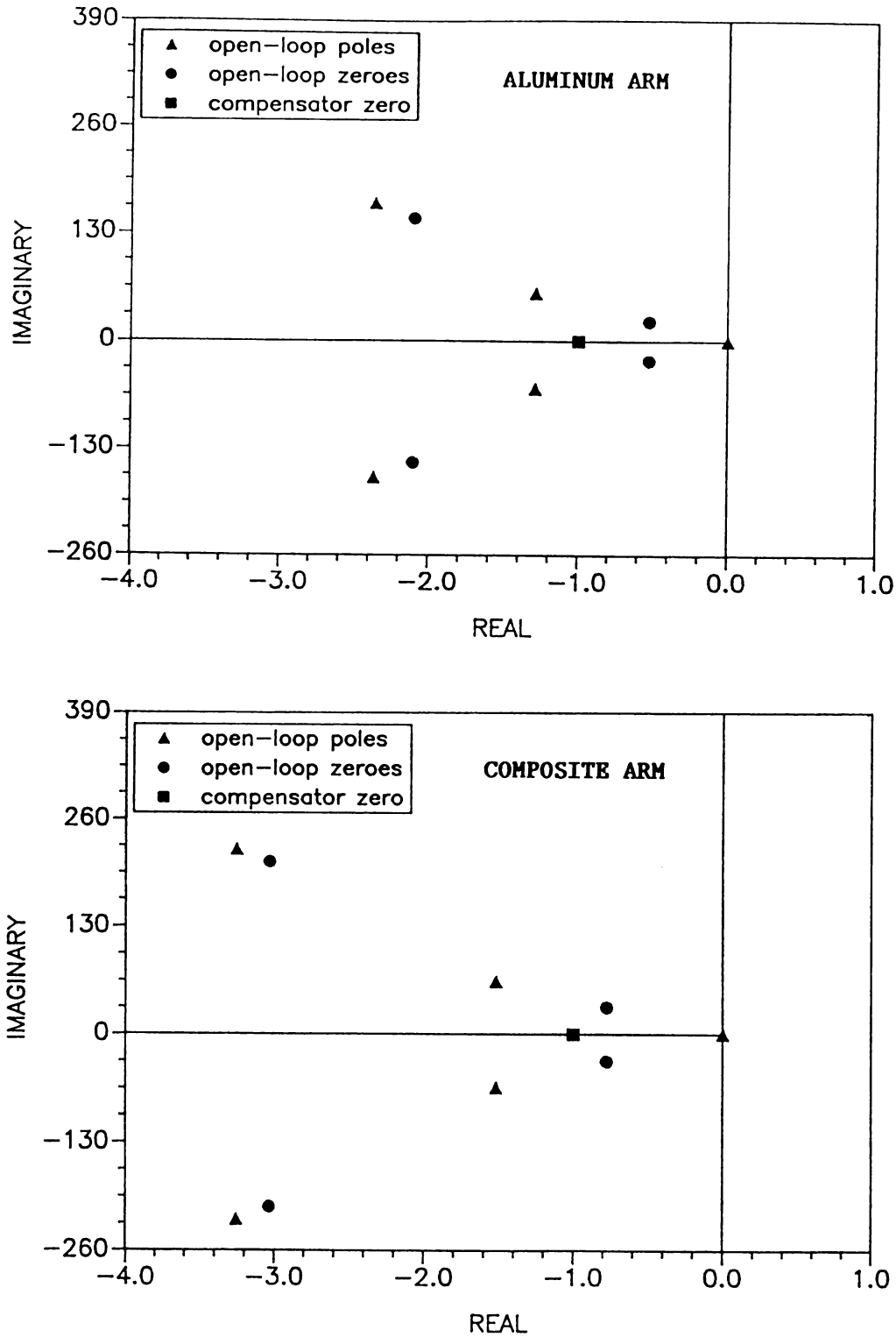


Figure 4.2 Open-Loop Pole-Zero Location with the Compensator Zero $Z_{co} = -1$

Figure 4.2 shows the open-loop pole-zero location with the compensator zero Z_{co}= -1 for the experimental aluminum and composite arm whose material and geometrical properties are presented in Tables 3.1 and 3.2 respectively. It is seen from this figure that all non-zero poles are located left to the given compensator zero. It is noted that open-loop zeros and poles physically represent the clamped-mode and pinned-mode natural frequencies of the arm respectively. Figure 4.3 presents the root-locus of the closed-loop system obtained by increasing the feedback gain K_v (or K_p, since the ratio is fixed) with the compensator zero Z_{co}=-1. Since the root-locus is symmetric with respect to real axis,only

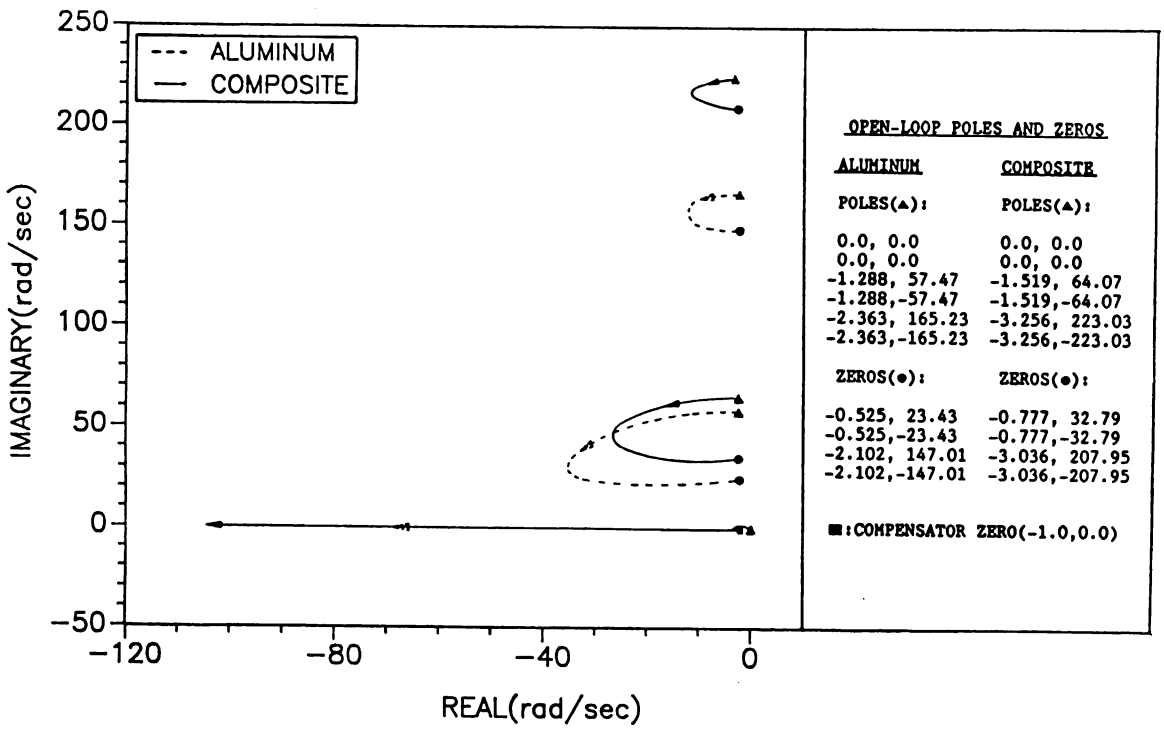


Figure 4.3 Root-Locus with the Compensator Zero Z_{co}= -1

upper plane of the locus is presented. It is interesting to observe that the open-loop poles located at the origin (rigid-body mode) start to move toward to have imaginary part of the poles, and quickly move toward to have real part only as the feedback gain increases for the both aluminum and composite arms. The one rigid-body pole goes to the negative infinite on the real axis, while the other rigid-body pole ends at the given compensator zero as the feedback gain goes to the infinity. This phenomenon will results in the sluggish response of the closed-loop system without generating large overshoot to the step commanded input. As the feedback gain increases, the other open-loop poles move toward close open-loop zeros which correspond to the finite two cantilevered-mode natural frequencies. The same type of root-locus shape is obtained with the compensator zero Z_{co}=-2 which is located between two non-zero poles on the real axis.

Now, for the same dynamic model, consider the pole-zero plot on the s-plane with the compensator zero Z_{co}=-15 which is positioned far left to the all open-loop poles and zeros as shown in Figure 4.4. Figure 4.5 presents the root-locus as a function of the feedback gain K_v with the compensator zero Z_{co}=-15. Two poles located at the origin (rigid-body mode) move toward close two open-loop zeros which correspond to the fundamental cantilevered-mode natural frequencies. Therefore, it may be said that the bandwidth of the rigid-body mode is limited by the fundamental cantilevered-mode natural frequency Ω_1=3.73 Hz and Ω_1=5.22 Hz for the aluminum and composite arm, respectively. The maximum bandwidth of the composite arm is larger than that of the aluminum arm by 28.5 percent. This larger bandwidth results in faster response to the

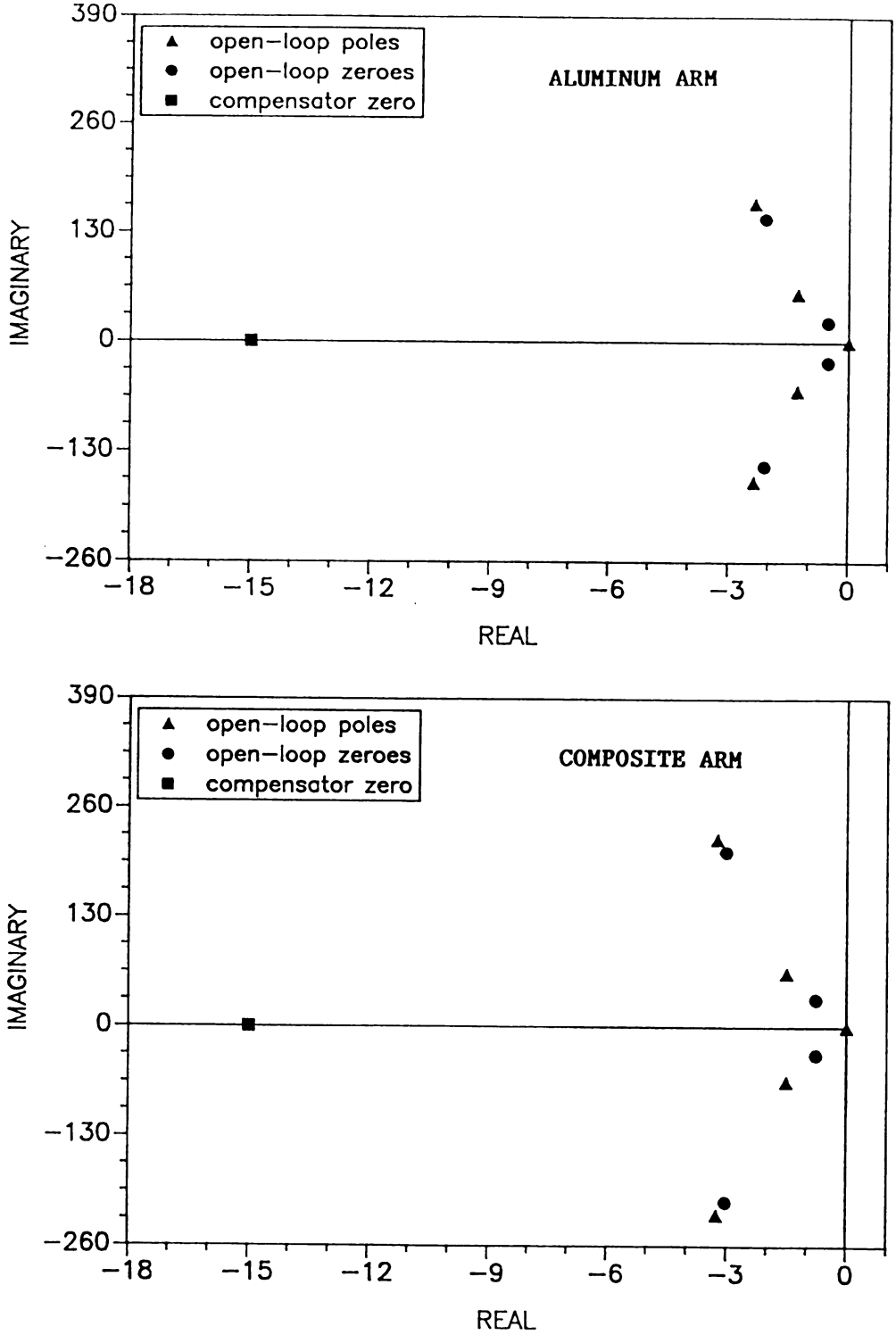


Figure 4.4 Open-Loop Pole Zero Location with the Compensator Zero Z_{co} = -15

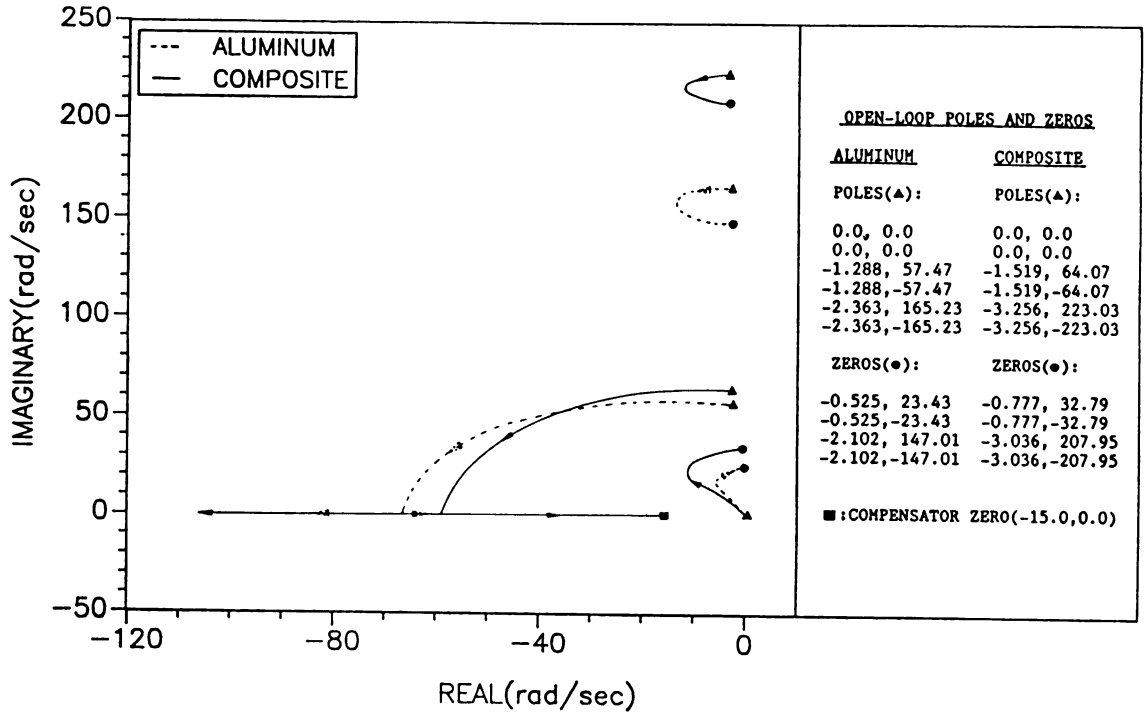


Figure 4.5 Root-Locus with the Compensator Zero Z_{co} = -15

commanded step input. From these characteristics of the closed-loop system depending upon the certain fixed compensator zero, appropriate output feedback gains have to be determined to evaluate the control performances for the aluminum and composite arm.

It is seen from Figures 4.3 and 4.5 that any choice of the feedback gains K_p and K_v assure the stability of the closed-loop system. This can be interpreted that the control law is equivalent to a mechanism consisting of the torsional spring and dashpot mounted at the pinned end of the arm. Therefore this dashpot always provides a damping to the system ensuring the stability. However, this guaranteed stability is no longer valid in practical system, since unmodelled dynamics of the

flexible link, actuators and sensors, delays caused by measuring and sampling feedback signal and the inherent limitation of servo-drive are always present. This instability will be investigated through the experimental test.

Another useful way to determine feedback gains which guarantee theoretically the stability of the system is to use the Lyapunov method. Consider a system described as

$$\ddot{x} + \tilde{P}\dot{x} + \tilde{Q}x = 0 \tag{4.7}$$

According to the Lyapunov theorem for the stability, if both matrices $\tilde{P}$ and $\tilde{Q}$ are symmetric and positive-definite, the system (4.7) is asymptotically stable. This theorem can be easily proved by choosing a Lyapunov function candidate $\tilde{V}$ by

$$\tilde{V} = \frac{1}{2} (x^T Q\, x + \dot{x}^T \dot{x}) \tag{4.8}$$

Then time derivative of $\tilde{V}$ becomes

$$\dot{\tilde{V}} = - \dot{x}^T \tilde{P}\, \dot{x} \tag{4.9}$$

Hence, this satisfies the stability condition; $\tilde{V} > 0$ and $\dot{\tilde{V}} < 0$ for all $x \neq 0$.

The dynamic equation (3.3) can be reformulated in the form of the equation (4.7) using the modal coordinate given in the equation (2.34). Hence, the equation (3.3) becomes

$$\ddot{\eta} + Z\dot{\eta} + \Omega\eta = \hat{B}_p \tilde{u} \tag{4.10}$$

where Ω (= diag $(0,\omega_1^2,\omega_2^2)$) is the modal frequency matrix, Z (= diag (0, $2\zeta_1\omega_1, 2\zeta_2\omega_2$)) is the modal damping matrix and $\hat{B}_p$ is the control influence matrix which is given by

$$\hat{B}_p = \frac{1}{I_T}\begin{bmatrix} 1 & \frac{d\phi_1(o)}{dx} & \frac{d\phi_2(o)}{dx} \end{bmatrix}^T \tag{4.11}$$

Also the output matrix given by equation (4.1) can be rewritten as

$$\begin{aligned} \tilde{y}_1 &= \hat{C}_1 \eta \\ \tilde{y}_2 &= \hat{C}_2 \dot{\eta} \end{aligned} \tag{4.12}$$

where

$$\hat{C}_1 = \hat{C}_2 = I_T \hat{B}_p^T \tag{4.13}$$

Since the system described by equation (4.10) is controllable, the PD output feedback controller is given by

$$\tilde{u} = -K_p\tilde{y}_1 - K_v\tilde{y}_2 \tag{4.14}$$

where K_p is the constant position feedback gain and K_v is the constant velocity feedback gain. The substitution of the equations (4.12) and (4.14) into the equation (4.10) yields

$$\ddot{\eta} + (Z + \hat{B}_p K_v \hat{C}_2)\dot{\eta} + (\Omega + \hat{B}_p K_p \hat{C}_1)\eta = 0 \tag{4.15}$$

It is noted that the matrices Z and Ω are symmetric and positive semi-definite due to the rigid-body mode which is characterized by zero natural frequencies. Thus, the feedback gains K_p and K_v in equation (4.15) should be carefully chosen such that the matrices $(Z + \hat{B}_p K_v \hat{C}_2)$ and

$(\Omega + \hat{B}_p K_p \hat{C}_1)$ are symmetric and positive definite. Then the resulting closed-loop system (4.15) will be asymptotically stable.

The following proposition is stated without a proof before determining the feedback gains.

Proposition 4.1 : Let P and Q be any two symmetric matrices with the same dimension. If P is the positive definite and Q is the positive semi-definite, then (P+Q) is the positive definite.

Now, under the condition stated in the Proposition 4.1, the feedback gains K_p and K_v can be chosen such that the closed-loop system be asymptotically stable. For example, let

$$\begin{aligned} \hat{B}_p K_p \hat{C}_1 &= \hat{P} \\ \hat{B}_p K_v \hat{C}_2 &= \hat{Q} \end{aligned} \tag{4.16}$$

where $\hat{P}$ and $\hat{Q}$ are arbitrary symmetric and positive definite matrices. Then the feedback gains K_p and K_v are obtained as follows.

$$\begin{aligned} K_p &= [\hat{B}_p^T \hat{B}_p]^{-1} \hat{B}_p^T \hat{P} \hat{C}_1^T [\hat{C}_1 \hat{C}_1^T]^{-1} \\ K_v &= [\hat{B}_p^T \hat{B}_p]^{-1} \hat{B}_p^T \hat{Q} \hat{C}_2^T [\hat{C}_2 \hat{C}_2^T]^{-1} \end{aligned} \tag{4.17}$$

It is noted that the minimum norm solution(least effort solution) and least error solution method [28] were employed to obtain the feedback gains. It is also noted that both matrices Z and Ω in equation (4.15) remain as symmetric and positive semi-definite, even though the model

parameters such as natural frequencies and damping ratios are perturbed in a certain threshold. Therefore, the perturbed system will be still asymptotically stable so long as the output feedback gains are chosen based on the above manner. Thus, it can be stated that the proposed output feedback controller assures the robustness of the system stability. The feedback gains determined from the aforementioned two approaches will be used in the following experimental implementation.

4.3 Implementation Results and Discussions

Figure 4.6 presents the experimental set-up for the output measurement. All experimental results presented in this section were obtained based on the following measurement procedures. The angular

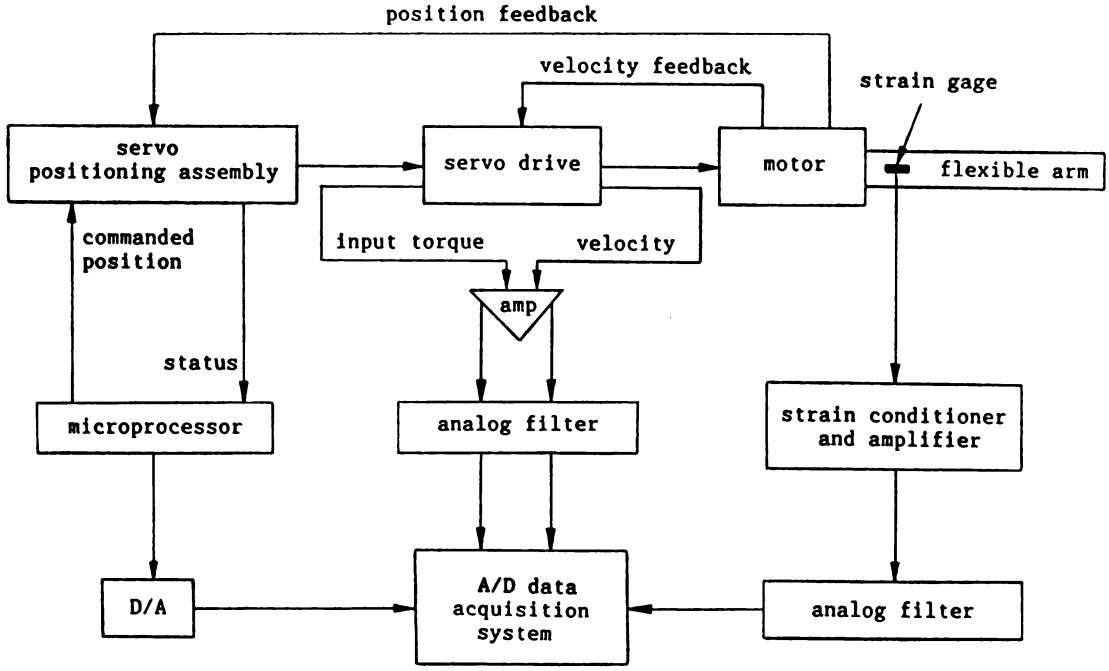


Figure 4.6 Experimental Set-Up for Output Measurements

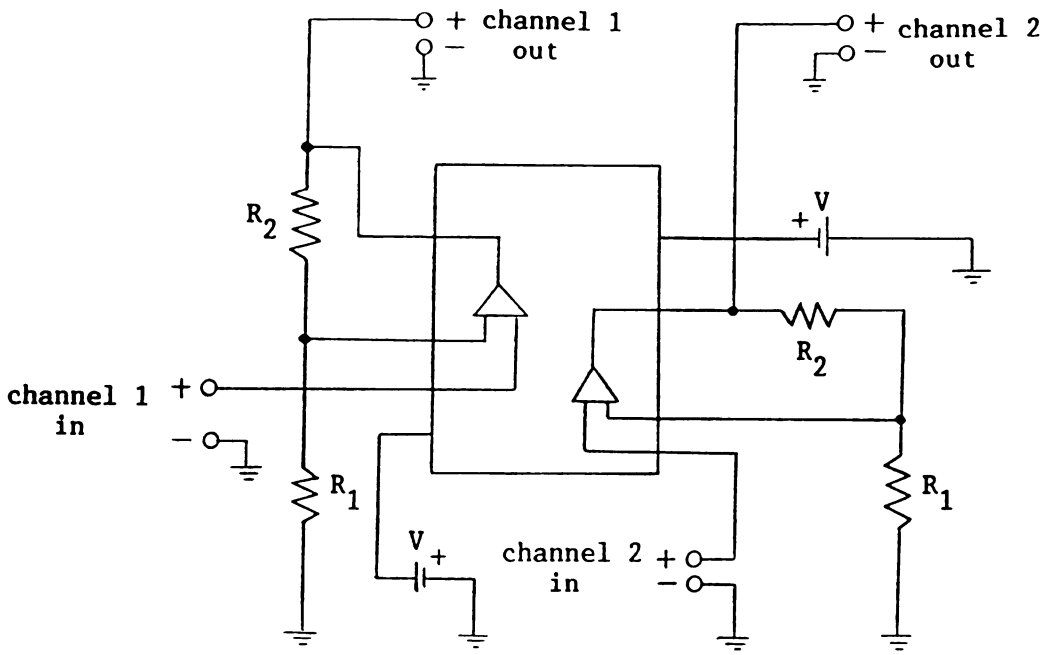


Figure 4.7 Circuit Diagram of Two Channel Operational Amplifier

position data stored in the microprocessor as digital values were transferred from the microprocessor to the data acquisition system through D/A converter, model 1771-OFE1, manufactured by Allen-Bradley. The D/A converter has output range of 0 to 10 volts DC. Since the data stored in the microprocessor was isolated from the main computer network which is employed for the data postprocessing and plotting the results, this transfer procedure was necessary.

The employed data acquisition system, model MicroVMS II/GPX 21, manufactured by Digital Equipment Corporation, has 15 channels of A/D converter. The data sampling rate of 150 Hz, which is far beyond the considered natural frequencies of the arm, was employed for the measurement of all output signals except the second mode exciting response where 800 Hz of sampling rate was used. The input torque and

angular velocity from the servo-drive were amplified through the operational amplifier, since the actual output signals were relatively small resulting in significant effect of the computer noise of the data acquisition system to the actual output signals. Two channel operational amplifier producing the amplification factor of 100 was assembled as shown in Figure 4.7.

The amplified signals then were fed to a dual analog filter, model 432, manufactured by Wavetek Inc., in order to eliminate high frequency components such as noises. The 100 Hz of cutoff frequency was employed before the filtered analog signals were digitized by A/D data acquisition system. The output signal from the strain gage mounted on the root of the flexible arm was conditioned and amplified through Wheatstone bridge amplifier, model 2100, manufactured by Measurement Groups Inc.,before the conditioned and amplified signal was fed to the low-pass analog filter with the cutoff frequency of 100 Hz.

4.3.1 Step Responses without Disturbances

For the first comparison of the closed-loop performances between the aluminum and composite arm, the small compensator zero Z_{co}=-2 was chosen. With this compensator zero, the feedback gains K_p and K_v were decided such a manner that the damping ratio of the closed-loop poles of the rigid-body mode is equal to 1 (critical damping). This means that the closed-loop poles of the rigid-body mode has no imaginary part for the first time as the feedback gain increases. From the root-locus analysis, the feedback gains K_p= 0.534 N•m, K_v= 0.267 N•m•sec and K_p= 0.292 N•m, K_v = 0.146 N•m•sec were obtained for the aluminum and composite arm

respectively. Table 4.1 the presents closed-loop poles of the system with these feedback gains.

Table 4.1 Closed-Loop Poles with the Compensator Zero Z_{co} = -2

Aluminum Arm (K_p = 0.534)		Composite Arm (K_p = 0.292)	
Real	Imaginary	Real	Imaginary
-3.820	0	-3.638	0
-4.425	0	-4.538	0
-19.736	52.19	-10.948	62.26
-19.736	-52.19	-10.948	-62.26
-6.119	164.03	-4.279	222.89
-6.119	-164.03	-4.279	-222.89

Figure 4.8 shows the measured step responses to a commanded step angular position of 7.2 degree. The hub angular position reaches its commanded position within 2.0 second for the both aluminum and composite arms. No overshoot in the angular position response is observed as expected by the employed feedback gains. The steady-state error between the commanded and actual position was 0.1 degree for the aluminum arm and 0.08 degree for the composite arm. This steady-state error is attributed to the joint friction and can be eliminated by applying the integral control action or manual calibration method. The significant different response between two arms is observed from the input torque response. The applied input torque for the composite arm is only 53 percent of the torque required for the aluminum arm. This amount of reduction of energy consumption will provide tremendous benefit of the economic area on the

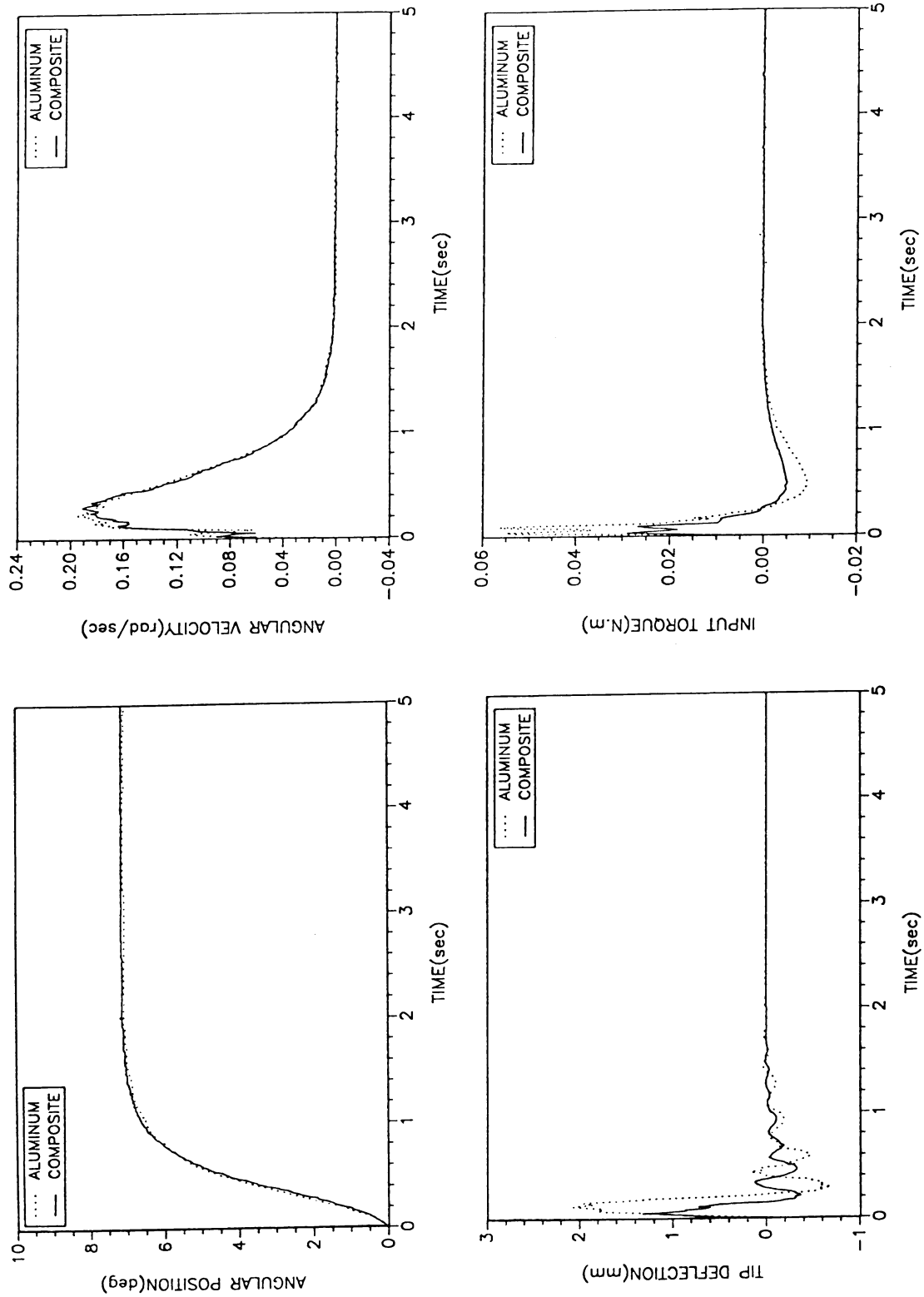


Figure 4.8 Measured Step Responses without Payload. K_p=0.534, K_v=0.267 for the Aluminum Arm, and K_p=0.292, K_v=0.146 for the Composite Arm.

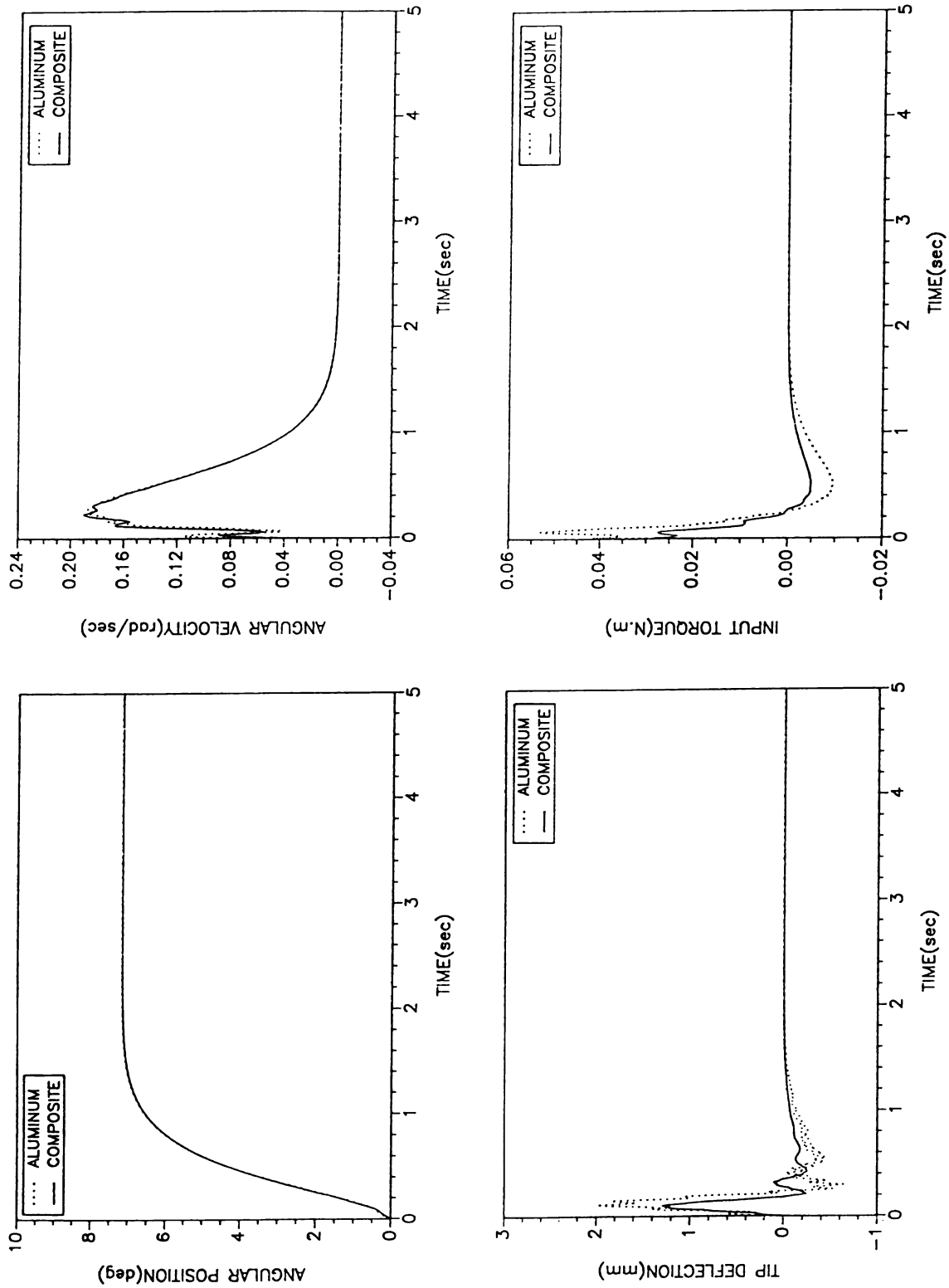


Figure 4.9 Simulated Step Responses without Payload. K_p=0.534, K_v=0.267 for the Aluminum Arm, and K_p=0.292, K_v=0.146 for the Composite Arm.

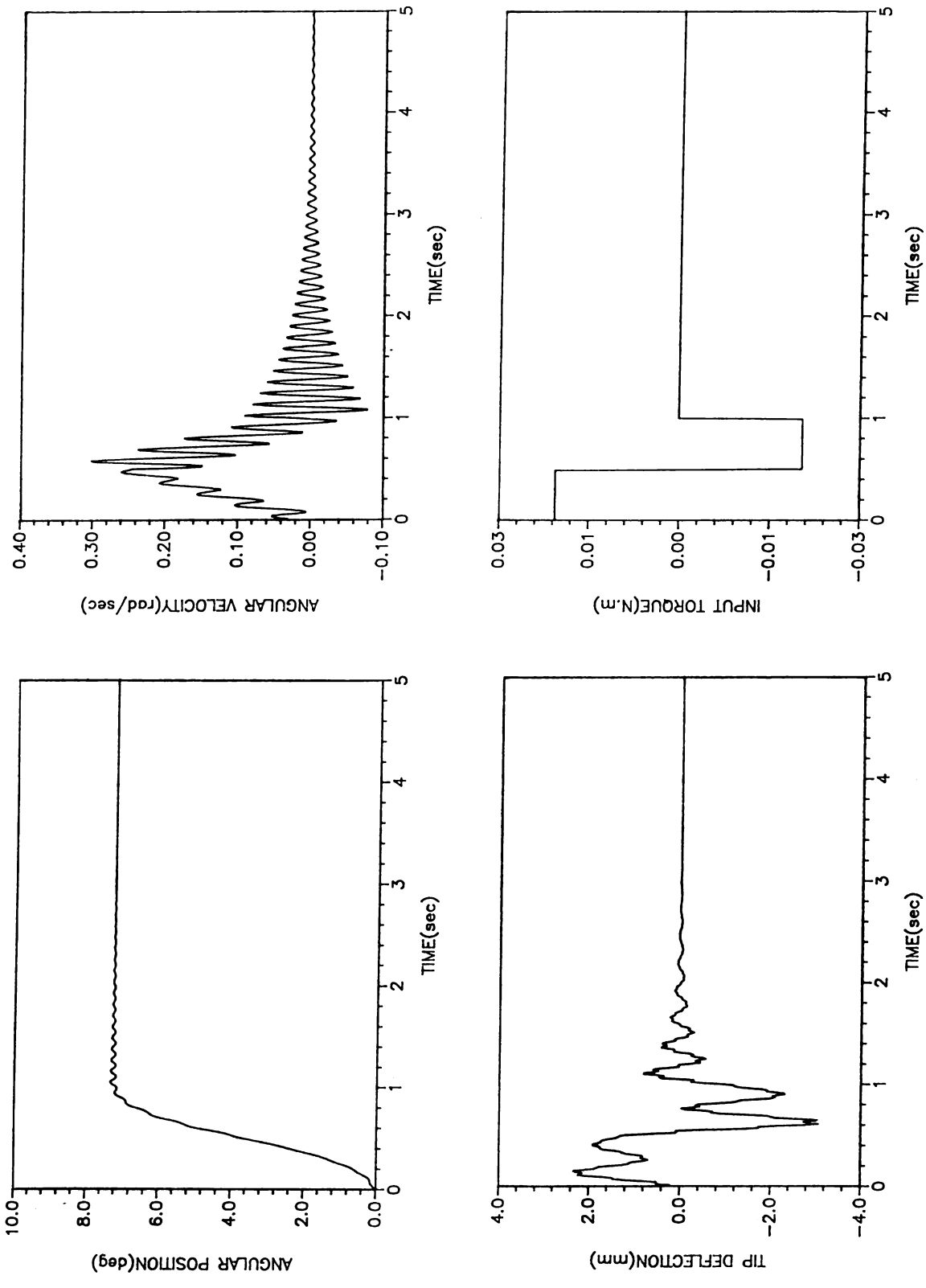


Figure 4.10 Simulated Open-Loop Step Responses of the Aluminum Arm without Payload

real production line. It is also observed from the tip deflection response that the magnitude of the vibration amplitude of the aluminum arm was reduced up to 30 percent by employing the composite arm. The second mode effect to the total tip deflection is very small for both aluminum and composite arms. The response decayed to zero within 2 second for the aluminum arm and 1.8 second for the composite arm respectively. It is noted from the angular velocity response that the ratio of the maximum angular velocity to the first pinned-mode natural frequency, i.e., $\dot{\theta}_{max}/\omega_1$, is 0.0033 and 0.0029 for the aluminum and composite arm respectively, hence eliminating the possibility of the resonance phenomenon due to the input torque.

Figure 4.9 shows the simulated step responses corresponding to the measured response presented in Figure 4.8. The agreement between two results is excellent, even though there exit small mismatch in the response of tip tip deflection. For the comparison of the step responses between the open-loop and closed-loop system, the open-loop step input torque was introduced to the model. Figure 4.10 presents the simulated open-loop responses of the aluminum arm for the commanded angular position of 7.2 degree. The magnitude and period of the step input torque was determined to have almost same delay time (0.42 second) as the case of the closed-loop system. It is clear from this figure that the angular position and velocity responses exhibit oscillations as expected, and the settling-time of the tip deflection is increased by 45 percent comparing with the closed-loop response shown in Figure 4.9.

For the second comparison of the control performances between the aluminum and composite arm, the compensator zero $Z_{co} = -5$ was chosen and

same feedback gains were employed to the both aluminum and composite arms. Table 4.2 presents the closed-loop poles of the system with feedback gains of $K_p = 1.0$ N•m and $K_v = 0.2$ N•m•sec for both arms. From this table, the damping ratio of rigid-body mode was obtained by 0.633 and 0.855 for the aluminum and composite arm respectively.

Table 4.2 Closed-Loop Poles with the Compensator Zero $Z_{co} = -5$

Aluminum Arm (K_p = 1.0)		Composite Arm (K_p = 1.0)	
Real	Imaginary	Real	Imaginary
-2.831	4.645	-5.526	5.159
-2.831	-4.645	-5.586	-5.159
-15.233	55.47	-14.523	61.18
-15.233	-55.47	-14.523	-61.18
-5.307	164.58	-4.630	222.80
-5.307	-164.58	-4.630	-222.80

Figure 4.11 presents the measured step responses to a command step angular position of 7.2 degree with above feedback gains. From the angular position response, the delay time was obtained by 0.26 second for the aluminum arm and 0.21 second for the composite arm. It is also observed from the angular position response that the maximum overshoot of the aluminum arm is 1.02 degree, while that of the composite arm is 0.3 degree. From the input torque response, it is also seen that the actual input torque required for the composite arm during the commanded motion is only 60 percent of the input torque required for the aluminum arm. The tip deflection of the aluminum arm induced from the step motion was decreased up to 50 percent by employing the composite arm. From these

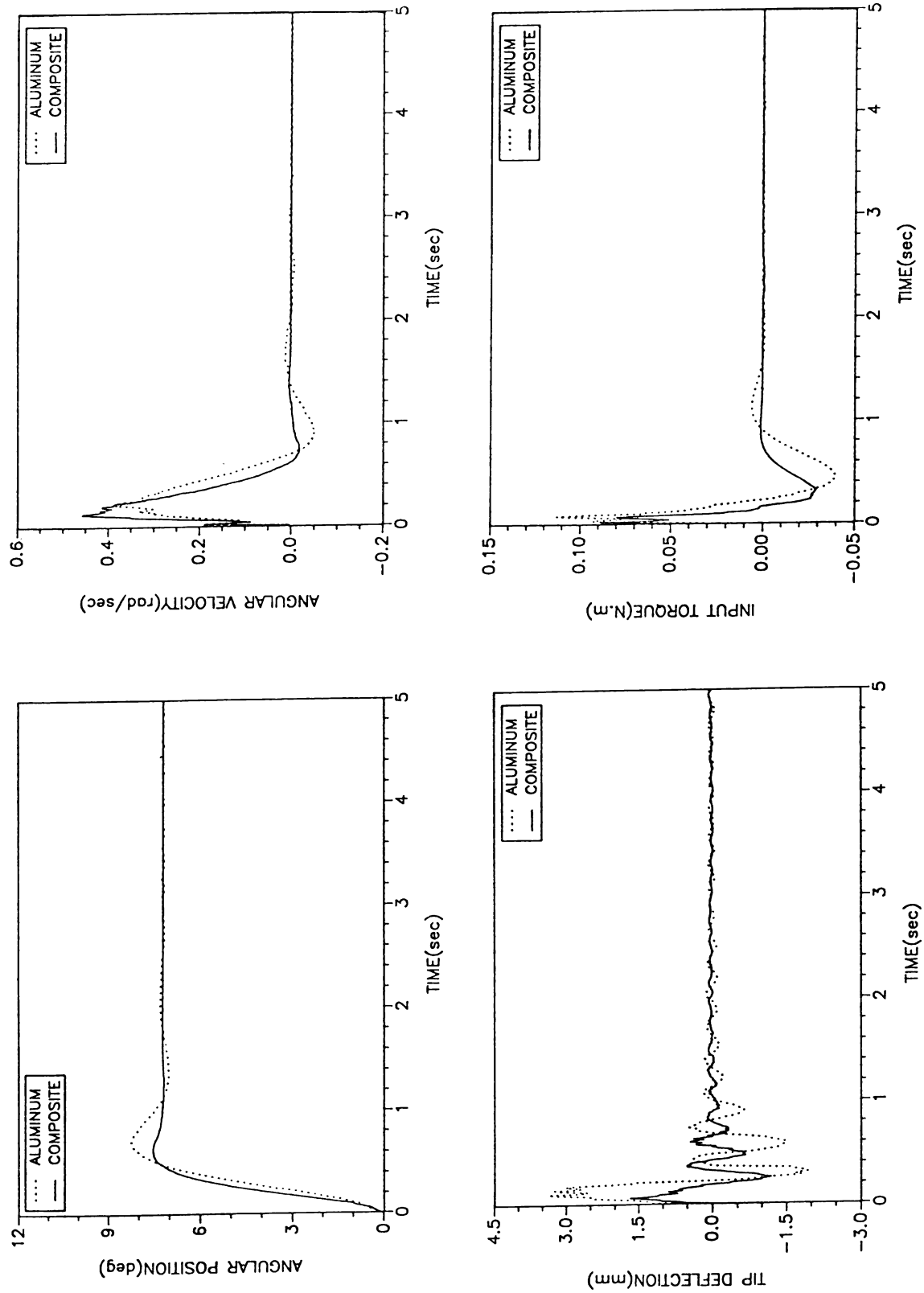


Figure 4.11 Measured Step Responses without Payload. K_p=1.0 and K_v=0.2 for both Aluminum and Composite Arms.

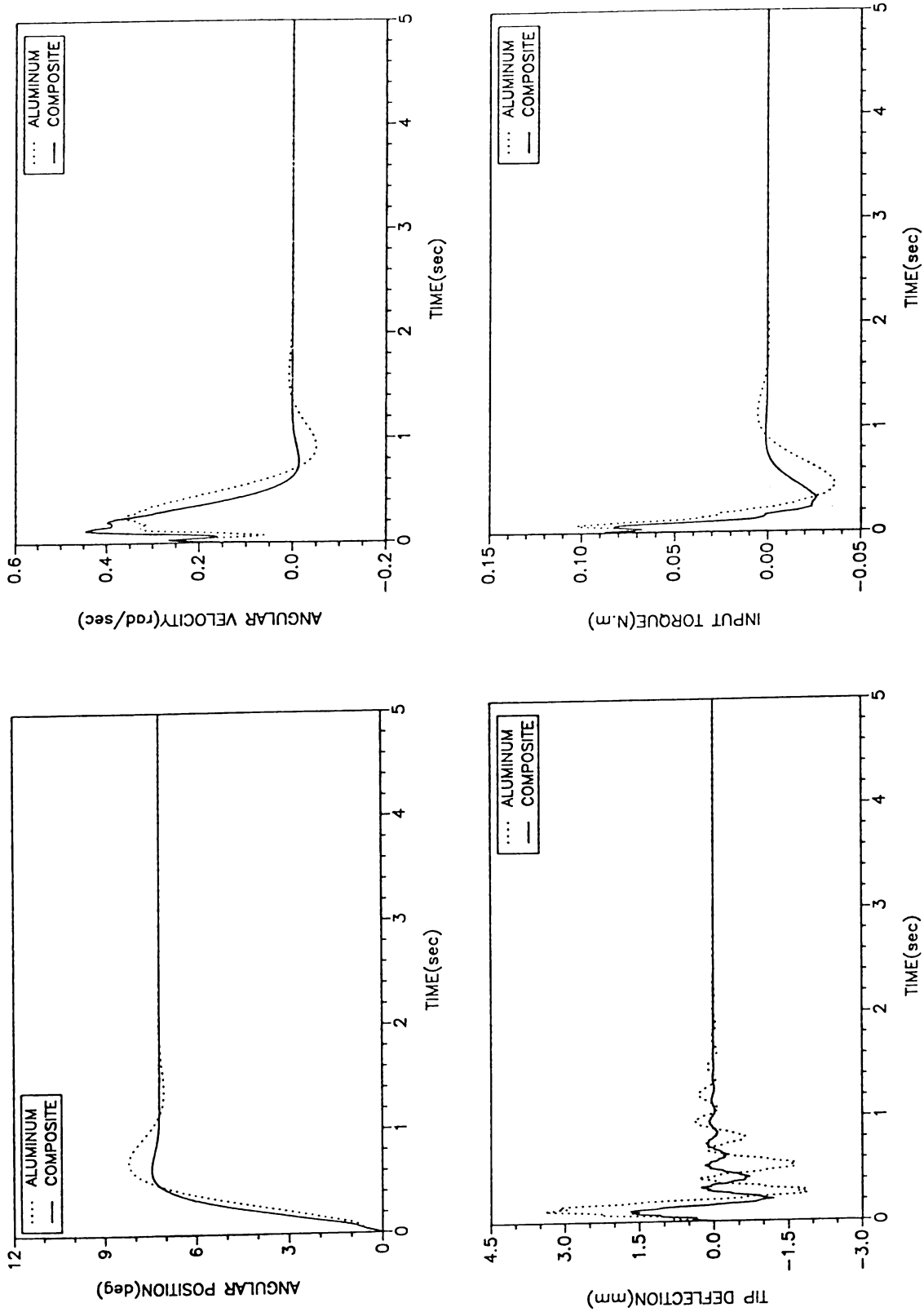


Figure 4.12 Simulated Step Responses without Payload. K_p=1.0 and K_v=0.2 for both Aluminum and Composite Arms.

results, it may be summarized that with same feedback gains, the system performances of the composite arm have been remarkably enhanced over those of the aluminum arm, exhibiting the smaller delay time by 20 percent, the smaller maximum overshoot by 70 percent, the less energy consumption by 40 percent, and the smaller tip deflection up to 50 percent. It is observed from the tip deflection response that the tip deflection is not zero even after the angular position damped out to reach its commanded position. This phenomenon arises from the increased hysteretic joint friction due to the relatively high employed position gain. Figure 4.12 shows the simulated step responses corresponding to the measured results shown in Figure 4.11. It is observed from Figures 4.11 and 4.12 that two corresponding responses agree well except for the first 0.2 second of the motion.

Next comparison of the control performances was undertaken with the payload of 0.061 kg which is 46.2 percent and 101.6 percent of the mass of the aluminum and composite arm respectively. The compensator zero Z_{co}=-1 was chosen with the feedback gains of K_p=0.48 N•m for the aluminum arm and K_p=0.24 N•m for the composite arm based on the same manner as in the first case. Table 4.3 presents the closed-loop poles of the system with these feedback gains, and from this table, it can be seen that the closed-loop poles of the rigid-body mode has no imaginary part for both arms, hence expecting the sluggish motion and no overshoot.

Figure 4.13 presents the measured step responses to a commanded angular position of 7.2 degree for both arms with the payload of 0.061 kg. As expected, it took 3.5 second to reach its commanded position without occurring overshoot. The required energy of the composite arm for

this movement was only 48 percent that of the aluminum arm, and tip deflection of the aluminum arm was reduced by up to 60 percent by employing the composite arm. With smaller energy consumption, the more accurate end-position was obtained. It is expected that with the same ratio of the payload to the arm mass, the better control performances of the composite arm can be achieved with appropriate feedback gains. Figure 4.14 shows the simulated step responses corresponding to the measured responses presented in Figure 4.13. Again the correlation between the measured and simulated responses is impressive.

The employment of the Lyapunov method is also another useful technique to determine the feedback gains which guarantee asymptotical stability of the closed-loop system as discussed earlier. Herein, the following symmetric and positive definite matrix $\hat{P}$ and $\hat{Q}$ in the equation (4.16) were chosen for the both aluminum and composite arms.

Table 4.3 Closed-Loop Poles with the Compensator Zero Z_{co} = -1

Aluminum Arm (K_p = 0.48)		Composite Arm (K_p = 0.24)	
Real	Imaginary	Real	Imaginary
-1.234	0	-1.679	0
-6.418	0	-2.578	0
-36.197	28.93	-20.125	44.14
-36.197	-28.93	-20.125	-44.14
-9.656	126.82	-5.171	166.96
-9.656	-126.82	-5.171	-166.96

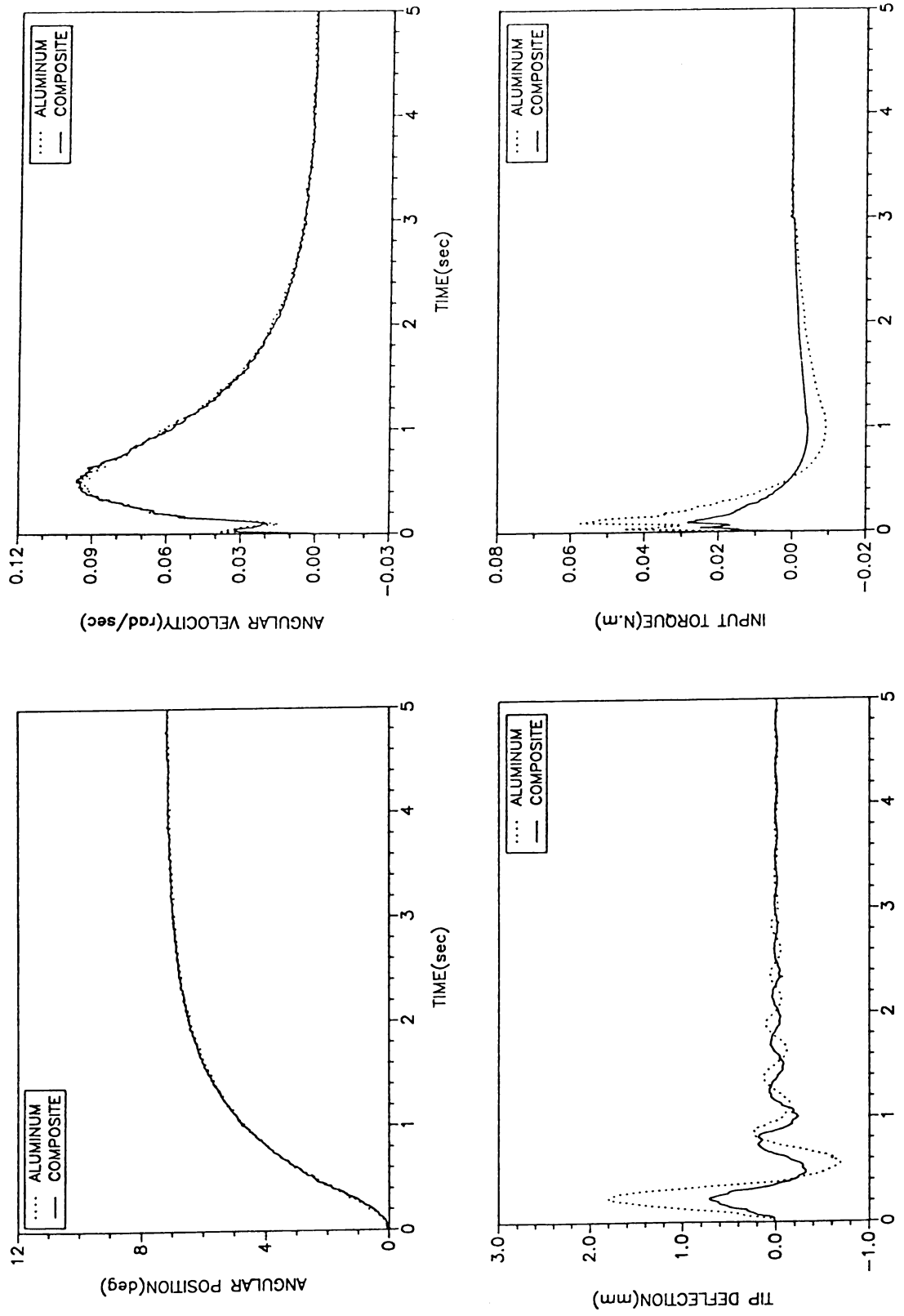


Figure 4.13 Measured Step Responses with Payload of 0.061 kg. K_p=K_v=0.48 for the Aluminum Arm, and K_p=K_v=0.24 for the Composite Arm.

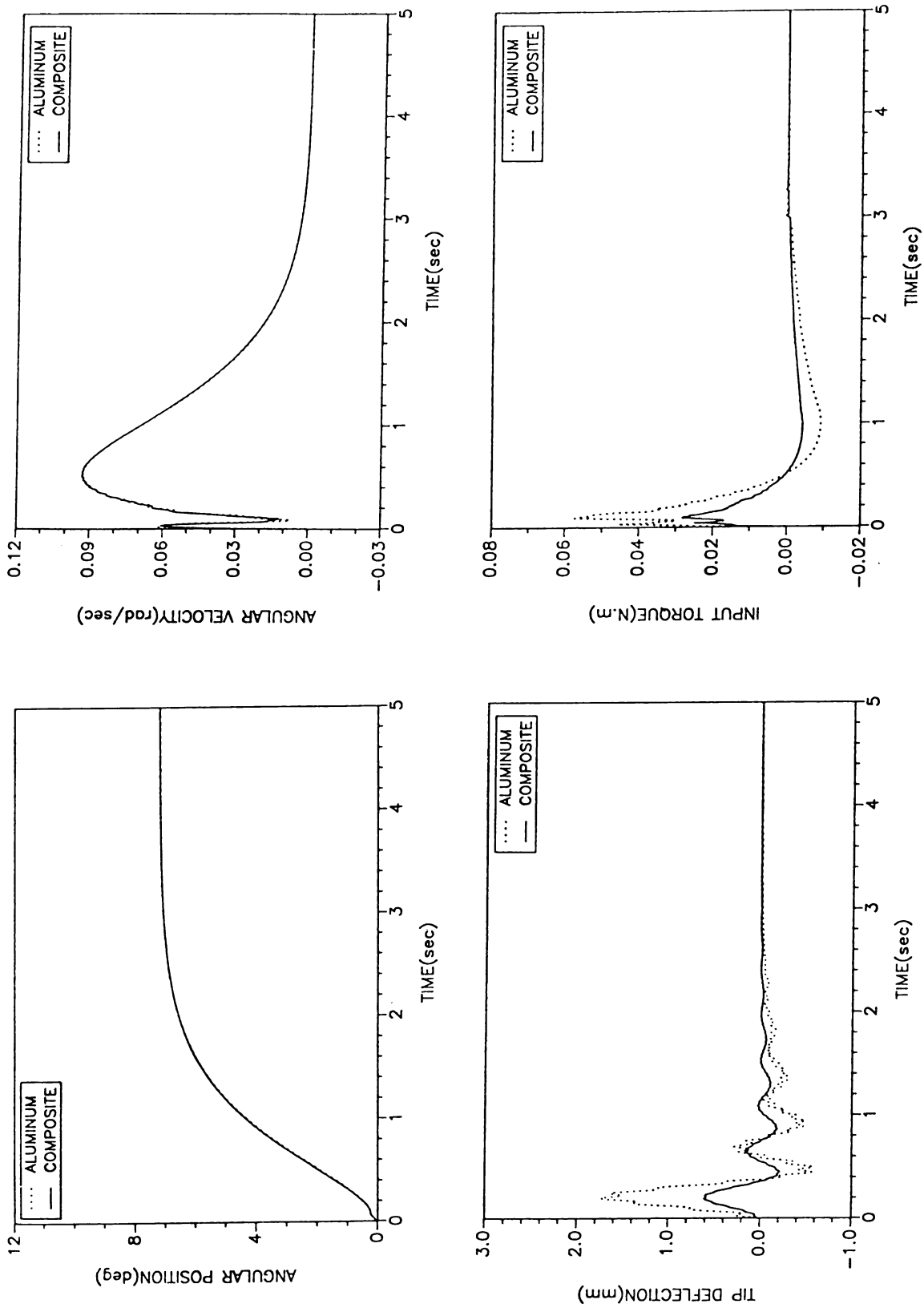


Figure 4.14 Simulated Step Responses with Payload of 0.061 kg. K_p=K_v=0.48 for the Aluminum Arm, and K_p=K_v=0.24 for the Composite Arm.

$$\hat{P} = \begin{bmatrix} 80 & 0 & 0 \\ 0 & 80 & 0 \\ 0 & 0 & 80 \end{bmatrix}$$

$$\hat{Q} = \begin{bmatrix} 50 & 0 & 0 \\ 0 & 50 & 0 \\ 0 & 0 & 50 \end{bmatrix} \qquad (4.18)$$

With above matrices, system input matrix $\hat{B}_p$, and the output matrices $\hat{C}_1$ and $\hat{C}_2$ without the payload, the feedback gains of K_p = 0.406 N•m, K_v = 0.254 N•m•sec for the aluminum arm, and K_p =0.403 N•m, K_v = 0.252 N•m•sec for the composite arm were obtained from the equation (4.17). Table 4.4 presents the closed-loop poles of the system with above feedback gains. As expected, all closed-loop poles for both arms have negative real part assuring the stability of the system.

Table 4.4 Closed-Loop Poles with K_p=0.406, K_v=0.254 for the Aluminum Arm, and K_p= 0.403, K_v= 0.252 for the Composite Arm

Aluminum Arm		Composite Arm	
Real	Imaginary	Real	Imaginary
-2.303	0	-1.843	0
-5.560	0	-13.430	0
-18.806	52.60	-17.268	58.17
-18.806	-52.60	-17.268	-58.17
-5.960	164.13	-4.937	222.64
-5.960	-164.13	-4.937	-222.64

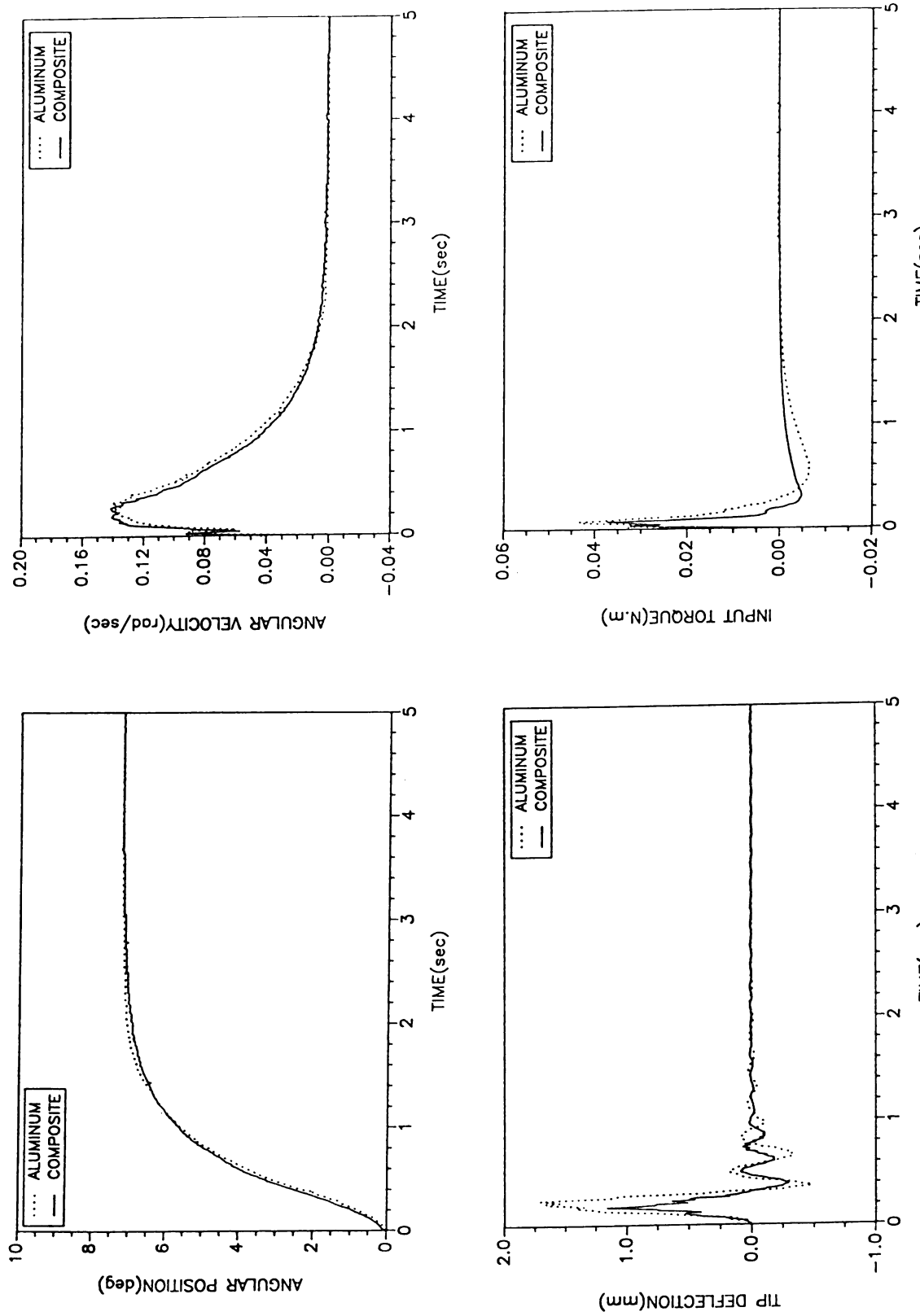


Figure 4.15 Measured Step Responses without Payload. K_p=0.406, K_v=0.254 for the Aluminum Arm, and K_p=0.403, K_v=0.252 for the Composite Arm.

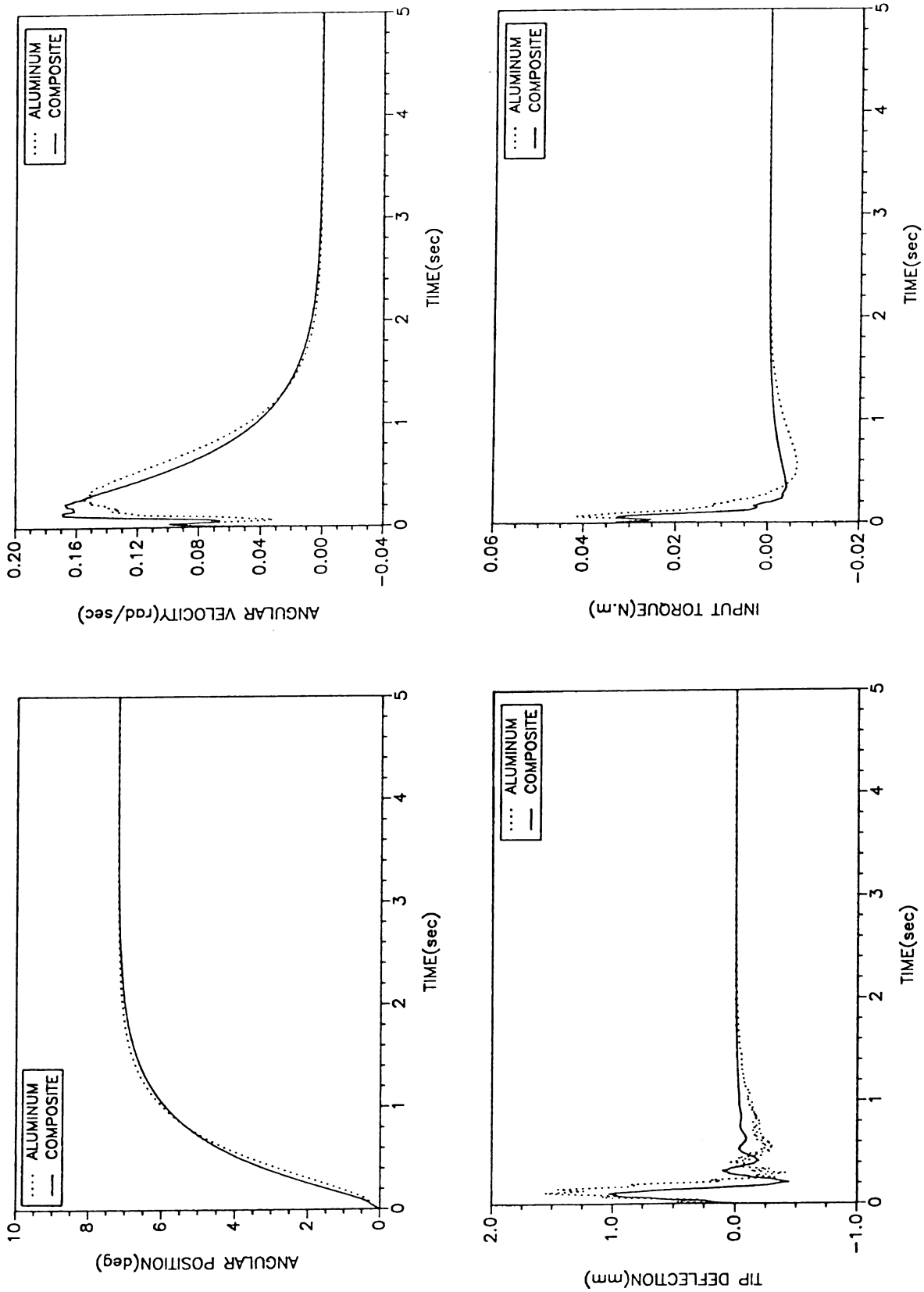


Figure 4.16 Simulated Step Responses without Payload. K_p=0.406, K_v=0.254 for the Aluminum Arm, and K_p=0.403, K_v=0.252 for the Composite Arm.

Figure 4.15 presents the measured step responses to a commanded angular position of 7.2 degree with above feedback gains. It is observed form the angular position response that there is no overshoot and it takes about 2.5 second to reach its commanded position for the both aluminum and composite arms. From the input torque response, it is distilled that the control input torque required for the composite arm is approximately 60 percent of that of the aluminum arm. It is also seen from the tip deflection response that the maximum tip deflection of the aluminum arm was reduced up to 35 percent by employing the composite arm. It should be noted that the different choice of the matrices $\hat{P}$ and $\hat{Q}$ will produce different control performances of the system. Figure 4.16 shows the simulated step responses corresponding to the measured results shown in Figure 4.15. The agreement between two results is again excellent.

It is noted from these results that no controller/observer spillover was occurred. This is attributed to the relatively high unmodelled frequencies (truncation effect is very small), large inherent damping of the system, and no state observer in the control system (no state estimation error, hence fast servo-sampling time).

4.3.2 Step Responses with Disturbances

It is generally known that the closed-loop system associated with the PD type of the output feedback controller is very sensitive to uncertainties such as parameter variation, internal and external disturbances. Herein, the investigation of this sensitiveness was accomplished by considering external inputs, which have forcing

frequencies close to the cantilevered-mode natural frequencies of the arm, as the disturbances. This attempt is made here to introduce a single-link flexible manipulator fabricated from smart materials incorporating electro-rheological fluids which will be discussed in the subsequent chapter. The robustness of the PD controller to the disturbances is to be expected with the help of the distributed parameter actuator which is characterized by embedded electro-rheological fluids in the structure.

With the introduced disturbance, the dynamic model given by the equation (3.3) becomes

$$\dot{\tilde{x}}_p = \tilde{A}_p \tilde{x}_p + \tilde{B}_p \tilde{u} + \tilde{B}_p \tilde{d}(t) \qquad (4.19)$$

$$\tilde{y}_p = \tilde{C}_p \tilde{x}_p$$

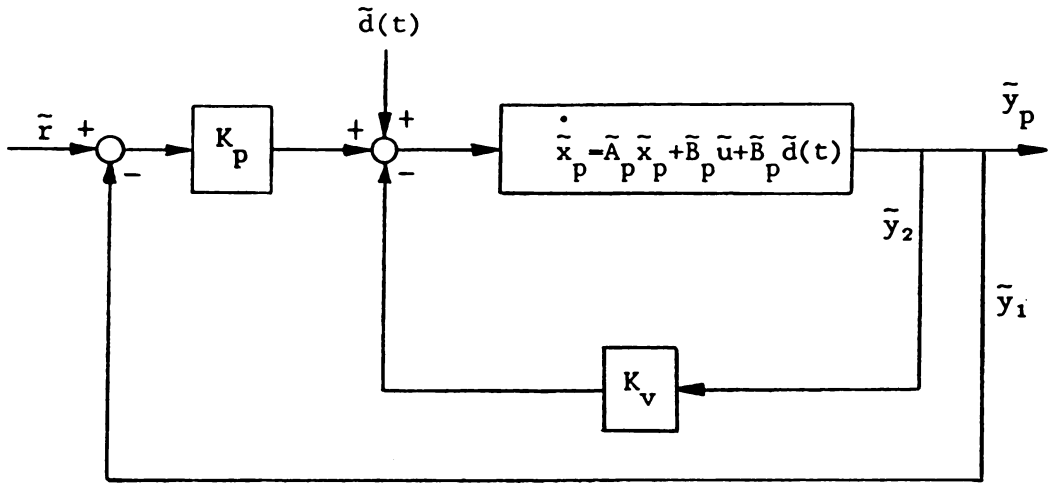


Figure 4.17 Block-Diagram of the PD Output Feedback Control System with the Disturbance of $\tilde{d}(t)$

where $\tilde{d}(t)$ is the imposed disturbance. Since the disturbance is applied to the servo-drive, the disturbance influence matrix is same as the input influence matrix $\tilde{B}_p$. Figure 4.17 presents a block-diagram of the closed-loop system with the PD output feedback controller subjected to the disturbance $\tilde{d}(t)$. This disturbance is supplied from the function generator, model 275, manufactured by Wavetek, to servo-drive.

Figure 4.18 shows the measured step responses of the aluminum arm without the payload to a commanded step angular position of 7.2 degree with the imposed disturbance of 0.08 sin $f_1 t$ N•m where $f_1 = 3.25$ Hz. The feedback gains of $K_p = 0.534$ and $K_v = 0.267$ used for Figure 4.8 were employed, and the disturbance was applied to the servo-drive from the starting of the motion. It is noted that the forcing frequency f_1=3.25 Hz is very close to the clamped-mode fundamental natural frequency $\Omega_1 = 3.73$ Hz in Table 3.5. As expected, the response of hub angular position and tip deflection are oscillated resulting near resonance phenomenon of the system. If the amplitude of the disturbance increase, the system response will be grown up resulting in the instability of the system.

Figure 4.19 presents a comparison of step responses of the aluminum arm with and without the disturbance. It is interesting to observe from the angular position response that the reached angle after 2 second is 7.2 degree with the disturbance, while it is 7.1 degree without the disturbance. The reason is that the disturbance helps to overcome joint friction so that the arm can reach to the commanded position with the tradeoff the induced oscillation.

Figure 4.20 shows a comparison of step responses between the

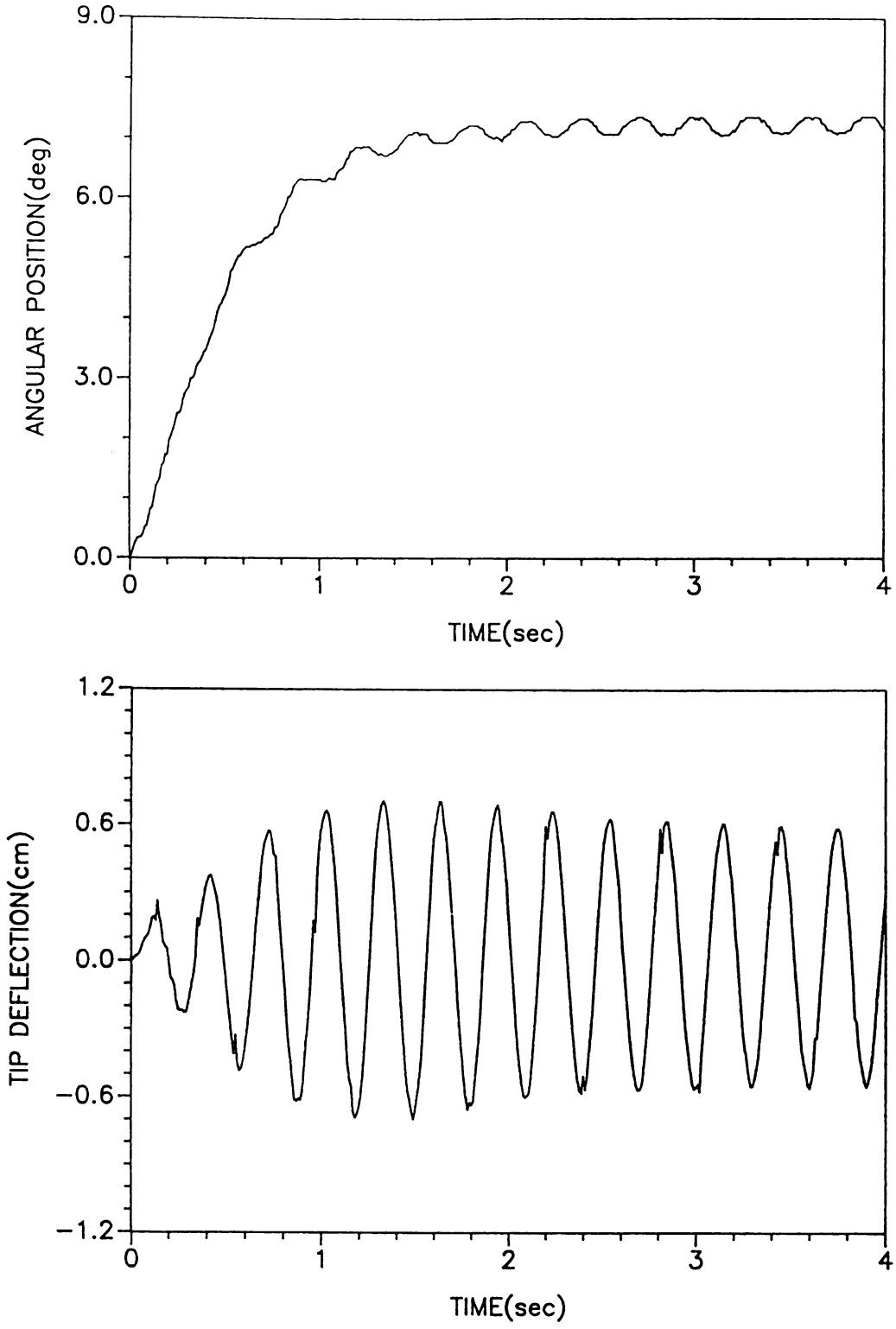


Figure 4.18 Measured Step Responses of the Aluminum Arm without Payload. K_p= 0.534, K_v= 0.267, and d(t)=0.08 sin(3.25 Hz)t

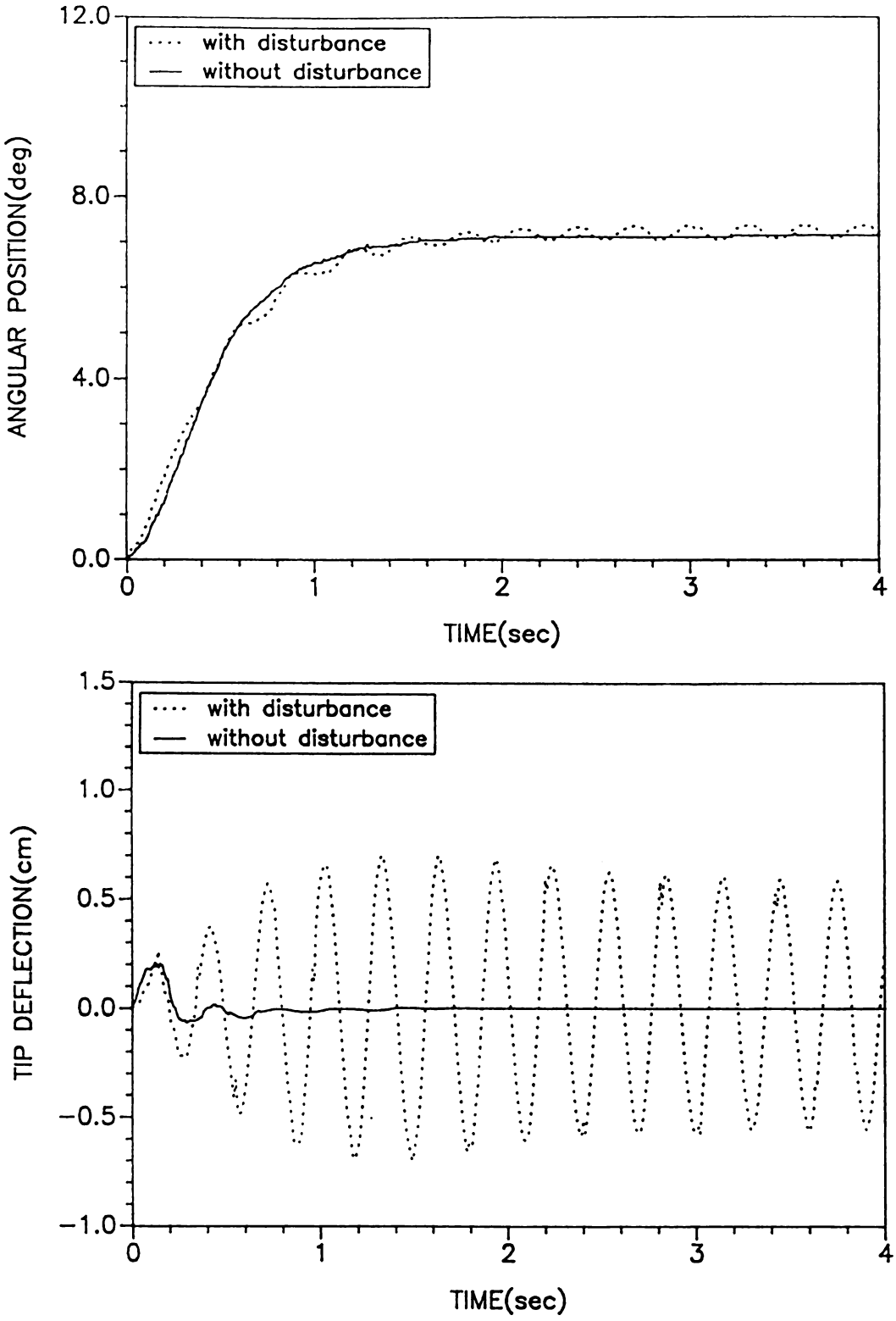


Figure 4.19 Comparison of the Measured Step Responses of the Aluminum Arm with and without the Disturbance.

K_p=0.534, K_v=0.267 and $\tilde{d}(t)$=0.08 sin(3.25 Hz)t

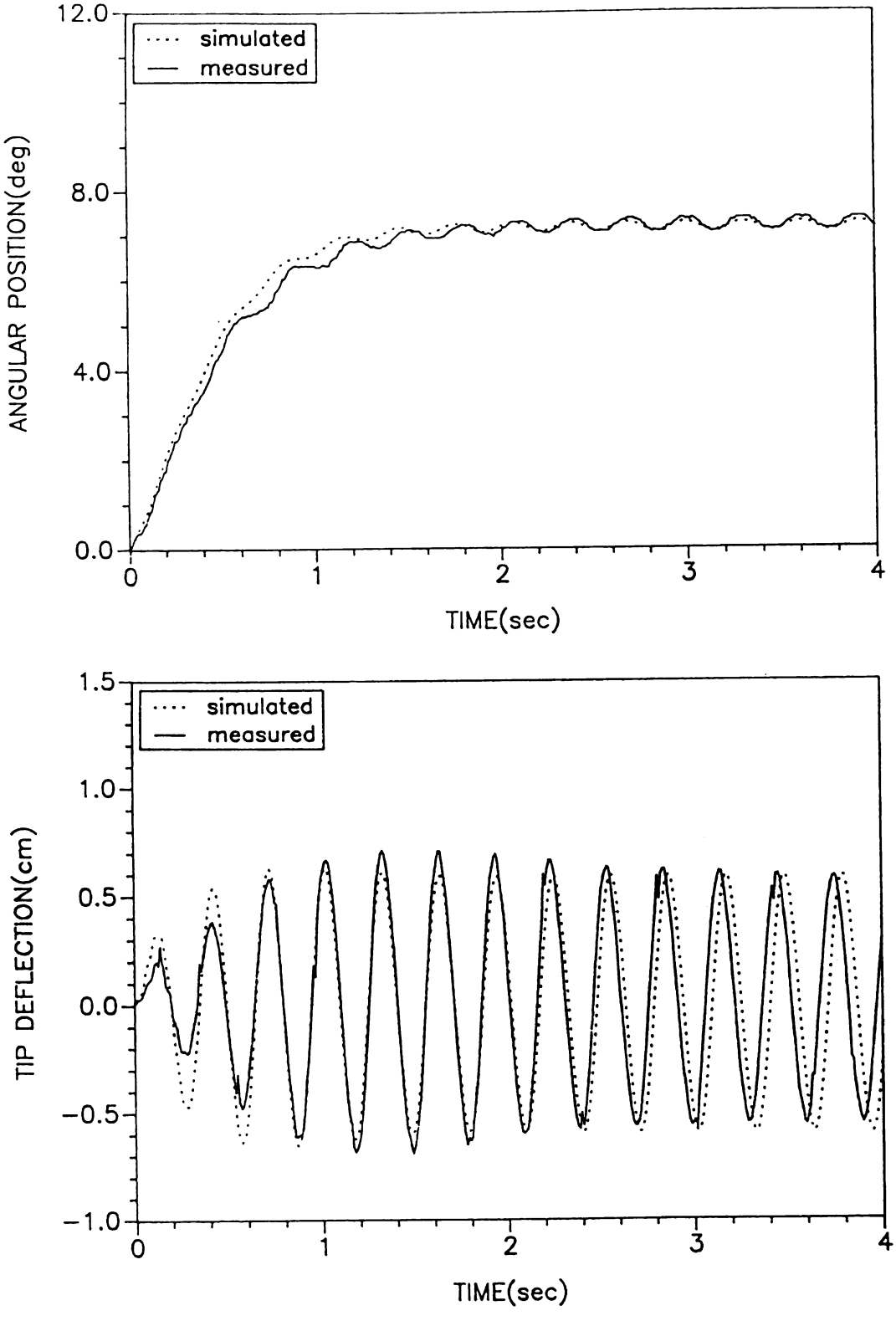


Figure 4.20 Comparison of the Simulated and Measured Step Responses of the Aluminum Arm with the Disturbance.

K_p=0.534, K_v=0.267, and $\tilde{d}(t)$=0.08 sin(3.25 Hz)t

simulation and measurement with the imposed disturbance. The agreement between two results is satisfactory except for the beginning the motion. The reason of this mismatch at the beginning of the motion is that the motion is delayed due to the applied disturbance which induces the motion in the opposite direction to the commanded position.

Figure 4.21 presents the measured step responses of the composite arm to a commanded angular position of 7.2 degree with feedback gains of K_p=0.2916 N•m, K_v= 0.1458 N•m•sec and the disturbance of $\tilde{d}(t) = 0.08 \sin f_1 t$ N•m where f_1= 4.75 Hz, which is close to the fundamental clamped-mode natural frequency of Ω_1= 5.22 Hz of the composite arm. As in the aluminum arm, near resonance phenomenon has been occurred even though the small oscillation amplitude is observed from the angular position response.

Figure 4.22 shows a comparison of the measured step responses of the composite arm with and without the disturbance. Similar characteristics to the aluminum arm are observed. Figure 4.23 presents a comparison of the measured and simulated step response in the presence of the disturbances. The agreement of two results is excellent except first portion of the angular position response. Again, the delay of the response arises from the imposed disturbance which hinders the motion in opposite direction to the commanded step position.

Figure 4.24 shows the measured step responses of the composite arm with the same feedback gains used for the Figure 4.21 and the disturbance $\tilde{d}(t)$=0.4 sin $f_2 t$ where f_2 = 34.5 Hz, which is very close to the second clamped-mode mode natural frequency Ω_2 = 33.09 Hz of the composite arm.

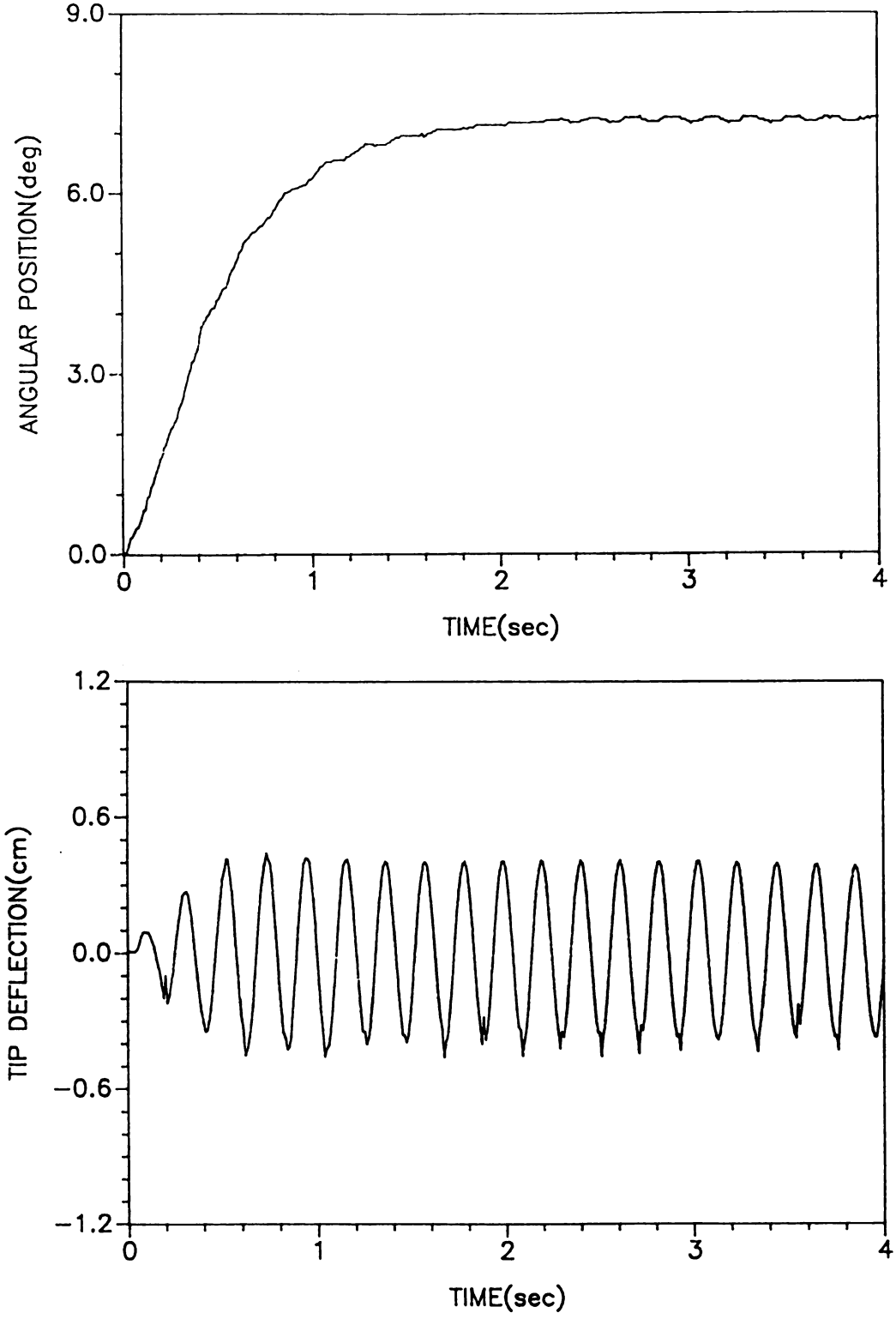


Figure 4.21 Measured Step Responses of the Composite Arm without Payload. K_p=0.292, K_v=0.146 and $\tilde{d}(t)$=0.08 sin(4.75 Hz)t

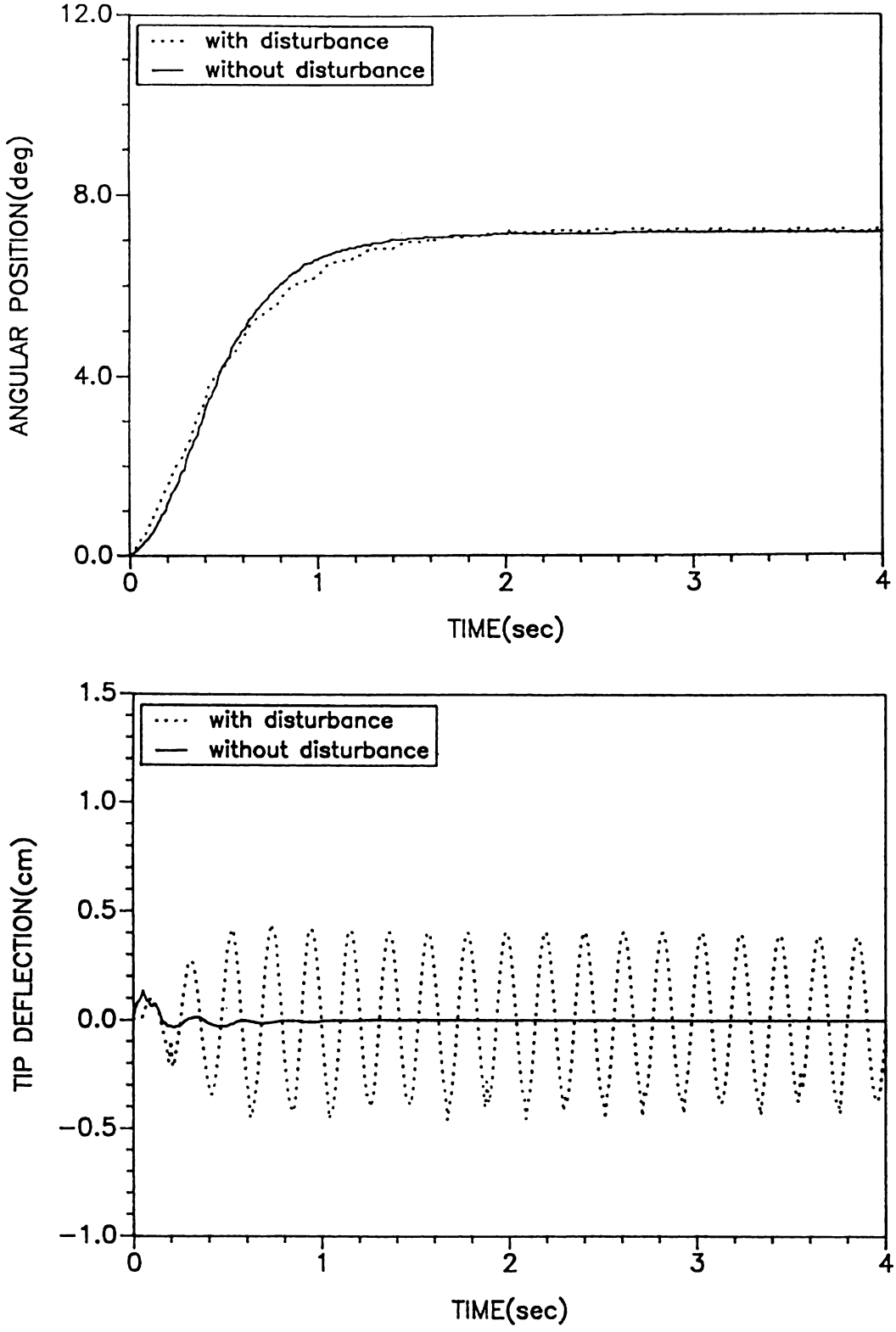


Figure 4.22 Comparison of the Measured Step Responses of the Composite Arm with and without the Disturbance.

K_p=0.292, K_v=0.146, and $\tilde{d}(t)$=0.08 sin(4.75 Hz)t

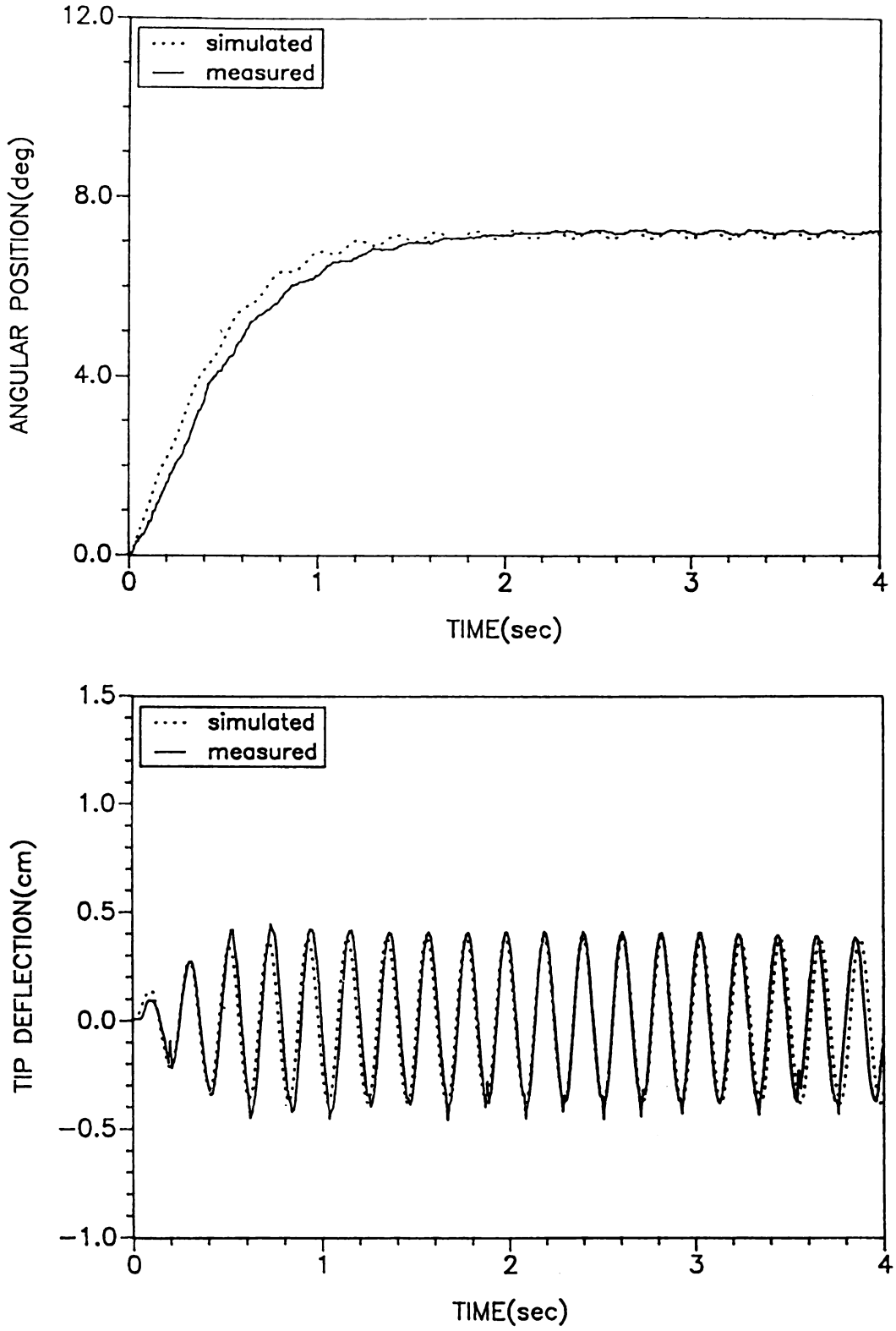


Figure 4.23 Comparison of the Simulated and Measured Step Responses of the Composite Arm with the Disturbance.

K_p=0.292, K_v=0.146, and $\tilde{d}(t)$=0.08 sin(4.75 Hz)t

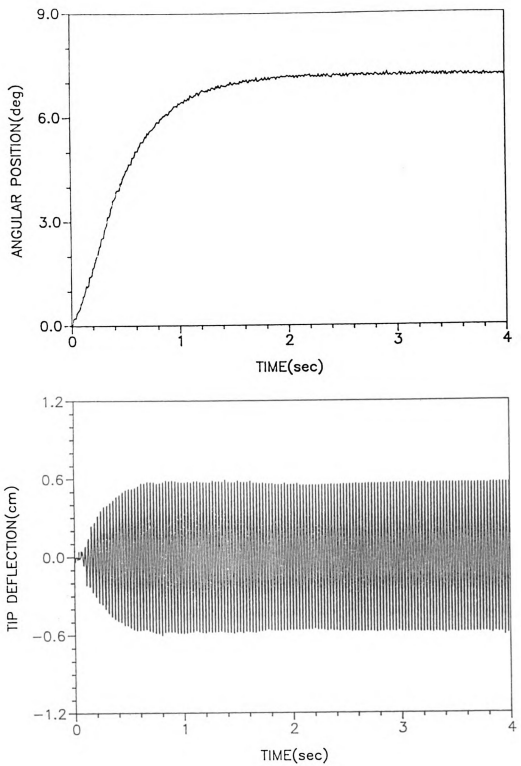


Figure 4.24 Measured Step Responses of the Composite Arm without Payload. $K_p = 0.292$, $K_v = 0.146$, and $\bar{d}(t) = 0.4 \sin(34.5 \text{ Hz})t$

As observed from the step responses of the closed-loop system in the presence of the disturbance which has a forcing frequency close to the clamped-mode natural frequency of the arm, the responses are very sensitive to the imposed disturbance regardless of either the aluminum or the composite arm. Even though significant advantages of the control performances with the composite arm in the absence of disturbance were accomplished, there is a limit to improve the overall control system especially in the presence of uncertainties such as introduced disturbances.

In order to circumvent this problem, a single-link flexible manipulator fabricated from smart materials incorporating electro-rheological fluids is proposed and investigated in the subsequent chapter. Since the natural frequencies of the arm is controllable in real time by employing an external voltage to the embedded electro-rheological fluid domains, the robustness of the PD output feedback control system is to be expected.

4.3.3 Instability of the System

As discussed in Section 4.2, the closed-loop system with the PD type of the output feedback controller associated with two colocated angular position and velocity sensors is theoretically stable for any choice of feedback gains. However, this is not true in practice since the unmodeled dynamics such as actuator and sensors, the neglected higher flexible modes, the presence of time delay in the controller implementation, and the limited inherent servo-characteristics of the closed-loop system may cause the system instability. In this section, the instability of the closed-loop system caused by the limited inherent servo-characteristics

will be discussed through the experimental investigation. The servo-drive system employed in this experimental investigation has an in-position band which defines the maximum allowable position from the commanded angular position (in other words, the allowable positional accuracy) as shown in Figure 4.25. In Figure 4.25, the T_1 and T_2 represent reacting torques to force the actual position to the in-position band. The magnitude of these torques depend on the employed feedback gains, and the geometrical and material properties of the arm and the hub. The actual position in general remains within the in-position band with the small feedback gains (small T_1 and T_2 due the small gains, small spring and inertia force). However, as the feedback gains increase, the reacting

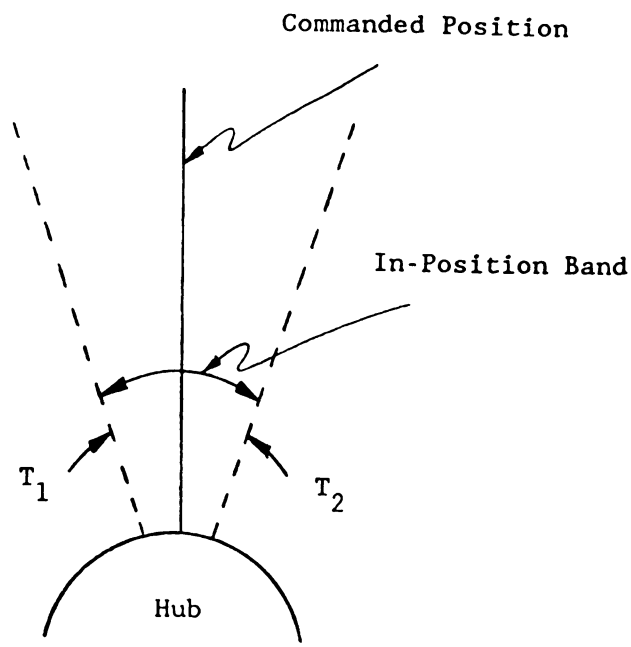


Figure 4.25 In-Position Band of the Servo-Drive System

torques T_1 and T_2 become larger in order to force the actual position to the in-position band. Hence, with certain critical feedback gains, the reacting torques continuously increase resulting in the system instability. The experimental test was undertaken in a such a manner that the position feedback gain was increased until the instability of the system was occurred, while the velocity feedback gain was fixed. Since the instability may cause serious injury to persons or damage to adjacent hardwares of the system, the emergency switch has been activated after just 4 seconds of the commanded motion.

Figure 4.26 presents the measured step responses of the aluminum arm to the commanded angular position of 7.2 degree with feedback gains of K_p= 6.2 N•m and K_v= 0.4 N•m•sec. With these feedback gains, the system became unstable resulting in the growing responses as time goes on. It is interesting to observe from the tip deflection response that the magnitude of oscillation does not grow up noticeably until 2 second, however after then, the response grows up rapidly. Figure 4.27 presents the simulated step responses corresponding to the measured responses given in Figure 4.26. As expected, the system is stable with these feedback gains. These feedback gains may be defined as maximum allowable feedback gains of the practical system featuring the aluminum arm. It is noted that the maximum allowable feedback gains have different combination of K_p and K_v. In other words, if the different velocity gain is chosen, the different maximum position feedback gain, which causes the instability of the closed-loop system, is determined. From these results, it may be recognized that the controller design of the system should be based on both analytical analysis and experimental

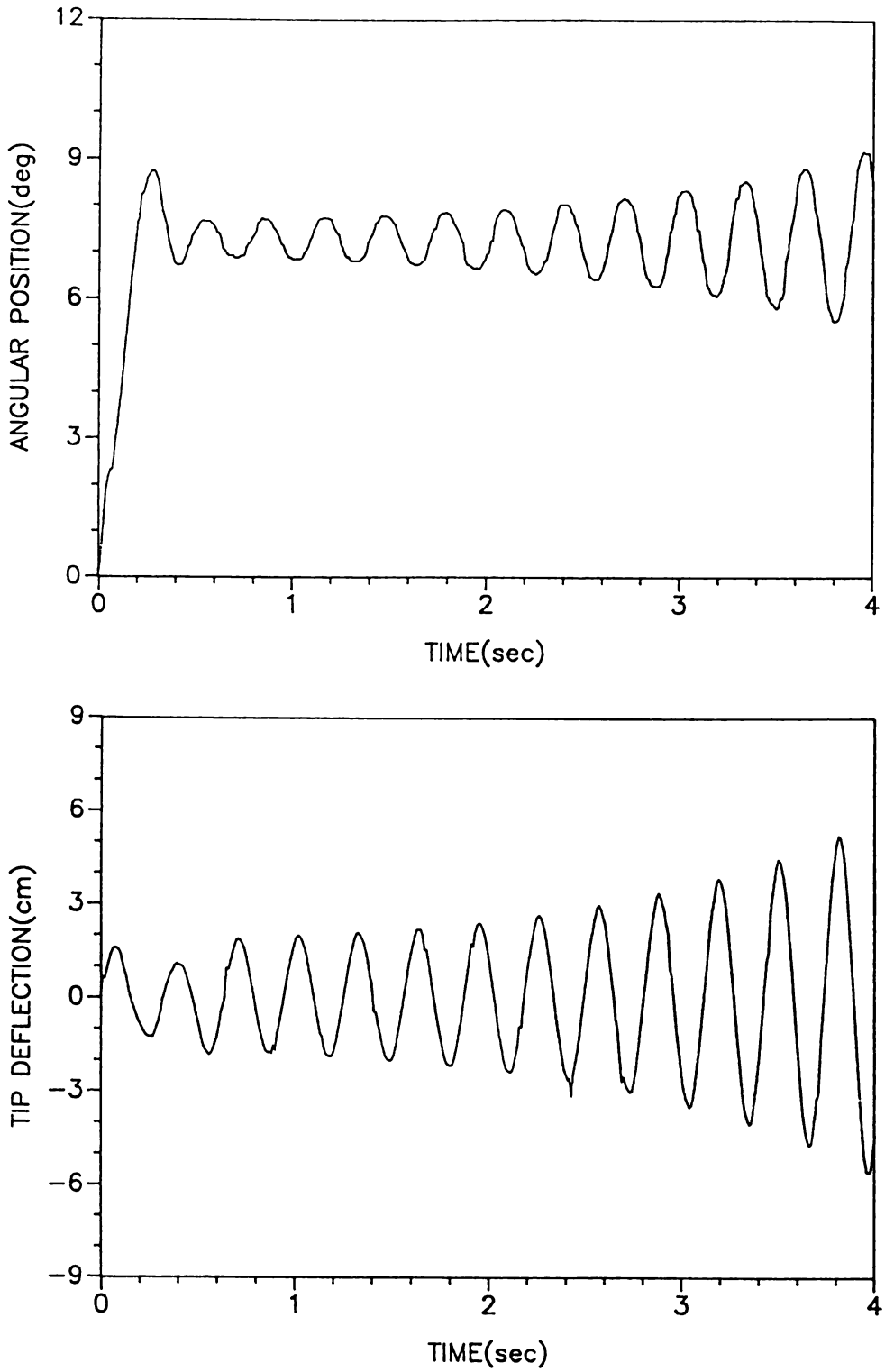


Figure 4.26 Measured Step Responses of the Aluminum Arm without Payload. K_p=6.2 and K_v=0.4

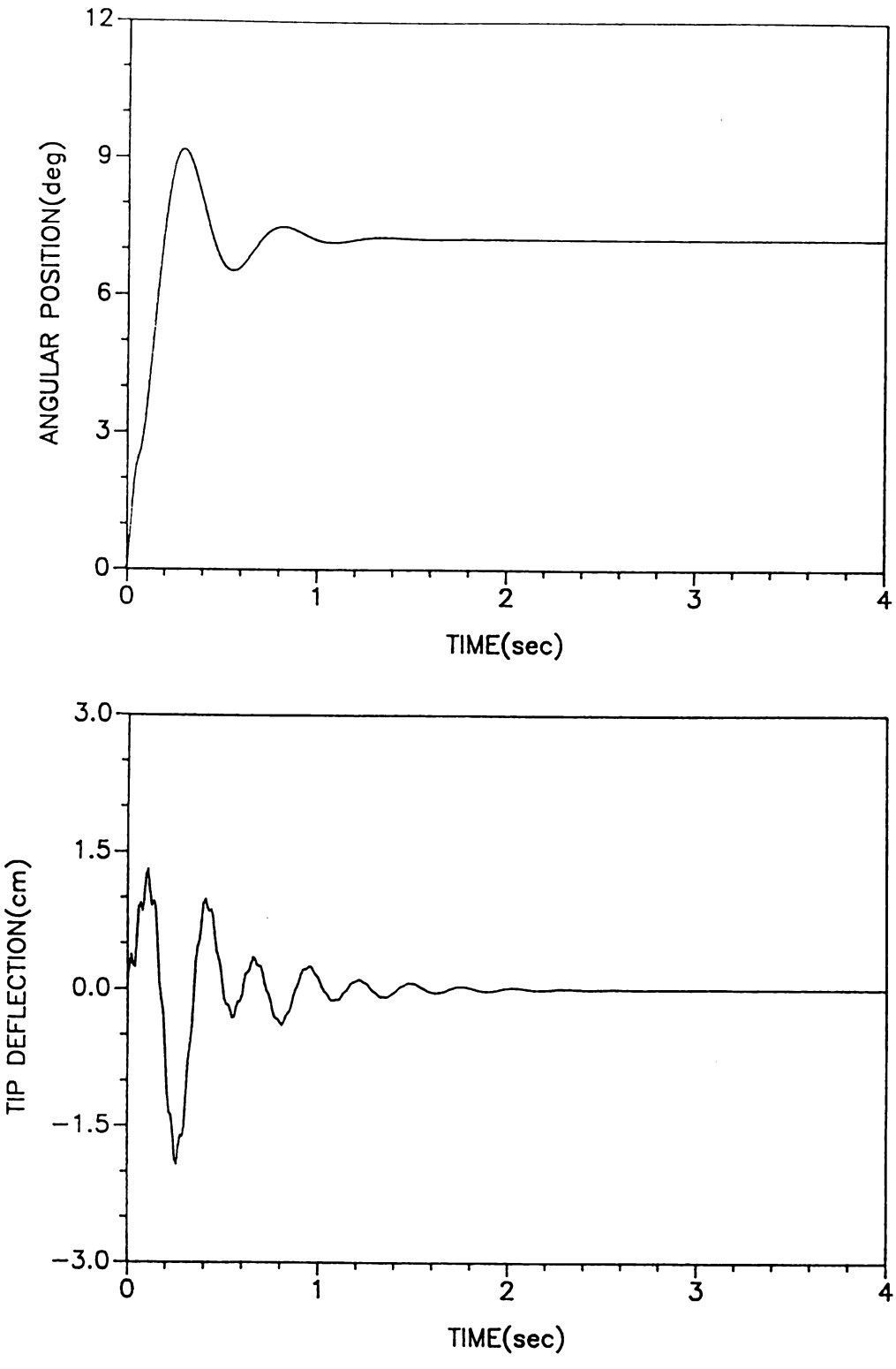


Figure 4.27 Simulated Step Responses of the Aluminum Arm without Payload. K_p=6.2, K_v=0.4

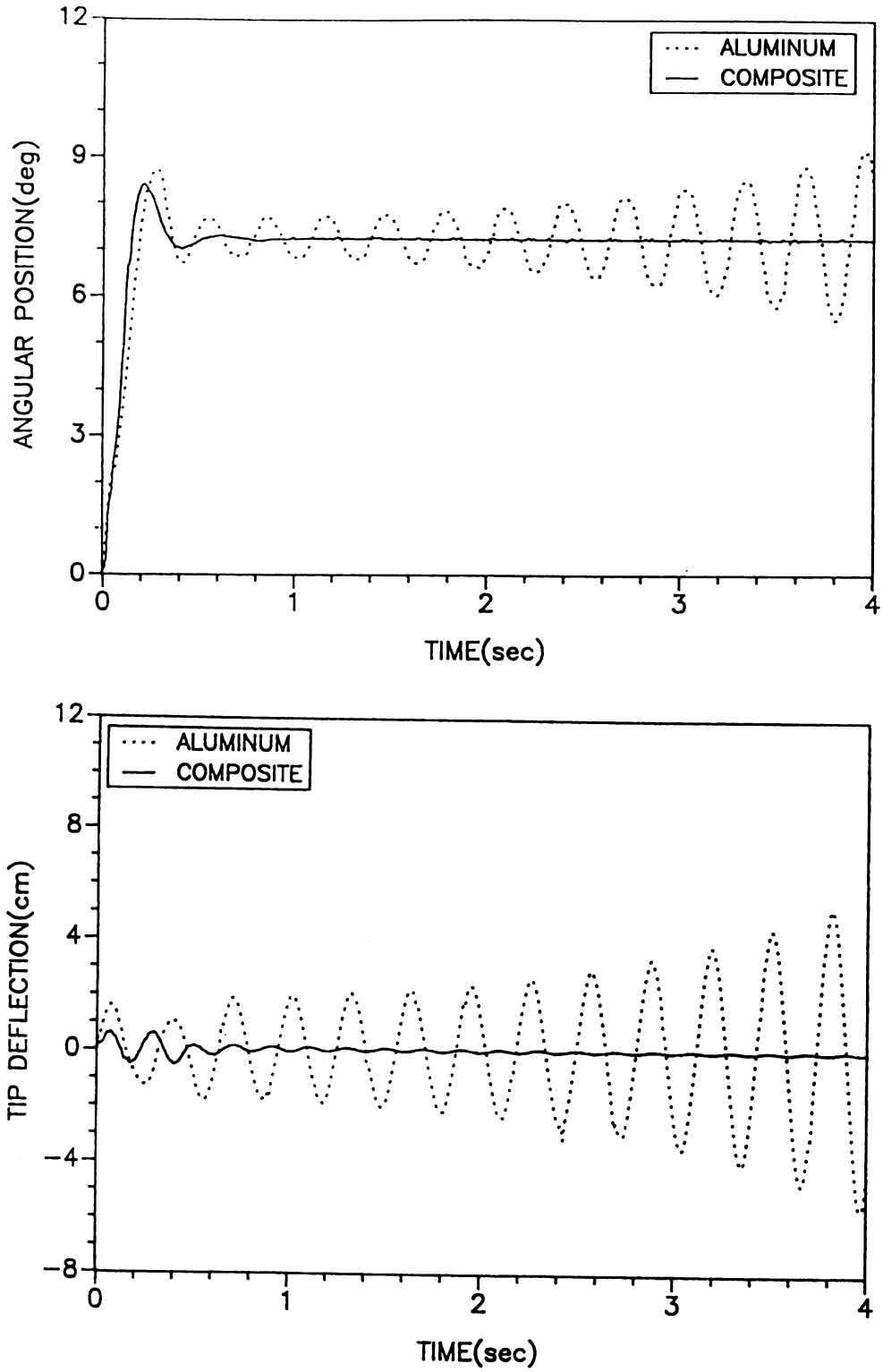


Figure 4.28 Measured Step Responses with Feedback Gains of K_p=6.2 and K_v=0.4 for both Aluminum and Composite Arms

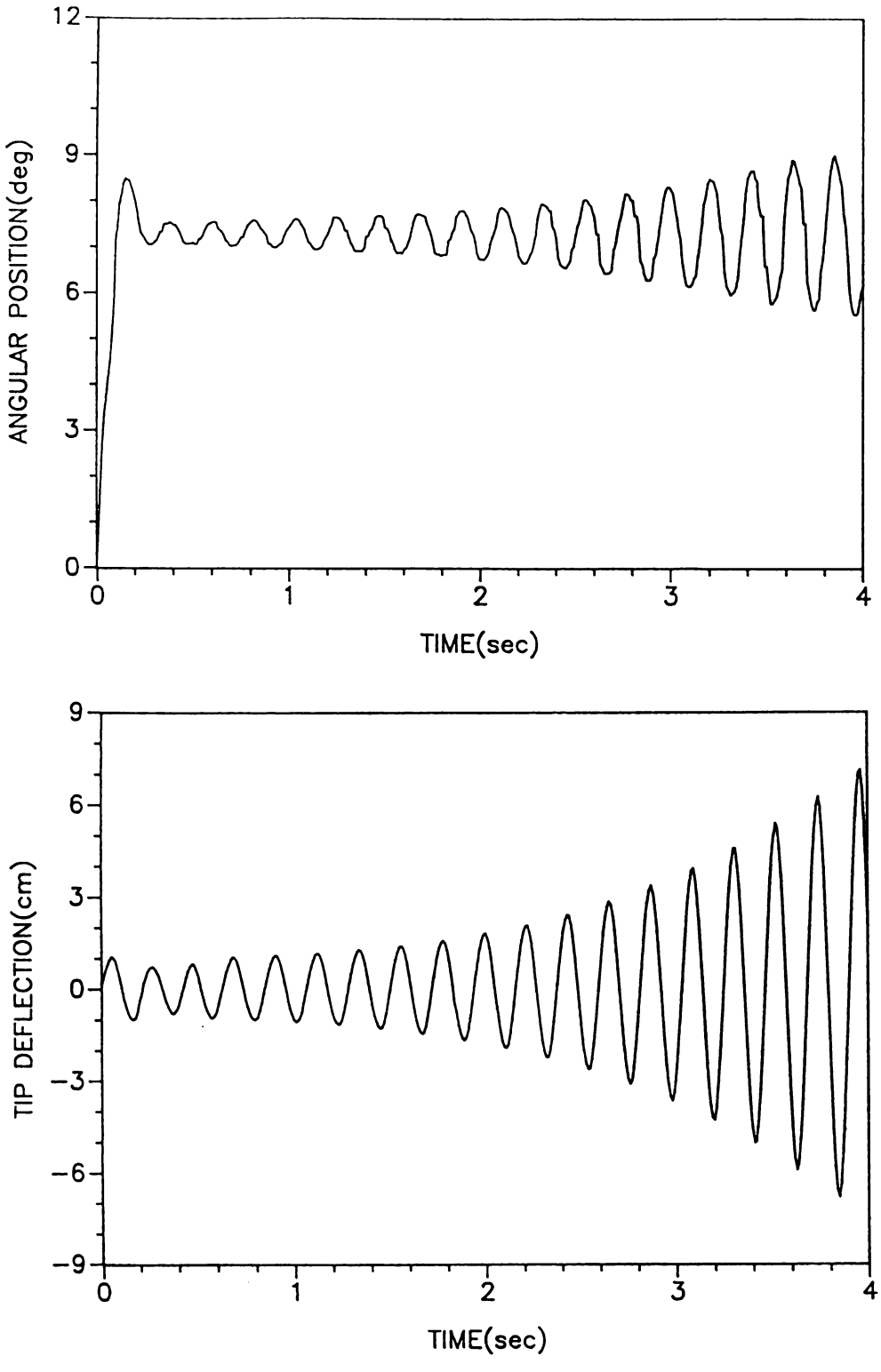


Figure 4.29 Measured Step Responses of the Composite Arm without Payload. K_p = 11.8, K_v = 0.4

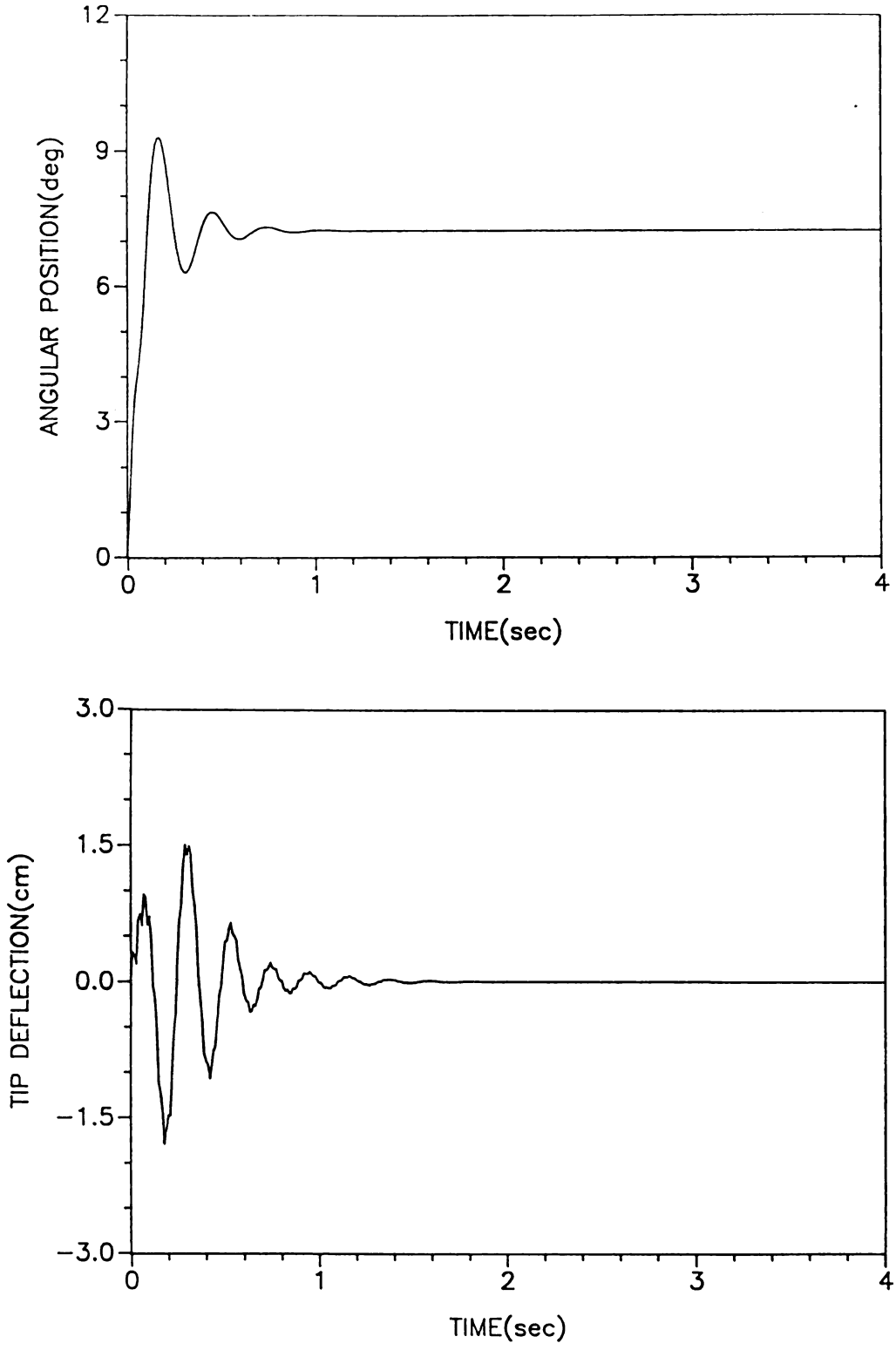


Figure 4.30 Simulated Step Responses of the Composite Arm without Payload. K_p= 11.8, K_v= 0.4

identification of the employed system. Figure 4.28 shows a comparison of the measured step responses of the aluminum and composite arm with feedback gains of K_p= 6.2 N•m and K_v= 0.4 N•m•sec. With these feedback gains, the composite arm exhibits stable closed-loop responses of the system, hence shows significant improvement of the stability of the employed practical system. It is recognized that the reduced spring and inertial force of the composite arm is contributed to this result.

The position feedback gain with the same fixed velocity feedback gain of K_v= 0.4 N•m•sec was increased until the instability of the composite arm was occurred. Figure 4.29 shows the measured step responses of the composite arm to a commanded angular position of 7.2 degree with the position gain of K_p= 11.8 N•m. From the response of the tip deflection, it is also observed that the response quickly grows up after 2 second as the case of the aluminum arm. Figure 4.30 presents the simulated step responses corresponding to the measured responses shown in Figure 4.29. The closed-loop system is stable with these feedback gains as expected. From this experimental investigation, it may be summarized that the stability margin of this employed particular robotic system featuring the aluminum arm can be enhanced up to 45 percent by employing the composite arm. This is also another significant advantage of the composite arm over the aluminum arm.

4.4 Summary of the Chapter

The output feedback controller associated with two colocated sensors was designed utilizing the root-locus technique and the Lyapunov method, and experimentally implemented for the aluminum and the composite arm.

The comparative experimental investigation was undertaken to evaluate the characteristics of the control performances of the aluminum and composite arm. It has been demonstrated from the analytical and experimental investigation that the control performances of the overall closed-loop system for the both aluminum and composite arms were satisfactory, and the composite arm exhibited some superior control performances relative to the aluminum arm such as faster settling-time, smaller input torque, smaller tip deflection (better positional accuracy), and superior increment of the stability of the practical system. These experimental results clearly indicate the significant payoffs associated with employing the composite materials featuring superior strength- and stiffness-to weight ratios to the commercial metals on the flexible manipulators. It has been also demonstrated that the aluminum and composite arm exhibited the inevitable sensitivity to the imposed disturbance which has a forcing frequency close to the cantilevered-mode natural frequency of the arms. This attempt was undertaken here in order to introduce a single-link flexible manipulator fabricated from smart materials incorporating electro-rheological fluids for the purpose of enhancing the robustness of the output feedback controller to the disturbance. Subsequent chapter addresses this new class of flexible manipulator fabricated from smart materials.

CHAPTER V

HYBRID CONTROL FEATURING A DISTRIBUTED ELECTRO-RHEOLOGICAL FLUID ACTUATOR

5.1 Introduction

As observed in the previous chapter, the closed-loop system associated with PD output feedback controller is very sensitive to the disturbance, which has a forcing frequency close to the clamped-mode natural frequency of the arm, regardless of the aluminum or the composite arm. In order to circumvent this problem, a single-link flexible manipulator fabricated from smart materials incorporating electro-rheological (ER) fluids (smart ER arm in short) will be investigated by proposing a hybrid control methodology. The hybrid controller consists of the output feedback controller employed for the aluminum and composite arm in the previous chapter, and a pseudo-state feedback controller characterized by a distributed ER fluid actuator [40]. A crucial ingredient in the development of an appropriate control algorithm for this class of smart materials is the development of an appropriate system (plant) model. Since the phenomenological behavior associated with the interaction of the structure and the embedded ER fluid is fairly complex, simplifying assumptions have been incorporated in the modeling process in order to furnish equations of motion which are analogous in mathematical structure to those encountered in beams fabricated from homogeneous monolithic materials. A phenomenological equation of motion, based on

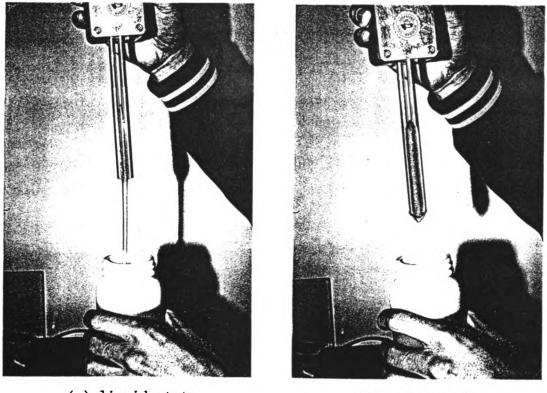
these simplifying assumptions and experimental observations, admits a pseudo-state feedback controller to be implemented. The pseudo-control force (external input voltage) associated with the pseudo-state feedback controller accounts for the change in the global damping and stiffness properties of the structure due to the electrical potential applied to ER fluid domains.

Since the natural frequencies and damping ratios of the flexible smart structures are tunable on real time by employing the external input voltage to the embedded ER fluid domain [41,56], the resonance phenomenon due to the imposed disturbance can be avoided by applying the pseudo-control forces. Hence, the robustness of the employed PD type output feedback controller is to be expected. In this chapter, a brief background on the ER fluids will be introduced prior to developing a phenomenological equation of motion of the proposed robotic system. Then a hybrid controller will be formulated based on the empirical model of the distributed ER fluid actuator. Finally, an experimental implementation of the proposed hybrid controller will be presented by investigating step responses of the system subjected to no disturbances and disturbances.

5.2 Background on Electro-Rheological Fluids

Electro-Rheological (ER) fluids are typically suspensions of micron-sized hydrophilic particles suspended in the suitable hydrophobic carrier liquids, which undergo significant instantaneous reversible changes in material characteristics when subjected to electrostatic potentials. References [20,41,55,56,57,136,137,138,140,151,160] provide a flavor of the research activities in this field. The most significant change in the

material characteristics of ER fluids is associated with the bulk viscosity of the suspension, which varies dramatically upon applying an electrical field to the fluid domain. This dramatic reversible change from a liquid-like state, as shown in Figure 5.1 (a) to a solid-like state as shown in Figure 5.1 (b) by the imposition of an appropriate electrical potential can be usefully exploited in vibration-control applications.



(a) liquid state (b) solid state

Figure 5.1 Electro-Rheological Fluid in Liquid and Solid State

Figure 5.2 presents a mechanism showing that how this reversible change works in terms of interaction between charges placed on electrodes and those in the particles in the ER fluid. The charges in the fluid may

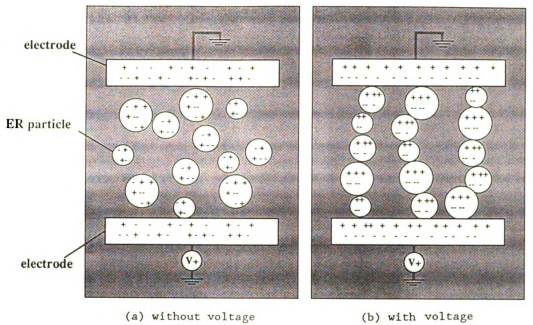
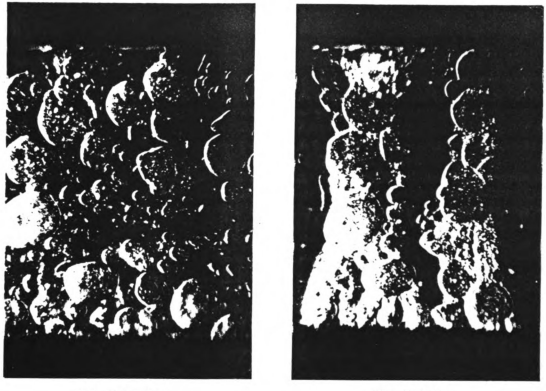


Figure 5.2 Interaction between Charges on Electrodes and Those in Electro-Rheological Fluid

be either positive or negative, and free to move in the material in the absence of charge on the electrodes as shown in Figure 5.2 (a). When a voltage is applied to the electrodes, the charges in the fluid form a chain-like formulation in milliseconds as shown in Figure 5.2 (b).

Figure 5.3 presents photomicrographs of an ER fluid subjected to electrical field intensities of 0 kV/mm and 2 kV/mm respectively. The photomicrographs were taken in the Biothermal Sciences Laboratory at Michigan State University using a Zeiss universal phase-contrast microscope with X40 magnification and a Chinon camera. The black regions at the top and bottom of the photographs are images of the electrodes employed to generate the electrical field in the ER fluid. Figure 5.3 (a) clearly illustrates the random structure of the suspension which imparts nominally isotropic global mechanical properties to the fluid mixture

when a potential difference is not generated between the electrodes. Figure 5.3 (b) clearly shows the truly dramatic change in the structure of the suspension upon developing a potential difference between the electrodes of magnitude 2 kV/mm. Under this condition, the particles in the suspension orientate themselves in relatively regular chain-like patterns to form a mixture with globally anisotropic mechanical properties. These columnar structures of particles restrict the fluid motion, thereby increasing the energy-dissipation or viscous characteristics of the suspension, in addition to increasing the stiffness characteristics of the fluid mixture. Thus, by imposing an



(a) 0 kV/mm (b) 2 kV/mm

Figure 5.3 Photomicrograph of Electro-Rheological Fluid

electric field upon an ER fluid, the stiffness and energy dissipation, or damping, characteristics of the electro-viscous suspension are changed. When the field returns to a state of zero potential, upon switching off the electrical energy supplied to the electrodes, the particles return to a state of random orientation in the carrier fluid as presented in Figure 5.3 (a).

The voltages required to activate the phase-change in ER fluids are typically in the order of 4 kV per millimeter of fluid thickness, but since current densities are in the order 10 $\mu A/cm^2$ or less, the total power required to trigger this phenomenon is quite low. Furthermore, the response of these ER fluids to the excitation voltage is almost instantaneous since the fluids can respond to voltage pulses with frequency up to approximately 11 kHz, which is, of course far beyond the requirements of most practical devices. ER fluid suspensions typically have viscosities of the order of 50 cP in the uncharged state, and some fluids are able to withstand a nonvanishing yield stress up to 60 kPa and shear rates up to 400/s. When an ER fluid suspension is stressed below this threshold, it behaves as a solid, but as the stresses are increased, then fluid flow occurs but the yield stress remains nominally constant.

Since the characteristic aspects of ER fluids have been recognized by Winslow [160] in 1949 for the first time, numerous applications of ER fluids in engineering practice have been and being proposed and developed. Possible ER fluids devices and mechanisms proposed and developed so far are well documented in [128]. Typical applications include ER actuators, ER active damper systems, ER clutches, ER hydraulic valves, ER brakes, ER suspension systems, ER shock absorbers, rotary ER

viscometers, tunable ER isolators, and wide-band-high power ER vibrators.

5.3 Phenomenological Equation of Motion

Phenomenologically, the global finite element equation governing the motion of the proposed smart ER robotic system has the following functional form [40,41,56,58]

$$[M]\{\ddot{U}\} + [C(\hat{V}(t))]\{\dot{U}\} + [K(\hat{V}(t))]\{U\} = \{Q(t)\} \qquad (5.1)$$

where the global mass,damping and stiffness matrices are denoted by $[M]$, $[C(\hat{V}(t))]$ and $[K(\hat{V}(t))]$ respectively. Clearly the stiffness and damping matrices are functions of the external voltage $\hat{V}(t)$ applied to the ER fluid domains within the robotic arm. It must be emphasized that the damping matrix $[C(\hat{V}(t))]$ in the equation (5.1) is, in general, not proportional to the stiffness and/or mass matrix. The nodal displacement is represented by the column vector $\{U\}$ and the generalized force is denoted by the column vector $\{Q(t)\}$. Without loss of generality, the equation (5.1) may be reformulated as follows:

$$[M]\{\ddot{U}\} + ([C]+[\Delta C(\hat{V}(t))])\{\dot{U}\} + ([K]+[\Delta K(\hat{V}(t))])\{U\} = \{Q(t)\} \qquad (5.2)$$

where $[K]$ and $[C]$ are the global stiffness and damping matrices associated with zero electric intensity, and $[\Delta K(\hat{V}(t))]$ and $[\Delta C(\hat{V}(t))]$ are the changed global stiffness and damping matrices due to the change in voltage from zero volts to $\hat{V}(t)$.

Consider now the modal analysis as did in Section 2.4, and in addition, assume that the ER fluid domains within the arm are not subjected to an external voltage. Then the equation (5.2) becomes

$$[M]\{\ddot{U}\} + [C]\{\dot{U}\} + [K]\{U\} = \{Q(t)\} \tag{5.3}$$

Now, by introducing modal coordinates $\{\eta\}$ and the modal matrix $[\Phi]$, i.e.,

$$\{U\}=[\Phi]\{\eta\} \tag{5.4}$$

the equation (5.3) becomes

$$\ddot{\{\eta\}} + [Z]\{\dot{\eta}\} + [\Omega]\{\eta\} = [B]\tilde{u} \tag{5.5}$$

where $[\Omega]$ ($= \text{diag}\ (0,\omega_1^2, \ldots,\omega_n^2)$) is the modal frequency matrix with the pinned-mode natural frequencies ω_i, $[Z]$ ($= [\Phi^T C\ \Phi]$) is the transformed modal damping matrix, $[B](= \frac{1}{I_T}[1 \quad d\phi_1(o)/dx\ , \ . \ . \ . \ . \ , d\phi_n(o)/dx]^T)$ is the input influence matrix with the modal slope coefficient $d\phi_i(o)/dx$, and $\tilde{u}$ is the input torque. The transformed modal damping matrix [Z] is coupled, since the damping matrix [C] is not assumed to be proportional to the stiffness and/or mass matrix. This coupling manifests itself in the non-zero values of the off-diagonal terms of the matrix [Z]. In order to investigate the magnitude and hence significance of these terms, an experimental program was undertaken by considering a smart beam structure which has a similar modal characteristics of the proposed smart robotic arm structure. Figure 5.4 presents the schematic diagram of the employed smart cantilevered beam whose fabrication procedure is presented in details in Section 5.5.

Figure 5.5 presents the measured first and second mode shapes (magnitude and phase) of the proposed cantilevered beam. In Figure 5.5, the symbols and lines are the measured values and the curve-fitted interpolation respectively, and the magnitude of mode shapes is normalized as well as the beam length. These experimental values were obtained from the frequency response data utilizing the procedures described in Section 5.5. It is clearly evident from the phase of the mode shapes that the phases are all near 0^{o} or 180^{o} at both 0 kV and 3 kV. Thus, the mode shapes are close to real [52], except in the region close to the nodal points where the phase transition occur. This is

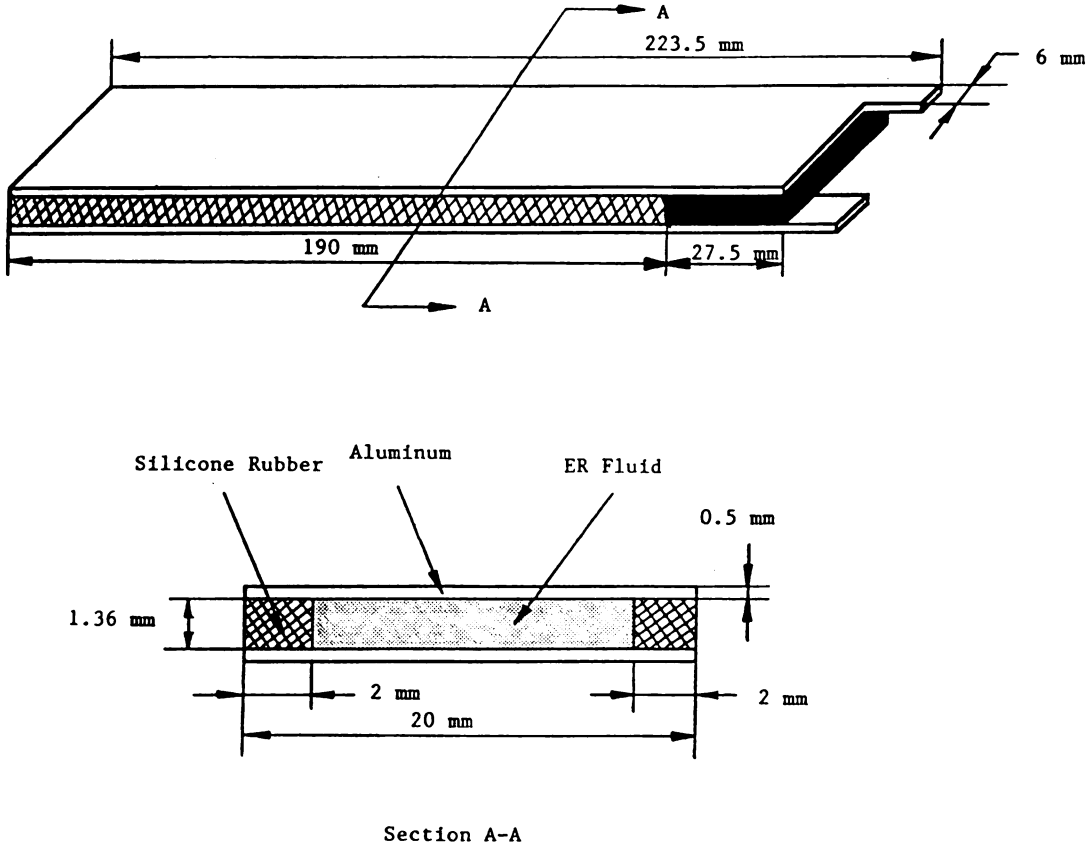


Figure 5.4 Smart Cantilevered Beam Structure

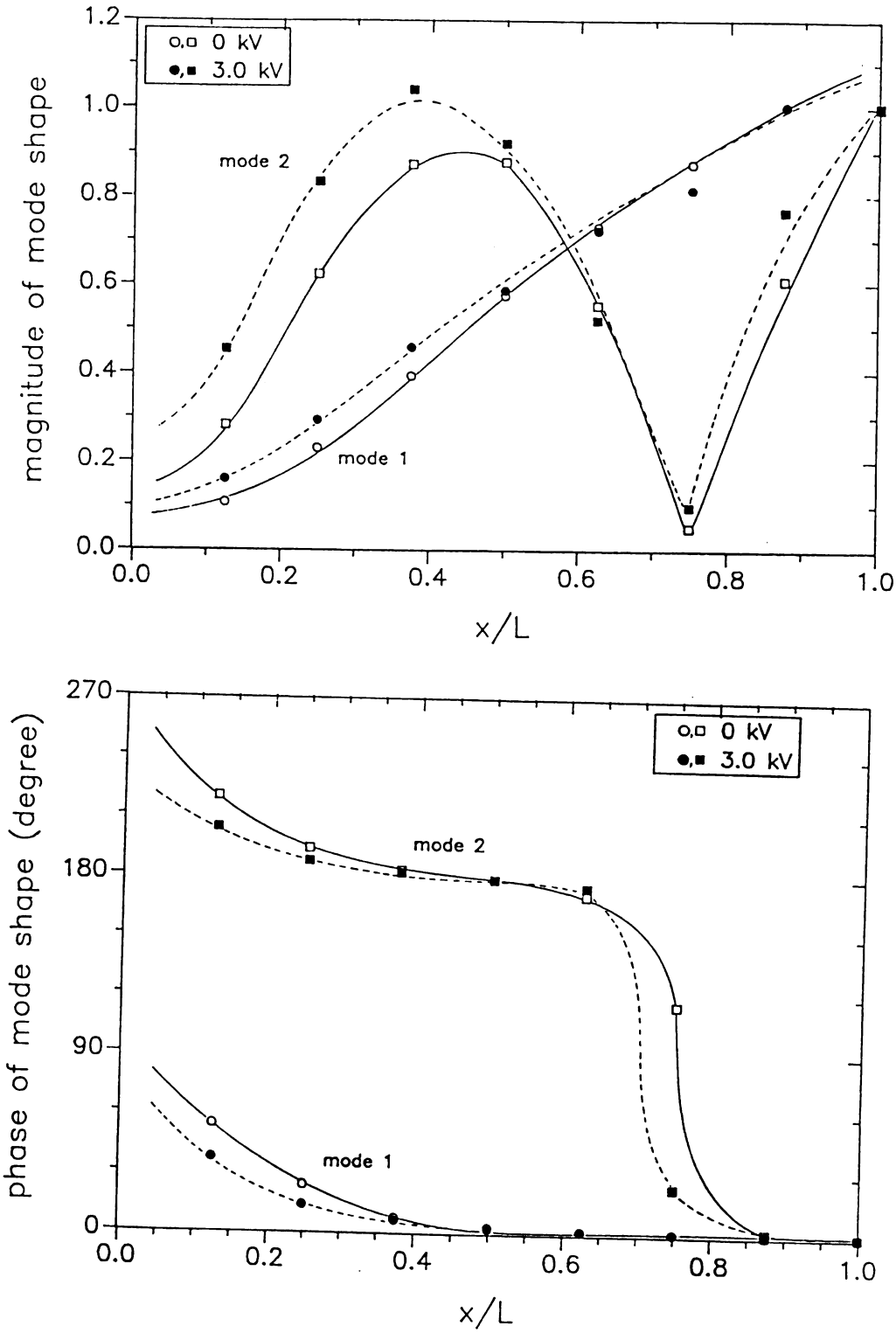


Figure 5.5 Mode Shapes of the Smart Cantilevered Beam

particularly true for the employed cantilevered beam structure or the proposed smart robotic arm structure, since the distribution of all the eigenvalues of these structures are well separated. However, this fact may not be true for the complicated structures such as truss-like structures which have clustered eigenvalues. It is, therefore, reasonable to assume that each mode is uncoupled from the others. Hence, the off-diagonal terms in the transformed modal damping matrix [Z] can be ignored without causing serious errors.

Assuming that the mode shapes are real, the coherence factor introduced in [75] is adopted here to investigate the viability of employing the modal matrix in the absence of externally-imposed voltage on the ER fluid domains, and also the situation where a non-zero voltage is imposed on these domains. The coherence factor is defined by

$$coh_{ij} \triangleq \frac{(\{\Phi_i^c\}^T\{\Phi_j^c\})^2}{(\{\Phi_i^c\}^T\{\Phi_i^c\})\cdot(\{\Phi_j^c\}^T\{\Phi_j^c\})} \tag{5.6}$$

where coherence of 1 means two modes of i and j are identical, while coherence of 0 represents an orthogonal set of two modes. In equation (5.6), Φ_i^c and Φ_j^c represent the ith and jth cantilevered-mode modal vector respectively. Table 5.1 presents the experimentally-determined coherence factors for the first two flexible modes of the cantilevered beam structure investigated herein at four discrete state of voltage. Upon reviewing these data it is clearly evident that there is an insignificant difference between the coherence factor in the 0 kV state and the other states. Clearly, therefore the mode shapes are identical for the range of voltages considered in this study.

Table 5.1 Coherence Factor of the First and Second Mode at Different Voltage

Mode	0 kV	1 kV	2 kV	3 kV
First	1	0.993	0.993	0.993
Second	1	0.987	0.984	0.983

From these experimental observations, the modified equations of motion for the proposed robotic system in the presence of an electrical field intensity can be expressed as

$$\ddot{\{\eta\}} + [\hat{C}]\dot{\{\eta\}} + [\hat{K}]\{\eta\} = [B]\tilde{u} \tag{5.7}$$

where

$$[\hat{C}]=[Z]+[\Phi]^T[\Delta C(\hat{V}(t))][\Phi],\ [Z]=\text{diag}(0,\ 2\zeta_1\omega_1,\ldots,\ 2\zeta_n\omega_n)$$

$$[\hat{K}]=[\Omega]+[\Phi]^T[\Delta K(\hat{V}(t))][\Phi]$$

Furthermore, from the experimental results presented in Table 5.1

$$\begin{aligned}[\Phi]^T[\Delta C(\hat{V}(t))][\Phi]&=[Z(\hat{V}(t))]\\ [\Phi]^T[\Delta K(\hat{V}(t))][\Phi]&=[\Omega(\hat{V}(t))]\end{aligned} \tag{5.8}$$

where $[Z(\hat{V}(t))]$ (= diag $(0,\ 2\zeta_1(\hat{V}(t))\omega_1(\hat{V}(t)),\ldots,\ 2\zeta_n(\hat{V}(t))\omega_n(\hat{V}(t)))$ is the changed modal damping matrix due to the electric field and $[\Omega(\hat{V}(t))]$ (= diag $(0,\ \omega_1^2(V(t)),\ \ldots,\ \omega_n^2(V(t)))$ is the changed undamped natural frequency matrix; namely

$$\zeta_i(\hat{V}(t))\omega_i(\hat{V}(t)) = (\zeta_i\omega_i)_{\hat{V}(t)\neq 0} - (\zeta_i\omega_i)_{\hat{V}(t)=0}$$

$$\omega_i^2(\hat{V}(t)) = (\omega_i^2)_{\hat{V}(t)\neq 0} - (\omega_i^2)_{\hat{V}(t)=0} \tag{5.9}$$

Equation (5.7) can be expressed in a state-space representation as follows.

$$\dot{\tilde{x}} = \tilde{A}\tilde{x} + \tilde{A}(\hat{V}(t))\tilde{x} + \tilde{B}\tilde{u}$$

$$\tilde{y} = \tilde{C}\tilde{x} \tag{5.10}$$

where state variable $\tilde{x}$, plant matrix $\tilde{A}$ in the absence of an external voltage, input matrix $\tilde{B}$, and the output matrix $\tilde{C}$ is same as that defined in equation (2.33), respectively. And the changed plant matrix $\tilde{A}(\hat{V}(t))$ due to the electrical potentials is given by

$$\tilde{A}(\hat{V}(t)) = \begin{bmatrix} 0 & 0 & 0 & 0 & \cdots & 0 & 0 \\ 0 & 0 & 0 & 0 & \cdots & 0 & 0 \\ 0 & 0 & 0 & 0 & \cdots & 0 & 0 \\ 0 & 0 & -a_{21} & -a_{11} & \cdots & 0 & 0 \\ \vdots & \vdots & \vdots & \vdots & \cdots & \vdots & \vdots \\ 0 & 0 & 0 & 0 & \cdots & 0 & 0 \\ 0 & 0 & 0 & 0 & \cdots & -a_{2n} & -a_{1n} \end{bmatrix} \tag{5.11}$$

where

$$a_{21} = \omega_1^2(\hat{V}(t)), \quad a_{2n} = \omega_n^2(\hat{V}(t))$$

$$a_{11} = 2\zeta_1(\hat{V}(t))\omega_1(\hat{V}(t)), \quad a_{1n} = 2\zeta_n(\hat{V}(t))\omega_n(\hat{V}(t))$$

It is noted that only flexible modes are voltage dependent.

5.4 Controller Formulation

As did in Section 2.4, the equation (5.10) can be decomposed into two subdynamic equations by considering the rigid-body mode and the first few critical flexible modes as primary modes and remaining modes as residual modes. The two subdynamic equations are

$$\begin{aligned} \dot{\tilde{x}}_p &= \tilde{A}_p \tilde{x}_p + \tilde{A}_p(\hat{V}(t))\tilde{x}_p + \tilde{B}_p \tilde{u} \\ \tilde{y}_p &= \tilde{C}_p \tilde{x}_p \end{aligned} \tag{5.12}$$

and

$$\begin{aligned} \dot{\tilde{x}}_r &= \tilde{A}_r \tilde{x}_r + \tilde{A}_r(\hat{V}(t))\tilde{x}_r + \tilde{B}_r \tilde{u} \\ \tilde{y}_r &= \tilde{C}_r \tilde{x}_r \end{aligned} \tag{5.13}$$

where subscript (p) denotes the primary modes and (r) represents the residual modes.

Before proceeding further, consider the stability problem of the system (5.12). Suppose the information about the changed plant matrix $\tilde{A}_p(\hat{V}(t))$, which will be later termed as a pseudo-control force after reformulating it based on experimental observations, is not available at this moment. Then, the matrix $\tilde{A}_p(\hat{V}(t))$ can be considered as a time-varying linear perturbation matrix due to the voltage $\hat{V}(t)$ with respect to the system in the absence of electrical potentials, that is, nominal system. Then following theorem for the stability can be established based on the Lyapunov function approach.

Remark 5.1 : In the following, the vector norm is taken to be Euclidean and the matrix norm is the corresponding induced norm, hence $||A|| = (\lambda_{max}(A^T A))^{1/2}$ where $\lambda_{max(min)}(\cdot)$ represents the operation of taking the maximum(minimum) eigenvalue.

Lemma 5.1 : Let Q be a symmetric and positive definite matrix. Then,

$$\lambda_{min}(Q)||\tilde{x}_p||^2 \leq \tilde{x}_p^T Q \tilde{x}_p \leq \lambda_{max}(Q)||\tilde{x}_p||^2 \tag{5.14}$$

for any $\tilde{x}_p$ (see [35] for the proof).

Theorem 5.1 : Suppose the system (5.12) in the absence of electrical potentials is stable with a linear output feedback controller $\tilde{u}$. Then, the system is stable if

$$||\tilde{A}_p(\hat{V}(t))|| < \frac{\lambda_{min}(Q)}{2\lambda_{max}(P)} \tag{5.15}$$

where P is a symmetric and positive definite matrix which is the solution of the Lyapunov equation

$$P \tilde{A}_c + \tilde{A}_c^T P + Q = 0 \tag{5.16}$$

where Q is a given positive definite matrix and

$$\tilde{A}_c = \tilde{A}_p + \tilde{B}_p \tilde{K} \tilde{C}_p \tag{5.17}$$

where $\tilde{K}$ is output feedback gains associated with the controller $\tilde{u}$.

Proof : With the equation (5.17), the state equation in (5.12) can be rewritten as

$$\dot{\tilde{x}}_p = \tilde{A}_c \tilde{x}_p + \tilde{A}_p(\hat{V}(t))\tilde{x}_p \tag{5.18}$$

Now, choose Lyapunov function candidate as

$$V(\tilde{x}_p) = \tilde{x}_p^T P \tilde{x}_p \tag{5.19}$$

It is noted that $V(\tilde{x}_p) > 0$ for all $x_p \neq 0$ and $V(\tilde{x}_p) \to \infty$ as $||\tilde{x}_p|| \to \infty$. Now, $\dot{V}(\tilde{x}_p) < 0$ is required to guarantee the stability of the system (5.12).

$$\begin{aligned}
\dot{V}(\tilde{x}_p) &= \dot{\tilde{x}}_p^T P \tilde{x}_p + \tilde{x}_p^T P \dot{\tilde{x}}_p \\
&= \tilde{x}_p^T (\tilde{A}_c^T P + P \tilde{A}_c) \tilde{x}_p + \tilde{x}_p^T \tilde{A}_p^T(\hat{V}(t)) P \tilde{x}_p \\
&\quad + \tilde{x}_p^T P \tilde{A}_p(\hat{V}(t)) \tilde{x}_p \\
&= - \tilde{x}_p^T Q \tilde{x}_p + 2 \tilde{x}_p^T \tilde{A}_p^T(\hat{V}(t)) P \tilde{x}_p
\end{aligned} \tag{5.20}$$

Hence,

$\dot{V}(\tilde{x}_p) < 0$ if

$$\tilde{x}_p^T Q \tilde{x}_p > 2 \tilde{x}_p^T \tilde{A}_p^T(\hat{V}(t)) P \tilde{x}_p \tag{5.21}$$

Therefore, from the Lemma 5.1 and also

$$\tilde{x}_p^T \tilde{A}_p(\hat{V}(t)) P \tilde{x}_p \leq ||\tilde{A}_p(\hat{V}(t))|| \; ||P|| \; ||\tilde{x}_p||^2 \tag{5.22}$$

it follows that the inequality (5.21) is satisfied if

$$||\tilde{A}_p(\hat{V}(t))|| < \frac{\lambda_{min}(Q)}{2\lambda_{max}(P)}$$

Note that $||P|| = \lambda_{max}(P)$.

Physically, this theorem states that if the bound of the unknown perturbed plant matrix $\tilde{A}_p(\hat{V}(t))$ due to the electrical potentials remains within the certain threshold value characterizing the closed-loop system in the absence of the voltage, then the system (5.12) is stable. However, this theorem can be modified once the perturbed plant matrix is defined as a distributed ER fluid actuator, and the characteristics of the ER fluid actuator are identified through the experimental observation. Later on in this section, a modified theorem will be established for the stability of the system featuring the proposed hybrid controller which consists of the output feedback controller employed in the previous chapter and a pseudo-state feedback controller associated with the ER fluid actuator.

The philosophy of developing the proposed hybrid control methodology for the system given by the equation (5.12) is motivated by the complementary experimental program which is focussed on the development of an empirical actuator dynamics associated with the uniformly distributed ER fluid actuator. The empirical actuator dynamics should be expressed as an explicit function of the applied voltage $\hat{V}(t)$ in order to formulate an appropriate control form. This can be accomplished by establishing the relationship between the stiffness and energy dissipation change and the applied electric field through the

experimental test. In order to obtain this relationship, frequency response was measured at various voltage levels.

Figure 5.6 presents the measured frequency response of the smart ER arm without payload at two different discrete voltage levels. This frequency response was obtained by applying random torques (white noise) input from the dynamic analyzer to the servo-drive, and measuring output signals from the strain gage mounted at the root of the smart ER arm. In Figure 5.6, the peaks correspond to the clamped-mode natural frequency having the maximum strain energy at the root of the arm, and the valleys represent the pinned-mode natural frequency having the minimum strain energy. It is noted that this phenomenon is opposite to the case shown in Figure 3.15. It is clearly evident from Figure 5.6 that the natural frequencies of the arm, and also the arm's energy dissipation characteristics are both voltage dependent.

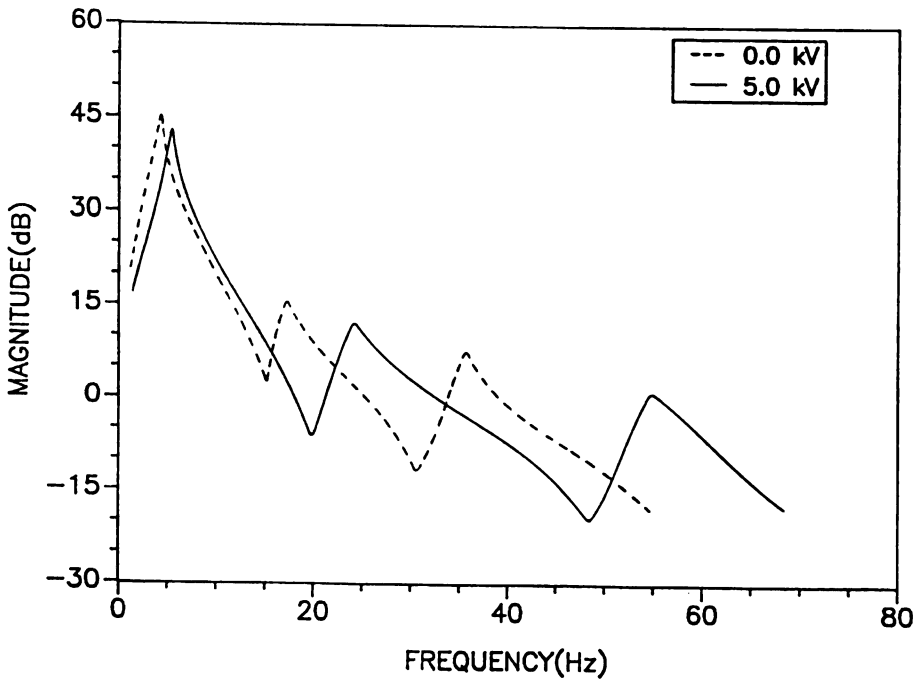


Figure 5.6 Measured Frequency Response of the Smart ER Arm without Payload

The increment of the natural frequency and the damping ratio of each mode at prescribed voltages relative to the no voltage state was obtained from Figure 5.6. And the distilled results suggest that the empirical actuator dynamics is governed by the following linear relationships of the form

$$\frac{\zeta_i(\hat{V}(t))\omega_i(\hat{V}(t))}{\zeta_i\,\omega_i} = \alpha_{1i}\hat{V}(t)$$

$$\frac{\omega_i^2(\hat{V}(t))}{\omega_i^2} = \alpha_{2i}\hat{V}(t) \qquad (5.23)$$

where α_{1i} and α_{2i} are experimentally determined constants which characterize the increment of the damping ratio and natural frequency of each mode as an explicit function of applied voltage $\hat{V}(t)$. Figure 5.7 presents this governing relationship for the first two flexible modes. In Figure 5.7, symbols are the measured values and the lines are the least-square error curves. From the slope of these curves, α_{11}=0.418, α_{12}=0.656, α_{21} = 0.303 and α_{22}= 0.666 were distilled. It should be noted that the governing relationship described by the equation (5.23) may be modified once a viable microstructural-level model of the system is developed. This microstructural-level model would include the different chemical composition of the ER fluids, the interface conditions between the solid and fluid layers, the conductivity of the face materials (electrodes), and also the dielectric properties of the insulation between the electrodes. The integration of all this information may provide a viable model for the distributed ER fluid actuator dynamics, which is a function of the electric field intensity. And also, the precise investigation on

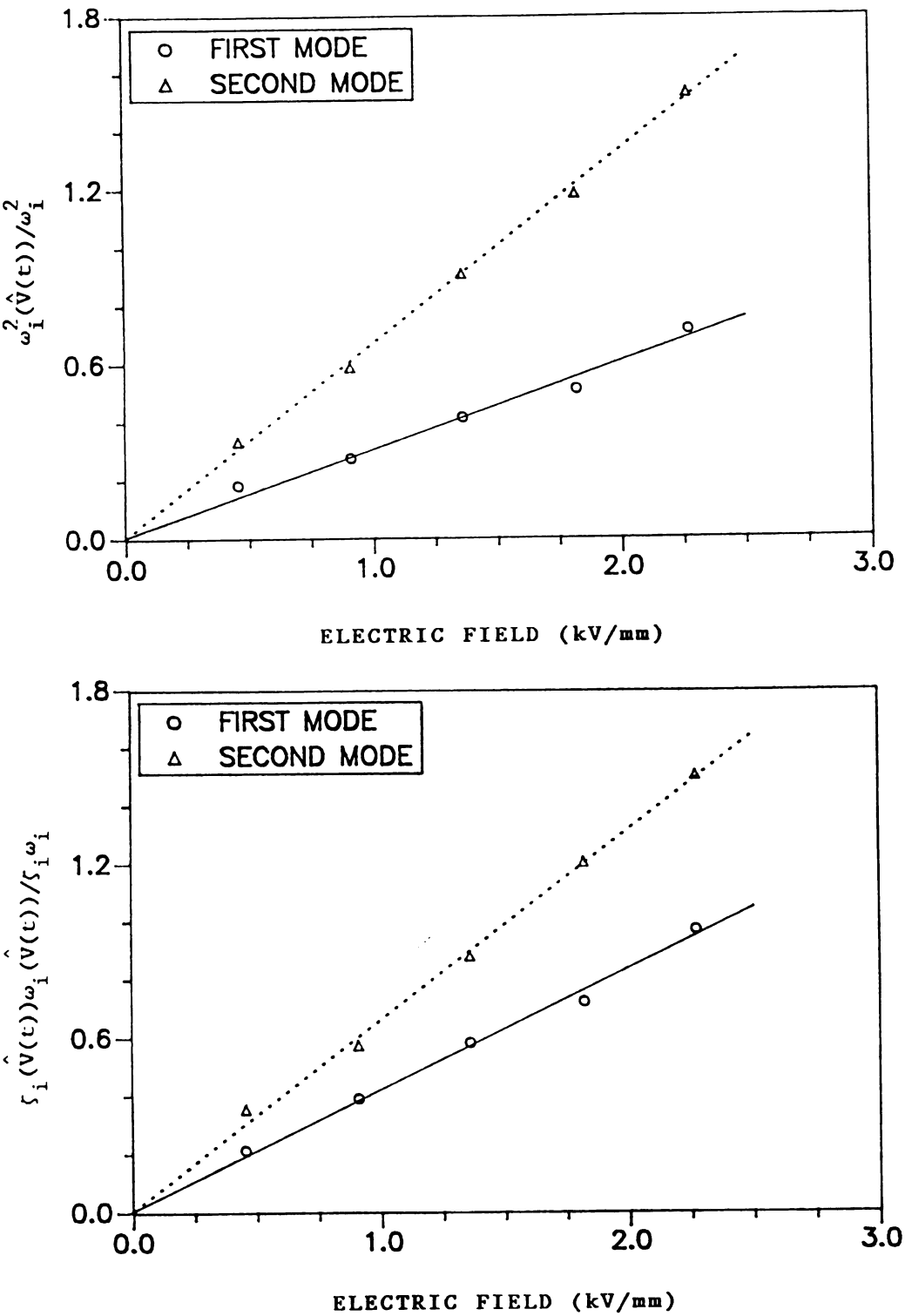


Figure 5.7 Governing Characteristics of the Employed Electro-Rheological Fluid Actuator

the ER effect to the different excitation amplitude will improve the accuracy of the dynamics.

Now with the equation (5.23), the system equation (5.12) may be reformulated as follows.

$$\begin{aligned} \dot{\tilde{x}}_p &= \tilde{A}_p \tilde{x}_p + \tilde{B}_p \tilde{u} + \tilde{K}_p \tilde{V}(t) \\ \tilde{y}_p &= \tilde{C}_p \tilde{x}_p \end{aligned} \tag{5.24}$$

where

$$\tilde{K}_p = \begin{bmatrix} 0 & 0 & 0 & 0 & \cdots & 0 & 0 \\ 0 & 0 & 0 & 0 & \cdots & 0 & 0 \\ 0 & 0 & 0 & 0 & \cdots & 0 & 0 \\ 0 & 0 & -k_{21} & -k_{11} & \cdots & 0 & 0 \\ \vdots & \vdots & \vdots & \vdots & \cdots & \vdots & \vdots \\ 0 & 0 & 0 & 0 & \cdots & 0 & 0 \\ 0 & 0 & 0 & 0 & \cdots & -k_{2p} & -k_{1p} \end{bmatrix} \tag{5.25}$$

$$k_{11} = 2\alpha_{11}\zeta_1\omega_1, \qquad k_{1p} = 2\alpha_{1p}\zeta_p\omega_p$$

$$k_{21} = \alpha_{21}\omega_1^2, \qquad k_{2p} = \alpha_{2p}\omega_p^2$$

$$\tilde{V}(t) = \tilde{x}_p \hat{V}(t)$$

Clearly the equation (5.24) admits a hybrid control featuring the output feedback control $\tilde{u}$ and the form of state feedback control $\tilde{V}(t)$. Even though external input voltage is imposed to an ER fluid domain in a fashion of the open-loop control, the distributed ER fluid actuator possesses a characteristic aspect showing the pseudo-state feedback controller which produces the associated pseudo-control force in a fashion of the closed-loop control. In fact, this pseudo-control force accounts for the increased stiffness and damping properties of the structure due to the imposed external voltage. Figure 5.8 presents a

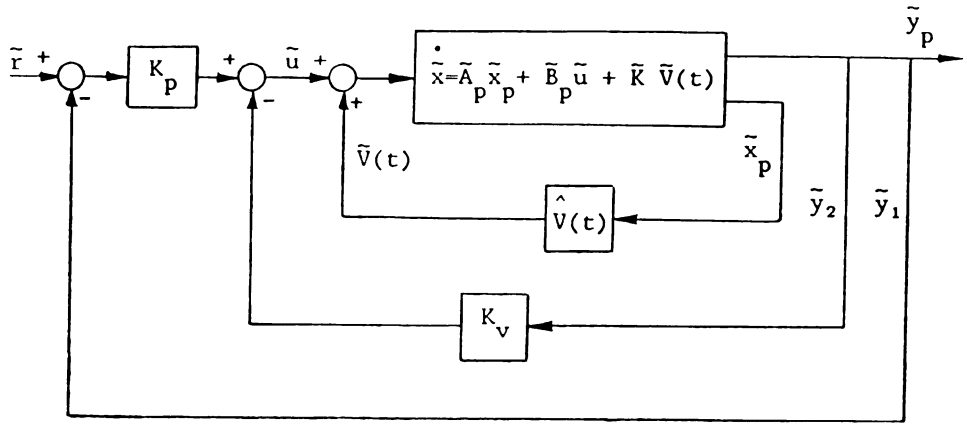


Figure 5.8 Block-Diagram of the Hybrid Control System

block-diagram of the proposed hybrid control system. In Figure 5.8, $\tilde{y}_1$ represents angular position output, $\tilde{y}_2$ denotes angular velocity output, $\tilde{r}$ stands for the commanded angular position and $\hat{V}(t)$ denotes applied external input voltage. Hence, the closed poles λ_d of the system is obtained from the following characteristics equation

$$\det(A_d - \lambda_d I) = 0 \tag{5.26}$$

where $A_d = (\tilde{A}_p + \tilde{B}_p\tilde{K}\,\tilde{C}_p + \tilde{K}_p\hat{V}(t))$

$$\tilde{K} = [-K_p \quad -K_v]$$

Now, as mentioned earlier in this section, the Theorem 5.1 can be modified for the proposed hybrid control system as followings.

Theorem 5.2 : If the position gain K_p and the velocity gain K_v are chosen such that the closed-loop system (5.24) is asymptotically stable in the absence of electrical potentials, the closed-loop system is asymptotically stable for any positive input voltage $\hat{V}(t)$ which does not exceed the limit considered in this experimental investigation (see Figure 5.7).

Sketch of the Proof : Let $\tilde{\lambda}$ be the eigenvalues of the original plant matrix $\tilde{A}_p$ in equation (5.24). Then, $Re(\tilde{\lambda}_i) \leq 0$ for all i. The equality holds for the rigid-body mode. Since experimental observations indicate that the natural frequency (pinned-mode and clamped-mode) and damping ratio of each mode increase as the input voltage increases [41,56], the eigenvalues $\hat{\lambda}$ of the matrix $(\tilde{A}_p + \tilde{K}_p \hat{V}(t))$ becomes $Re(\hat{\lambda}_i) = Re(\tilde{\lambda}_i) + \gamma_i(t) \leq 0$ for all i, and $\gamma_i(t) \leq 0$. The variable $\gamma_i(t)$ may be defined as the degree of the stability and it is absolutely dependent upon the ER actuator characteristics which are given by the matrix $\tilde{K}_p$. Hence, it can be shown that with the feedback gains of K_p and K_v the closed-loop system (5.24) is asymptotically stable for any positive input voltage $\hat{V}(t)$. It is noted that since the rigid-body mode is not affected by the input voltage, the corresponding $\gamma_i(t)=0$.

Therefore, once the output feedback gains of K_p and K_v are determined in a same manner mentioned in Section 4.2, the external input voltage

$\hat{V}(t)$ can be chosen based on the degree of the stability, i.e., $\gamma_i(t)$. However, the choice of the $\gamma_i(t)$ is limited by the maximum applicable electric field which can be imposed on the smart ER arm without causing any insulation problems. The input voltage can be constant during whole commanded motion or can be bang-off-bang type as shown in Figure 5.9. This bang-off-bang type voltage can be easily implemented in practice since the response time of the ER fluids is typically in the order of milliseconds, and a direct current (DC) pulse square input voltage can be readily imposed on the ER fluid domains of the arm [140]. With this type of the input voltage, the system given by the equation (5.24) becomes

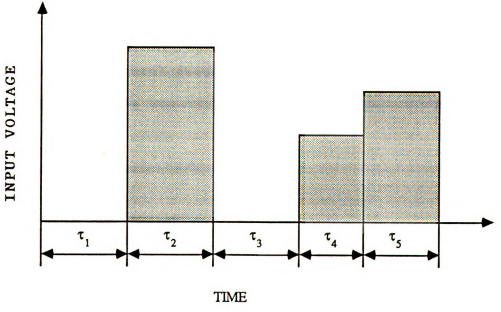


Figure 5.9 Bang-off-Bang Type Input Voltage

$$
\begin{cases}
\dot{\tilde{x}}_p = \tilde{A}_p \tilde{x}_p + \tilde{B}_p \tilde{u} + \tilde{K}_p \tilde{V}_1(t) \\
\tilde{y}_p = \tilde{C}_p \tilde{x}_p
\end{cases}
\qquad \text{for } 0 \le t \le \tau_1
$$

$$
\vdots \qquad\qquad \vdots
$$

$$
\begin{cases}
\dot{\tilde{x}}_p = \tilde{A}_p \tilde{x}_p + \tilde{B}_p \tilde{u} + \tilde{K}_p \tilde{V}_m(t) \\
\tilde{y}_p = \tilde{C}_p \tilde{x}_p
\end{cases}
\qquad \text{for } \tau_{m-1} \le t \le \tau_m
\tag{5.27}
$$

Clearly the closed-loop poles of the system during the motion vary depending upon a certain period of τ_i. Hence, the system can respond at any time to the desired requirements of the system performance by simply changing the input voltage. This is one of the salient features of the proposed hybrid control methodology. The robustness of this hybrid control system to the disturbance which has a forcing frequency close to the clamped-mode natural frequency of the robot arm is also to be expected. This will be investigated in the subsequent section.

5.5 Experimental Implementation

5.5.1 Apparatus and Instrumentation

Most of experimental apparatus and procedures for the implementation of the hybrid controller are same as those described in Chapter III. Hence, only experimental procedures for the measurement of frequency response of the cantilevered beam shown in Figure 5.5, the application procedure of the external input voltage (pseudo-control force) and the

fabrication procedure of the smart ER arm will be presented in this section.

Figure 5.10 presents a schematic diagram of the experimental cantilevered beam shown in Figure 5.4 and the associated instrumentation for monitoring and recording the frequency response. The random external

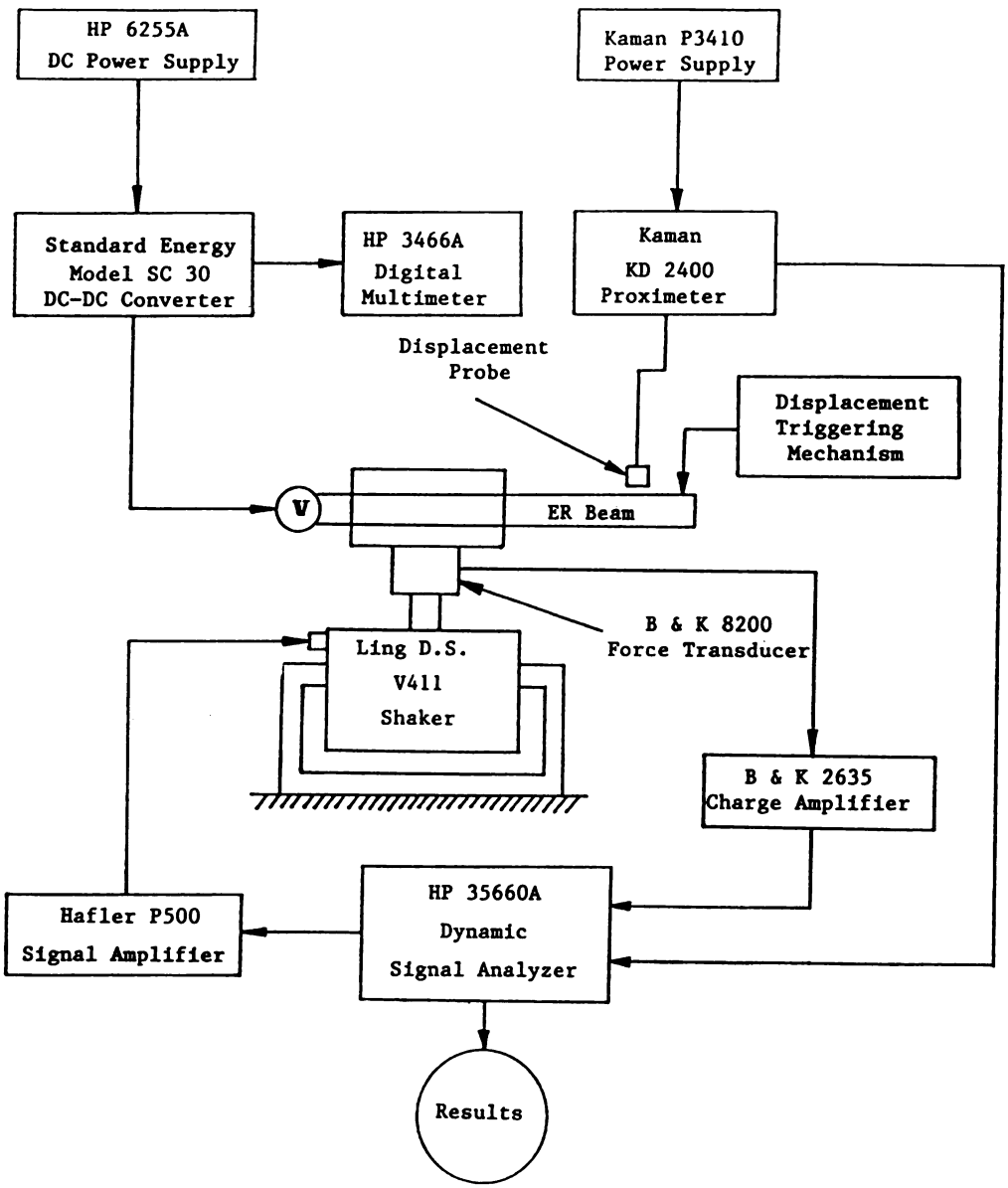


Figure 5.10 Experimental Set-Up for the Frequency Response Measurement of the Smart Cantilevered Beam

forcing function (white noise) was applied from a dynamic signal analyzer, model 35660A, manufactured by Hewlett-Packard, to the structure. This forcing signal was passed through an amplifier, model P500, manufactured by Hafler and then employed to energize a shaker, model V411, manufactured by Ling Dynamic Systems Limited. The amplitude of this excitation was kept below a certain level to reduce the influence of nonlinearity of the ER fluids and other parasitic effects such as air damping, cable drag,etc. A force transducer, type 8100, manufactured by Bruel and Kjaer was mounted on the head of the shaker in order to determine the input force to the beam, whereas the displacement probe was positioned at several locations along the beam in order to measure the output signal which was monitored by a non-contacting displacement transducer, model KD2400, manufactured by Kaman Corporation. Then these two signals were processed by the signal analyzer to obtain the frequency response (magnitude and phase) corresponding to each location.

In order to reduce the influence of the noise and get more consistent results , an average of 40 times measurements was used. Figure 5.11 presents one of the frequency responses of the cantilevered beam at two discrete voltage levels using the displacement probe mounted on the tip of the beam. The phase-change in the ER fluid was initiated by energizing the upper and lower faces of the beam specimen. The various voltages were generated by a Hewlett-Packard dc power supply, model 6255A, and amplified through a dc-to-dc converter, model SC30, manufactured by Standard Energy. The desired input voltage was measured using a dc high voltage probe, model 3411A and digital multimeter, model 3566A which are both manufactured by Hewlett-Packard.

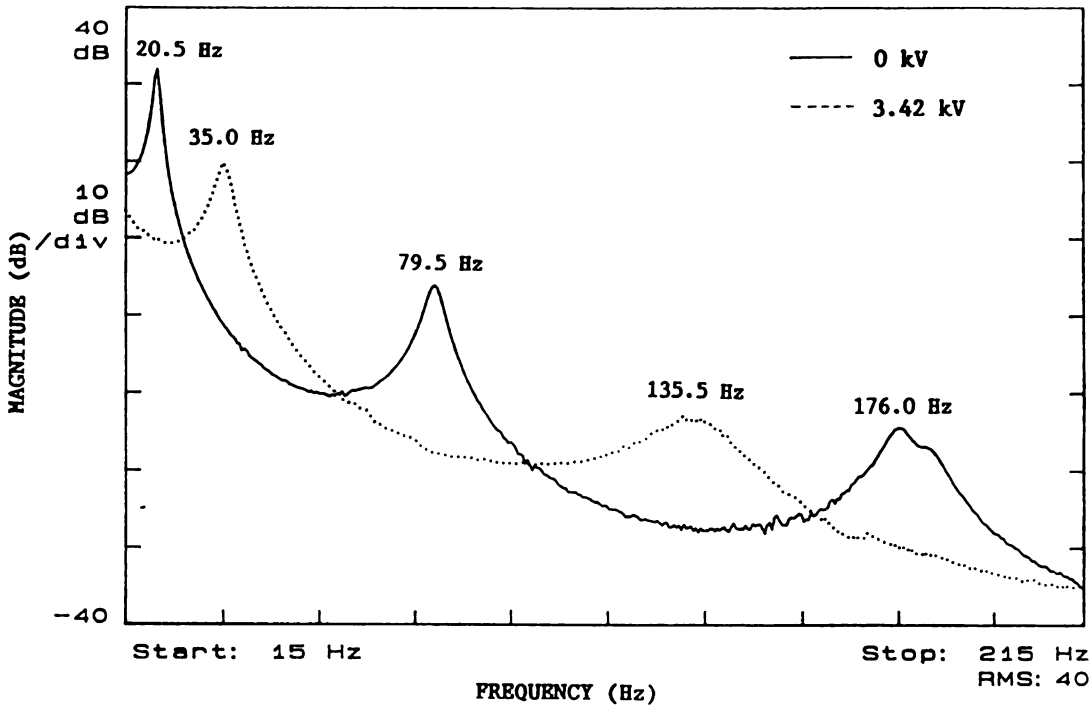


Figure 5.11 Frequency Response of the Smart Cantilevered Beam

The detail-design features of the smart ER arm are schematically presented in Figure 5.12, and the salient features of the fabrication process for the smart robot arm incorporating the ER fluid are highlighted in the flow diagram presented in Figure 5.13. RTV silicone rubber adhesive was selected as an insulator in order to provide both excellent bonding between the electrodes and to also furnish a high dielectric constant. The arm was fabricated by employing an appropriate die to generate the hollow section and also to control both the thickness of the ER fluid layer and the insulator . The die was subsequently removed after partial curing of the sealant, and the arm was maintained at room temperature for 24 hours in order to achieve the full strength of the silicone rubber adhesive. During this time an air blower,

manufactured by Air Control Installations, Ltd., U.K., was employed to remove the acid from the silicone rubber by exposing the arm to an air stream for two hours. After curing at room temperature, the arm subsequently cured at 65°C for 2 hours in a hygrothermal chamber, model TH27S, manufactured by BMA Inc. The arm was then exposed to room temperature for 24 hours before checking the dielectric behavior. After checking the dielectricity of the arm, an acrylic sheet was employed at one end where it needs to be inserted into the hub. The hollow arm, which featured a cavity of uniform rectangular cross-section, was filled with

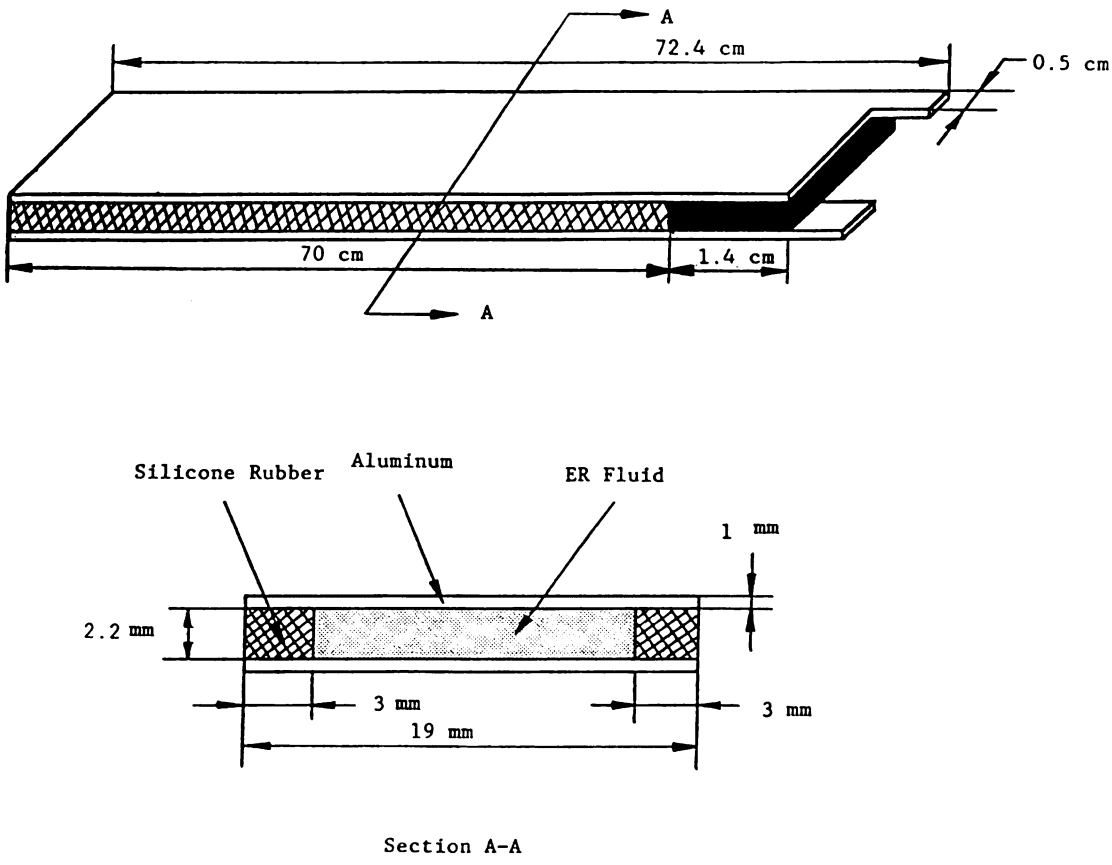


Figure 5.12 Schematic Diagram of the Smart ER Arm

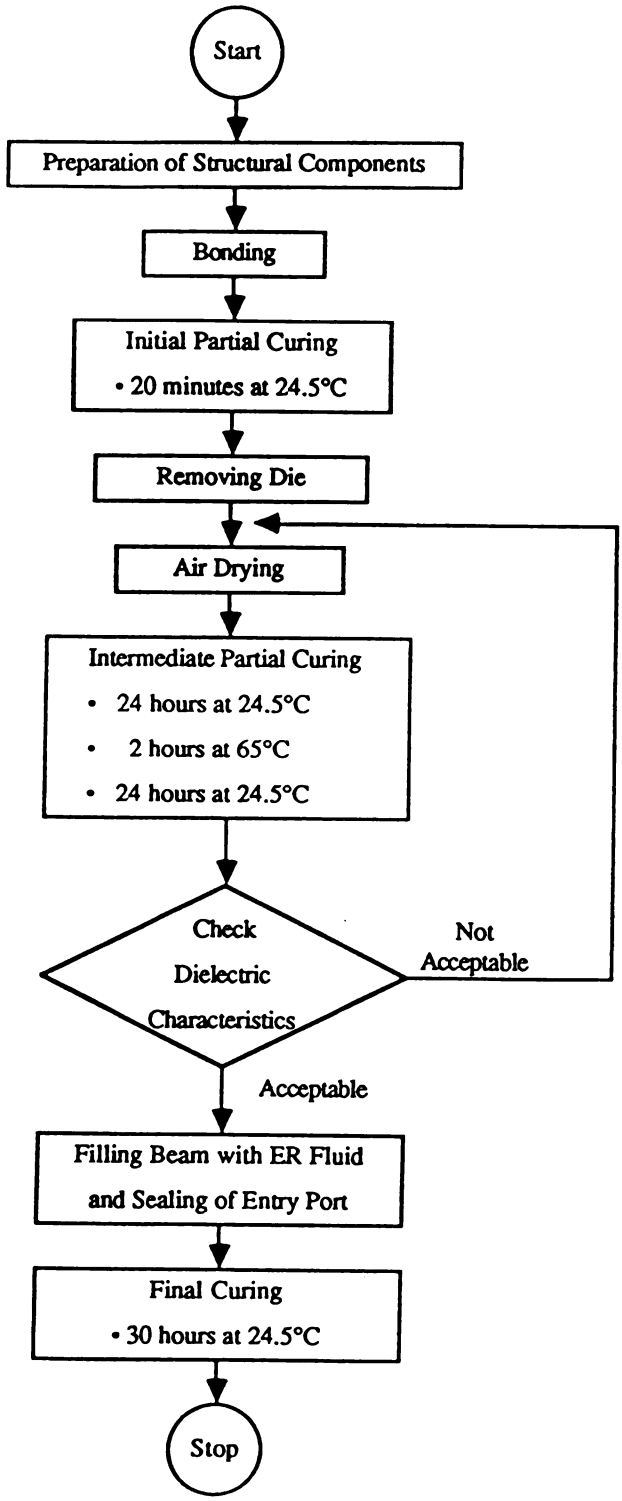


Figure 5.13 Flow Diagram for Fabrication Procedures of the Smart ER Arm

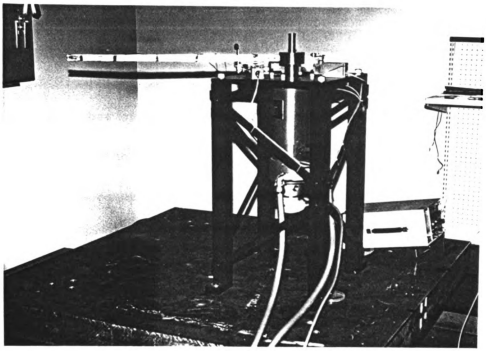


Figure 5.14 Photograph of the Smart ER Arm

the silicone-oil-based ER fluid. The ER fluid volume fraction to the total volume was 36 percent. Finally a Measurements Group strain gages, type WD-DY-250BG-350 were mounted at the root of the arm. It is noted that the fabrication procedure of the cantilevered beam shown in Figure 5.4 is same as that for the smart ER arm. Figure 5.14 presents a photograph of the smart ER arm clamped on the rigid hub.

From the measured frequency response shown in Figure 5.6, system model parameters such as natural frequencies and damping ratios were identified. The modal slope coefficient $d\phi_i(o)/dx$ was determined as followings. The open-loop transfer function $G_o(s)$ in the equation (4.2) is also given by [127]

$$G_o(s) = \frac{1}{I_T s^2} \prod_{i=1}^{p} \frac{(s^2/\Omega_i^2 + 2\zeta_i s/\Omega_i + 1)}{(s^2/\omega_i^2 + 2\zeta_i s/\omega_i + 1)} \tag{5.28}$$

where p is the number of primary mode, Ω_i is the ith clamped-mode natural frequency and ω_i is the ith pinned-mode natural frequency. On the other hand, the $G_o(s)$ in equation (4.2) can be expressed as

$$G_o(s) = \frac{1}{I_T s^2} + \frac{1}{I_T} \sum_{i=1}^{p} (d\phi_i(o)/dx)^2 (1/(s^2+2\zeta_i\omega_i s+\omega_i^2)) \tag{5.29}$$

Therefore, the modal slope coefficient $d\phi(o)/dx$ can be determined by equating equations (5.28) and (5.29). Table 5.2 presents the measured

Table 5.2 Measured System Model Parameters of the Smart Robotic Arm

Parameters	Values
ω_1 (Hz)	15.2
ω_2 (Hz)	30.5
Ω_1 (Hz)	4.3
Ω_2 (Hz)	17.1
ζ_1	0.0526
ζ_2	0.0426
$\frac{d\phi_1(o)}{dx}$	3.12
$\frac{d\phi_2(o)}{dx}$	5.38

system model parameters of the smart ER arm in the absence of the electrical field. In this investigation, rigid-body mode and first two flexible modes were considered as the primary modes.

5.5.2 Results and Discussions

Figure 5.15 presents the measured step responses to a commanded step angular position of 7.2 degree with the compensator zero Z_c=-2. The feedback gains of K_p=0.5 and K_v=0.25 were employed. The external input voltage (pseudo-control force) of 2.0 kV/mm was employed continuously throughout the motion to the ER fluid domain. It is clear from this figure that the responses with and without input voltage are basically same except the tip deflection response of the arm. This aspect may be expected since the mass of the robotic arm remains same regardless of the input voltage, and the pseudo-control force does not affect the rigid-body motion. The amplitude of the tip deflection of the robot arm in the absence of the electric field was reduced up to 35 percent by employing the input voltage of 2.0 kV/mm. It is also observed from this response that the settling-time (decaying time) is about 1.3 second with the input voltage, while it is about 1.6 second without the input voltage. This can be interpreted as the enhancement of the positional accuracy of the robotic system. No second flexible mode effect to the total tip deflection is observed for both cases. The corresponding simulated results are presented in Figure 5.16 which compare very favorably with the measured results shown in Figure 5.15.

For the second comparison of control performances with and without the input voltage, the compensator zero Z_{co}=-5.6 was chosen. Figure 5.17

shows the measured step responses with feedback gains of K_p=1.4 and K_v=0.25. From the angular position response, the rise time was obtained by 0.42 second for both cases, and the maximum overshoot was about 0.89 degree without the input voltage and 0.93 degree with the input voltage. This is basically same for both cases, and the input torque is also same for both cases as expected. The tip deflection without the input voltage was reduced up to 20 percent by employing the input voltage for whole duration of the response. With these feedback gains, it is also observed jittering phenomenon as in the case of the aluminum or composite arm (see Figure 4.11) due to the hysteretic joint friction of the motor. Figure 5.18 presents the simulated step responses corresponding to the measured results shown in Figure 5.17.

In order to implement the bang-off-bang type input voltage shown in Figure 5.9, on-off switched response was obtained by imposing a non-zero input voltage at certain time. Figure 5.19 presents the measured step responses with the same output feedback gains used for the results in Figure 5.17. The input voltage was imposed from the beginning up to the peak time (0.61 second) of the angular position response in Figure 5.17, and was released throughout the response. It is observed that the tip deflection without the input voltage was reduced up to same amount as achieved in Figure 5.17. This experimental result illustrates the speed with which the smart ER arm can respond to the imposed input voltage (pseudo-control force) in order to synthesize the desired vibrational response of the flexible robot arm. It is noted that the determination of the best switching time depends on various parameters such as rise time, peak time and settling-time, and also depends upon the system performance requirements such as minimum time or minimum effort problem.

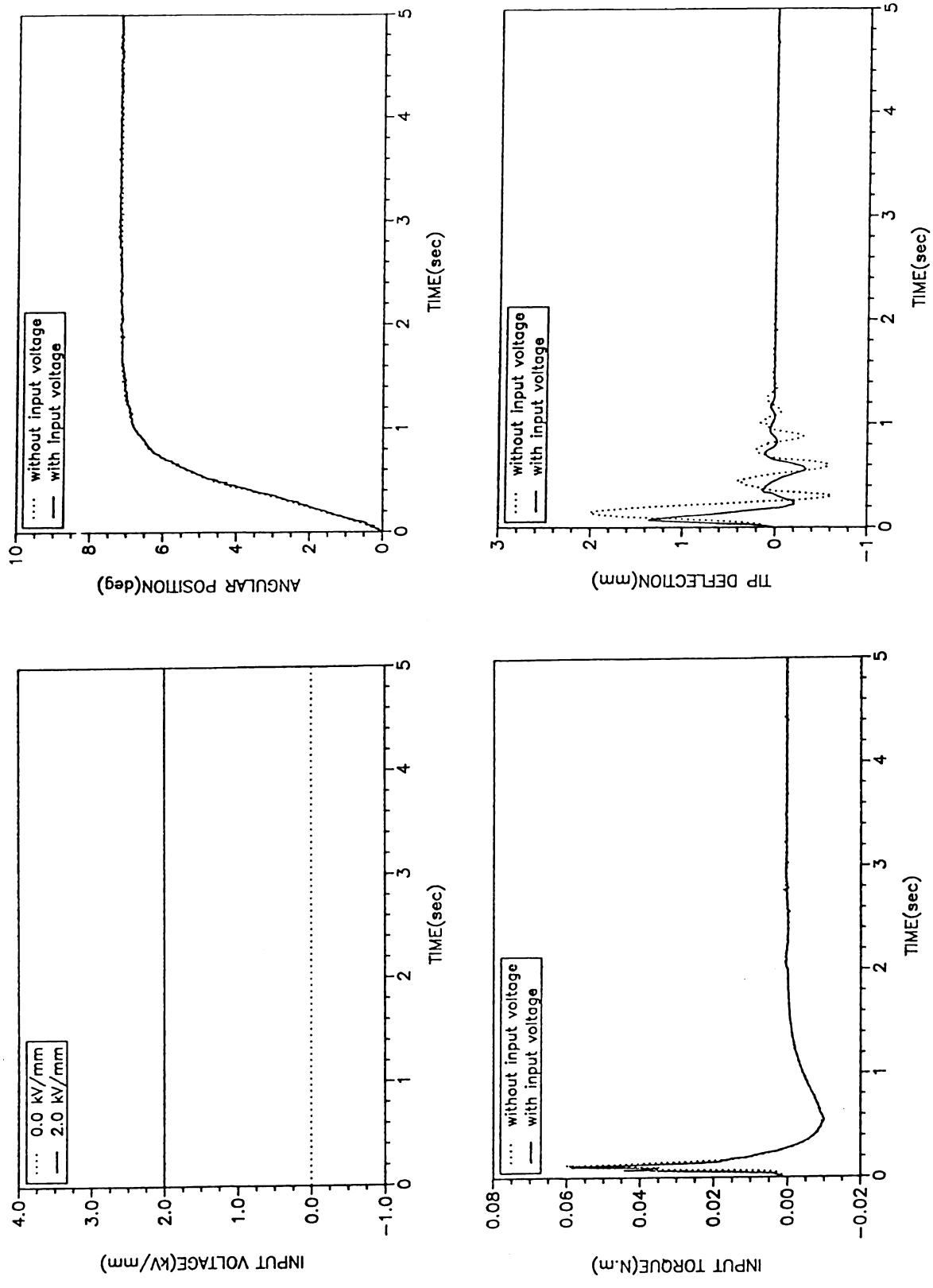


Figure 5.15 Measured Step Responses with Feedback Gains of K_p = 0.5 and K_v = 0.25.

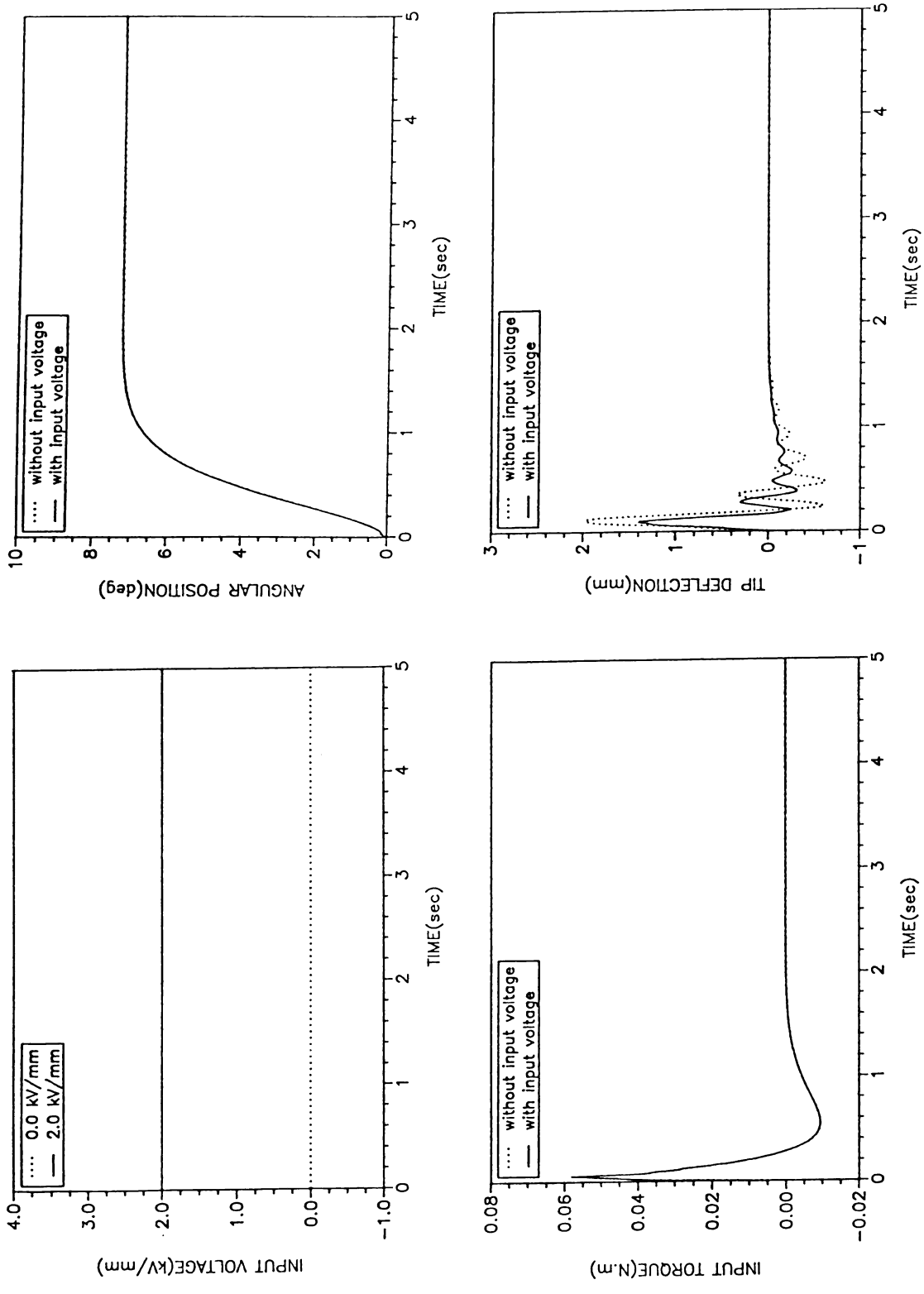


Figure 5.16 Simulated Step Responses with Feedback Gains of K_p = 0.5 and K_v = 0.25.

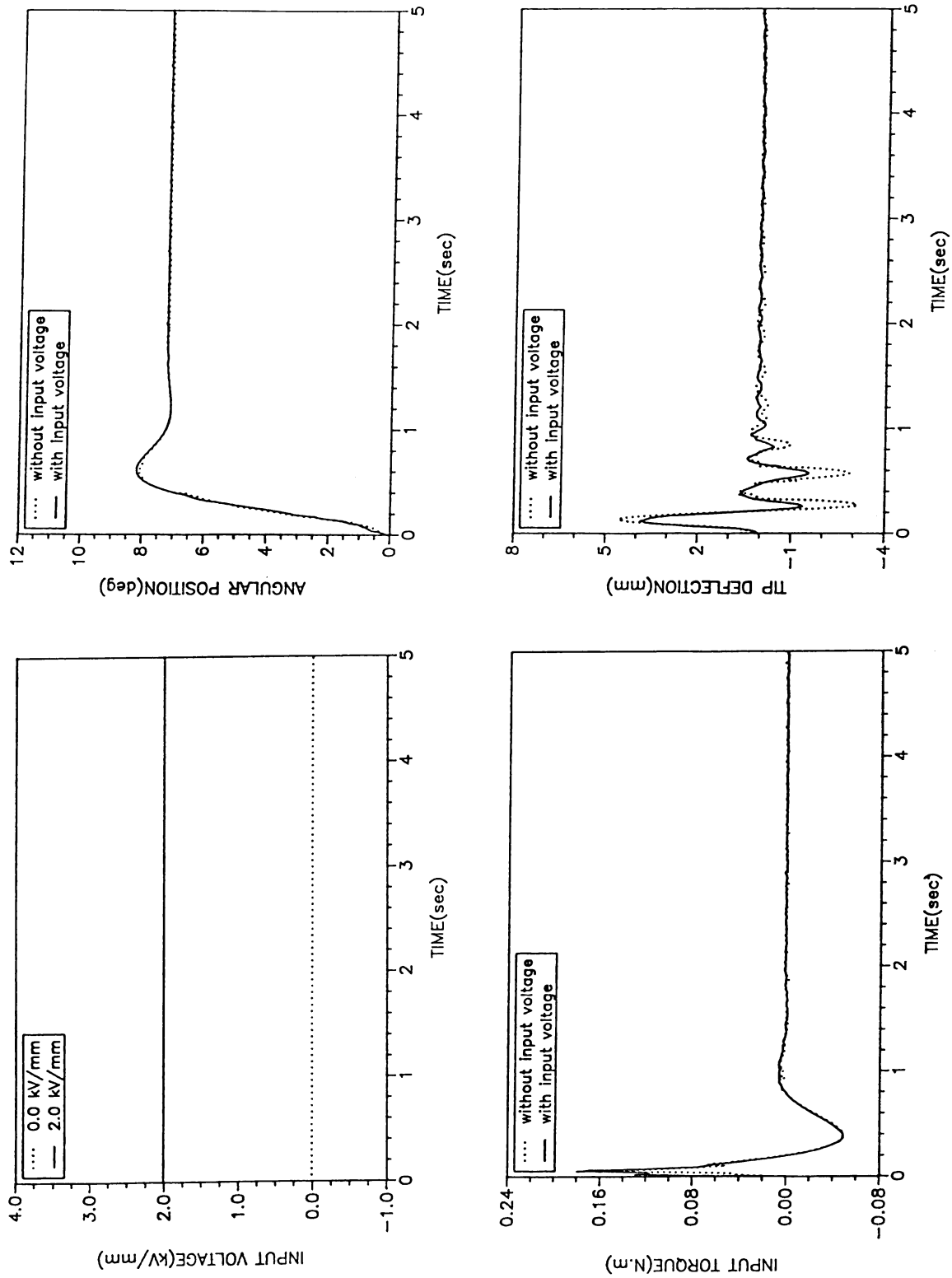


Figure 5.17 Measured Step Responses with Feedback Gains of $K_p = 1.4$ and $K_v = 0.25$.

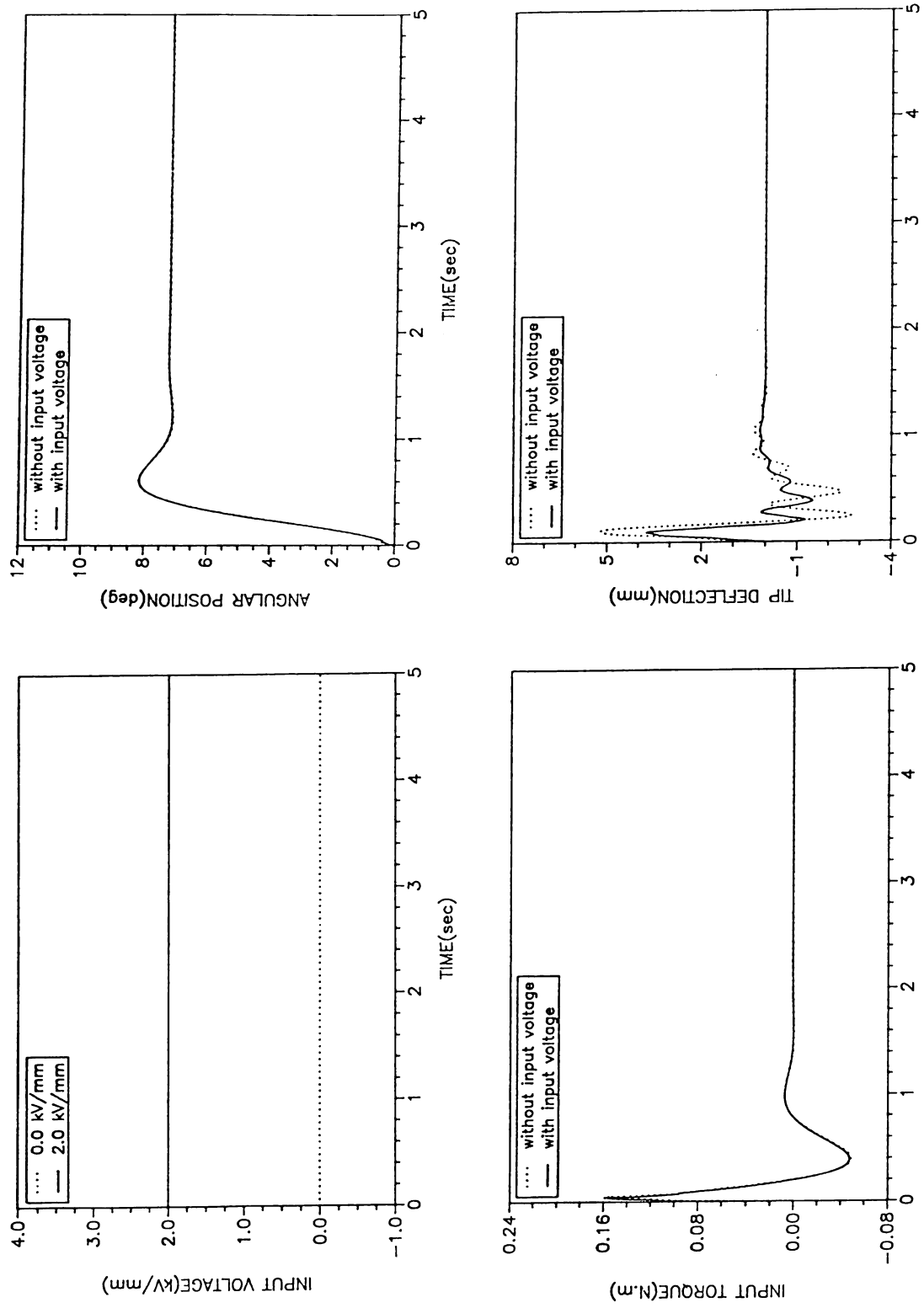


Figure 5.18 Simulated Step Responses with Feedback Gains of K_p = 1.4 and K_v = 0.25.

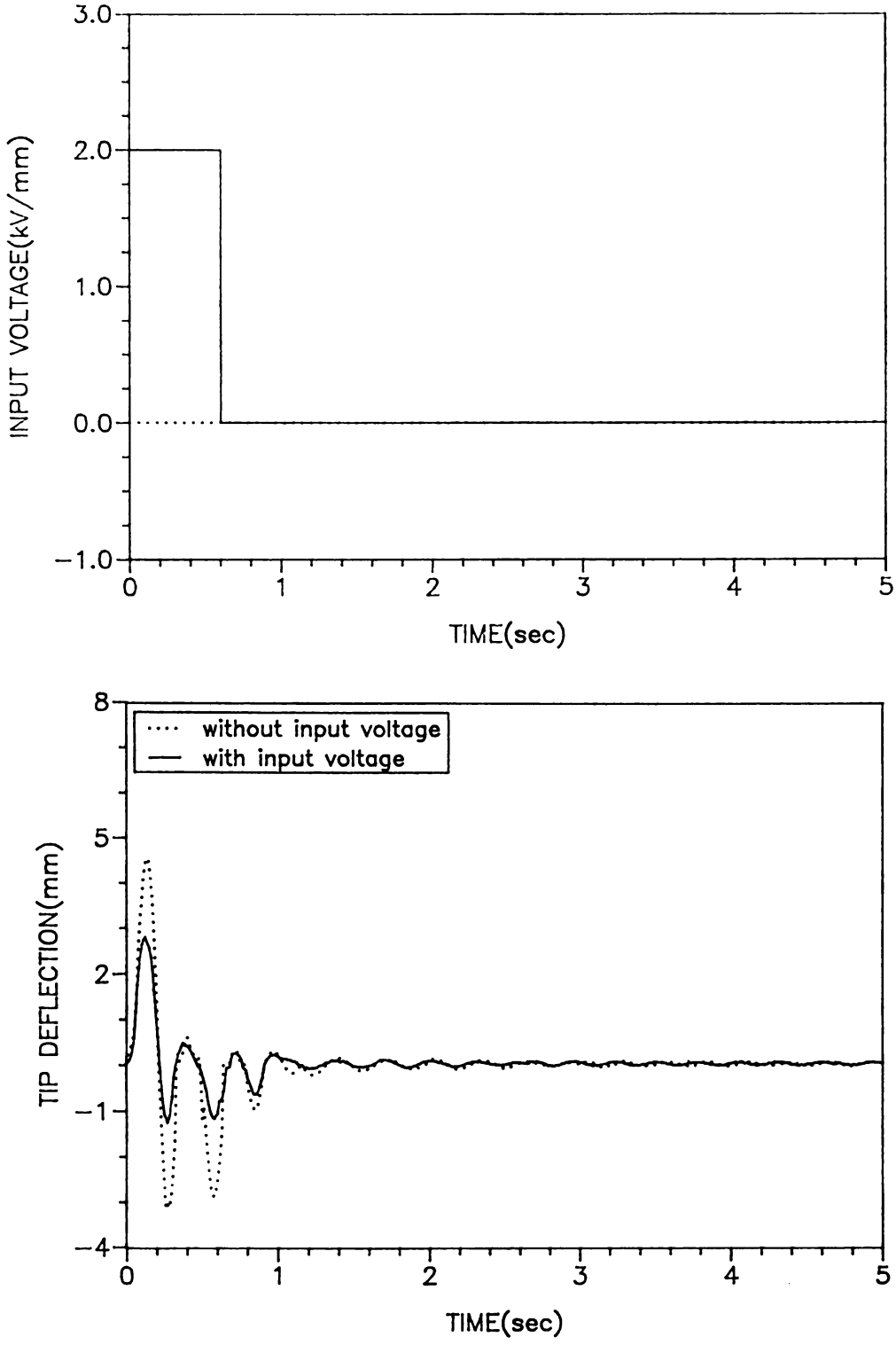


Figure 5.19 Measured Step Responses with Bang-off-Bang Type Input Voltage. K_p=1.4, K_v=0.25

The proposed hybrid controller gets its distinguished credit when the system is subjected to a disturbance which has a forcing frequency close to the clamped-mode natural frequency of the arm. In other words, the robustness of the employed PD type output feedback controller to the imposed disturbance can be improved by employing the pseudo-control force which accounts for the increased stiffness and energy dissipation of the robot arm. With the introduced disturbance, the system given by the equation (5.24) becomes

$$\begin{aligned} \dot{\tilde{x}}_p &= \tilde{A}_p \tilde{x}_p + \tilde{B}_p \tilde{u} + \tilde{B}_p \tilde{d}(t) + \tilde{K}_p \tilde{V}(t) \\ \tilde{y}_p &= \tilde{C}_p \tilde{x}_p \end{aligned} \tag{5.30}$$

where $\tilde{d}(t)$ is the imposed disturbance. This disturbance is supplied from the function generator, model 275, manufactured by Wavetek, to the servo-drive.

Figure 5.20 presents the measured step responses to a commanded step angular position of 7.2 degree with the disturbance $\tilde{d}(t)=0.08 \sin f_1 t$ N•m where f_1 = 4.1 Hz. The feedback gains used for the results in Figure 5.15 were employed and the disturbance was applied from the beginning the commanded motion. It is noted that the forcing frequency f_1=4.1 Hz is almost same as the fundamental clamped-mode natural frequency Ω_1 = 4.3 Hz in the absence of the electrical field as shown in Table 5.2. AS expected, the response of the hub angular position and tip deflection are oscillated resulting in near resonance phenomenon of the system. However, the amplitude of the oscillated tip deflection was reduced by 40 percent by employing the external input voltage. The reduction of this amplitude

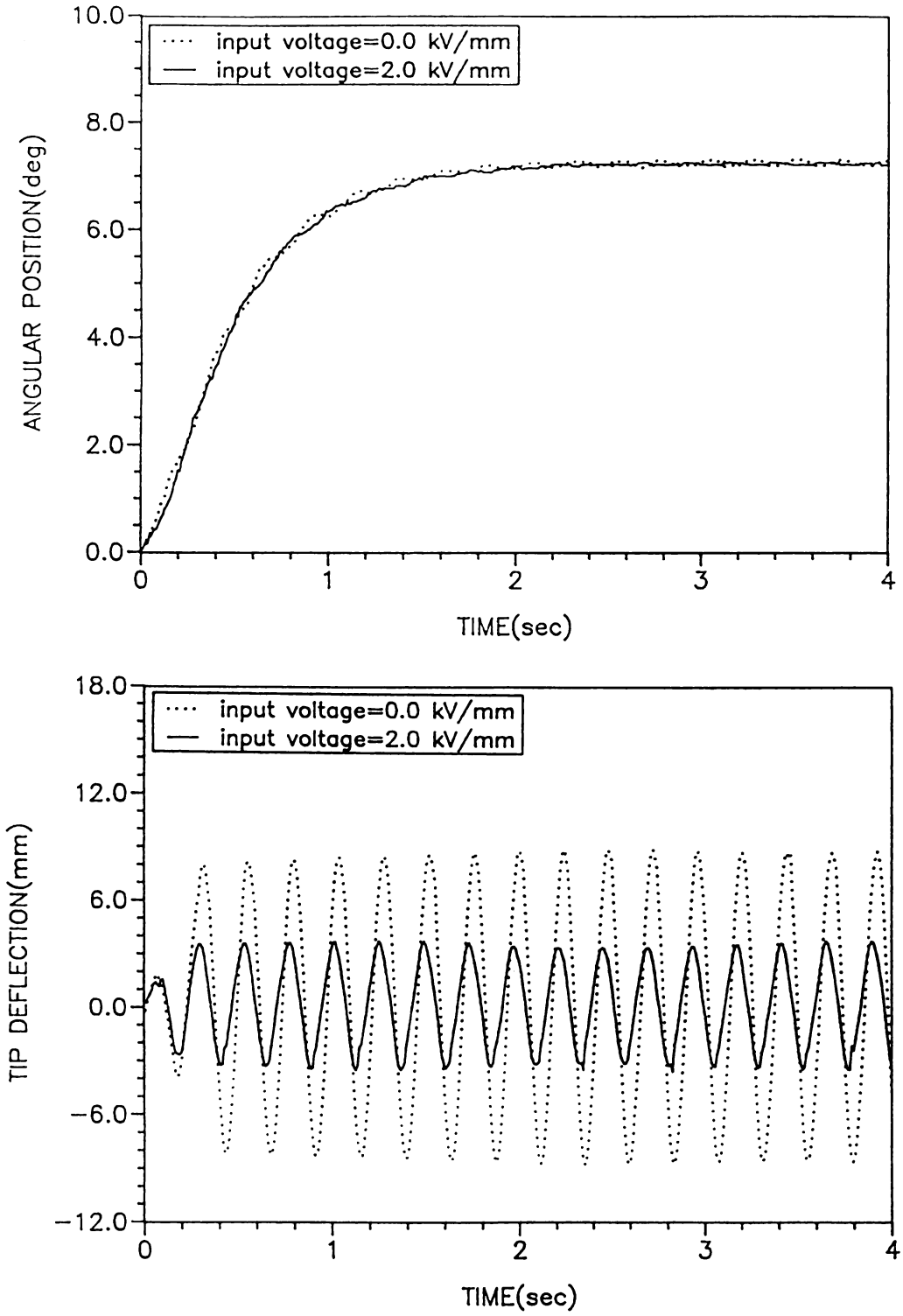


Figure 5.20 Measured Step Responses with the Disturbance.
K_p= 0.5, K_v= 0.25, $\tilde{d}(t)$=0.08 sin(4.1 Hz)t

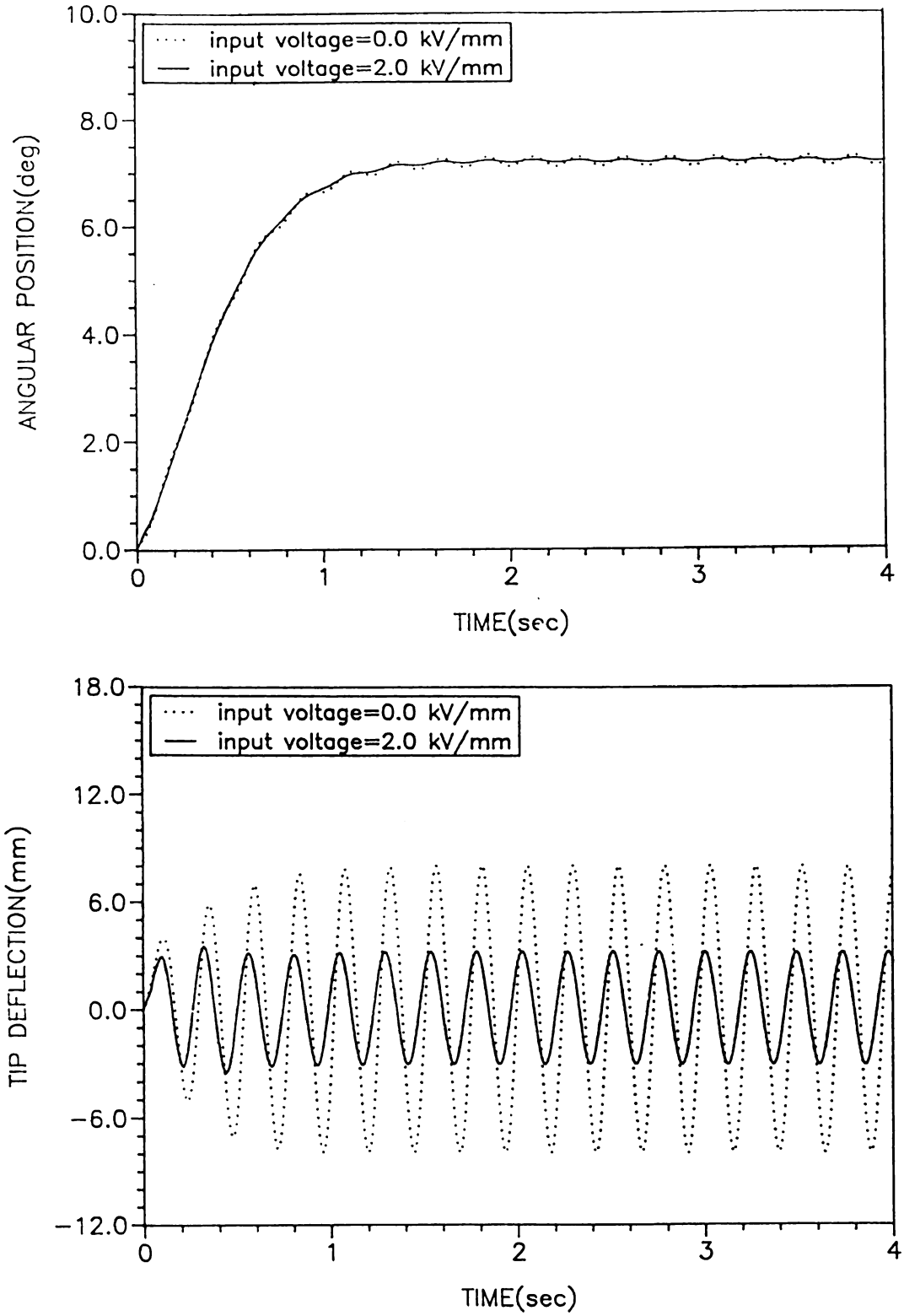


Figure 5.21 Simulated Step Responses with the Disturbance.
K_p= 0.5, K_v= 0.25, $\tilde{d}(t)$=0.08 sin(4.1 Hz)t

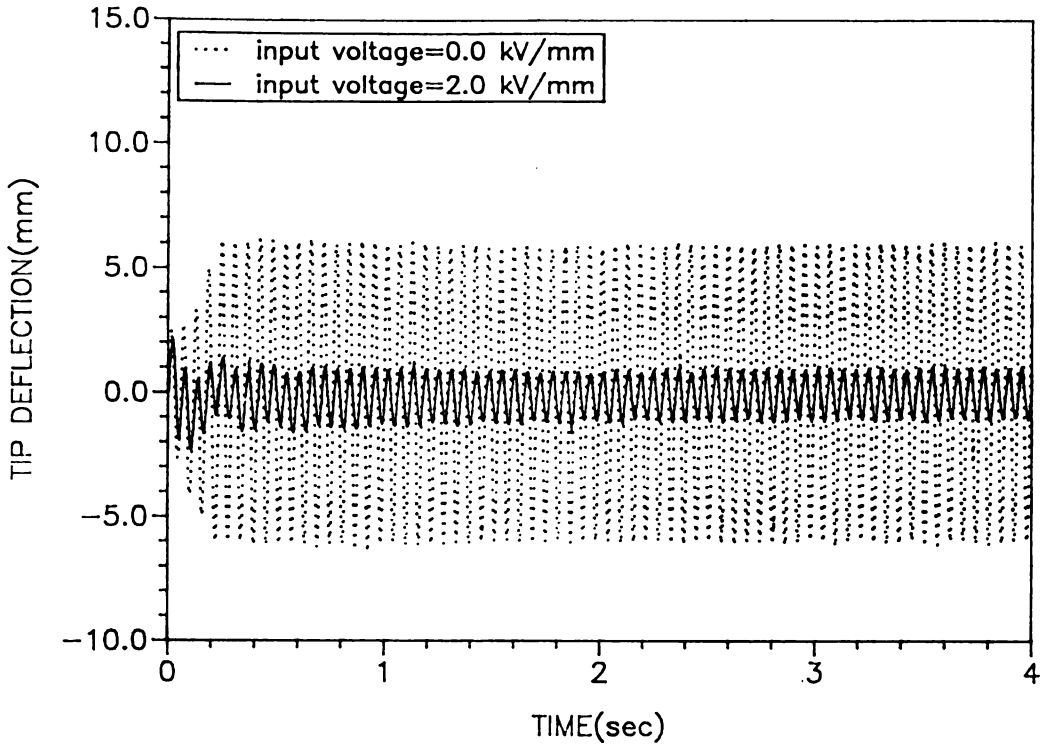


Figure 5.22 Measured Step Response with the Disturbance. K_p= 0.5, K_v= 0.25, $\tilde{d}(t)$=0.4 sin(16.8 Hz)t

is attributed to both increased stiffness and energy dissipation due to the imposed electric field. A quantitative measure of the contribution of each effect can be inferred from the frequency response presented in Figure 5.6. Figure 5.21 shows the simulated step responses corresponding to the results presented in Figure 5.20. The agreement between two results is satisfactory.

Figure 5.22 presents the measured step responses with the disturbance $\tilde{d}(t)$=0.4 sin f_2t where f_2=16.8 Hz. The forcing frequency f_2 is very close to the second clamped-mode natural frequency of Ω_2 = 17.1 Hz in the absence of electrical field. The amplitude of oscillation

without input voltage was reduced by 80 percent by employing the input voltage of 2.0 kV/mm. Since the increment ratio of the second mode due to the electrical field is larger than that of the first mode, the larger reduction of the amplitude is obtained.

It is clear from these results that the proposed hybrid controller is highlighted by enhancing the robustness of the conventional PD type output feedback controller to the imposed disturbance. Even though the pseudo-control force was applied in the fashion of the open-loop control in this study, it is possible to set up the closed-loop algorithm once the dynamics of the distributed ER actuator are identified more accurately, and the information about the disturbance are available from the output measurement of the system. More details on this matter are documented in Section 7.2 as a future work.

5.6 Summary of the Chapter

The phenomenological equation of motion was developed for the smart ER arm based on the experimental observation of the modal characteristics of the beam structure. The hybrid controller featuring the output feedback controller employed for the composite arm in the previous chapter, and the pseudo-state feedback controller obtained from the empirical dynamics of the ER fluid actuator has been formulated. The two types of pseudo-control forces (input voltage), namely constant and bang-off-bang type, were applied to the distributed ER fluid actuator. It has been shown through the experimental implementation that the robustness of the employed output feedback controller subjected to the disturbance which has a forcing frequency close to the clamped-mode natural frequency

of the robot arm was impressively enhanced by employing the pseudo-control force. This methodology can be extended to the control of other flexible structures such as helicopter blades, aircraft wings and appendages of satellites. These potential applications can be exploited by the successful incorporation with other existing control strategies such as optimal feedback and nonlinear feedback controllers. It is anticipated that the successful transition of this embroynic technology into an emerging technology would significantly accelerate the evolution of this innovative class of multi-functional, dynamically-tunable, intelligent materials for military, aerospace and advanced manufacturing environments of the future.

CHAPTER VI

NONLINEAR STATE FEEDBACK CONTROL ROBUST TO SYSTEM PARAMETER VARIATIONS

6.1 Introduction

The variations of system model parameters such as natural frequencies, damping ratios and model slope coefficients may arise in practice due to a wide spectrum of various conditions associated with design and manufacturing process of the flexible manipulators, dynamic modeling, and operating environments. These parameter variations will be more serious in the robotic system featuring the flexible arm fabricated from composite materials than those in the robotic system featuring the flexible arm fabricated from conventional materials. The reason follows that the flexible robot arm fabricated from composite laminates involve more number of design variables, more complicated manufacturing process, and also higher sensitivities to the environmental conditions such as temperature and moisture. Hence, a robust control algorithm for the position control of a single-link flexible manipulator fabricated from composite laminates (composite arm in short) with parameter variations will be developed in this chapter.

A robust controller which guarantees stable performances of the system for all possible variations of the parameters is designed by treating the variations as uncertainties. In other words, the robust controller which guarantees that the response of the uncertain system

enters and remains within a particular bounded set after a finite interval of time is to be formulated. Relating works on the robust control to system uncertainties can be found in [13,36,44,61,79,80, 81, 133]. In these references, the controllers were designed based on possible bound of uncertainties, and it has been assumed that so-called matching conditions are satisfied except references [13,36,133]. The matching conditions simply say that the uncertain quantities can not enter arbitrary into the state equations. The robust controllers without the matching conditions were considered first in [13], and [36,133] later on. The basic approach without matching conditions is same for the case with matching condition except establishing more stringent bound on uncertain parameters by introducing so-called a measure of mismatch and a mismatch threshold. The system dynamics of the flexible robotic manipulators lend themselves to the dynamics which can not formulated to be assumed that the matching conditions are satisfied as will be seen in the next section, while the dynamics featuring the rigid-body arms only are adapted in nature to satisfy the matching conditions. And also, it will be observed in the next section that one uncertain parameter causes the variation of all flexible modes in the system dynamics of the flexible manipulators, while it is not true in the system dynamics of the rigid-body manipulators.

In this chapter, a nonlinear robust controller for the composite arm will be designed by utilizing the properties of uniform and uniform ultimate boundedness of the solution. The main difference of this approach from those considered in current literature is that the effect of each uncertain parameter as well as the effect of the interaction of all employed uncertain parameters to the total system performance are

considered in this study. Hence, a certain measure of allowable magnitude of each uncertain parameter can be achieved. The advantage of this approach may come from that the considered uncertain parameters can be properly weighed by adjusting the magnitude of the uncertain quantities. Therefore, the system can be prevented from serious conditions associated with the system instability caused by the uncertain parameters. In the subsequent section, the problem formulation for the composite arm will be presented, and Section 6.3 presents the robust controller design based on the problem formulation. Finally, an illustrative example will be taken and simulated in Section 6.4 to demonstrate the viability of the proposed robust controller.

The author believes that this is the first work to design a robust controller for a single-link flexible manipulator fabricated from advanced composite laminates which accounts for serious uncertainties. Even though the proposed controller is not experimentally implemented in this study, the experimental realization of this controller may be accomplished by incorporating the advanced high speed of microprocessors as well as other necessary experimental hardwares such as modal filters.

6.2 Problem Formulation

The parameter variations of the composite arm may be arisen from three different processes. First, the variation may arise from the mismatch between the design and manufacturing process of the composite arm associated with the factors of lamina angle, curing cycle, fiber volume fraction, delamination, cracks, voids, etc. Since it is hard maintain the designed lamina angle in the manufacturing process, there always exists a mismatch of the lamina angle. And also, since curing

facilities are in general different at different place, there exists an error regarding to material and geometrical properties as observed in Section 3.2. A recent study [149] shows a frequency variation of the composite laminates with respect to the delamination of the laminate. Second, the variation may come from the dynamic modeling process. Since the dynamic model is developed in general based on some assumptions such as small elastic deflection, there exists an error whenever the motion of the robot is over a certain level of these assumptions. Furthermore, the nonlinear joint friction is often neglected in the modeling process resulting in significant difference of the system performance between the predicted and measured values in certain situations. Finally, the variations may arise from the operating conditions such as varying payload, varying temperature and moisture, and existence of obstacle in the operation. Suppose that the robot is assigned to work for welding job under high temperature condition, or oil exploring under the ocean. Then, the parameter variations caused by the high temperature and moisture should be accounted for the desirable system performance requirements.

All these uncertain parameters may cause system parameter variations such as natural frequencies and input influence coefficients. In this study, two most important factors; the varying payload and the mismatched lamina angle are considered as uncertain parameters to develop the robust controller. However, the proposed methodology can be exploited to account for other uncertain parameters such as delamination and temperature. The varying payload is encountered in operating environment and the mismatched lamina angle is encountered in the manufacturing process of the composite arm.

Now rewrite the state equation in (2.35) by

$$\begin{aligned} \dot{x}_p &= A_p x_p + B_p u \\ x_p(t_0) &= x_{p0} \end{aligned} \tag{6.1}$$

where

$$x_p = \begin{bmatrix} \eta_0 \\ \dot{\eta}_0 \\ \eta_1 \\ \dot{\eta}_1 \\ \cdot \\ \cdot \\ \cdot \\ \eta_q \\ \dot{\eta}_q \end{bmatrix}, \quad A_p = \begin{bmatrix} 0 & 1 & 0 & 0 & \cdots & 0 & 0 \\ 0 & 0 & 0 & 0 & \cdots & 0 & 0 \\ 0 & 0 & 0 & 1 & \cdots & 0 & 0 \\ 0 & 0 & -\omega_1^2 & -2\zeta_1\omega_1 & \cdots & 0 & 0 \\ \cdot & \cdot & \cdot & \cdot & \cdots & \cdot & \cdot \\ \cdot & \cdot & \cdot & \cdot & \cdots & \cdot & \cdot \\ \cdot & \cdot & \cdot & \cdot & \cdots & \cdot & \cdot \\ 0 & 0 & 0 & 0 & \cdots & 0 & 1 \\ 0 & 0 & 0 & 0 & \cdots & -\omega_q^2 & -2\zeta_q\omega_q \end{bmatrix}$$

$$B_p = [\, 0 \quad b_0 \quad 0 \quad b_1 \quad \cdots \quad b_q \,]^T \tag{6.2}$$

$$b_0 = 1/I_T \,, \quad b_i = (d\phi_i(o)/dx)/I_T \,, \quad i = 1, \ldots, q$$

where subscript (q) is the number of primary flexible modes, and x_{p0} are arbitrary initial conditions. Let

$$\begin{aligned} \omega_i &= \omega_{0i} + \Delta\omega_i^p + \Delta\omega_i^\ell \,, \quad i = 1, \ldots, q \\ b_i &= b_{0i} + \Delta b_i^p + \Delta b_i^\ell \,, \quad i = 0, \ldots, q \end{aligned} \tag{6.3}$$

where ω_{0i} and b_{0i} are nominal natural frequency and control influence coefficient respectively under the conditions that (i) no payload, (ii) known fixed lamina angle, (iii) satisfied all other assumptions made in the modeling and manufacturing process as well as operating conditions. The $\Delta\omega_i^p$ and $\Delta\omega_i^\ell$ are possible frequency deviation due to the varying

payload and the mismatched lamina angle respectively. And the Δb_i^p and Δb_i^ℓ are the corresponding deviations of the input influence coefficient.

Defining relative variation as

$$\omega_{ri}^p \triangleq \frac{\Delta\omega_i^p}{\omega_{0i}} , \quad \omega_{ri}^\ell \triangleq \frac{\Delta\omega_i^\ell}{\omega_{0i}} \quad , i = 1, \ldots, q$$

$$b_{ri}^p \triangleq \frac{\Delta b_i^p}{b_{0i}} , \quad b_{ri}^\ell \triangleq \frac{\Delta b_i^\ell}{b_{0i}} \quad , i = 0, \ldots, q \tag{6.4}$$

the deviations can be expressed as follows.

$$\Delta\omega_i^p = \omega_{ri}^p \omega_{0i}^p , \quad \Delta\omega_i^\ell = \omega_{ri}^\ell \omega_{0i}^\ell \quad , i = 1, \ldots, q$$

$$\Delta b_i^p = b_{ri}^p b_{0i}^p , \quad \Delta b_i^\ell = b_{ri}^\ell b_{0i}^\ell \quad , i = 0, \ldots, q \tag{6.5}$$

Thus, the state equation (6.1) becomes

$$\dot{x}_p = (A_0 + \Delta A(p) + \Delta A(\ell) + \Delta A(p,\ell))x_p + (B_0 + \Delta B(p) + \Delta B(\ell))u$$

$$x_p(t_o) = x_{p0} \tag{6.6}$$

where

$$A_0 = \begin{bmatrix} 0 & 1 & 0 & 0 & \cdot & \cdot & \cdot & 0 & 0 \\ 0 & 0 & 0 & 0 & \cdot & \cdot & \cdot & 0 & 0 \\ 0 & 0 & 0 & 1 & \cdot & \cdot & \cdot & 0 & 0 \\ 0 & 0 & -\omega_{01}^2 & -2\zeta_1\omega_{01} & \cdot & \cdot & \cdot & 0 & 0 \\ \cdot & \cdot & \cdot & \cdot & \cdot & \cdot & \cdot & \cdot & \cdot \\ \cdot & \cdot & \cdot & \cdot & \cdot & \cdot & \cdot & \cdot & \cdot \\ \cdot & \cdot & \cdot & \cdot & \cdot & \cdot & \cdot & \cdot & \cdot \\ 0 & 0 & 0 & 0 & \cdot & \cdot & \cdot & 0 & 1 \\ 0 & 0 & 0 & 0 & \cdot & \cdot & \cdot & -\omega_{0q}^2 & -2\zeta_q\omega_{0q} \end{bmatrix} \tag{6.7a}$$

$$\Delta A(p) = \begin{bmatrix} 0 & 0 & 0 & 0 & \cdot & \cdot & \cdot & 0 & 0 \\ 0 & 0 & 0 & 0 & \cdot & \cdot & \cdot & 0 & 0 \\ 0 & 0 & 0 & 0 & \cdot & \cdot & \cdot & 0 & 0 \\ 0 & 0 & -p_{11} & -p_{21} & \cdot & \cdot & \cdot & 0 & 0 \\ \cdot & \cdot & \cdot & \cdot & \cdot & \cdot & \cdot & \cdot & \cdot \\ \cdot & \cdot & \cdot & \cdot & \cdot & \cdot & \cdot & \cdot & \cdot \\ \cdot & \cdot & \cdot & \cdot & \cdot & \cdot & \cdot & \cdot & \cdot \\ 0 & 0 & 0 & 0 & \cdot & \cdot & \cdot & 0 & 0 \\ 0 & 0 & 0 & 0 & \cdot & \cdot & \cdot & -p_{1q} & -p_{2q} \end{bmatrix} \tag{6.7b}$$

$$p_{11} = \omega_{01}^2 \omega_{r1}^p (\omega_{r1}^p + 2) \quad , \quad p_{21} = 2\zeta_1 \omega_{01} \omega_{r1}^p$$
$$p_{1q} = \omega_{0q}^2 \omega_{rq}^p (\omega_{rq}^p + 2) \quad , \quad p_{2q} = 2\zeta_q \omega_{0q} \omega_{rq}^p$$

$$\Delta A(\ell) = \begin{bmatrix} 0 & 0 & 0 & 0 & \cdot & \cdot & \cdot & 0 & 0 \\ 0 & 0 & 0 & 0 & \cdot & \cdot & \cdot & 0 & 0 \\ 0 & 0 & 0 & 0 & \cdot & \cdot & \cdot & 0 & 0 \\ 0 & 0 & -\ell_{11} & -\ell_{21} & \cdot & \cdot & \cdot & 0 & 0 \\ \cdot & \cdot & \cdot & \cdot & \cdot & \cdot & \cdot & \cdot & \cdot \\ \cdot & \cdot & \cdot & \cdot & \cdot & \cdot & \cdot & \cdot & \cdot \\ \cdot & \cdot & \cdot & \cdot & \cdot & \cdot & \cdot & \cdot & \cdot \\ 0 & 0 & 0 & 0 & \cdot & \cdot & \cdot & 0 & 0 \\ 0 & 0 & 0 & 0 & \cdot & \cdot & \cdot & -\ell_{1q} & -\ell_{2q} \end{bmatrix} \tag{6.7c}$$

$$\ell_{11} = \omega_{01}^2 \omega_{r1}^{\ell} (\omega_{r1}^{\ell} + 2) \quad , \quad \ell_{21} = 2\zeta_1 \omega_{01} \omega_{r1}^{\ell}$$
$$\ell_{1q} = \omega_{0q}^2 \omega_{rq}^{\ell} (\omega_{rq}^{\ell} + 2) \quad , \quad \ell_{2q} = 2\zeta_q \omega_{0q} \omega_{rq}^{\ell}$$

$$\Delta A(p,\ell) = \begin{bmatrix} 0 & 0 & 0 & 0 & \cdot & \cdot & \cdot & 0 & 0 \\ 0 & 0 & 0 & 0 & \cdot & \cdot & \cdot & 0 & 0 \\ 0 & 0 & 0 & 0 & \cdot & \cdot & \cdot & 0 & 0 \\ 0 & 0 & -p\ell_1 & 0 & \cdot & \cdot & \cdot & 0 & 0 \\ \cdot & \cdot & \cdot & \cdot & \cdot & \cdot & \cdot & \cdot & \cdot \\ \cdot & \cdot & \cdot & \cdot & \cdot & \cdot & \cdot & \cdot & \cdot \\ \cdot & \cdot & \cdot & \cdot & \cdot & \cdot & \cdot & \cdot & \cdot \\ 0 & 0 & 0 & 0 & \cdot & \cdot & \cdot & 0 & 0 \\ 0 & 0 & 0 & 0 & \cdot & \cdot & \cdot & -p\ell_q & 0 \end{bmatrix} \tag{6.7d}$$

$$p\ell_1 = 2\omega_{01}^2 \omega_{r1}^p \omega_{r1}^{\ell} \quad , \quad p\ell_q = 2\omega_{0q}^2 \omega_{rq}^p \omega_{rq}^{\ell}$$

$$B_0 = [0 \quad b_{00} \quad 0 \quad b_{01} \quad \cdot \quad \cdot \quad \cdot \quad 0 \quad b_{0q}]^T \tag{6.8a}$$

$$\Delta B(p) = [0 \quad b_{00} b_{r0}^p \quad 0 \quad b_{01} b_{r1}^p \quad \cdot \quad \cdot \quad \cdot \quad 0 \quad b_{0q} b_{rq}^p]^T \tag{6.8b}$$

$$\Delta B(\ell) = [0 \quad b_{00}b_{r0}^{\ell} \quad 0 \quad b_{01}b_{r1}^{\ell} \quad \cdots \quad 0 \quad b_{0q}b_{rq}^{\ell}]^T \quad (6.8c)$$

It is clear from the equations (6.7) and (6.8) that the uncertainty matrices $\Delta A(\cdot)$ and $\Delta B(\cdot)$ can not be decomposed into a manner such that the matching conditions are met, i.e.,

$$\Delta A(\cdot) = B_0 D(\cdot)$$

$$\Delta B(\cdot) = B_0 E(\cdot)$$

where $D(\cdot)$ and $E(\cdot)$ will be defined in the subsequent section. Therefore, without consideration of the matching conditions, a nonlinear robust state feedback controller which guarantees the stability of the system (6.6) for arbitrary initial conditions x_{p0} will be designed in the next section.

6.3 Controller Design

For generality, consider following dynamical system described by the state equation

$$\dot{x}(t) = (A_0 + \Delta A(\sigma_1(t)) + \Delta A(\sigma_2(t)) + \Delta A(\sigma_1(t),\sigma_2(t))) x(t)$$
$$+ (B_0 + \Delta B(\sigma_1(t)) + \Delta B(\sigma_2(t))) u(t) \quad (6.9)$$
$$x(t_0) = x_0 \ , \text{ for } \ t \in [t_0,t_1]$$

where $x(t) \in \mathbf{R}^n$ is the state, $u(t) \in \mathbf{R}^m$ is the input, and A_0, B_0 are the prescribed nominal system matrices of appropriate dimensions. In equation (6.9), $\Delta A(\sigma_1(t))$ and $\Delta A(\sigma_2(t))$ are plant uncertain matrices associated with uncertain parameters $\sigma_1(t)$ and $\sigma_2(t)$ respectively, and $\Delta A(\sigma_1(t),$

$\sigma_2(t))$ is the plant uncertain matrix associated with the both parameters $\sigma_1(t)$ and $\sigma_2(t)$. $\Delta B(\sigma_1(t))$ and $\Delta B(\sigma_2(t))$ are input uncertain matrices depending on parameters $\sigma_1(t)$ and $\sigma_2(t)$, respectively. Now following assumptions and definitions are made before proceeding further.

Assumption 6.1 : The uncertain matrices $\Delta A(\cdot)$ and $\Delta B(\cdot)$ are prescribed functions which are continuous on $\mathbf{R}^p$.

Assumption 6.2 : Uncertain parameters

$$\sigma_1(\cdot) : \mathbf{R}^1 \to \Gamma_1 \subset \mathbf{R}^p$$

$$\sigma_2(\cdot) : \mathbf{R}^1 \to \Gamma_2 \subset \mathbf{R}^p \tag{6.10}$$

are Lebesgue measurable, where Γ_1 and Γ_2 are prescribed compact subsets of appropriate spaces.

Assumption 6.3 : The pair (A_0, B_0) is controllable. This assumption in fact can be released for the system (6.6).

Assumption 6.4 : All state variable x(t) are available from direct measurements or state estimators.

Remark 6.1 : In this chapter, the vector norm is taken to be Euclidean and the matrix norm is the corresponding induced norms, hence $||A|| = (\lambda_{max(min)}(A^T A))^{1/2}$ where $\lambda_{max(min)}(\cdot)$ denotes the operation of taking the maximum (minimum) eigenvalue.

Definition 6.1 : Given a solution $x(\cdot)$: $[t_0,t_1] \to \mathbf{R}^n$, $x(t_0) = x_0$ for the equation (6.9), it is said that the solution is uniformly bounded if there is a positive constant $\delta(x_0) < \infty$, possibly dependent on initial value x_0, but not on initial time t_0, such that

$$||x(t)|| \leq \delta(x_0) \quad \text{for all } t \in [t_0,t_1]$$

Definition 6.2 : Given a solution $x(\cdot)$: $[t_0,\infty) \to \mathbf{R}^n$, $x(t_0) = x_0$ for the equation (6.9), it is said that the solution is uniformly ultimately bounded with respect to a set S if there is a non-negative constant $\tau(x_0, S) < \infty$, possibly dependent on x_0 and S, but not on t_0, such that

$$x(t) \in S \quad \text{for all } t \geq t_0 + \tau(x_0,S)$$

Definition 6.3 : The equation (6.9) is said to be decomposable if there exist continuous matrix functions

$$\begin{aligned} &D(\sigma_1(t)): \Gamma_1 \to \mathbf{R}^{nxn} \\ &D(\sigma_2(t)): \Gamma_2 \to \mathbf{R}^{nxn} \\ &D(\sigma_1(t),\sigma_2(t)): (\Gamma_1,\Gamma_2) \to \mathbf{R}^{nxn} \\ &E(\sigma_1(t)): \Gamma_1 \to \mathbf{R}^{mxn} \\ &E(\sigma_2(t)): \Gamma_2 \to \mathbf{R}^{mxn} \end{aligned} \tag{6.11}$$

and $\Delta\tilde{A}(\cdot)$ and $\Delta\tilde{B}(\cdot)$ having following properties.

$$\Delta A(\sigma_1(t)) = B_0 D(\sigma_1(t)) + \Delta\tilde{A}(\sigma_1(t))$$

$$\Delta A(\sigma_2(t)) = B_0 D(\sigma_2(t)) + \Delta\tilde{A}(\sigma_2(t))$$

$$\Delta A(\sigma_1(t),\sigma_2(t)) = B_0 D(\sigma_1(t),\sigma_2(t)) + \Delta\tilde{A}(\sigma_1(t),\sigma_2(t)) \qquad (6.12)$$

$$\Delta B(\sigma_1(t)) = B_0 E(\sigma_1(t)) + \Delta\tilde{B}(\sigma_1(t))$$

$$\Delta B(\sigma_2(t)) = B_0 E(\sigma_2(t)) + \Delta\tilde{B}(\sigma_2(t))$$

Remark 6.2 : The argument t is often omitted throughout this section when no confusion can arise.

It is observed from the equation (6.12) that the uncertain matrices $\Delta A(\cdot)$ and $\Delta B(\cdot)$ are decomposed into two parts ; the matched part $B_0 D(\cdot)$ and $B_0 E(\cdot)$, and the mismatched part $\Delta\tilde{A}(\cdot)$ and $\Delta\tilde{B}(\cdot)$. It is noted that this decomposition is highly nonunique. In some sense, a 'good' decomposition may be achieved by lumping uncertainties as much as into the matched part, hence minimizing the portion of the mismatched part. One way to obtain a 'good' decomposition is to apply the least-square error method [28]. For example, by letting

$$\Delta A(\cdot) = B_0 D(\cdot)$$

$$\Delta B(\cdot) = B_0 E(\cdot) \qquad (6.13)$$

following decomposition can be accomplished in the least-square error sense.

$$D(\sigma_1) = (B_0^T B_0)^{-1} B_0^T \Delta A(\sigma_1)$$

$$D(\sigma_2) = (B_0^T B_0)^{-1} B_0^T \Delta A(\sigma_2)$$

$$
\begin{aligned}
&D(\sigma_1,\sigma_2) = (B_0^T B_0)^{-1} B_0^T \Delta A(\sigma_1,\sigma_2) \\
&E(\sigma_1) = (B_0^T B_0)^{-1} B_0^T \Delta B(\sigma_1) \\
&E(\sigma_2) = (B_0^T B_0)^{-1} B_0 \Delta B(\sigma_2) \\
&\Delta\tilde{A}(\sigma_1) = \Delta A(\sigma_1) - B_0 D(\sigma_1) \\
&\Delta\tilde{A}(\sigma_2) = \Delta A(\sigma_2) - B_0 D(\sigma_2) \\
&\Delta\tilde{A}(\sigma_1,\sigma_2) = \Delta A(\sigma_1,\sigma_2) - B_0 D(\sigma_1,\sigma_2) \\
&\Delta\tilde{B}(\sigma_1) = \Delta B(\sigma_1) - B_0 E(\sigma_1) \\
&\Delta\tilde{B}(\sigma_2) = \Delta B(\sigma_2) - B_0 E(\sigma_2)
\end{aligned}
\tag{6.14}
$$

The purpose of this problem is to design a state feedback controller which assures that every solution of the equation (6.9) is uniformly bounded and uniformly ultimately bounded with respect to a set S to be specified, no matter what the uncertainties and initial conditions are. For the sake of generality, suppose that the nominal plant matrix A_0 is not stable. However, there exist a constant feedback gain matrix K such that

$$A_c = A_0 + B_0 K \tag{6.15}$$

is stable, since the pair (A_0, B_0) is assumed to be controllable. This implies that the real parts of all eigenvalues of A_c are negative. Now, consider a state feedback controller which has the form of

$$u = Kx + p(x) \quad \text{for all } x \in \mathbf{R}^n \tag{6.16}$$

where the function $p(\cdot)$: $\mathbf{R}^n \to \mathbf{R}^m$ is such that

$$p(x) = \begin{cases} -\dfrac{B_0^T Px}{||B_0^T Px||}\,(\rho_1(x) + \rho_2(x) + \rho_3(x)), & \text{if } ||B_0^T Px|| > \epsilon \\ -\dfrac{B_0^T Px}{\epsilon}\,(\rho_1(x) + \rho_2(x) + \rho_3(x)), & \text{if } ||B_0^T Px|| \le \epsilon \end{cases} \tag{6.17}$$

where ϵ is a prescribed positive constant, P is the solution of the Lyapunov equation

$$A_c^T P + P A_c = -Q \tag{6.18}$$

for a given constant positive definite (nxn) matrix Q, and $\rho_i(\cdot)$: $\mathbf{R}^n \to \mathbf{R}_+^1$ will be specified subsequently.

Substituting equations (6.12) and (6.16) into the equation (6.9) yields

$$\begin{aligned} \dot{x} &= A_c x + B_0 p(x) + B_0(e_{m1}(x,t) + e_{m2}(x,t) + e_{m3}(x,t)) \\ &\quad + \tilde{e}_1(x,t) + \tilde{e}_2(x,t) + \tilde{e}_3(x,t) \end{aligned} \tag{6.19}$$

where

$$\begin{aligned} e_{m1}(x,t) &= D(\sigma_1)x + E(\sigma_1)Kx + E(\sigma_1)p(x) \\ e_{m2}(x,t) &= D(\sigma_2)x + E(\sigma_2)Kx + E(\sigma_2)p(x) \\ e_{m3}(x,t) &= D(\sigma_1,\sigma_2)x \\ \tilde{e}_1(x,t) &= (\Delta\tilde{A}(\sigma_1) + \Delta\tilde{B}(\sigma_1)K)x + \Delta\tilde{B}(\sigma_1)p(x) \\ \tilde{e}_2(x,t) &= (\Delta\tilde{A}(\sigma_2) + \Delta\tilde{B}(\sigma_2)K)x + \Delta\tilde{B}(\sigma_2)p(x) \end{aligned} \tag{6.20}$$

$$\tilde{e}_3(x,t) = (\Delta\tilde{A}(\sigma_1,\sigma_2))x$$

for all $(x,t) \in \mathbf{R}^n \times \mathbf{R}^1$. In equation (6.19), $B_0 e_{mi}(x,t)$ and $\tilde{e}_i(x,t)$ are called as the matched error vector and mismatched error vector respectively. From the equation (6.20)

$$\begin{aligned}
||e_{m1}(x,t)|| &\le \max_{\sigma_1\in\Gamma_1} ||D(\sigma_1)x|| + \max_{\sigma_1\in\Gamma_1} ||E(\sigma_1)Kx|| \\
&\quad + \max_{\sigma_1\in\Gamma_1} ||E(\sigma_1)||\rho_1(x) \triangleq \rho_1(x) \\
||e_{m2}(x,t)|| &\le \max_{\sigma_2\in\Gamma_2} ||D(\sigma_2)x|| + \max_{\sigma_2\in\Gamma_2} ||E(\sigma_2)Kx|| \\
&\quad + \max_{\sigma_2\in\Gamma_2} ||E(\sigma_2)||\rho_2(x) \triangleq \rho_2(x) \\
||e_{m3}(x,t)|| &\le \max_{\substack{\sigma_1\in\Gamma_1 \\ \sigma_2\in\Gamma_2^1}} ||D(\sigma_1,\sigma_2)x|| \triangleq \rho_3(x)
\end{aligned} \tag{6.21}$$

The defined parameter $\rho_i(x)$ in equation (6.21) can be solved provided

$$\begin{aligned}
\max_{\sigma_1\in\Gamma_1} ||E(\sigma_1)|| < 1 \\
\max_{\sigma_2\in\Gamma_2} ||E(\sigma_2)|| < 1
\end{aligned} \tag{6.22}$$

Thus, with conditions (6.22), $\rho_i(x)$ are obtained as follows.

$$\begin{aligned}
\rho_1(x) &= [1 - \max_{\sigma_1\in\Gamma_1} ||E(\sigma_1)||]^{-1}[\max_{\sigma_1\in\Gamma_1} ||D(\sigma_1)x|| + \max_{\sigma_1\in\Gamma_1} ||E(\sigma_1)Kx||] \\
\rho_2(x) &= [1 - \max_{\sigma_2\in\Gamma_2} ||E(\sigma_2)||]^{-1}[\max_{\sigma_2\in\Gamma_2} ||D(\sigma_2)x|| + \max_{\sigma_2\in\Gamma_2} ||E(\sigma_2)Kx||]
\end{aligned} \tag{6.23}$$

$$\rho_3(x) = \max_{\substack{\sigma_1\in\Gamma_1 \\ \sigma_2\in\Gamma_2}} ||D(\sigma_1,\sigma_2)x||$$

Now define $\tilde{\rho}_i(x)$: $\mathbf{R}^n \to \mathbf{R}^1_+$ by

$$\begin{aligned} \tilde{\rho}_1(x) &\triangleq \alpha_1 ||x|| \\ \tilde{\rho}_2(x) &\triangleq \alpha_2 ||x|| \\ \tilde{\rho}_3(x) &\triangleq \alpha_3 ||x|| \end{aligned} \tag{6.24}$$

where

$$\begin{aligned} \alpha_1 &= [1 - \max_{\sigma_1\in\Gamma_1} ||E(\sigma_1)||]^{-1}[\max_{\sigma_1\in\Gamma_1} ||D(\sigma_1)|| + \max_{\sigma_1\in\Gamma_1} ||E(\sigma_1)K|| \\ \alpha_2 &= [1 - \max_{\sigma_2\in\Gamma_2} ||E(\sigma_2)||]^{-1}[\max_{\sigma_2\in\Gamma_2} ||D(\sigma_2)|| + \max_{\sigma_2\in\Gamma_2} ||E(\sigma_2)K|| \\ \alpha_3 &= \max_{\substack{\sigma_1\in\Gamma_1 \\ \sigma_2\in\Gamma_2}} ||D(\sigma_1,\sigma_2)|| \end{aligned} \tag{6.25}$$

Thus, from the equations (6.23) and (6.24)

$$\begin{aligned} \rho_1(x) &\le \tilde{\rho}_1(x) \\ \rho_2(x) &\le \tilde{\rho}_2(x) \\ \rho_3(x) &\le \tilde{\rho}_3(x) \end{aligned} \tag{6.26}$$

for all $x \in \mathbf{R}^n$. Furthermore, from the equations (6.21) and (6.26)

$$\begin{aligned} &||e_{m1}(x,t) + e_{m2}(x,t) + e_{m3}(x,t)|| \\ &\le ||e_{m1}(x,t)|| + ||e_{m2}(x,t)|| + ||e_{m3}(x,t)|| \\ &\le \rho_1(x) + \rho_2(x) + \rho_3(x) \end{aligned}$$

$$\leq \tilde{\rho}_1(x) + \tilde{\rho}_2(x) + \tilde{\rho}_3(x) - (\alpha_1 + \alpha_2 + \alpha_3)||x|| \tag{6.27}$$

Now in order to handle the mismatched error vector in equation (6.20), following definitions are introduced.

Definition 6.4 : Let the measure of mismatch be defined as follows.

$$M_1 \triangleq \max_{\sigma_1 \in \Gamma_1} ||\Delta\tilde{A}(\sigma_1)|| + \max_{\sigma_1 \in \Gamma_1} ||\Delta\tilde{B}(\sigma_1)K|| + \alpha_1 \max_{\sigma_1 \in \Gamma_1} ||\Delta\tilde{B}(\sigma_1)||$$

$$M_2 \triangleq \max_{\sigma_2 \in \Gamma_2} ||\Delta\tilde{A}(\sigma_2)|| + \max_{\sigma_2 \in \Gamma_2} ||\Delta\tilde{B}(\sigma_2)K|| + \alpha_2 \max_{\sigma_2 \in \Gamma_2} ||\Delta\tilde{B}(\sigma_2)|| \tag{6.28}$$

$$M_3 \triangleq \max_{\substack{\sigma_1 \in \Gamma_1 \\ \sigma_2 \in \Gamma_2}} ||\Delta\tilde{A}(\sigma_1, \sigma_2)||$$

Definition 6.5 : Define the mismatch threshold as

$$M^* \triangleq \frac{\lambda_{min}(Q)}{2\lambda_{max}(P)} \tag{6.29}$$

Definition 6.6 : Define the mismatch index as

$$\beta \triangleq \frac{(M_1 + M_2 + M_3)}{M^*} \tag{6.30}$$

It is noted in Definition 6.4 that M_1 and M_2 account for the mismatch associated with uncertain parameters $\sigma_1(\cdot)$ and $\sigma_2(\cdot)$ respectively, and M_3 accounts for the mismatch associated with both parameters. From the equations (6.20) and (6.28)

$$||\tilde{e}_1(x,t)|| \leq M_1 \, ||x||$$

$$||\tilde{e}_2(x,t)|| \leq M_2 \, ||x|| \tag{6.31}$$

$$||\tilde{e}_3(x,t)|| \leq M_3 \, ||x||$$

Thus,

$$||\tilde{e}_1(x,t) + \tilde{e}_2(x,t) + \tilde{e}_3(x,t)||$$

$$\leq ||\tilde{e}_1(x,t)|| + ||\tilde{e}_2(x,t)|| + ||\tilde{e}_3(x,t)||$$

$$\leq (M_1 + M_2 + M_3) \, ||x|| \tag{6.32}$$

The mismatch threshold M^* defined in (6.29) implies a limit on the amount of the mismatched uncertainties, defined as the measure of mismatch M_i, which can be tolerated. The mismatch index β in (6.30) indicates the normalized total measure of mismatch $(M_1 + M_2 + M_3)$ with respect to the mismatch threshold. Now consider the uniform and uniform ultimately bounded sets which satisfy the conditions given in Definitions 6.2 and 6.3. With a hypothesis that the total measure of mismatch is not two large, i.e.,

$$\beta < 1$$

$$\text{or} \quad (M_1 + M_2 + M_3) < M^* \tag{6.33}$$

form the scalar function $h(\cdot)$: $[0, \infty) \rightarrow \mathbf{R}$ given by

$$h(\eta) \triangleq (\lambda_{min}(Q) - 2\lambda_{max}(P)(M_1 + M_2 + M_3))\eta^2 - ((\alpha_1 + \alpha_2 + \alpha_3)\epsilon/2)\eta \tag{6.34}$$

Then, letting

$$\tilde{\eta} \triangleq \max \{ \eta : h(\eta) \leq 0 \} \tag{6.35}$$

yields

$$\tilde{\eta} = \frac{(\alpha_1 + \alpha_2 + \alpha_3)\epsilon}{2(\lambda_{min}(Q) - 2\lambda_{max}(P)(M_1 + M_2 + M_3))} \tag{6.36}$$

It is noted that the $\tilde{\eta}$ in (6.36) implies the radius of the largest closed ball which is wholly contained within the bounded set (see Theorem 6.1).

Remark 6.3 : It is observed from the condition (6.33) that the mismatch threshold M^* depends on eigenvalues of the matrices Q and P. The larger M^* tolerates the larger uncertainties. The maximization of the M^* will be discussed later in this section.

Since A_c in equation (6.15) is stable and the matrix Q in equation (6.18) is positive definite, and hence the matrix P is positive definite, following Lyapunov ellipsoids can be constructed.

$$X(k) = \{ x \in \mathbb{R}^n \mid x^T P x \leq k \} \tag{6.37}$$

where k is positive constant. Now define the smallest ellipsoid containing ball $B(\tilde{\eta})$ as

$$k^m \triangleq \min \{ k \mid B(\tilde{\eta}) \subseteq X(k) \} = \lambda_{max}(P)\, \tilde{\eta}^2 \tag{6.38}$$

And also, for given any $\tilde{k} > k^m$, and any initial condition $x_0 \notin X(\tilde{k})$, define the constant

$$k^0 \triangleq x_0^T P x_0 \tag{6.39}$$

and

$$c(x_0,\tilde{k}) \triangleq \min \{ h(\eta) : (\tilde{k}/\lambda_{max}(P))^{1/2} \leq \eta \leq (k^0/\lambda_{min}(P))^{1/2} \} \quad (6.40)$$

Finally, following theorem regarding to the boundedness of the solution of the equation (6.9) can be established.

Theorem 6.1 : Consider the dynamical system given by equation (6.9). And suppose that the conditions given by the equations (6.22) and (6.33) are satisfied. Then, the controller given by the equation (6.16) assures the uniform boundedness of every solution $x(\cdot):[t_0, t_1] \rightarrow \mathbf{R}^n$, and uniform ultimate boundedness of every solution $x(\cdot)$ extended over $[t_0,\infty)$. Furthermore, given any $\tilde{k} > k^m$, every solution corresponding to initial condition $(x_0,t_0) \in \mathbf{R}^n \times \mathbf{R}$ is uniformly bounded with

$$\delta(x_0) = \begin{cases} (\lambda_{max}(P)/\lambda_{min}(P))^{1/2} ||x_0|| & \text{for } x_0 \notin X(\tilde{k}) \\ (\tilde{k}/\lambda_{min}(P))^{1/2} & \text{for } x_0 \in X(\tilde{k}) \end{cases} \quad (6.41)$$

and is uniformly ultimately bounded with respect to a set $S \triangleq X(\tilde{k})$ with

$$\tilde{\tau}(x_0,S) = \begin{cases} (k^0 - \tilde{k})/c(x_0, \tilde{k}) & \text{for } x_0 \notin S \\ 0 & \text{for } x_0 \in S \end{cases} \quad (6.42)$$

Proof : Denote the right-hand side of the equation (6.19) by

$$f(x,t) \triangleq A_c x + B_0 p(x) + B_0(e_{m1}(x,t) + e_{m2}(x,t) + e_{m3}(x,t)) + \tilde{e}_1(x,t) + \tilde{e}_2(x,t) + \tilde{e}_3(x,t) \quad (6.43)$$

where f(x,t) is Caratheodory function ; f(x,t) is continuous in x and Lebesgue measurable in t. Now let $X(k^*)$ be a superset of $X(\tilde{k})$ containing all initial conditions. Then for given initial conditions, f(x,t) can be uniformly bounded over the domain $D \triangleq X(k^*) \times \mathbf{R}$ from the observation

$$\begin{aligned} ||f(x,t)|| &\le ||A_c||\ ||x|| + (\alpha_1+\alpha_2+\alpha_3)||B_0||\ ||x|| \\ &\quad + ||B_0(e_{m1}(x,t) + e_{m2}(x,t) + e_{m3}(x,t))|| \\ &\quad + ||\tilde{e}_1(x,t) + \tilde{e}_2(x,t) + \tilde{e}_3(x,t)|| \\ &\le ||A_c||\ ||x|| + 2(\alpha_1+\alpha_2+\alpha_3)||B_0||\ ||x|| \\ &\quad + (M_1+M_2+M_3)||x|| \\ &\triangleq g(x) \end{aligned} \tag{6.44}$$

Since g(•) is continuous [19] on $X(k^*)$, there exist a finite maximum value

$$\hat{k} = \max_{x \in X(k^*)} g(x) \tag{6.45}$$

Thus, it is clear that $\hat{k}$ plays a role of a uniform bound for f(x,t) over domain D. Therefore, it follows from [43] that there exist a solution $x(\cdot) : [t_0, t_1] \to \mathbf{R}^n$. The extension of this solution will be shown later of this proof.

Now, introduce a Lyapunov function candidate given by

$$V(x) = x^T P\, x \qquad \text{for all } x \in \mathbf{R}^n \tag{6.46}$$

where $V(\cdot): \mathbf{R}^n \to \mathbf{R}$ is continuously differentiable. To show that it is indeed a Lyapunov function for the system (6.9) with controller (6.16), consider the Lyapunov derivative as follows.

$$\dot{V}(x,t) = \dot{x}^T P\, x + x^T P\, \dot{x}$$

$$= - x^T Q\, x + 2(B_0^T P\, x)^T\, (p(x) + e_{m1}(x,t) + e_{m2}(x,t)$$

$$+ e_{m3}(x,t)) + 2\, x^T P\, (\tilde{e}_1(x,t) + \tilde{e}_2(x,t) + \tilde{e}_3(x,t))$$

$$\leq - x^T Q\, x + 2(B_0^T P\, x)^T\, (p(x) + ((B_0^T P\, x/||B_0^T P\, x||) \quad (6.47)$$

$$(\rho_1(x) + \rho_2(x) + \rho_3(x))) + 2\, x^T P\, (\tilde{e}_1(x,t)$$

$$+ \tilde{e}_2(x,t) + \tilde{e}_3(x,t))$$

It is observed from the equation (6.17) that, if $||B_0^T\, P\, x|| > \epsilon$, the term of $p(x) + (B_0^T\, P\, x\, /\, ||B_0^T\, P\, x||)\, (\rho_1(x) + \rho_2(x) + \rho_3(x))$ vanishes, and if $||B_0^T\, P\, x|| < \epsilon$, then it has maximum value of $\epsilon\, (\rho_1(x) + \rho_2(x) + \rho_3(x))/2$. Hence, from the equations (6.27) and (6.32), the equation (6.47) becomes

$$\dot{V}(x,t) \leq - x^T Q\, x + ((\alpha_1 + \alpha_2 + \alpha_3)\epsilon/2)||x||$$

$$+ 2\lambda_{max}(P)(M_1 + M_2 + M_3)||x||^2 \quad (6.48)$$

Thus

$$\dot{V}(x,t) < 0 \quad (6.49)$$

for all $t \in \mathbf{R}^1$ and all x such that

$$x^T Q\, x - ((\alpha_1 + \alpha_2 + \alpha_3)\epsilon/2)||x||$$

$$- 2\lambda_{max}(P)(M_1 + M_2 + M_3)||x||^2 > 0 \quad (6.50)$$

However, from the Lemma 4.1 in the previous chapter

$$\lambda_{min}(Q)||x||^2 \leq x^T Q\, x \leq \lambda_{max}(Q)||x||^2 \tag{6.51}$$

where $\lambda_{min}(Q) > 0$, since $Q > 0$. Thus, the condition (6.49) is satisfied for all $t \in \mathbf{R}^1$ and all x such that

$$(\lambda_{min}(Q) - 2\lambda_{max}(P)(M_1 + M_2 + M_3))||x||^2$$
$$- ((\alpha_1 + \alpha_2 + \alpha_3)\epsilon/2)||x|| > 0 \tag{6.52}$$

Hence, it can be said that the inequality given by the equation (6.49) is guaranteed for all $t \in \mathbf{R}^1$ and all $x \notin B(\tilde{\eta})$, where $\tilde{\eta}$ is given by the equation (6.36), provided that the condition (6.33) is satisfied. It should be noted, however, that the condition (6.52) is only a sufficient condition.

Now consider the smallest Lyapunov ellipsoid that contains the ball $B(\tilde{\eta})$, that is, $X(k^m)$, where k^m is given by the equation (6.38). From the Lemma 4.1,

$$\lambda_{min}(P)||x||^2 \leq x^T P\, x \leq \lambda_{max}(P)||x||^2 \tag{6.53}$$

where $\lambda_{min}(P) > 0$, since $P > 0$. The condition (6.49) implies boundedness of all solution. That is, if $x(\cdot):[t_0,t_1] \rightarrow \mathbf{R}^n$ with initial condition $x(t_0)=x_0$ is a solution of the equation (6.9) with the controller given by the equation (6.16) and allowable uncertainties, then there are following two cases to be considered: if $x_0 \notin X(\tilde{k})$, that is, $x(t) \in X(k^0)$ for all $t \in [t_0,t_1]$, then following inequality can be obtained in view of the equation (6.53).

$$0 < \lambda_{min}(P)||x(t)||^2 \leq x^T(t)\ P\ x(t) \leq x_0^T\ P\ x_0 \leq \lambda_{max}(P)||x_0||^2 \quad (6.54)$$

If $x_0 \in X(\tilde{k})$, that is $x(t) \in X(\tilde{k})$ for all $t \in [t_0,t_1]$, then following inequality can be obtained again in view of the equation (6.53).

$$0 < \lambda_{min}(P)||x(t)||^2 \leq x^T(t)\ P\ x \leq \tilde{k} \quad (6.55)$$

Therefore, $\delta(x_0)$ given by the equation (6.41) can be achieved from the equations (6.54) and (6.55) for $x_0 \notin X(\tilde{k})$ and $x_0 \in X(\tilde{k})$ respectively. And from this uniform boundedness and existence of the solution, it follows that a solution $x(\cdot)$: $[t_0,t_1] \rightarrow \mathbf{R}^n$ can be extended over time interval $[t_0,\infty)$.

The proof of ultimate boundedness follows again from the condition (6.49). If $x_0 \in X(\tilde{k})$, it is an immediate consequence of the boundedness result, hence it suffices to take $\tilde{\tau}(x_0,S) = 0$. If $x_0 \notin X(\tilde{k})$, the V(x(t)) decreases as long as $x(t) \notin X(k^m)$ and x(t) reach the boundary $\partial X(\tilde{k})$ in a finite time. From the equations (6.54) and (6.55)

$$(\tilde{k}/\lambda_{max}(P))^{1/2} \leq ||x(t)|| \leq (k^0/\lambda_{min}(P))^{1/2} \quad (6.56)$$

whenever $x(t) \in X(k^0)/X(\tilde{k})>$. Hence, from the equations (6.48) and (6.52)

$$\begin{aligned}\dot{V}(x,t) &\leq -h(||x(t)||) \\ &\leq -\min\{h(\tilde{\eta}):\ (\tilde{k}/\lambda_{max}(P))^{1/2} \leq \tilde{\eta} \leq (k^0/\lambda_{min}(P))^{1/2}\} \\ &= -c(x_0,\tilde{k}) < 0 \end{aligned} \quad (6.57)$$

where

$$h(||x(t)|| = (2(M_1+ M_2+ M_3)||P|| - \lambda_{min}(Q))||x||^2 + ((\alpha_1+ \alpha_2+ \alpha_3)\epsilon/2)||x|| \quad (6.58)$$

Suppose $x(t) \notin X(\tilde{k})$ for all $t \in [t_0,t^*]$, where $t^*= (k^0- \tilde{k})/c(x_0,\tilde{k})$. Then from the equation (6.57)

$$V(x(t_0+ t^*)) - V(x_0) \leq - c(x_0, \tilde{k})t^* \leq - (k^0- \tilde{k}) \quad (6.59)$$

so that $V(x(t_0- t^*)) \leq \tilde{k}$. Then this contradicts the supposition. Thus there exist a time $\hat{t} \leq t^*$ such that $x(\hat{t}) \in X(\tilde{k}) = S$. Therefore, from the boundedness and $x(t) \in S$ for all $t \geq t^*$, $t^*= \tilde{\tau}(x_0,S)$. This concludes the proof of the Theorem 6.1.

Now, consider the maximization of the mismatch threshold M^* given by the equation (6.29) as noted in Remark 6.3. It is clear from this equation that the threshold depends on the eigenvalues of the positive definite matrices Q, and P which is a solution of the Lyapunov equation associated with closed-loop eigenvalues of the nominal system. Hence, the maximization of M^* can be accomplished by considering either given matrix Q or the linear feedback gains in equation (6.16). Herein, the maximization of the M^* is achieved by considering the matrix Q with fixed feedback gains. Before establishing a theorem regarding to the maximization of M^*, following lemma is introduced.

Lemma 6.1 (see [113]) : Let $\tilde{P}$ be the unique positive definite solution of the Lyapunov equation

$$A_c^T \tilde{P} + \tilde{P} A_c = -\tilde{Q} = - \gamma Q \tag{6.60}$$

where γ is positive scalar constant, and A_c and Q are in equation (6.18). Then

$$M^* = \lambda_{min}(Q)/2\lambda_{max}(P) = \lambda_{min}(\tilde{Q})/2\lambda_{max}(\tilde{P}) \tag{6.61}$$

where P is the solution of the Lyapunov equation (6.18).

Proof : Rewrite the equation (6.60) as

$$A_c^T (\tilde{P}/\gamma) + (\tilde{P}/\gamma)A_c = - Q \tag{6.62}$$

Since $P > 0$ and $\tilde{P} > 0$, and also there is an unique solution of the equation (6.18) and (6.60) respectively, it follows from the equations (6.18) and (6.62), $P = \tilde{P}/\gamma$. Hence

$$\lambda_{max}(P) = \lambda_{max}(\tilde{P})/\gamma \tag{6.63}$$

Thus the equation (6.61) is satisfied

Theorem 6.2 : Suppose the linear feedback gains in equation (6.16) are fixed. Then the mismatch threshold M^* is maximum when the positive definite matrix $Q = I$ (identity matrix).

Proof : Let the matrix Q in equation (6.60) be arbitrary positive definite matrix and let $\gamma = 1/\lambda_{min}(Q)$. Then $\lambda_{min}(\tilde{Q})=1$, where $\tilde{Q}$ is in the equation (6.60). The solution of the equation (6.60) is given [18] by

$$\tilde{P} = \int_o^\infty e^{A_c^T t} \tilde{Q} e^{A_c t} dt \tag{6.64}$$

And also consider

$$A_c^T \hat{P} + \hat{P} A_c = - I \tag{6.65}$$

with the solution

$$\hat{P} = \int_o^\infty e^{A_c^T t} I e^{A_c t} dt \tag{6.66}$$

Now define

$$\begin{aligned} \tilde{M} &\triangleq 1/\lambda_{max}(\tilde{P}) \\ \hat{M} &\triangleq 1/\lambda_{max}(\hat{P}) \end{aligned} \tag{6.67}$$

Then from the equations (6.64) and (6.66)

$$\tilde{P} - \hat{P} = \int_o^\infty e^{A_c^T t} (\tilde{Q} - I) e^{A_c t} dt \tag{6.68}$$

However $\tilde{Q}$-I≥0 since all eigenvalues of the $\tilde{Q}$ greater or equal to 1. Hence $\tilde{P} - \hat{P} \geq 0$, $\lambda_{max}(\tilde{P}) \geq \lambda_{max}(\hat{P})$ and $\hat{M} \geq \tilde{M}$ from the equation (6.67). Since $\tilde{M}$ is invariant under any choice of the positive scalar γ by the Lemma 6.1, $\hat{M} \geq \tilde{M}$ holds for all $\tilde{Q}$. This completes the proof of the Theorem 6.2

Therefore, the mismatch threshold defined by the equation (6.29) can be modified as

$$M^* \triangleq \frac{1}{2\lambda_{max}(P)} \tag{6.69}$$

by choosing $Q = I$. Other quantities involving $\lambda_{min}(Q)$ are modified by replacing $\lambda_{min}(Q)$ by 1. For example, the radius of the largest closed ball $\tilde{\eta}$ defined by the equation (6.36) becomes

$$\tilde{\eta} = \frac{(\alpha_1 + \alpha_2 + \alpha_3)\ \epsilon}{2 - 4\lambda_{max}(P)(M_1 + M_2 + M_3)}$$

6.4 Illustrative Example

In order to demonstrate the robustness of the developed nonlinear state feedback controller, the composite arm, which has geometrical and material properties given in Table 6.1, is considered. It is clear from this table that the nominal system has no payload and 20^0 of lamina angle (fiber orientation) for each lamina. These two parameters will be considered as uncertain parameters in this example. The parameter variations of the proposed robotic system associated with the varying payload and the mismatched lamina angle are presented in Figures 6.1 and 6.2 respectively. It is observed from Figure 6.1 that the modal slope coefficient $d\phi_1(o)/dx$ is very sensitive to a whole range of the payload, while the first mode natural frequency is sensitive to only a small range of the payload. And it is clear from Figure 6.2 that both the first and second mode natural frequencies are very sensitive to the lamina angle.

Table 6.1 Geometrical and Material Properties of the Nominal Composite Arm

Parameters and Properties	Specifications (Graphite-Epoxy)
Beam Length (L)	1.5 m
Beam Width (b)	3.0 cm
Beam Thickness (h)	1.8 mm
Payload (m_t)	0.0 kg
Hub Moment of Inertia (I_H)	0.00496 kg•m^2
Number of Lamina	6
Lamina Thickness	d_i = 0.3 mm (i = 1,....,6)
Fiber Orientation	θ_i = 20° (i = 1,....,6)
Fiber Volume Fraction	V_f^i = 0.60 (i = 1,....,6)
Young's Modulus	E_{fiber} = 220 GPa E_{matrix}=4.27 GPa
Density	ρ_{fiber}=1750 kg/m^3 ρ_{matrix}=1200 kg/m^3
Poisson's Ratio	ν_{fiber} = 0.20 ν_{matrix} = 0.34

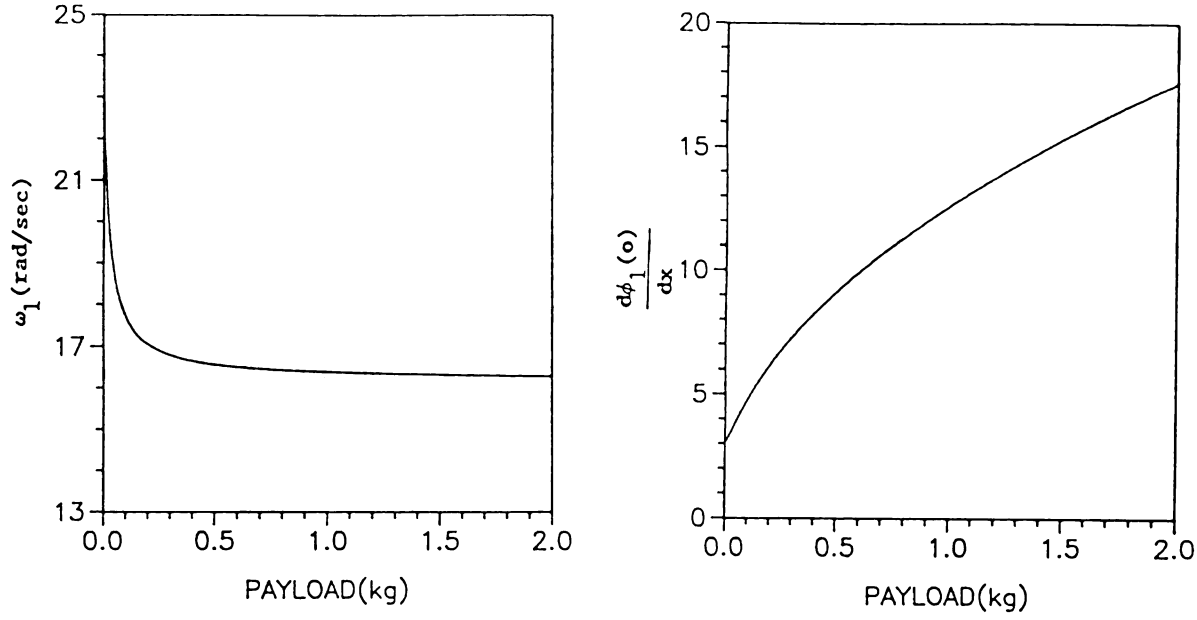


Figure 6.1 Parameter Variation of the Composite Arm with respect to the Payload

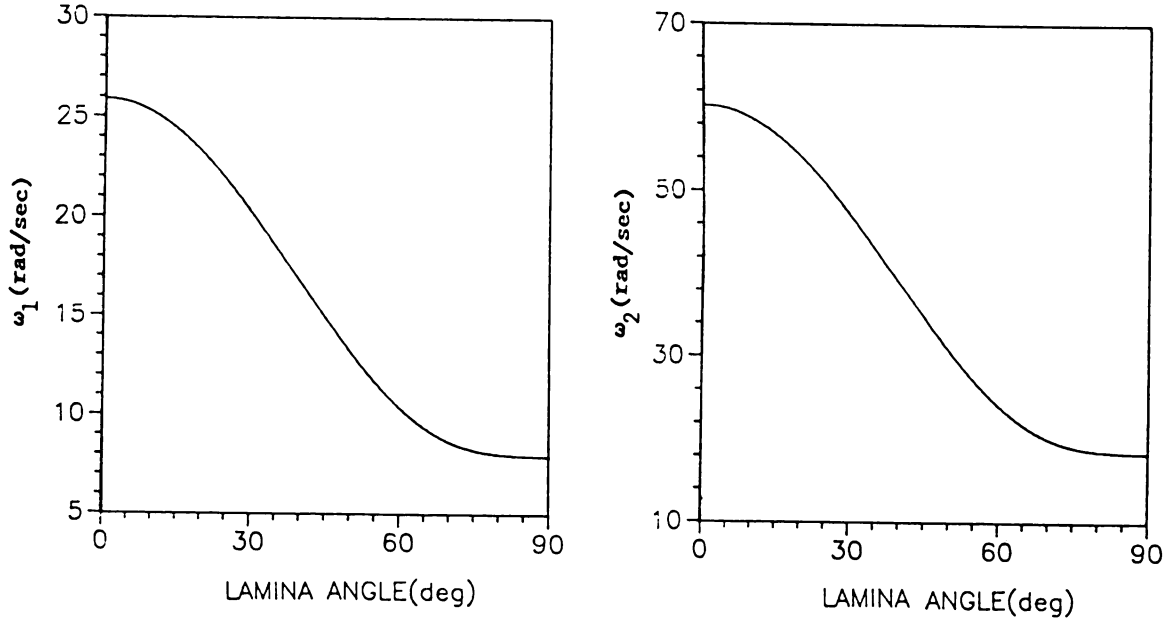


Figure 6.2 Parameter Variation of the Composite Arm with respect to the Lamina Angle

The system model parameters of the nominal system are presented in Table 6.2. For the determination of these parameters, two-node element was employed with two degrees of freedom at each node, and the number of elements was ten.

In this simulation, the rigid-body mode and the first flexible mode are considered as the primary modes. Hence the system matrices in equation (6.6) become

$$A_0 = \begin{bmatrix} 0 & 1 & 0 & 0 \\ 0 & 0 & 0 & 0 \\ 0 & 0 & 0 & 1 \\ 0 & 0 & -539.9 & -0.3253 \end{bmatrix} \tag{6.70a}$$

$$B_0 = \begin{bmatrix} 0 \\ 10.2135 \\ 0 \\ 30.7323 \end{bmatrix} \tag{6.70b}$$

Table 6.2 System Model Parameters of the Nominal System

Mode	ω_i(Hz)	$\frac{d\phi_i}{dx}(0)$	$\phi_i(L)$
1	3.698	3.009	-0.960
2	8.603	2.798	0.993
3	19.800	1.139	-1.156
4	37.931	0.566	1.180
5	62.484	0.338	-1.188

$$\Delta A(p) = \begin{bmatrix} 0 & 0 & 0 & 0 \\ 0 & 0 & 0 & 0 \\ 0 & 0 & 0 & 0 \\ 0 & 0 & -p_{11} & -p_{21} \end{bmatrix} \tag{6.70c}$$

$$p_{11} = 539.9\omega_{r1}^{p}(\omega_{r1}^{p} + 2),\ p_{21} = 0.3253\omega_{r1}^{p}$$

$$\Delta A(\ell) = \begin{bmatrix} 0 & 0 & 0 & 0 \\ 0 & 0 & 0 & 0 \\ 0 & 0 & 0 & 0 \\ 0 & 0 & -\ell_{11} & -\ell_{21} \end{bmatrix} \tag{6.70d}$$

$$\ell_{11} = 539.9\omega_{r1}^{\ell}(\omega_{r1}^{\ell} + 2),\ \ell_{21} = 0.3253\omega_{r1}^{\ell}$$

$$\Delta A(p,\ell) = \begin{bmatrix} 0 & 0 & 0 & 0 \\ 0 & 0 & 0 & 0 \\ 0 & 0 & 0 & 0 \\ 0 & 0 & -p\ell_1 & 0 \end{bmatrix} \tag{6.70e}$$

$$p\ell_1 = 1079.9\omega_{r1}^{p}\omega_{r1}^{\ell}$$

$$\Delta B(p) = \begin{bmatrix} 0 \\ 10.2135b_{r0}^{p} \\ 0 \\ 30.7323b_{r1}^{p} \end{bmatrix} \tag{6.70f}$$

$$\Delta B(\ell) = 0 \tag{6.70g}$$

It is noted that the damping ratio of the first flexible mode was chosen by 0.007. And the input uncertain matrix $\Delta B(\ell)$ was chosen by 0, since the variation of the lamina angle does not affect the variation of the control influence coefficient.

Now the decomposition of the system uncertain matrices can be accomplished in view of the equation (6.14) as follows.

$$D(p) = [\ 0 \quad 0 \quad -15.82\omega_{r1}^{p}(\omega_{r1}^{p}+2) \quad -0.00953\omega_{r1}^{p}\ ]$$

$$D(\ell) = [\ 0 \quad 0 \quad -15.82\omega_{r1}^{\ell}(\omega_{r1}^{\ell}+2) \quad -0.00953\omega_{r1}^{\ell}\ ] \qquad (6.71)$$

$$D(p,\ell) = [\ 0 \quad 0 \quad -31.64\omega_{r1}^{p}\omega_{r1}^{\ell} \quad 0]$$

$$E(p) = 0.09946b_{r0}^{p} + 0.9b_{r1}^{p}$$

The feedback gains K in equation (6.15) were chosen by

$$K = [\ -35 \quad -5 \quad -50 \quad -4\ ] \qquad (6.72)$$

Hence with the positive definite matrix Q=I, the solution of the Lyapunov equation (6.18) was obtained as

$$P = \begin{bmatrix} 8.683 & 0.730 & 1.295 & -0.242 \\ 0.730 & 0.189 & 1.397 & -0.0548 \\ 1.295 & 1.397 & 27.133 & -0.343 \\ -0.242 & -0.0548 & -0.343 & 0.0194 \end{bmatrix} \qquad (6.73)$$

The variation of the control influence coefficient was assumed to be bounded with $-0.06 \le b_{r0}^{p} \le 0$, and $-0.05 \le b_{r1}^{p} \le 0$ so that the condition (6.22) is satisfied. Then the p(x), which is nonlinear portion of the controller, is obtained as follows in view of the equations (6.23) and (6.26)

$$p(x) = -(\rho_1(x) + \rho_2(x) + \rho_3(x))\ \mathrm{sgn}(B_0^{T}Px), \qquad (6.74a)$$

$$\text{if} \quad |0.00143x_1 + 0.2461x_2 + 3.7167x_3 + 0.0376x_4| > \epsilon$$

or

$$p(x) = -(\rho_1(x) + \rho_2(x) + \rho_3(x))(0.00143x_1 + 0.2461x_2 + 3.7167x_3 + 0.0376x_4)/\epsilon, \tag{6.74b}$$

$$\text{if} \quad |0.00143x_1 + 0.2461x_2 + 3.7167x_3 + 0.0376x_4| \leq \epsilon$$

where

$$\rho_1(x) = \max_{\omega^p_{r1}} \{1.05374\ (15.82(2.0|\omega^p_{r1}| + (\omega^p_{r1})^2)|x_3| + 0.051(35|x_1| + 5|x_2| + 50|x_3| + 4|x_4|))\}$$

$$\rho_2(x) = \max_{\omega^\ell_{r1}} \{15.82(2.0|\omega^\ell_{r1}| + (\omega^\ell_{r1})^2)|x_3| + 0.00953|\omega^\ell_{r1}|\ |x_4|\} \tag{6.75}$$

$$\rho_3(x) = \max_{\substack{\omega^p_{r1} \\ \omega^\ell_{r1}}} \{31.64(|\omega^p_{r1}|\ |\omega^\ell_{r1}|)|x_3|\}$$

and $\text{sgn}(B_0^T P x)$ is defined by

$$\text{sgn}(B_0^T P x) = \begin{cases} 1, & \text{if } B_0^T P x > 0 \\ 0, & \text{if } B_0^T P x = 0 \\ -1, & \text{if } B_0^T P x < 0 \end{cases} \tag{6.76}$$

Figure 6.3 presents the open-loop tip displacement of the nominal system. The vibration of the first flexible mode was invoked by taking the initial conditions as

$$x(0) = \{\ 0 \quad 0 \quad 0.06 \quad 0\}^T \tag{6.77}$$

It is clear from the figure that the amplitude decays with only assumed damping ratio of the first mode.

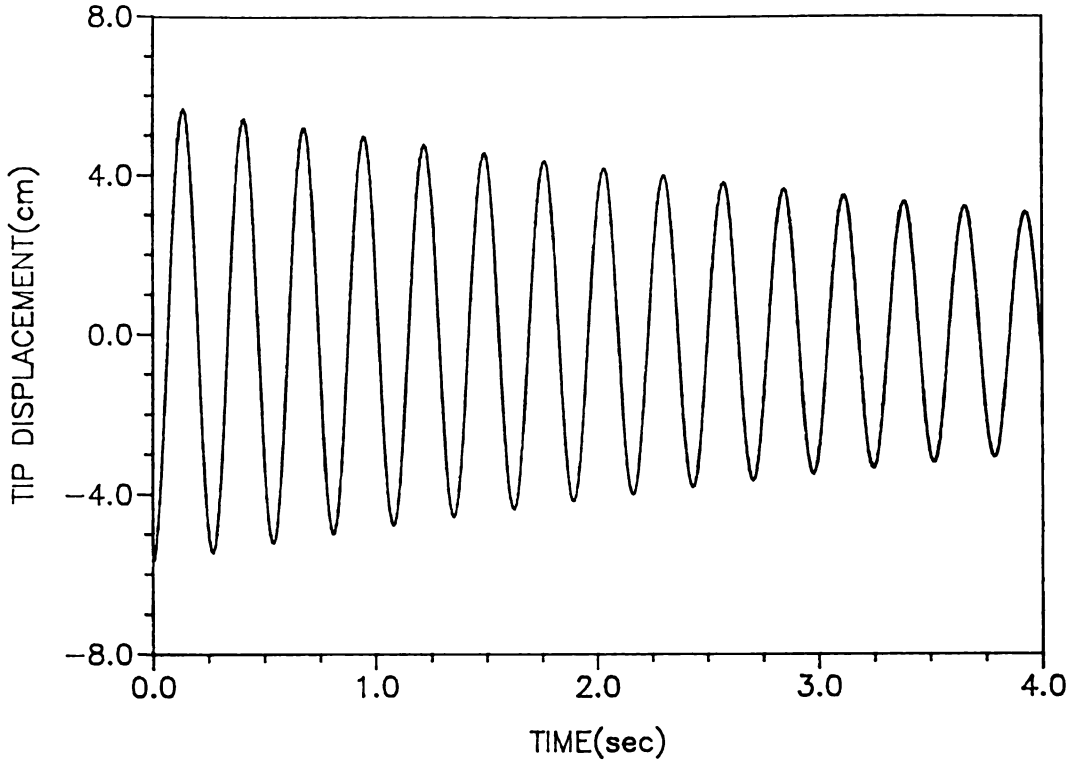


Figure 6.3 Open-Loop Tip displacement of the Nominal System

Figure 6.4 presents the simulated step responses for the commanded tip position of 15 cm with the linear and nonlinear controller. Herein the linear controller is given by $u = Kx$, and the nonlinear controller is defined by equation (6.16). The typical value of $\epsilon = 0.003$ was chosen, and the actual bound on the variation of the uncertain parameters were chosen by

$$-0.2 \leq \omega_{r1}^{p} \leq 0$$
$$-0.4 \leq \omega_{r1}^{\ell} \leq 0 \qquad (6.78)$$

The variation of ω_{r1}^{p} corresponds to the variation of payload from 0 kg to about 0.17 kg. It is noted that the mass of the flexible arm is 0.124 kg.

On the other hand, the variation of ω_{r1}^{ℓ} corresponds to the variation of the lamina angle from 20^{o} to approximately 48^{o}. For the larger variation of the uncertain parameters, both ω_{r1}^{p} and ω_{r1}^{ℓ} were taken as negative. The situation of the positive ω_{r1}^{p} and ω_{r1}^{ℓ}, which correspond to an increment of the fundamental natural frequency is not considered in this study. In fact, an increment of the natural frequency due to the payload can not be happened in practice. Furthermore, choosing the positive of ω_{r1}^{ℓ} makes the system be undergone with the smaller perturbation due to the compensation between the negative ω_{r1}^{p} and positive ω_{r1}^{ℓ}.

It is observed from the tip displacement response in Figure 6.4 that the response with the nonlinear controller settles in the commanded position in 5.8 seconds (settling-time) inducing maximum overshoot of 9 cm, while the response with the linear controller settles in the commanded position in 12 seconds (settling-time) inducing maximum overshoot of 13.8 cm. This shows that the nonlinear controller have a much better capability for regulation of the response than the linear controller in the presence of system uncertainties. This can be also interpreted that the nonlinear controller can tolerates larger system parameter variations than the linear controller. It is also interesting to observe from the input torque response that the required input torque of the nonlinear controller is about 60 percent that of the linear controller for the simulated response time.

Table 6.3 presents a comparison of the tip displacement response (settling-time and maximum overshoot) between the linear and nonlinear

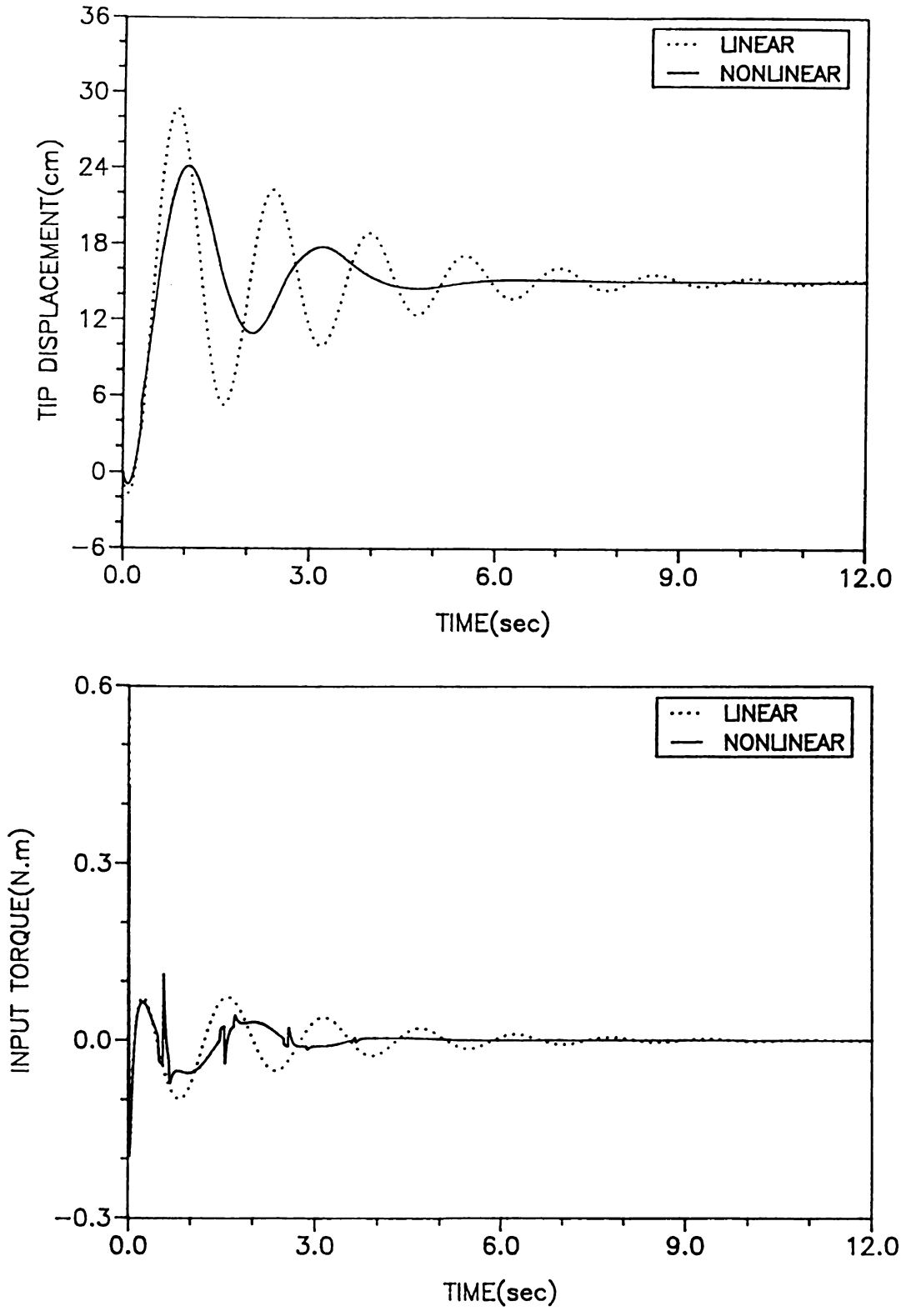
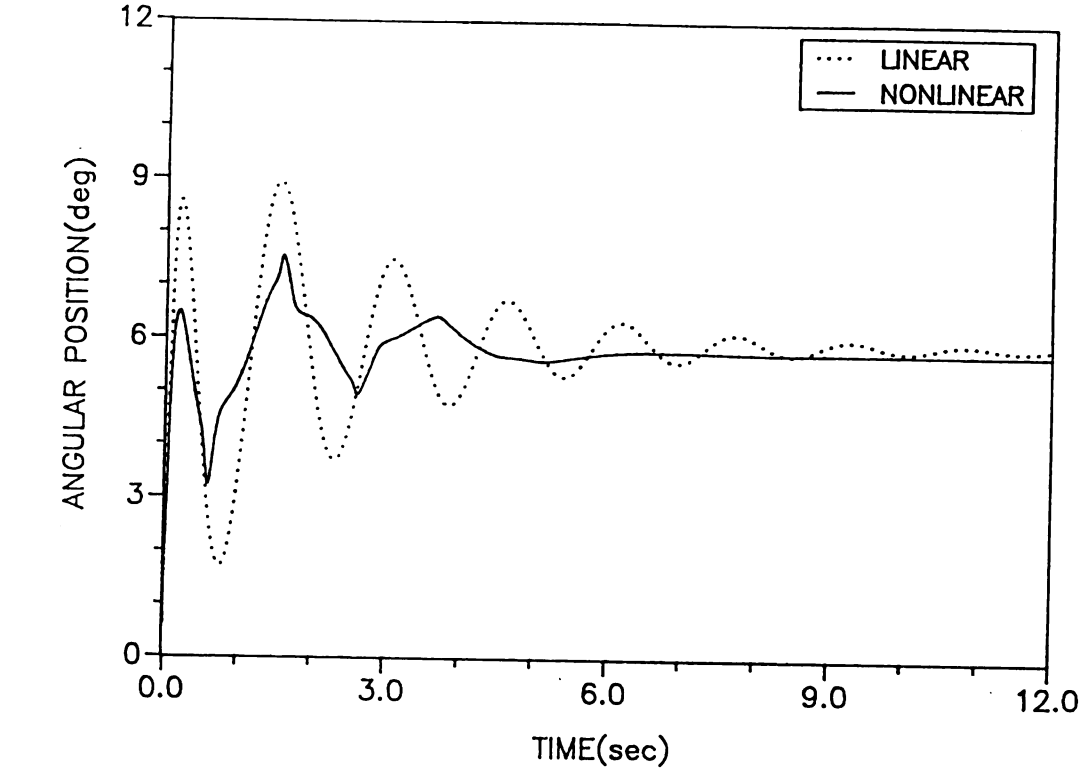


Figure 6.4 Comparison of Step Responses with the Linear and the Nonlinear Controller



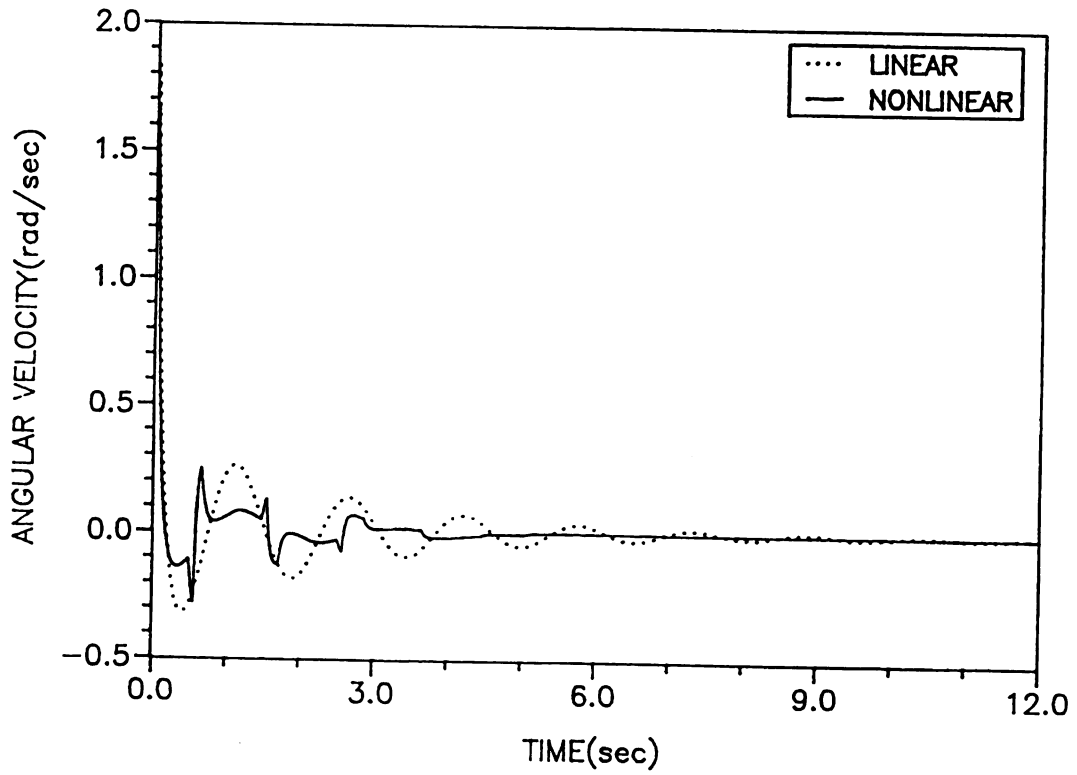


Figure 6.4 (Continued)

Table 6.3 Comparison of the Tip Displacement Response (Settling Time and Maximum Overshoot)

Variation Bound	Settling Time (sec)		Maximum Overshoot (cm)	
	Nonlinear	Linear	Nonlinear	Linear
$\omega^p_{r1} = 0$	2.9	5.8	7.1	11.3
$-0.1 \le \omega^p_{r1} \le 0$	4.5	8.6	8.2	12.6
$-0.2 \le \omega^p_{r1} \le 0$	5.8	12.0	9.4	13.8
$-0.3 \le \omega^p_{r1} \le 0$	11.6	22.1	10.8	15.5
$-0.4 \le \omega^p_{r1} \le 0$	24.3	44.5	12.4	17.0

controller under various bounds of ω^p_{r1}. The variation of the lamina angle was fixed as $-0.4 \le \omega^{\ell}_{r1} \le 0$. It is clear from the table that the settling-time with the nonlinear controller is half of that with the linear controller in all variation bounds. The bound $-0.3 \le \omega^p_{r1} \le 0$ corresponds to the varying payload from 0 kg to about 2.0 kg which is about 16 times of the arm mass. Similar results are anticipated from the various variations of the ω^{ℓ}_{r1} with the fixed variation of the ω^p_{r1}. Therefore, it is possible to adjust the variation bound of each uncertain parameter for achieving the required system performances.

Next, in order to observe the sensitiveness of the controller parameter ϵ in the equation (6.17), the different value of $\epsilon = 0.1$ was

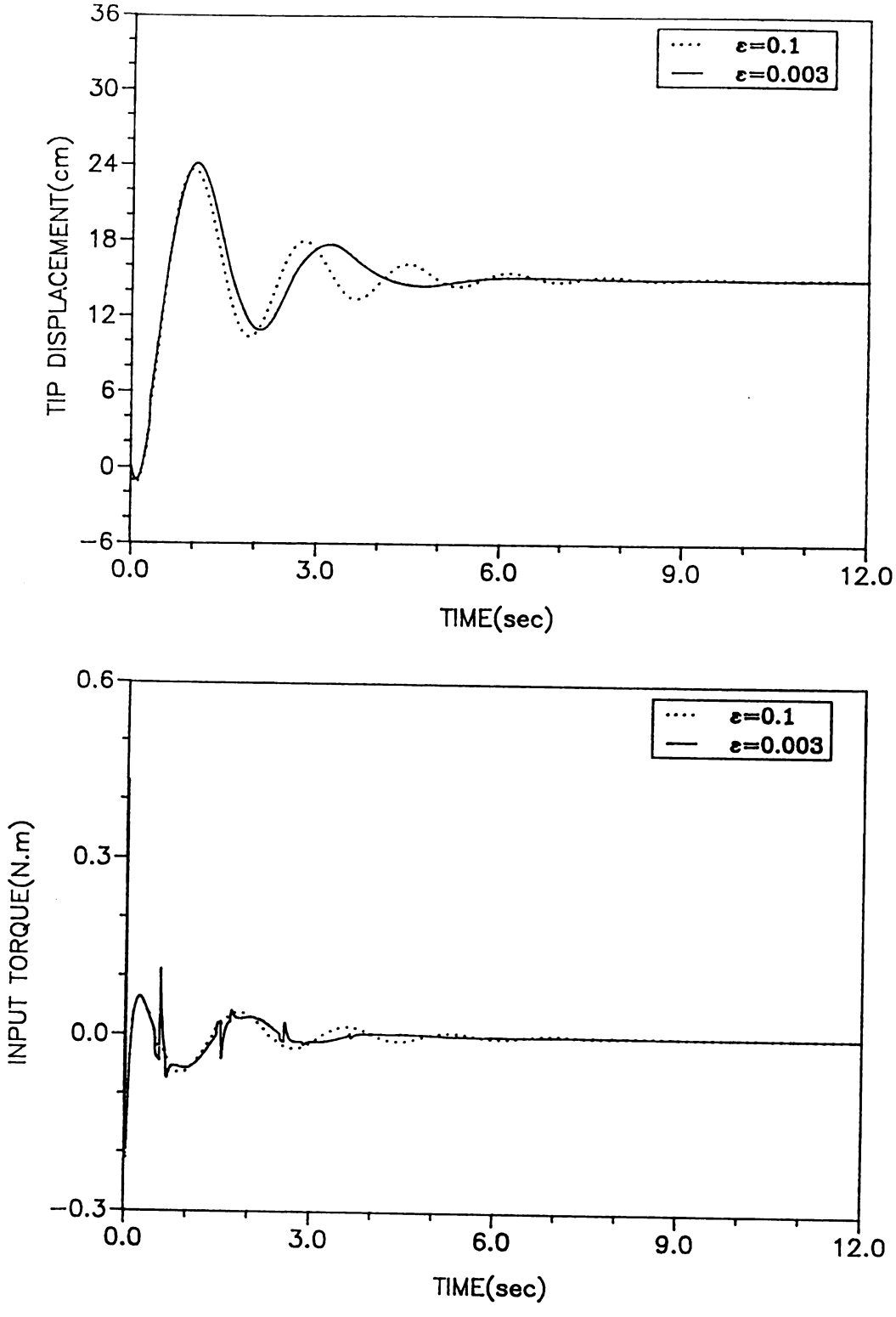


Figure 6.5 Comparison of Step Responses with ϵ=0.1 and ϵ=0.003

chosen. Figure 6.5 presents the comparison of the step responses with two different values of ϵ. It is clear from this figure that the smaller ϵ produces the better system responses. This fact is obvious from the largest ball $\tilde{\eta}$ defined by the equation (6.36). For stabilization problem, it is desirable to have $\tilde{\eta}$ as small as possible, hence increasing the robustness of the system stability. As $\epsilon \to 0$, $\eta \to 0$. However, the smaller ϵ may produce the larger unwanted vibration in practice due to the larger chattered input torque as shown in Figure 6.5.

It is finally noted that even though two uncertain parameters;the varying payload and the mismatched lamina angle were considered in this study, the approach developed herein can be extended to the case which accounts for many uncertain parameters. The manner of choosing uncertain parameters should be dependent on the physical environments conditions. For example, if the robotic system is supposed to operate under high temperature or moisture environment, these uncertain parameters should be taken into consideration.

6.5 Summary of the Chapter

The nonlinear robust controller for the composite arm was designed by utilizing the properties of the uniform and uniform ultimate boundedness of the solution. The varying payload and the lamina angle were chosen as uncertain parameters. It has been demonstrated that the nonlinear controller had much better capability for regulation of the response than the linear controller in the presence of the uncertain parameters. This implies that the larger tolerance of the fabrication error (lamina angle) of the composite arm can be allowed for the nonlinear control system, and

also the larger bound of the unknown payload is allowed with guaranteed system stability. Even though the proposed nonlinear controller was not experimentally implemented in this study, the realization of this controller would accelerate the relevant research area in the future. The extension of this controller to flexible multi-link robotic systems, and other flexible structure systems fabricated from composite materials are remained as further research areas as well as the experimental realization of this controller.

CHAPTER VII

CONCLUSIONS AND RECOMMENDATIONS

7.1 Conclusions of the Thesis

Three different control schemes for a single-link flexible manipulator fabricated from composite laminates or smart materials incorporating electro-rheological (ER) fluids were developed in this thesis ; the output feedback control, the hybrid control, and the nonlinear state feedback control robust to system parameter variations.

The output feedback controller featuring two colocated angular position and velocity sensors was designed and experimentally implemented in order to investigate and compare the control performance of the flexible manipulator fabricated from aluminum (aluminum arm) and composite laminates (composite arm). The controller design was accomplished by utilizing the root-locus technique and the Lyapunov method. In the root-locus analysis, the effect of the compensator zero was investigated by considering various location of the compensator zero. When all non-zero open-loop poles and zeros were located left to the given compensator, the system exhibited a sluggish motion without inducing overshoot. However, when the compensator zero was positioned far left to all open-loop poles and zeros, the system exhibited a fast motion with tradeoff the overshoot.

It has been demonstrated through the analytical and experimental

investigation that the composite arm had superior system performances such as faster settling-time, smaller input torque, smaller overshoot and a superior increment of stability relative to the aluminum arm. It was obtained from the measured step responses that with certain position and velocity feedback gains the delay time was 0.26 second for the aluminum arm and 0.21 second for the composite arm, and the maximum overshoot was 1.02 degree for the aluminum arm and 0.3 degree for the composite arm. It was also observed that the reduction of energy consumption by 40-50 percent for the commanded motion, and the reduction of the tip deflection up to 50 percent was accomplished by employing the composite arm. These experimental results clearly indicate the significant payoffs associated with implementing composite materials featuring superior strength- and stiffness-to-weight ratios to the commercial metals on the flexible manipulators.

It has been also shown that the implemented output feedback controller was very sensitive to the external disturbance which has a forcing frequency close to the cantilevered-mode natural frequency of the arm, regardless of the aluminum and composite arm. This attempt was undertaken herein to introduce a single-link flexible manipulator fabricated from smart materials incorporating electro-rheological fluids (smart ER arm) to obtain the robustness of the output feedback controller to the imposed disturbance with the help of distributed parameter actuator, which is characterized by embedded electro-rheological (ER) fluids in the structure.

As a sequel, the hybrid controller featuring the output feedback controller employed for the aluminum and composite arm, and the pseudo-state feedback controller associated with the distributed ER fluid

actuator was proposed and implemented on the smart ER arm in the Chapter V. Before developing the hybrid control scheme, the phenomenological equation of motion of the smart robotic system has been developed based on the experimental observations of the modal characteristics of the smart beam structure. Then, the hybrid controller was formulated based on the phenomenological equation of motion and the empirical dynamic model of the ER fluid actuator. The pseudo-control force (input voltage) associated with the pseudo-state feedback controller accounts for the change in the global damping and stiffness properties of the smart robotic arm due to electrical potentials imposed on the ER fluid domains. The stability criterion has been established for the robotic system by considering the changed properties as the plant perturbation due to electrical potentials. Moreover, this stability criterion has been modified by incorporating the empirical dynamic model of the ER fluid actuator. The modified criterion says that the stable closed-loop system with the output feedback controller remains as stable for positive input voltage considered in this investigation. It has been shown through the experimental implementation that the robustness of the employed conventional output feedback controller was significantly enhanced by employing the proposed pseudo-state feedback controller in the presence of the disturbance.

The nonlinear robust state feedback controller for the composite arm was developed for the first time to overcome uncertain system parameters associated with the varying payload encountered in the operation and the mismatched lamina angle encountered in the manufacturing process. The controller design has been accomplished by utilizing the properties of uniform and uniform ultimate boundedness of the solution. The major

difference of this approach from the currently existing approaches was that the effect of each uncertain parameter as well as the effect of the interaction of the uncertain parameters to the total system performance was considered in this study, hence providing a certain measure of the magnitude of each uncertain parameter. It has been demonstrated from the simulation that the proposed nonlinear controller could tolerate larger system parameter variations than the conventional linear controller, showing much faster settling-time and smaller overshoot with the nonlinear controller. It has been also shown that the system performance was very sensitive to control parameters such as ϵ.

The author believes that the research prosecuted in this thesis will provide significant impact on the diverse marketplace such as automobile industry and aerospace industry. And also, this complementary theoretical, computational and experimental investigation on the control methodologies for the flexible manipulators fabricated from composite laminates or smart materials incorporating ER fluids will furnish fundamental and important guidelines, and precious information for the development of the next generation robotic system characterized by high-speed of operation, high end-point positional accuracy, and also high adaptability to unstructured environments.

7.2 Recommendations for Future Work

As observed in Chapter V of this thesis, the proposed hybrid controller was implemented on the smart robot arm by applying the pseudo-control force (input voltage) in the fashion of the open-loop control. Hence, the information of the disturbance such as a forcing frequency should be identified prior to applying the proper input voltage. However,

it is possible to construct a closed-loop control system of the pseudo-state controller by employing appropriate output sensors to obtain the information of the imposed disturbance, and by identifying the system parameters as a function of the input voltage in the frequency domain. From the disturbance information and identified system parameters, the appropriate pseudo-control force can be obtained and supplied from the microprocessor to the embedded ER domains in real time. This closed-loop system will highlight the distinct merit of employing the smart robotic system which can respond to unstructured environmental conditions.

Another potential future work is to develop a flexible robotic system featuring a high level of hybrid controller associated with conventional actuators and various type of actuators incorporating smart materials. The high level of controller consists of more than three actuators which provide own individual actuating force for the different purpose and also in a different manner. Since each smart material such as ER fluids, piezoelectric materials and shape memory alloys has its own distinct characteristic as observed in the literature review in Chapter I, it is possible to construct the high level of controller which can adaptively respond to highly unstructured environments. As an example, consider a flexible robotic system featuring a conventional actuator, an ER fluid actuator and a piezoelectric actuator. When the system needs to be settled very fast, then the control force associated with the conventional actuator and the piezoelectric actuator are supposed to be activated to increase damping properties. However, if the system is subjected to a disturbance which has a forcing frequency close to the natural frequency of the robot arm, the control force associated with the ER actuator and the conventional actuator are supposed to be activated in

order to avoid the resonance phenomenon of the system. This high level of hybrid controller will provide tremendous advantages over the conventional controller in real world. The potential advantages include the self-controllability of the plant, the robustness of the controller to the uncertainties such as external and internal disturbances, the flexibility of the trajectory or work space, and the flexibility of all control parameters.

In parallel with above mentioned future work, it may be useful to develop a hierarchical control methodology for the smart flexible structures. The principal idea behind the hierarchical control methodology is that the overall control system is divided into more than two sub-control system ; for example, global controller, intermediate controllers and regional controllers in the flexible structure. By considering each finite segment actuator incorporating ER fluids or piezoelectric materials as a regional controller, sum of several segment actuators as an intermediate controller, and sum of all intermediate controllers as a global controller, the total system can be controlled for the desired system performances. This control scheme will be very useful especially for the very large flexible structures such as space station. Since there always exist wave propagation delay during the sensing of the outputs in the large flexible structures, the system instability may be arisen due to the observation spillover caused by the delay. This observation spillover problem can be eliminated by employing the hierarchical control methodology. The optimal placement of the appropriate actuator associated with each regional controller is one of the problem to be solved in the process of formulating the hierarchical controller.

Finally, the extension of the nonlinear robust state feedback controller developed in Chapter VI to the multi-links flexible manipulators, and experimental implementation of this controller are remained as a future work.

APPENDIX

APPENDIX

List of Publications

Thesis

1. S.B. Choi, " On Robust Tracking in Uncertain Systems - A Variable Structure Approach," Master Thesis, Department of Mechanical Engineering, Michigan State University, June 1986.

2. S.B. Choi, " Control of Single-Link Flexible Manipulators Fabricated from Advanced Composite Laminates and Smart Materials Incorporating Electro-Rheological Fluids," Ph.D. Thesis, MEL/IMSL, Department of Mechanical Engineering, Michigan State University, June 1990.

Refereed Journal Publications

1. M.V. Gandhi, B.S. Thompson, S.B. Choi and S. Shakir, " Electro-Rheological-Fluid-Based Articulating Robotic Systems," ASME Journal of Mechanisms, Transmissions, and Automation in Design, Vol.111, No. 3, 1989, pp. 328-336.

2. S.B. Choi, M.V. Gandhi, B.S. Thompson and C.Y. Lee, " An Experimental Investigation of an Articulating Robotic Manipulator with a Graphite-Epoxy Composite Arm," Journal of Robotic Systems, Vol.5, No.1, 1988, pp. 73-79.

3. M.V. Gandhi, B.S. Thompson and S.B. Choi, " A New Generation of Innovative Ultra-Advanced Intelligent Composite Materials Featuring Electro-Rheological Fluids: An Experimental Investigation," Journal of Composite Materials, Vol.23, 1989, pp. 1232-1255.

4. M.V. Gandhi, B.S. Thompson and S.B. Choi, " A Proof-of-Concept Experimental Investigation of a Slider-Crank Mechanism Featuring a Smart Dynamically-Tunable Connecting-Rod Incorporating Embedded Electro-Rheological Fluid Domains," Journal of Sound and Vibration, Vol. 135, No.3, 1989, pp. 511-515.

5. S.B. Choi, C.Y. Lee, B.S. Thompson and M.V. Gandhi, " Elastodynamic Characteristics of Smart Beams Incorporating Electro-Rheological Fluids.," AIAA Journal of Guidance, Control, and Dynamics (under review).

6. S.B. Choi, A. Magolan, B.S. Thompson and M.V. Gandhi, " An Experimental and Theoretical Investigation of the Static and Elastodynamic Responses of an Industrial Robotic Manipulator Featuring a Graphite-Epoxy Composite Arm," Journal of Robotic Systems (under review).

7. S.B. Choi and R.L. Tummala, " Modeling and Control of a Flexible Single-Link Robotic Arm Fabricated from Composite Materials," IEEE Transactions on Robotics and Automation (under review).

8. S.B. Choi, B.S. Thompson and M.V. Gandhi, " Smart Structures Incorporating Electro-Rheological Fluids for Vibration-Control and Active-Damping Applications: An Experimental Investigation," ASME Journal of Vibration, Acoustics, Stress and Reliability in Design (under review).

9. S.B. Choi, B.S. Thompson and M.V. Gandhi, " Modeling and Position Control of a Single-Link Flexible Robotic Manipulator Fabricated from Advanced Composite Materials," Journal of Robotic Systems (under review).

10. S.B. Choi, B.S. Thompson and M.V. Gandhi, " Modeling and Output Feedback Control of a Single-Link Flexible Robotic Manipulator Featuring a Graphite-Epoxy Composite Arm," ASME Journal of Dynamic Systems, Measurement, and Control (under review).

11. " A Nonlinear Control Robust to System Parameter Variations with Application to a Single-Link Flexible Manipulator Fabricated from Composite Laminates," (in preparation).

12. " Modeling and Control of Smart Flexible Structures Incorporating Piezoelectric Materials," (in preparation).

13. " Active-Vibration-Tuning of a Simply-Supported Beam Featuring Electro-Rheological Fluids," (in preparation).

14. " Modeling and Control of a Single-Link Flexible Robotic Manipulator Fabricated from Smart Materials Incorporating Electro-Rheological Fluids," (in preparation).

Conference Publications

1. S.B. Choi and S. Jayasuriya, " A Sliding Mode Controller Incorporating Matching Conditions Applied to Manipulators," Proceedings of the 10th IFAC World Congress, Munich, West Germany, July 1987.

2. S. Jayasuriya and S.B. Choi, " On the Sufficiency Condition for Existence of a Sliding Mode," Proceedings of 1987 American Control Conference, Minneapolis, Minn., 1987, Vol.1, pp. 84-89.

3. S.B. Choi, F. Sun, B.S. Thompson and M.V. Gandhi, " An Experimental Investigation of the Static and Dynamic Responses of an Industrial Robotic Manipulator," Proceedings of 1987 ASME Design Automation Conference, Boston, Mass., Sept. 1987, ASME Paper No. 87-DAC-50, DE-Vol.10-2, pp. 421-427.

4. M.V. Gandhi, B.S. Thompson, S.B. Choi and S. Shakir, " Electro-Rheological-Fluid-Based Articulating Robotic System," Proceedings of 1987 ASME Design Automation Conference, Boston, Mass., Sept. 1987, ASME Paper No. 87-DAC-55, DE-Vol.10-2, pp. 1-10.

5. M.V. Gandhi, B.S. Thompson and S.B. Choi, " Smart Ultra-Advanced Composite Materials Incorporating Electro-Rheological Fluids for Military, Aerospace, and Advanced Manufacturing Applications," Proceedings of the 3rd Annual ASM/ESD Advanced Composite Conference and Exposition, Detroit, MI, Sept. 1987, pp. 23-30.

6. S.B. Choi, B.S. Thompson and M.V. Gandhi, " Electro-Rheological Fluids Technology Stimulates a New Generation of Robotic and Machine Systems," Proceedings of the 10th Applied Mechanism Conference, New Orleans, La., December 1987, Vol.1, pp. 3B.1-3B1.8.

7. S.B. Choi, M.V. Gandhi, B.S. Thompson and C.Y. Lee, " An Experimental Investigation of an Articulating Robotic Manipulator with a Graphite-Epoxy Composite Arm," Proceedings of the 10th Applied Mechanism Conference, New Orleans, La., December 1987, Vol.1, pp. 3B2.1-3B2.8.

8. M.V. Gandhi, B.S. Thompson and S.B. Choi, " Ultra-Advanced Composite Materials Incorporating Electro-Rheological Fluids," Proceedings of the 4th Japan-US Composite Conference, Washington D.C., June 1988, pp. 875-884.

9. M.V. Gandhi, B.S. Thompson and S.B. Choi, " Smart Materials Incorporating Electro-Rheological Fluids: A Theoretical and Experimental Investigation," Proceedings of the 18th Annual Meeting of the Fine Particle Society, 1987 Particle/Power Technology, Microcontamination and Biotechnology Exhibition and Technology Forum.

10. S.B. Choi, B.S. Thompson and M.V. Gandhi, " An Experimental Investigation on the Active-Damping Characteristics of a Class of Ultra-Advanced Intelligent Composite Materials Featuring Electro-Rheological Fluids," Proceedings of the Damping '89 Conference, West Palm Beach, Fl., February 1989, Organized by the Flight Dynamics Laboratory of the Air Force Wright Aeronautical Laboratories, Wright Patterson Air Bases, Ohio.

11. S.B. Choi, B.S. Thompson and M.V. Gandhi, " An Active Vibration-Tuning Methodology for Smart Flexible Structures Incorporating Electro-Rheological Fluids: A Proof-of-Concept Investigation," Proceedings of 1989 American Control Conference, Pittsburgh, Pa., June 1989.

12. S.B. Choi, B.S. Thompson and M.V. Gandhi, " Smart Structures Incorporating Electro-Rheological Fluids for Vibration-Control and Active-Damping Applications: An Experimental Investigation," Proceedings of the 12th Biennial ASME Conference on Mechanical Vibration and Noise, Montreal, Canada, Sept. 1989.

13. S.B. Choi, A. Magolan, B.S. Thompson and M.V. Gandhi, " An Experimental and Theoretical Investigation of the Static and Elastodynamic Responses of an Industrial Robotic Manipulator Featuring a Graphite-Epoxy Composite Arm," Proceedings of the 1st National Conference on Applied Mechanisms and Robotics, Cincinnati, Ohio, Nov. 1989, Vol.2, pp. 8B5.1-8B5.11.

14. S.B. Choi, L.P. Chao, B.S. Thompson and M.V. Gandhi, " An Integrated Design Strategy for the Optimal Structural Fabrication and the Optimal Control of a Single-Link Flexible Manipulator Fabricated from Advanced Composite Laminates," Proceedings of the 1st National Conference on Applied Mechanisms and Robotics, Cincinnati, Ohio, Nov. 1989, Vol.2, pp. 8B4.1-8B4.10.

15. S.B. Choi, M.V. Gandhi and B.S. Thompson, " An Experimental Investigation of the Elastodynamic Responses of a Slider-Crank Mechanism Featuring a Smart Connecting-Rod Incorporating Embedded Electro-Rheological Fluid Domains," Proceedings of the 1st National Conference on Applied Mechanism and Robotics, Cincinnati, Ohio, Nov. 1989, Vol.2, pp. 9B3.1-9B3.7.

16. C.Y. Lee, S.B. Choi, B.S. Thompson and M.V. Gandhi, " A Variational Formulation for the Finite Element Analysis and Control of Linkage and Robotics Systems Featuring Smart Materials Incorporating Piezoelectric Materials," Proceedings of the 1st National Conference on Applied Mechanisms and Robotics, Cincinnati, Ohio, Nov. 1989, Vol.1, pp. 2C1.1-2C1.10.

17. S.B. Choi, B.S. Thompson and M.V. Gandhi, " A Theoretical and Experimental Investigation on the Control of a Single-Link Flexible Robotic Manipulator Fabricated from Composite Materials," to be presented at the 1990 American Control Conference, San Diego, CA, May 1990.

18. S.B. Choi, B.S. Thompson and M.V. Gandhi, " Modeling and Feedback Control of a Single-Link Flexible Robotic Manipulator Featuring a Graphite-Epoxy Composite Arm," to be presented at the 1990 IEEE International Conference on Robotics and Automation, Cincinnati, Ohio, May 1990.

Technical Reports

1. S. Shakir, L.P. Chao, S.B. Choi, M.V. Gandhi and B.S. Thompson, " Smart Materials Incorporating Electro-Rheological Fluids Technology for Articulating Systems and Advanced Structures," MSU Machinery Elastodynamics Lab. Report, Report No. 870108801, Feb. 1987.

2. S.B. Choi, B.S. Thompson and M.V. Gandhi, " The Synthesis of Smart Materials Incorporating Electro-Rheological Fluids for Military, Aerospace and Advanced Manufacturing Applications: An Interim Report," MSU Machinery Elastodynamics Lab. Report to Lord Corporation, NC, Report No. 87082501, July 1987.

3. S.B. Choi, B.S. Thompson and M.V. Gandhi, " The Synthesis of Smart Materials Incorporating Electro-Rheological Fluids for Military, Aerospace and Advanced Manufacturing Applications: An Interim Report," MSU Machinery Elastodynamics Lab. Report to Lord Corporation, NC, Report No. 87082502, December 1987.

4. S.B. Choi, B.S. Thompson and M.V. Gandhi, " The Synthesis of Smart Materials Incorporating Electro-Rheological Fluids for Military, Aerospace and Advanced Manufacturing Applications: A Final Report," MSU Machinery Elastodynamics Lab. Report to Lord Corporation, NC, Report No. 87082503, March 1988.

BIBLIOGRAPHY

BIBLIOGRAPHY

1. Abou-Hanna,J.J. and Evces,C.R., " Dynamics and Control of Flexible Manipulators," Proceedings of ASME Winter Annual Meeting, Boston, Mass., DSC-Vol.6, 1987, pp. 269-276.

2. Adriani, P.M. and Gast, A.P., " A Microscopic Model of Electro-Rheology," Journal of Physics :Fluids, Vol.31, No.10, 1988, pp. 2757-2768.

3. Arbel,A. and Gupta,N.K., " Robust Colocated Control for Large Flexible Space Structures," AIAA Journal of Guidance, Control, and Dynamics, Vol.4, No.5, 1981, pp. 480-486.

4. Archer, J.S., " Consistent Mass Matrix for Distributed Mass Systems," Proceedings of the American Society of Civil Engineers, Vol.89, 1963, pp.161-171.

5. Asada,H., Ma,Z.D. and Tokumaru,H., " Inverse Dynamics of Flexible Robot Arms for Trajectory Control," Proceedings of ASME Winter Annual Meeting, Boston, Mass., DSC-Vol.6, 1987, pp. 329-336.

6. Bailey, T. and Hubbard, J.E., " Distributed Piezoelectric-Polymer Active Vibration Control of a Cantilever Beam," AIAA Journal of Guidance and Control, Sept. 1985, Vol. 8, No. 5, pp. 605-611.

7. Balas,M.J., " Modal Control of Certain Flexible Dynamic Systems," SIAM Journal of Control and Optimization, Vol.16, No.13, 1978, pp. 450-462.

8. Balas,M.J., " Feedback Control of Flexible Systems," IEEE Transactions on Automatic Control, Vol.AC-23, No.4, 1978, pp. 674-679.

9. Balas,M.J., " Direct Velocity Feedback Control of Large Space Structures," AIAA Journal of Guidance, Control, and Dynamics, Vol.2, No.3, 1979, pp. 252-253.

10. Balas,M.J., " Trends in Large Space Structure Control Theory: Fondest Hopes, Wildest Dreams," IEEE Transactions on Automatic Control,Vol. AC-27, No.3, 1982, pp. 522-535.

11. Balas, M.J., Kaufman, H. and Wen, J., " Stable Direct Adaptive Control of Linear Infinite-Dimensional Systems Using a Command Generator Tracker Approach," Workshop on Identification and Control of Flexible Structures, San Diego, CA, June 1984.

12 Bar-kana,I. and Kaufman,H., " Some Applications of Direct Adaptive Control to Large Structural Systems," AIAA Journal of Guidance, Control,and Dynamics, Vol.7, No.6, 1984, pp.717-724.

13. Barmish,B.R. and Leitmann,G., " On Ultimate Boundedness Control of Uncertain Systems in the Absence of Matching Assumptions," IEEE Transactions on Automation Control, Vol. AC-27, No.1, 1982, pp. 153-158.

14. Barraco,A., Cuny,B. and Ishiomin,G., " Dynamic Models for Flexible Robots: Different Approaches," Proceedings of International Conference on Robotics and Automation, 1986, pp. 1038-1043.

15. Baruh,H. and Silverberg,L., " Robust Natural Control of Distributed Systems," AIAA Journal of Guidance, Control, and Dynamics, Vol.8, No.6, 1985, pp. 717-724.

16. Bayo,E., " A Finite-Element Approach to Control the End-Point Motion of a Single-Link Flexible Robot," Journal of Robotic Systems, Vol.4, No.1, 1987, pp. 63-75.

17. Baz,A. and Poh, S., " Performance of an Active Control System with Piezoelectric Actuators," Journal of Sound and Vibration, Vol.126, No. 2, 1988, pp.327-343.

18. Bellman,R., Stability Theory of Differential Equations, Dover, New York, 1969.

19. Berge,C., Topological Spaces, Oliver and Boyd, London, England, 1963.

20. Block, H. and Kelly, J.P., " Electro-Rheology," Journal of Physics D: Applied Physics, Vol.21, 1988, pp. 1661-1677.

21. Bodden,D.S. and Junkins,J.L., " Eigenvalue Optimaization Algorithms for Structure/Controller Design Iterations," AIAA Journal of Guidance, Control, and Dynamics, Vol.8, No.6, 1985, pp.697-706.

22. Book,W.J., " Analysis of Massless Elastic Chains with Servo Controlled Joints," ASME Journal of Dynamic Systems, Measurement, and Control, Vol.101, 1979, pp. 187-192.

23. Book,W.J., " Recursive Lagrangian Dynamics of Flexible Manipulator Arms," The International Journal of Robotics Research, Vol.3, No.3, 1984, pp. 87-101.

24. Book,W.J., Alberts,T.E. and Hastings,G.G., " Design Strategies for High Speed Lightweight Robots," Computers in Mechanical Engineering, Vol.26, 1986, pp. 26-33.

25. Book,W.J. and Cetinkunt,S., " Near Optimum Control of Flexible Robot Arms on Fixed Paths," Proceedings of 24th Conference on Decision and Control, Ft.Lauderdale, FL, 1985, pp. 1522-1528.

26. Book,W.J. and Majette,M., " Controller Design for Flexible, Distributed Parameter Mechanical Arms via Combined State Space and Frequency Domain Techniques," ASME Journal of Dynamic Systems, Measurement, and Control, Vol.105, 1983, pp. 245-254.

27. Book,W.J., Maizza-Neto,O. and Whitney,D.E.," Feedback Control of Two Beam, Two Joint Systems with Distributed Flexibility," ASME Journal of Dynamic Systems, Measurement, and Control, Vol.97, No.4, 1975, pp. 424- 431.

28. Brogan, W.L., Modern Control Theory, Quantum Press, New York, 1974.

29. Bullough, W.A. and Foxon, M.B., " A Proportionate Coulomb and Viscously Damped Isolation System," Journal of Sound and Vibration, Vol.56, No.1, 1978, pp. 35-44.

30. Burke, S.E. and Hubbard, J.E., " Active Vibration Control of a Simply Supported Beam Using a Spatially Distributed Actuator," IEEE Control System Magazine, Aug. 1987, pp. 25-30.

31. Cannon,R.H. and Schmitz,E., " Initial Experiments on the End-Point Control of a Flexible One-Link Robot," The International Journal of Robotics Research, Vol.3, No.3, 1984, pp. 62-75

32. Chalhoub,N.G. and Ulsoy,A.G., " Control of a Flexible Robot Arm: Experimental and Theoretical Results," ASME Journal of Dynamic Systems, Measurement, and Control, Vol.109, 1987, pp. 299-309.

33. Chang,L.W., " Dynamic Analysis of Robotic Manipulators with Flexible Links," Ph.D. Thesis, Purdue University, 1984.

34. Chassiakos,A.G. and Bekey,G.A., " On the Modeling and Control of a Flexible Manipulator Arm by Point Actuators," Proceedings of 25th Conference on Decision and Control, Athens, Greece, December 1986, pp. 1145-1150.

35. Chen, C.T., Linear System Theory and Design, Holt, Reinehart and Winston Co., New York, 1984.

36. Chen, Y.H., " On the Robustness of Mismatched Uncertain Dynamical Systems," ASME Journal of Dynamic Systems, Measurement, and Control, Vol.109, 1987, pp. 29-35.

37. Choi, S.B., Chao, L.P., Thompson, B.S. and Gandhi, M.V., " An Integrated Design Strategy for the Optimal Structural Fabrication and the Optimal Control of a Single-Link Flexible Manipulator Fabricated from Advanced Composite Laminates," Proceedings of the 1st National Conference on Applied Mechanisms and Robotics, Cincinnati, Ohio, Nov. 1989, Vol.2, pp. 8B4.1-8B4.10.

38. Choi, S.B., Gandhi, M.V., Thompson, B.S. and Lee, C.Y., "An Experimental Investigation of an Articulating Robotic Manipulator with a Graphite-Epoxy Arm," Journal of Robotic Systems, Vol. 5, 1988, pp.73-79.

39. Choi, S.B., Thompson, B.S. and Gandhi, M.V., " Electro-Rheological Fluids Technology Stimulates a New Generation of Robotic and Machine Systems," Proceedings of the 10th Applied Mechanism Conference, New Orleans, La., Dec. 1987, Vol.1, pp. 3B.1-3B1.8.

40. Choi, S.B., Thompson, B.S. and Gandhi, M.V., An Active Vibration-Tuning Methodology for Smart Flexible Structures Incorporating Electro-Rheological Fluids: A Proof-of-Concept Investigation," Proceedings of 1989 American Control Conference, Pittsburgh, Pa., June 1989.

41. Choi, S.B., Thompson, B.S. and Gandhi, M.V., " Smart Structures Incorporating Electro-Rheological Fluids for Vibration-Control and Active-Damping Applications: An Experimental Investigation," Proceedings of the 12th Biennial ASME Conference on Mechanical Vibration and Noise, Montreal, Canada, Sept. 1989.

42. Claus, R.O., Mckeeman, J.C., May, R.G. and Bennett, K.D., " Optimal Fiber Sensors and Signal Processing for Smart Materials and Structures Applications," U.S. Army Research Office Workshop on Smart Materials, Structures and Mathematical Issues, Blacksburg, VA, 1988.

43. Coddington, E.A. and Levinson, N., Theory of Ordinary Differential Equations, McGraw-Hill, New York, 1955.

44. Corless, M.J. and Leitmann, G., " Continuous State Feedback Guaranteeing Uniform Ultimate Boundedness for Uncertain Dynamic Systems," IEEE Transactions on Automatic Control, Vol. AC-26, No.5, 1981, pp. 1139-1144.

45. Crawley, E.F. and de Luis, J., " Use of Piezoelectric Actuators as Elements of Intelligent Structures," AIAA Journal, Vol. 25, No.10, 1987, pp. 1373-1385.

46. Dado,M. and Soni,A.H., " A Generalized Approach for Forward and Inverse Dynamics of Elastic Manipulators," Proceedings of IEEE International Conference on Robotics and Automation, 1986, pp. 359-364.

47. Davis,J.H. and Hirschorn,R.M., " Tracking Control of a Flexible Robot Link," IEEE Transactions on Automatic Control, Vol.33, No.3, 1988, pp. 238-248.

48. Davis,R., Henshell,R.D. and Warburton,G.B., " A Timoshenko Beam Element," Journal of Sound and Vibration, Vol.22, No.4, 1972, pp. 475-487.

49. Denavit, J. and Hartenberg, R.S., " A Kinematic Notation for Lower-Pair Mechanisms Based on Matrices," ASME Journal of Applied Mechanics, NO.22, June 1955.

50. Elliott,L.E., Mingori,D.L. and Iwens,R.P., " Performance of Robust Output Feedback Controller for Flexible Spacecraft," Proceedings of 2nd Symposium on Dynamics and Control of Large Flexible Spacecraft, Blacksburg, Virginia, 1979, pp. 409-420.

51. Everett,L.J., " Modeling and Robust Control of Compliant Robotic Manipulator via the Finite Element Method," Ph.D. Thesis, Texas A&M University, 1983.

52. Ewins,D.J., Modal Testing : Theory and Practice, Research Studies Press LTD, Bruel & Kjaer, Letchworth, England, 1984.

53. Fukuda,T., " Flexibility Control of Elastic Robotic Arms," Journal of Robotic Systems, Vol.2, No.1, 1985, pp. 73-88.

54. Gamache,D. and Thompson,B.S., " The Finite Element Design of Linkages-A Comparison of Timoshenko and Euler-Bernoulli Elements," Proceedings of ASME Conference on Design Engineering, Hartford, Connecticut, 1981, ASME Paper No. 81-DET-109.

55. Gandhi, M.V. and Thompson, B.S., Smart Materials and Structures Technologies : The Impending Revolution, Technomic Publishing Company, Inc., Lancaster, PA, 1989 (in press).

56. Gandhi, M.V., Thompson, B.S. and Choi, S.B., " A New Generation of Innovative Ultra-Advanced Intelligent Composite Materials Featuring Electro-Rheological Fluids: An Experimental Investigation," Journal of Composite Materials, Vol.23, 1989, pp. 1232-1255.

57. Gandhi, M.V., Thompson, B.S. and Choi, S.B., " A Proof-of-Concept Experimental Investigation of a Slider-Crank Mechanism Featuring a Smart Dynamically-Tunable Connecting-Rod Incorporating Embedded Electro-Rheological Fluid Domains," Journal of Sound and Vibration, Vol. 135, No.3, 1989, pp. 511-515.

58. Gandhi, M.V., Thompson, B.S., Choi, S.B. and Shakir, S., " Electro-Rheological-Fluid-Based Articulating Robotic Systems," ASME Journal of Mechanisms, Transmissions and Automation in Design, Vol.111, No.3, 1989, pp. 328-336.

59. Gevarter,W.B., " Basic Relations for Control of Flexible Vehicles," AIAA Journal, Vol.8, 1970, pp. 666-672.

60. Goldenberg,A.A. and Rakhsha,F., " Feedforward Control of a Single-Link Flexible Robot," Mechanism and Machine Theory, Vol.21, No.4, 1986, pp. 325-335.

61. Gutman, S., " Uncertain Dynamical Systems - A Lyapunov Min-Max Approach," IEEE Transactions on Automatic Control, Vol. AC-24, No.3, 1979, pp. 437-443.

62. Hale,A.L., Lisowski,R.J. and Dahl,W.E., " Optimal Simultaneous Structural and Control Design of Maneuvering Flexible Spacecraft," AIAA Journal of Guidance, Control, and Dynamics, Vol.8, No.1, 1985, pp. 86-93.

63. Hanagud, S., Won, C.C. and Obal, M.W., " Optimal Placement of Piezoceramic Sensors and Actuators," Proceedings of American Control Conference, Aug. 1988, pp. 1884-1889.

64. Hastingg, G.G. and Book, W.J., " Experiments in Optimal Control of a Flexible Arm," Proceedings of 25th IEEE Conference on Decision and Control, Athens, Greece, Dec. 1986, pp. 86-90.

65. Hastings, G.G., " Controlling Flexible Manipulators, An Experimental Investigation," Ph.D Thesis, Department of Mechanical Engineering, Georgia Institute of Technology, 1986.

66. Hughes,P.C., " Space Structure Vibration Modes: How Many Exit ? Which Ones are Important ?," IEEE Control Systems Magazine, Feb. 1987, pp. 22-28.

67. Iman, I. and Sander, G.N., " High-Speed Mechanism Design- A General Analytical Approach," ASME Journal of Engineering for Industry, Vol. 97, No. 2, 1975, pp. 609-238.

68. Johnson,T.L., " Progress in Modeling and Control of Flexible Spacecraft," Journal of the Franklin Institute, Vol.315, No.5/6, 1983, pp. 495-520.

69. Jones, R.M., Mechanics of Composite Materials, McGraw-Hill, Inc., New York, 1975.

70. Joshi,S.M., " Robustness Properties of Collocated Controllers for Flexible Spacecraft," AIAA Journal of Guidance, Control, and Dynamics, Vol.9, No.1, 1986, pp. 85-91.

71. Kapur,K.K., " Vibrations of a Timoshenko Beam, Using Finite-Element Approach," Journal of the Acoustical Society of America, Vol.40, No.5, 1966, pp. 1058-1063.

72. Khot,N.S., Eastep,F.E. and Venkayya,V.B., " Optimal Structure Modifications to Enhance the Optimal Active Vibration Control of Large Flexible Structures," Proceedings of 26th Structures, Structural Dynamics and Materials Conference, 1985, pp. 134-142.

73. Korolov,V.V. and Chen,Y.H., " Controller Design Robust to Frequency Variation in a One-Link Flexible Robot Arm," ASME Journal of Dynamic Systems, Measurement, and Control, Vol.119, 1989, pp. 9-14.

74. Krishnan,H. and Vidyasagar,M., " Control of a Single-Link Flexible Beam using a Hankel-Norm-Based Reduced Order Model," Proceedings of International Conference on Robotics and Automation, 1988, pp. 9-14.

75. Kuang,J.H. and Tsuei,Y.G., " A More General Method of Substructure Mode Synthesis for Dynamic Analysis," AIAA Journal, Vol.23, No.4, 1985, pp. 618-623.

76. Laurenson,R.M., " Modal Analysis of Rotating Flexible Structure," AIAA Journal, Vol.14, No.10, 1976, pp. 1444-1450.

77. Lawson, A.W., " The Vibration of Piezoeletric plates," Physical Review, Vol.62, July 1942, pp. 71-76.

78. Lee,H. and Castelazo,A., " Nonlinear Feedback Control of a Flexible Robot Arms," Proceedings of ASME Winter Annual Meeting, Boston, Mass., DSC-Vol.6, 1987, pp. 307-314.

79. Leitman, G., " Guaranteed Asymptotic Stability for Some Linear Systems with Bounded Uncertainties," ASME Journal of Dynamic Systems, Measurement, and Control, Vol.101, 1979, pp. 212-216.

80. Leitman, G., " On the Efficacy of Nonlinear Control in Uncertain Linear Systems," ASME Journal of Dynamic Systems, Measurement, and Control, Vol.102, 1981, pp. 95-102.

81. Leitman,G, Ryan,E.P. and Steinberg, A., " Feedback Control of Uncertain Systems : Robustness with respect to Neglected Actuator and Sensor Dynamics," International Journal of Control, Vol.43, No.4, 1986, pp. 1243-1256.

82. Liao,D.X., Sung,C.K. and Thompson,B.S., " The Design of Flexible Robotic Manipulators with Optimal Arm Geometries Fabricated from Composite Laminates with Optimal Material Properties," The International Journal of Robotics Research, Vol.6, No.3, 1987, pp. 116-130.

83. Liegeois,A., Dombre,Z. and Borrel,P., " Learning and Control for a Compliant Computer-Controlled Manipulator," IEEE Transactions on Automatic Control, Vol.AC-25, No.6, 1980, pp. 1097-1102.

84. Lin, D.X., Ni. R.G. and Adams, R.D., " Prediction and Measurement of the Vibration Damping Parameters of Carbon and Glass Fiber-Reinforced Plastics Plates," Journal of Composite Materials, Vol. 18, March 1984, pp. 132-152.

85. Lin,J.G., Hegg,D.R., Lin,Y.H. and Keat, J.E., " Output Feedback Control of Large Space Structures: An Investigation of Four Design Methods," Proceedings of 2nd Symposium on Dynamics and Control of Large Flexible Spacecraft, Blacksburg, Virginia, 1979, pp. 1-18.

86. Lin,Y.H. and Lin,J.G., " An Improved Output Feedback Control of Flexible Large Space Structures," Proceedings of 19th IEEE Conference on Decision and Control, Albuquerque, NM, 1980, pp. 1248-1250.

87. Lindberg,R.E. and Longman,R.W., " On the Number and Placement of Actuators for Independent Modal Space Control," AIAA Journal of Guidance, Control, and Dynamics, Vol.7, No.2, 1984, pp. 215-221.

88. Low,K.H., " A Systematic Formulation of Dynamic Equations for Robot Manipulators with Elastic Links," Journal of Robotic Systems, Vol.4, No.3, 1987, pp. 435-456.

89. Low,K.H. and Vidyasagar,M., " Dynamic Study of Flexible Manipulators with Open and Closed Chain Mechanism," Proceedings of ASME Winter Annual Meeting, Boston, Mass., DSC-Vol.6, 1987, pp. 277-286.

90. Low,K.H. and Vidyasagar,M., " A Lagrangian Formulation of the Dynamic Model for Flexible Manipulator Systems," ASME Journal of Dynamic Systems, Measurement, and Control, Vol.110, 1988, pp. 175-181.

91. Matsuno,F., Fukushima,S., Ohsawa,Y., Kiyohara,M. and Sakawa,Y., " Feedback Control of a Flexible Manipulator with a Parallel Drive Mechanism," The International Journal of Robotics Research, Vol.6, No.4, 1987, pp. 76-84.

92. McLaren,M.D. and Slater,G.L., " Robust Multivariable Control of Large Space Structures using Positivity," AIAA Journal of Guidance, Control, and Dynamics, Vol.10, NO.4, 1987, pp. 393-400.

93. Meckl,P. and Seering,W., " Active Damping in a Three-Axis Robotic Manipulator," Proceedings of ASME Conference on Design and Production Engineering, Dearborn, MI, Sept. 1983, ASME Paper No. 83-DET-80.

94. Meirovitch, L., Analytical Method in Vibrations, MacMillan Publishing Co., New York, 1967.

95. Meirovitch,L., Baruh,H., Montgomery,R.C. and Williams,J.P., " Nonlinear Natural Control of an Experimental Beam," AIAA Journal of Guidance, Control, and Dynamics, Vol.7, No.4, 1984, pp. 437-442.

96. Meirovitch,L. and Silverberg,L.M., " Globally Optimal Control of Self-Adjoint Distributed Systems," Proceedings of 4th Symposium on Dynamics and Control of Large Spacecraft, Blacksburg, Virginia, 1981, pp.

97. Meirovitch,L. and Silverberg,L.M., " Active Vibration Suppression of a Cantilever Wing," Journal of Sound and Vibration, Vol.97, No.3, 1984, pp. 489-498.

98. Meldrum,D.R. and Balas,M.J., " Application of Modal Reference Adaptive Control to a Flexible Remote Manipulator Arm," Proceedings of American Control Conference, Seattle, Washington, 1986, pp. 825-832.

99. Mesquita,L. and Kamat,M.P., " Structural Optimization for Control of Stiffened Laminated Composite Structures," Journal of Sound and Vibration, Vol.116, No.1, 1987, pp.33-48.

100. Miller, S.E. and Hubbard, J.E., " Smart Components for Structural Vibration Control," Proceedings of American Control Conference, 1988, pp. 1897-1902.

101. Mindlin, R.D., " High Frequency Vibrations of Piezoelectric Plates," International Journal of Solids Structures, Vol.8, 1972, pp.895-906.

102. Moerder, D.D. and Calise, A.J., " Convergence of a Numerical Algorithm for Calculating Optimal Output Feedback Gains," IEEE Transactions on Automatic Control, Vol. AC-30, No.9, 1985, pp. 900-903.

103. Morimoto,Y., Inamura,J. and Hizoguchi,K., " Dynamic Control of a Flexible Robot Arm by using Experimental Modal Analysis," Proceedings of ASME Winter Annual Meeting, Boston, Mass., DSC-Vol.6, 1987, pp. 337-343.

104. Mufti,I.H., " Modal Reference Adaptive Control for Large Structural Systems," AIAA Journal of Guidance, Control, and Dynamics, Vol.10, No.5, 1987, pp. 507-509.

105. Naganathan,G. and Soni,A.H., " Coupling Effects of Kinematics and Flexibility in Manipulators," The International Journal of Robotics Research, Vol.6, No.1, 1987, pp.75-84.

106. Nelson,W.L., Mitra,D. and Boie,R.A., " End-Point Sensing and Load-Adaptive Control of a Flexible Robot Arm," Proceedings of 24th Conference on Decision and Control, Ft.Lauderdale, FL, December 1985, pp. 1410-1415.

107. Nemir,D., Koivo,A.J. and Kashyap,R.L., " Control of Gripper Position of a Compliant Link using Strain Gage Measurements," Proceedings of 25th Conference on Decision and Control, Athens, Greece, December,1986, pp. 1140-1144.

108. Neto,O.M., " Modal Analysis and Control of Flexible Manipulator Arms," Ph.D. Thesis, Massachusetts Institute of Technology, 1974.

109. Ni, R.G. and Adams, R.D., " A Rational Method for Obtaining the Dynamic Mechanical Properties of Lamina for Predicting Stiffness and Damping of Laminated Plates and Beams," Composites, Vol. 15, No. 3, 1984, pp. 193-199.

110. Nicosia,S., Tomei,P. and Tornambe,A., " Dynamic Modeling of Flexible Robot Manipulators," Proceedings of International Conference on Robotics and Automation, 1986, pp. 365-372.

111. Omatu,S., Koide,S. and Soeda,T., " Optimal Sensor Location Problem for a Linear Distributed Parameter Systems," IEEE Transactions on Automatic Control, Vol.AC-23, No.4, 1978, pp. 665-673.

112. Onoda,J. and Haftka,R.T., " An Approach to Structure/Control Simultaneous Optimization for Large Flexible Spacecraft," AIAA Journal, Vol.25, No.8, 1987, pp. 1133-1138.

113. Patel, R.V. and Toda, M., " Quantitative Measures of Robustness for Multivariable Systems," Proceedings of JACC, San Francisco, CA, 1980, TP8-A.

114. Pestel, E.C. and Leckie, F.A., Matrix Method in Elastomechanics, McGraw-Hill Co., 1963.

115. Plump, J.M., Hubbard, J.E. and Bailey, T., " Nonlinear Control of a Distributed System : Simulation and Experimental Results," ASME Journal of Dynamic Systems, Measurement, and Control, Vol. 109, June 1987, pp. 133-139.

116. Preumont,A., " Spillover Alleviation for Nonlinear Active Control of Vibration," AIAA Journal of Guidance, Control, and Dynamics, Vol.11, No.2, 1988, pp. 124-130.

117. Rakhsha,F. and Goldenberg,A.A., " Dynamics Modeling of a Single-Link Flexible Robot," Proceedings of International Conference on Robotics and Automation, 1985, pp. 984-989.

118. Ramirez,R.B., " Design of a High Speed Graphite Composite Robot Arm," ASME Paper No. 84-DET-50.

119. Reddy, J.N., An Introduction to the Finite Element Method, McGraw-Hill, Inc., New York, 1986.

120. Rogers, C.A., Liang, C. and Barker, K.D., " Dynamic Control Concepts Using Shape Memory Alloy Reinforced Plates," U.S. Army Research Office Workshop on Smart Materials, Structures, and Mathematical Issues, Blacksburg, VA, 1988.

121. Rogowski, R.S., Heyman, J.S. and Claus, R.O., " The Evolution of Smart Composite Materials," NASA Tech Briefs, Vol. 12, No. 10, 1988, pp. 20-22.

122. Rovner,R.M. and Cannon, R.H., " Experiments Toward On-Line Identification and Control of a Very Flexible One-Link Manipulators," The International Journal of Robotics Research, Vol.6, No.4, 1987, pp. 3-19.

123. Sakawa,Y., Matsuno,F. and Fukushima,S., " Modeling and Feedback Control of a Flexible Arm," Journal of Robotic Systems, Vol.2, No.4, 1985, pp. 453-472.

124. Schaechter,D.B. and Eldred,D.B., " Experimental Demonstration of the Control of Flexible Structures," AIAA Journal of Guidance, Control, and Dynamics, Vol.7, No.5, 1984, pp. 527-534.

125. Schafer,B.E. and Holzach,H., " Experimental Research on Flexible Beam Modal Control," AIAA Journal of Guidance, Control, and Dynamics, Vol.8, No.5, 1985, pp. 597-604.

126. Schmitz,E., " Dynamics and Control of a Planar Manipulator with Elastic Links," Proceedings of 25th Conference on Decision and Control, Athens, Greece, 1986, pp. 1135-1139.

127. Schmitz, E., " Experiments on the End-Point Position Control of a Very Flexible One-Link Manipulator," Ph.D. Thesis, Department of Aeronautics and Astronautics, Stanford University, 1985.

128. Shulman, Z.P., Gorodkin, R.G., Korobko, E.V. and Gleb, V.K., " The Electro- Rheological Effect and its Possible Uses," Journal of Non-Newtonian Fluid Mechanics, Vol. 8, 1981, pp. 29-41.

129. Siciliano,B. and Book,W.J., " A Singular Perturbation Approach to Control of Lightweight Flexible Manipulators," The International Journal of Robotics Research, Vol.7, No.4, 1988, pp. 79-90.

130. Siciliano,B., Book,W.J. and Maria,G., " An Integral Manifold Approach to Control of a One Link Flexible Arm," Proceedings of 25th Conference on Decision and Control, Athens, Greece, December 1986, pp. 1131-1134.

131. Siciliano,B., Calise,A.J. and Jonnalagadda,V.R.P., " Optimal Output Fast Feedback in Two-Time Scale Control of Flexible Arms," Proceedings of 25th Conference on Decision and Control, Athens, Greece, 1986, pp. 1400-1403.

132. Siciliano,B., Yuan,B.S. and Book,W.J., " Model Reference Adaptive Control of a One Link Flexible Arm," Proceedings of 25th Conference on Decision and Control, Athens, Greece, 1986, pp. 91-95.

133. Singh,S.N. and Coelho, A.A.R., " Nonlinear Control of Mismatched Uncertain Linear Systems and Application to Control of Aircraft," ASME Journal of Dynamic Systems, Measurement, and Control, Vol.106, 1984, 00. 203-210.

134. Singh,S.N. and Schy,A.A., " Control of Elastic Robotic Systems by Nonlinear Inversion and Modal Damping," ASME Journal of Dynamic Systems, Measurement, and Control, Vol.108, 1986, pp. 180-189.

135. Skaar,S.B., Michel,A.N. and Miller,R.K., " Stability of Viscoelastic Control Systems," IEEE Transactions on Automatic Control, Vol.33, No.4, 1988, pp. 348-357.

136. Stanway, R., Sproston, J. and Firoozian, R., " Identification of the Damping Law of an Electro-Rheological Fluid : A Sequential Filtering Approach," ASME Journal of Dynamic Systems, Measurement, and Control, Vol. 111, 1989, pp. 91-96.

137. Stevens, N.G., Sproston, J.L. and Stanway, R., " An Experimental Study of Electro-Rheological Torque Transmission," ASME Journal of Mechanisms, Transmission, and Automation in Design, Vol. 110, 1988, pp. 182-188.

138. Stevens, N.G., Sproston, J.L. and Stanway, R., " The Influence of Pulsed D.C. Input Signals on Electro-Rheological Fluids," Journal of Electrostatics, Vol.17, 1985, pp. 181-191.

139. Stevens, N.G., Sproston, J.L. and Stanway, R., " On the Mechanical Properties of Electro-Rheological Fluids," ASME Journal of Applied Mechanics, Vol.54, 1987, pp. 456-458.

140. Stangroom, J.E., " Electrorheological Fluids," Journal of Physics Technology, Vol. 14, 1983, pp. 290-296.

141. Streit,D.A., Krousgrill,C.M. and Bajaj,A.K., " Dynamic Stability of Flexible Manipulators Performing Repetitive Tasks," Proceedings of Robotics and Manufacturing Automation, 1985, pp. 121-136.

142. Sunada,W.H. and Dubowsky,S., " The Application of Finite Element Methods to the Dynamic Analysis of Flexible Spatial and Co-Planar Linkage Systems," ASME Journal of Mechanical Design, Vol.103, 1981, pp. 643-651.

143. Sunada,W.H. and Dubowsky,S., " On the Dynamic Analysis and Behavior of Industrial Robotic Manipulators with Elastic Members," ASME Journal of Mechanisms, Transmissions, and Automation in Design, Vol.1035, 1983, pp. 43-51.

144. Thomas,D.L., Wilson,J.M. and Wilson,R.R., " Timoshenko Beam Finite Elements," Journal of Sound and Vibration, Vol.31, No.3, 1973, pp. 315-330.

145. Thompson,B.S., " Composite Laminate Components for Robotic and Machine Systems: Research Issues in Design," ASME Applied Mechanics Review, Vol.40, No.11, 1987, pp. 1545-1552.

146. Thompson,B.S. and Sung,K.S., " A Variational Formulation for the Dynamic Viscoelastic Finite Element Analysis of Robotic Manipulators Constructed from Composite Materials," ASME Journal of Mechanisms, Transmission, and Automation in Design, Vol.106, 1984, pp. 183-190.

147. Thompson,B.S. and Sunk,C.K., " The Design of Robots and Intelligent Manipulators using Modern composite Materials," Mechanism and Machine Theory, Vol.20, No.6, 1985, pp. 471-482.

148. Thomson, W.T., Theory of Vibration with Applications, Prentice-Hall Inc., Englewood Cliffs, NJ, 1091.

149. Tracy, J.J. and Pardoen, G.C., " Effect of Delamination on the Natural Frequency of Composite Laminates," Journal of Composite Materials, Vol.23, No.12, 1989, pp. 1200-1215.

150. Truckenbrodt,A., " Modeling and Control of Flexible Manipulator Structures," Proceedings of 4th CISM-IFToMM Symposium, Theory and Practice of Robots and Manipulators, Warsaw, 1981.

151. Uejima, H., " Dielectric Mechanism and Rheological Properties of Electro-Fluids," Japanese Journal of Applied Physics, Vol. 11, No. 3, 1972, pp. 319-326.

152. User's Manual for PLC-2/16 and PLC 2/17 Microprocessor, Allen-Bradley, 1987.

153. Usoro,P.B., Nadira,R. and Mahil,S.S., " A Finite/Lagrange Approach to Modeling Lightweight Flexible Manipulators," ASME Journal of Dynamic Systems, Measurement, and Control, Vol.108, 1986, pp. 199-205.

154. Waite, S.R., Tatan, R.P. and Jackson, A., " Use of Optical Fibre for Damage and Strain Detection in Composite Materials," Composites, Vol. 19, No.6, 1988, pp. 435-442.

155. Wang,P.K.C. and Wei,J.D., " Vibrations in a Moving Flexible Robot Arm," Journal of Sound and Vibration, Vol.116, No.1, 1987, pp.149-160.

156. Wang,S.H., Hsia,T.C. and Wiederrich,J.L., " Open-Loop Control of a Flexible Robotic Manipulator," International Journal of Robotics and Automation, Vol.1, No.2, 1986, pp. 54-57.

157. Wang,W.J., Lu,S.S. and Hsu,C.F., " Output Feedback Control of a Flexible Robot Arm," Proceedings of 25th Conference on Decision and Control, Athens, Greece, 1986, pp. 86-90.

158. Wang,W.J., Lu,S.S. and Hsu,C.F., " Experiments on the Position Control of a One-Link Flexible Robot Arm," IEEE Transactions on Robotics and Automation, Vol.5, No.3, 1989, pp. 373-377.

159. West-Vukovich,G.S., Davison,E.J. and Hughes,P.C., " The Decentralized Control of Large Flexible Space Structures," IEEE Transactions on Automatic Control, Vol.AC-29, No.10, 1984, pp. 866-879.

160. Winslow, W.M., " Induced Fibration Suspensions, " Journal of Applied Physics, Vol. 20, 1949, pp. 1137-1140.

161. Yaeger, J.R., " A Practical Shape-Memory Electromechanical Actuator," Proceedings of International Symposium on Automotive Technology and Automation, Milan, Italy, 1984, pp. 633-642.

162. Yuan,B.S. and Book,W.J., " A Robust Scheme for Direct Adaptive Control of Flexible Arms," Proceedings of ASME Winter Annual Meeting, Boston, Mass., DSC-Vol.6, 1987, pp. 261-268.

163. Zalucky,A. and Hardt,D.E., " Active Control of Robot Structure Deflection," ASME Journal of Dynamic Systems, Measurement and Control, Vol.106, 1984, pp.63-69.